



USDOT Tier 1  
University Transportation Center  
on Improving Rail Transportation  
Infrastructure Sustainability and Durability

Final Report UNLV-1

**MOBILE 3D PRINTING OF RAIL TRACK SURFACE FOR RAPID  
REPAIRMENT**

by

Arman Ali Mohammadi, Graduate Student

Ershad Mortazavian, Graduate Student,

Zhiyong Wang, Ph.D., Associate Professor  
Department of Mechanical Engineering

and

Hualiang (Harry) Teng, Ph.D., Professor  
Department of Civil and Environmental Engineering and Construction  
University of Nevada Las Vegas

September 2024

Grant Number: 69A3551747132



## **DISCLAIMER**

The contents of this report reflect the views of the authors, who are responsible for the facts and the accuracy of the information presented herein. This document is disseminated in the interest of information exchange. The report is funded, partially or entirely, by a grant from the U.S. Department of Transportation's University Transportation Centers Program. However, the U.S. Government assumes no liability for the contents or use thereof.

## ABSTRACT

This study reports on mobile 3D printing of rail track surface for rapid repairment. The frequent replacement of worn rails on tracks brings an immense economic burden on the railroad industry, and also causes significant interruptions to railroad operation. Restoration of worn rails via additive manufacturing, i.e., 3D printing, can considerably reduce the associated maintenance costs. The scope of this study is to utilize metal additive manufacturing (AM) technologies to repair worn rails that are used in the U.S. railway transportation system (e.g. 75-lb/yd light transit rails, or 136-lb/yd heavy freight rails). More specifically, this study aims to understand the interactive mechanisms between the deposited materials and the high-carbon rail steel to identify and alleviate the effect of the associated drawbacks, i.e., residual thermal stresses, micro pores, micro cracks, and martensite nucleation, on the resulting mechanical and metallurgical properties of the repaired rail.

Submerged arc welding (SAW) and laser powder deposition (LPD) have been selected as two potential AM approaches for rail repair. Various deposition steels such as rutile E71T-1C and Lincore 40-S wire for the SAW process, and 304L stainless steel, 410L stainless steel, Stellite 6, and Stellite 21 in the powder form for the LPD process have been chosen to be deposited on the surface of the railhead.

A finite element (FE) model is developed and later fine-tuned in which the thorough process of the AM rail repair is simulated through an element-birth-and-kill method and all of the involved interactions including thermal interactions, mechanical evolutions, and kinetics of phase transformation are defined and given to the model. The FE model development is simultaneously followed by similar experimental lab investigations to verify the model outcomes and hence, validate the developed FE model.

This study attempts to modify the mechanical and metallurgical properties of the repaired rail through different approaches, i.e., deposition material alteration, preheating, post heat treatment, AM method alteration, and tool path alteration. Regarding the mechanical properties, distribution of hardness and residual stresses are measured via Rockwell hardness test and X-ray diffraction (XRD) stress measurement, respectively. Evaluation of the distribution of micro-pores, micro-cracks, and metallurgical phases is carried out through scanning electron microscope (SEM), optical microscope (OM), and XRD analysis. The tensile/compressive yield and shear strength of the repaired rail are assessed via 3-point bending and tensile tests, respectively. Initial efforts are performed through experimental lab measurements, and further efforts for various deposition materials and AM process parameters are conducted through the validated FE model and numerous lab tests.

One set of 3D printing configurations for heavy rail (136-lb/yd) received yield strength exceeding the AREMA standards in the lab test, and tensile strength slightly below the standards. Three sets of 3D printing configurations for light rails (75-lb/yd) obtained good results (exceeding the AREMA standards) for both yield strength and tensile strength. However, 3D printing leads to high hardness and low elongation to rails, which requires post heat treatment for property adjustment.

## CONTENTS

DISCLAIMER .....	ii
ABSTRACT.....	iii
1. CHAPTER 1 INTRODUCTION.....	1
1.2. Background and Motivation .....	1
1.2.1. Repair via submerged arc welding (SAW).....	1
1.2.2. Repair via laser powder deposition (LPD).....	2
References for Chapter 1 .....	5
2. CHAPTER 2 MATERIALS AND EXPERIMENTAL METHODS .....	10
2.1. Materials .....	11
2.1.1. Rail.....	11
2.1.2. Deposition.....	12
2.2. Additive manufacturing (AM) repair mechanism.....	13
2.2.1. Submerged arc welding (SAW).....	13
2.2.2. Laser powder deposition (LPD).....	14
2.2.3. Tool path.....	14
2.3. Sample preparation .....	15
References for Chapter 2 .....	20
3. CHAPTER 3 MICROSTRUCTURAL ANALYSIS OF THE REPAIRED RAIL ...	21
3.1. Light rail.....	21
3.1.1. SAW-repaired light rail.....	21
3.1.2. LPD-repaired light rail.....	31
3.2. Heavy rail.....	43
3.2.1. SAW-repaired heavy rail .....	43
References for Chapter 3 .....	47
4. CHAPTER 4 HARDNESS MEASUREMENT OF THE REPAIRED RAIL.....	49
4.1. Light rail.....	49
4.1.1. SAW-repaired light rail.....	49
4.1.2. LPD-repaired light rail.....	51
4.2. Heavy rail.....	54
4.2.1. SAW-repaired heavy rail .....	54
4.2.2. LPD-repaired heavy rail.....	56
References for Chapter 4 .....	58
5. Chapter 5 RESIDUAL STRESS MEASUREMENT OF THE REPAIRED RAIL ...	59
5.1. Light rail.....	59
5.1.1. LPD-repaired light rail.....	59
5.2. Heavy rail.....	64
5.2.1. SAW-repaired heavy rail .....	64
5.2.2. LPD-repaired heavy rail.....	67
References for Chapter 5 .....	72
6. Chapter 6 SIMULATING THE RAIL-REPAIR PROCESS USING FINITE ELEMENT ANALYSIS (FEA).....	73
6.1. Finite element (FE) model development.....	73
6.1.1. Thermal calculation .....	74
6.1.2. Kinetic calculation .....	79



6.1.3. Mechanical calculation .....	83
6.2. FE model validation .....	85
6.2.1. Thermal field.....	85
6.2.2. Hardness and microstructure distribution .....	85
6.2.3. Residual stress distribution .....	88
References for Chapter 6 .....	91
7. Chapter 7 STUDY ON THE EFFECT OF PREHEATING AND DEPOSITION MATERIALS ON THE RESIDUAL STRESSES IN THE REPAIRED RAIL USING THE VERIFIED FE MODEL .....	93
7.1. Effect of preheating and deposition alloy .....	93
7.1.1. Case I .....	94
7.1.2. Case II .....	95
7.1.3. Case III.....	97
7.1.4. Case IV.....	98
7.2. Optimum preheating temperature and deposition alloy.....	98
References for Chapter 7 .....	102
8. Chapter 8 FLEXURAL AND SHEAR STRENGTH EVALUATION .....	103
8.1. Flexural evaluation of the weld materials in SAW-repaired heavy rail.....	103
8.1.1. Calculation of flexural and shear stress .....	103
8.1.2. Failure mode analysis .....	108
8.2. Flexural evaluation at the rail-weld interface in SAW-repaired heavy rail .....	112
8.2.1. Calculation of flexural and shear stress .....	112
8.2.2. Failure mode analysis .....	118
References for Chapter 8 .....	125
9. Chapter 9 MODIFIED FINITE ELEMENT MODELING AND VALIDATION OF SUBMERGED ARC WELDING FOR REPAIRING 136RE HEAVY RAILS .....	126
10. Chapter 10 ADDITIONAL MECHANICAL AND METALLURGICAL ASSESSMENT OF SUBMERGED ARC SURFACED RAIL .....	142
11. Chapter 11 LAB TESTS ON RAILS WITH ESAB SAW EQUIPMENT .....	163
Chapter 12 CONCLUSIONS AND RECOMMENDATIONS.....	169
ACKNOWLEDGEMENTS.....	191
ABOUT THE AUTHOR .....	192

## LIST OF FIGURES

Fig. 2.1 (a) worn light rail, (b) repaired light rail, (c) worn heavy rail, and (d) repaired heavy rail. .....	11
Fig. 2.2 Schematic illustration of a SAW setup.....	13
Fig. 2.3 Schematic illustration of an LPD setup.....	15
Fig. 2.4 Graphical illustration of the AM tool path. Every single layer is deposited along +/-x direction, and the layers are built upon one another along +y direction.....	15
Fig. 2.5 (a) the LPD-repaired rail, (b) a slice cut from the head of the repaired rail (the boundaries between deposition layers are shown as black dashed lines), and (c) the extracted specimen from the slice cut. ....	16
Fig. 2.6 (a) Locations of extracting thin bending specimen from weld materials for flexural tensile/compressive strength evaluation, (b) typical thin bending specimen dimensions, (c) location of extracting thick bending specimen for shear strength evaluation at the rail-weld interface, and (d) typical thick bending specimen dimensions (all dimensions are in millimeters).....	19
Fig. 3.1 (a) a chopped piece from the metallographic as-built (AB) specimen; (b) Optical macrograph covering weld zone (WZ), heat-affected zone (HAZ), and rail zone; OM micrographs of (c) WZ1, (d) WZ2, (e) WZ3, (f) HAZ, (g) rail, (h) WZ/HAZ fusion boundary, and (i) HAZ/rail fusion boundary are also illustrated. ....	22
Fig. 3.2 (a) a chopped piece from the metallographic specimen of the as-built (AB) specimen; (b) Optical macrograph covering weld zone (WZ), heat-affected zone (HAZ), and rail zone; SEM micrographs of (c) WZ1, (d) WZ2, (e) WZ3, (f) HAZ, and (g) rail are also illustrated.....	23
Fig. 3.3 Fe-Al quasi-binary phase diagram for the low-aluminum (0.5 wt.% of Al content) E71T-1C weld wire used for SAW-repair process [2]; $\delta$ : $\delta$ -ferrite, $\alpha$ : $\alpha$ -ferrite, $\gamma$ : austenite, and Fe <sub>3</sub> C: cementite. ....	25
Fig. 3.4 (a) a chopped piece from the metallographic as-quenched (AQ) specimen; (b) Optical macrograph covering weld zone (WZ), heat-affected zone (HAZ), and rail zone; OM micrographs of (c) WZ1, (d) WZ2, (e) WZ3, (f) HAZ, (g) rail, (h) WZ/HAZ fusion boundary, and (i) HAZ/rail fusion boundary are also illustrated. ....	28
Fig. 3.5 (a) a chopped piece from the metallographic as-quenched (AQ) specimen; (b) Optical macrograph covering weld zone (WZ), heat-affected zone (HAZ), and rail zone; SEM micrographs of (c) WZ1, (d) WZ2, (e) WZ3, (f) HAZ, and (g) rail are also illustrated.....	29
Fig. 3.6 (a) The metallographic sample chopped from the AB specimen; (b) A comprehensive OM macrograph covering DZ, HAZ, and rail; (c) OM micrograph of the rail and (d) HAZ; OM micrographs of DZ are separated layer-wise in (e), (f), (g), (h), (i), and (j), representing first, second, third, fourth, fifth, and sixth deposition layers, respectively. ....	32
Fig. 3.7 (a) The metallographic sample chopped from the AB specimen; (b) A comprehensive SEM macrograph covering DZ, HAZ, and rail; (c) SEM micrograph of the rail and (d) HAZ; SEM micrographs of DZ are separated layer-wise in (e), (f), (g), (h), (i), and (j), representing first, second, third, fourth, fifth, and sixth deposition layers, respectively. ....	33
Fig. 3.8 Phase diagram of the Fe-Cr-Ni pseudobinary system for 304L (70 wt.% Fe) used in powder form for the LPD repair process. L: liquid; $\delta$ : $\delta$ -ferrite; $\gamma$ : austenite; $\sigma$ : sigma. ....	35
Fig. 3.9 (a) The metallographic sample chopped from the heat-treated (HT) specimen; (b) A comprehensive OM macrograph covering DZ and rail; (c) OM micrograph of rail and (d) HAZ; due to the disappearance of the interlayer boundaries at the DZ, OM micrographs are taken from	

the same corresponding locations in Fig. 7 at the (e) first, (f) second, (g) third, (h) fourth, (i) fifth, and (j) sixth deposition layers. ....	38
Fig. 3.10 (a) The metallographic sample chopped from the heat-treated (HT) specimen; (b) A comprehensive SEM macrograph covering DZ and rail; (c) SEM micrograph of rail and (d) HAZ; due to the disappearance of the interlayer boundaries at the DZ, OM micrographs are taken from the same corresponding locations in Fig. 8 at the (e) first, (f) second, (g) third, (h) fourth, (i) fifth, and (j) sixth deposition layers. ....	39
Fig. 3.11 Close view of the microcracks that are developed in the heat-treated (HT) specimen at the rail-DZ interface through (a) OM and (b) SEM morphology. ....	41
Fig. 3.12 (a) An etched specimen extracted from the head of the repaired rail, (b) A thorough OM capture from the entire weld zone with the four layers deposited, the heat-affected zone (HAZ), and the rail; closer OM shots are taken from (c) fourth, (d) third, (e) second, and (f) first weld layers, (g) weld-HAZ interface, (h) HAZ, (i) HAZ-rail interface, and (j) rail.....	44
Fig. 3.13 Fe-Cr phase diagram for the Lincore 40-S hard-facing wire used in the SAW process	46
Fig. 4.1 (a) Hardness test plan showing the lines along which hardness is measured on the demonstrated points; (b) hardness distribution for the as-built (AB) sample; (c) hardness distribution for the as-quenched (AQ) sample; (d) putting both the AB and AQ hardness distribution results together (the red dashed line represents the minimum acceptable hardness for light-duty rail, assigned according to AREMA's standards [1]). ....	50
Fig. 4.2 Hardness distribution: (a) in the as-built (AB) rail; (b) in the heat-treated (HT) rail. The red dashed lines represent the minimum required hardness for standard U.S. light rails assigned by AREMA [1]. ....	52
Fig. 4.3 Hardness distribution on the head of the repaired rail showing the (a) hardness test plan and hardness distribution along (b) Line 1 (c) Line 2, and (d) Line 3; the vertical dashed line in all of the graphs located the rail-weld interface and the horizontal red dash-dot line shows the minimum acceptable hardness based on AREMA standards [1]......	55
Fig. 4.4 Hardness test results from the as-built (AB) LPD-repaired heavy rail; (a) schematic map of the points and lines on which the hardness is measured; (b) hardness distribution along line 1, (c) line 2, and (d) line 3; the horizontal red dashed line represents the minimum acceptable hardness for heavy rails, assigned according to AREMA's standards [1], and the vertical green line represents the location of the rail-deposition interface. ....	57
Fig. 5.1 Coordinate system upon which the results are presented for the LPD-repaired light rail. ....	59
Fig. 5.2 Diffraction Peak Pattern through the full range of $2\theta$ for (a) 304L deposition steel and (b) C-Mn light rail. ....	60
Fig. 5.3 Horizontal line profile from the surface of the repaired rail specimen at three different stages of as-built (AB), as-polished (AP), and as-etched 1 (AE1). ....	61
Fig. 5.4 The measured (a) longitudinal, $\sigma_l$ , (b) transversal, $\sigma_t$ , and (b) normal, $\sigma_n$ , residual stresses via XRD at point $(x,y,z) = (20,3,13)$ (See Fig. 1 for configuration of the coordination system) for different stages of sample preparation, i.e., as-built (AB), as-polished (AP), and five etching steps (AE1 to AE5). ....	62
Fig. 5.5 Obtained plots of inter-planar spacing, $d$ , versus $\sin^2\psi$ from XRD measurement of (a) $\sigma_l$ at $(z, y) = (0, 0)$ , (b) $\sigma_t$ along rail-deposition interface at $x = 0$ plane, and (c) $\sigma_n$ at $(x, z) = (0, 0)$ . Refer to Fig. 1 for configuration of the reference coordination system.....	63
Fig. 5.6 XRD phase scan analysis at the (a) weld section, and (b) rail section of the repaired rail. ....	65

Fig. 5.7 Measured residual stresses using XRD method at spot 1 (shown in red in Sec. 2.3, Fig. 5c) along the (a) longitudinal and (b) transversal directions at different stages of the specimen; As-built (A-B), Polished (P) and first to fifth time of etching (E-1 to E-5). .....	66
Fig. 5.8 Measured (a) longitudinal and (b) transversal residual stresses using XRD on the E-5 specimen at all the spots shown in Sec. 2.3, Fig. 5c; the upper $x$ axis shows the spot numbers and the lower $x$ axis shows their distance from spot 5. ....	67
Fig. 5.9 Diffraction Peak Pattern through the full range of $2\theta$ for (a) 304L deposition steel and (b) heavy rail.....	68
Fig. 5.10 The XRD measured (a) longitudinal ( $\sigma_{xx}$ ) and (b) transversal ( $\sigma_{zz}$ ) residual stress distribution in the repaired rail. the upper $x$ -axis denotes the corresponding measuring point (refer to Sec. 2.3, Fig. 5c for configuration of the points). .....	69
Fig. 6.1 A flowchart illustrating the designated work plan for coupled thermal-kinetic-mechanical calculations in the developed FE model for simulating AM rail repair process.....	74
Fig. 6.2 Distribution of laser source power and laser ultimate power along the laser strike diameter at $y' = S = 11$ mm (refer to Sec. 2.2.2, Fig. 3 for $(x',y')$ coordination).....	77
Fig. 6.3 Graphical illustration of the element-birth-and-kill method that is used to simulate the LPD process in the FE model in 4 steps, i.e., (a) modeling the solution domain, (b) discretizing the solution domain into finite elements, (c) killing the deposition elements at the beginning (here shown for the $T_i = 25^\circ\text{C}$ ), and (d) bearing the killed deposition elements step by step. ....	78
Fig. 6.4 Schematic diagrams showing the defined phase-transformation paradigms applied to the kinetic analysis of the FE model for each of the deposition tool steels, i.e., (a) 304L stainless steel and (b) 410L stainless steel, (c) Stellite 6 and Stellite 21 ( $M_{s(S6)}$ and $A_{c(S6)}$ correspond to the Stellite 6 case, and $M_{s(S21)}$ and $A_{c(S21)}$ correspond to the Stellite 21 case), and (d) rail. ....	80
Fig. 6.5 General mapping of the areas where the dimensional comparison of the dilution depth between the predicted and measured results is performed. Referring to Sec. 5.1.1, Fig. 1, this figure shows the rail transversal cross section at $x = 75$ mm. ....	85
Fig. 6.6 Thermal contour distribution of the FE model versus the OM macrograph for dimensional comparison of dilution region between the numerical and experimental results at the (a) and (b) 5th, (c) and (d) 11th, and (e) and (f) 17th deposition row of the first and fifth deposition layers, respectively. ....	86
Fig. 6.7 Experimental vs. numerical hardness results; (a) schematic map of the points and lines on which the hardness is measured; (b) hardness distribution along line 1, (c) line 2, and (d) line 3. ....	87
Fig. 6.8 Distribution of hardness and austenite volume fraction, $f_\delta$ , along line 2 (refer to Fig. 7a for configuration of line 2). ....	88
Fig. 6.9 Experimental vs. numerical residual stress distribution; (a) longitudinal stress, $\sigma_l$ , along $x$ direction at $(y, z) = (0, 0)$ , (b) transversal stress, $\sigma_t$ , along $z$ direction at rail-deposition interface for $x = 0$ , and (c) normal stress, $\sigma_n$ , along $y$ direction at $(x, z) = (0, 0)$ . Refer to Sec. 5.1.1, Fig. 1 for configuration of the reference coordination system. ....	89
Fig. 7.1 (a) Longitudinal, (b) transversal, and (c) normal residual stress distributions for 304L repaired rail (Case I) along paths along $x$ , $z$ , and $y$ directions, respectively. (Refer to Sec. 5.1.1, Fig. 1 for configuration of the coordinate system.) .....	94
Fig. 7.2 (a) Longitudinal, (b) transversal, and (c) normal residual stress distributions for 410L repaired rail (Case II) along $x$ , $z$ , and $y$ directions, respectively. (Refer to Sec. 5.1.1, Fig. 1 for configuration of the coordinate system.) .....	96

Fig. 7.3 (a) Longitudinal, (b) transversal, and (c) normal stress distributions for Stellite 6 repaired rail (Case III) along x, z, and y directions, respectively. (Refer to Sec. 5.1.1, Fig. 1 for configuration of the coordinate system.)	97
Fig. 7.4 (a) Longitudinal, (b) transversal, and (c) normal stress distributions for Stellite 21 repaired rail (Case IV) along x, z, and y directions, respectively. (Refer to Sec. 5.1.1, Fig. 1 for configuration of the coordinate system.)	98
Fig. 7.5 (a) Longitudinal, (b) transversal, and (c) normal stress distributions along x, z, and y directions, respectively, for the repaired rails with different deposition alloys at the preheating temperature of 600°C. (Refer to Sec. 5.1.1, Fig. 1 for configuration of the coordinate system.)	100
Fig. 7.6 Normalized (a) longitudinal, (b) transversal, and (c) normal stress distributions along x, z, and y directions, respectively, for the repaired rails with different deposition alloys at the preheating temperature of 600°C. (Refer to Sec. 5.1.1, Fig. 1 for configuration of the coordinate system.)	100
Fig. 8.1 Force (P) – displacement ( $\delta$ ) diagram extracted instantly from 3-point bending test of the thin specimen extracted from the weld materials of the SAW-repaired heavy rail.	103
Fig. 8.2 Schematic depiction of the 3-point bending test on the thin specimen extracted from weld materials.	103
Fig. 8.3 Bending stress distribution at the location of the applied 3-point bending test.	104
Fig. 8.4 Shear and moment diagrams for the sample under bending load in 3-point bending test.	105
Fig. 8.5 Shear flow diagram at the cross section of the thin bending specimen shown in Fig. 2.	106
Fig. 8.6 The resultant stress-strain diagram from the 3-point bending test of the thin specimen extracted from the weld materials of the SAW-repaired heavy rail. The related force-displacement diagram is given in Fig. 1.	108
Fig. 8.7 A schematic view of the deflected thin bending specimen.	108
Fig. 8.8 SEM macrograph from the fracture surface of the 3-point bending specimen; (a) an overall view from the whole fracture surface and (b) a closer view to the surface.	109
Fig. 8.9 EDS scan analysis of different locations of the fracture surface of the bending specimen to figure out the nature of the observable black islands based on their chemical composition (each chemical element is represented by its wt.%).	112
Fig. 8.10 Force (P) – displacement ( $\delta$ ) diagram extracted instantly from 3-point bending test of the thick specimen extracted from the rail-weld interface of the SAW-repaired heavy rail.	113
Fig. 8.11 (a) Schematic depiction of the 3-point bending test on the thick specimen extracted from rail-weld interface, and (b) a closer look at the cross section of the specimen in Y-Z plane.	114
Fig. 8.12 The resultant stress-strain diagram from the 3-point bending test of the thick specimen extracted from the rail-weld interface of the SAW-repaired heavy rail. The related force-displacement diagram is given in Fig. 10.	116
Fig. 8.13 Cross section of the bending specimen divided into 3 zones as a reference for calculation of the first moment of area and moment of inertia.	117
Fig. 8.14 Mohr’s circle drawn based on the applied plane and shear failure stresses to the thick bending specimen extracted from the rail-weld interface.	119
Fig. 8.15 SEM macrograph from the fracture surface of the thick 3-point bending specimen extracted from the rail-weld interface; (a) an overall view from the whole fracture surface and (b) a closer view to the surface.	120

Fig. 8.16 EDS scan analysis of random locations of the upper side of the fracture surface of the thick bending specimen to figure out the chemical consistency of the rail material compared to that of the weld material shown in Fig. 9 (each chemical element is represented by its wt.%). .....	121
Fig. 8.17 Distribution of the weight percentage of different chemical elements in separate graphs throughout the weld and rail areas. The b-g measurement locations on the x-axis correspond to the locations where EDS chemical measurement is conducted, as shown in Figs. 9b-g and Figs. 16b-g for the weld and rail materials, respectively. ....	123
Fig. 8.18 Distribution of the weight percentage of different chemical elements in a single graph throughout the weld and rail areas. The b-g measurement locations on the x-axis correspond to the locations where EDS chemical measurement is conducted, as shown in Figs. 9b-g and Figs. 16b-g for the weld and rail materials, respectively. ....	124
Figure 9.1 (a) The to-be-repaired 136RE worn rail; (b) milled rail; (c) repaired rail .....	128
Figure 9.2 Original and worn rail profiles .....	131
Figure 9.3 mesh zones generated in the solid bodies.....	132
Figure 9.4 Graphical show of the model's procedure (step1).....	133
Figure 9.5 Graphical and numerical temperature distribution resulted from the model.....	133
Figure 9.6 Graphical show of the model's procedure (step 2).....	134
Figure 9.7 Fe-Cr phase diagram for the Lincore 40-S hard-facing wire used in the SAW process .....	134
Figure 9.8 A Schematic Diagram of the Microstructure Evolution Pattern Defined in Fe Modeling During the Additive Manufacturing (Lpd) Process, and its Cyclic Heating and Cooling for (A) Deposition Materials (304l Stainless Steel), and (B) Substrate (Rail). $\Delta$ : $\Delta$ Ferrite; A: A Ferrite; and $\Gamma$ : Austenite .....	137
Figure 10.1 (a) The to-be-repaired 136RE worn rail, (b) milled rail, and (c) repaired rail .....	144
Figure 10.2(a) Repaired Rail, (b) The extracted slice from the repaired rail, (c) the extracted, polished XRD specimen from the slice, and (d) the etched XRD specimen .....	146
Figure 10.3 (a) Extracted slice as the hardness test specimen and (b) the hardness test plan ....	147
Figure 10.4(a) Locations of extracting the tensile specimens from weld and rail materials, (b) typical tensile test specimen dimensions (all dimensions are in millimeters), (c) the tensile test specimen fixed in the machine test jigs. ....	148
Figure 10.5 Surface roughness measurement of the XRD specimen at different conditions; before polishing (i.e., As-built), after polishing (i.e., Polished), and after etching (i.e., Etched).....	149
Figure 10.6 XRD phase scan analysis at the (a) weld section and (b) rail section of the repaired rail .....	151
Figure 10.7 Measured residual stresses using the XRD method at spot 1 (shown in red in Fig. 2d) along the (a) longitudinal and (b) transversal directions at different stages of the specimen; As-built (A-B), Polished (P) and first to fifth time of etching (E-1 to E-5) .....	152
Figure 10.8 Measured (a) longitudinal and (b) transversal residual stresses using XRD on the E-5 specimen at all the spots shown in Fig. 2d; the upper x-axis shows the spot numbers, and the lower x-axis shows their distance from spot 5 .....	153
Figure 10.9(a) An etched specimen extracted from the head of the repaired rail, (b) A thorough O.M. capture from the entire weld zone with the four layers deposited, the heat-affected zone (HAZ), and the rail; closer O.M. shots are taken from (c) fourth, (d) third, (e) second, and (f) first weld layers, (g) weld-HAZ interface, (h) HAZ, (i) HAZ-rail interface, and (j) rail.....	156
Figure 10.10 Fe-Cr phase diagram for the Lincore 40-S hard-facing wire used in the SAW process .....	156

Figure 10.11 Hardness distribution on the head of the repaired rail showing the (a) hardness test plan and hardness distribution along (b) Line 1, (c) Line 2, and (d) Line 3; the vertical dashed line in all of the graphs located the rail-weld interface and the horizontal red dash-dot line shows the minimum acceptable Hardness based on AREMA standards [30].....	158
Figure 10.12 Stress-Strain diagram resulting from tensile tests on samples of (a) weld area and (b) base area.....	159
Figure 10.13 Failure shapes of the weld area samples.....	159
Figure 11.1 ESAB SAW equipment .....	164
Figure 11.2: Control console.....	164

## LIST OF TABLES

Table 1 Chemical composition of the to-be-repaired rail steels (wt.%) .....	11
Table 2 Required mechanical properties for the light and heavy rails .....	12
Table 3 Chemical composition of the utilized SAW wires (wt.%).....	12
Table 4 Chemical composition of the agglomerated flux used for the SAW-repairing process (wt.%).....	12
Table 5 Chemical composition of the utilized LPD steel powders (wt.%).....	13
Table 6 Chemical composition of different zones of the as-built (AB) SAW-repaired light rail specimen (wt.%) .....	24
Table 7 Chemical composition of different zones of the as-quenched (AQ) SAW-repaired light rail specimen (wt.%) .....	30
Table 8 Chemical composition of the as-built (AB) LPD-repaired light rail specimen at different zones (wt.%) .....	34
Table 9 Chemical composition of the heat-treated (HT) LPD-repaired light rail specimen at different zones (wt.%).....	40
Table 10 Chemical composition (wt.%) of different areas of the repaired rail .....	43
Table 11 Measured residual stress values at different locations of the as-etched 5 (AE5) LPD-repaired rail sample (Refer to Fig. 1 for configuration of the coordinate system) .....	62
Table 12 Grid Independence Test .....	79
Table 13 Temperature/microstructure-dependent mechanical and thermal properties of the rail and deposition tool steels used in FE modeling of the LPD-rail-repair process .....	84
Table 14 Chemical composition of the utilized LPD steel powders (wt.%).....	93
Table 15 An overview of the employed study plan to investigate the residual stress out of the FE model results .....	93
Table 16 Estimation of the yield strength of the weld materials of the SAW-repaired rail based on the measured hardness data using the developed relationship by Juvinall and Marshek [6], i.e., Eq. 14.....	110
Table 17 Young’s modulus of the rail and weld materials .....	117



# 1. CHAPTER 1 INTRODUCTION

## 1.2. Background and Motivation

It is more than a decade that additive manufacturing (AM), i.e., 3D printing, is introduced as a viable technique for repairing damaged surfaces of metallic components [8,9]. There are various available AM methods such as submerged arc welding (SAW), gas metal arc welding (GMAW), plasma arc welding (PAW), laser powder deposition (LPD), and selective laser sintering (SLS). These AM techniques can be generally categorized into two groups: laser-based and arc-based. On one hand, there is an extensive agreement on laser-based methods because of their lower limitations regarding metallurgical consistency and a wider range of available deposition materials. On the other hand, arc-based techniques are quite popular because of their much faster scanning speed and deposition rate than the laser-based processes; which is a very important factor in case of mass production [10].

Among the available laser-based methods, while SLS is indeed practical for manufacturing metallic tools from the scratch, LPD (i.e., laser cladding) is the appropriate technique for repairing/restoring an already-manufactured steel component. In the matter of arc-based approaches, SAW has the highest quality and productivity along with the easiest applicability and is the most appropriate method for high-thickness welding [11,12].

In railroad industry, incorporation of AM for repairing worn rails has become the focal point of most of the studies attributed to railway maintenance during the recent years. This research stream was initiated by Kral et al. [13] in 2004, and ever since a growing amount of studies are investigating different aspects of this idea. Deterioration of rails typically occurs as a result of the rail-wheel interactions, resulting in detrimental damages such as wear and rolling contact fatigue [14,15]. In the following, the backgrounds of utilization of SAW and LPD as potential repair tools for repairing impaired steels are presented separately.

### 1.2.1. Repair via submerged arc welding (SAW)

Arc-based weld surfacing is generally an imperative process in hard-facing and cladding for the maintenance and repair of tools in order to extend their operating life under wear and corrosion conditions [16]. A compelling enhancement in wear and fatigue performance of submerged arc surfaced components is demonstrated in numerous studies. Grum et al. [17] accomplished an experimental investigation on surfacing Ni-Co-Mo alloys on a parent structural steel using SAW method. The results indicated admirable hardness and fine dendritic microstructure in the surface layers. In another study [10], they compared the SAW process with laser process for surface repairing of a maraging steel using homemade alloys as the cladding materials, where the results are compared based on the micro-structural, micro-chemical, and micro-hardness properties. Researchers in [18–22] conducted a regression analysis according to a set of lab results obtained through their tests on submerged arc surfaced metal substrates. They subsequently developed a model regarding the available regression using different methods such as neural networks and factorial design. The specified model presented a correlation between process inputs such as voltage, nozzle-to-plate distance, traveling speed, wire feed rate, and the process responses including dilution dimensions, reinforcement, and penetration. The models are viable in finding the optimum SAW process parameters for a specific surfacing application. Wang et al. [23, 24]

explored surface repair of an H13 steel via SAW technology. They used homemade flux-cored wires composed of deoxidizer and alloys along with a commercial wire. They examined the microstructure, hardness, and dry sliding wear and illustrated that the added layer has superior properties compared to the parent H13 steel.

All of the aforementioned studies are devoted to analysis of the SAW process for surface repairing of components in use in different industries like aerospace and agriculture. In railway application, Lee et al. [25] assessed the lifetime of a UIC60 rail that is protectively coated via overlay arc welding. They developed an FE model to predict residual stress distribution for different welding depths to figure out the optimum welding geometry. Jun et al. [26] conducted a consecutive analysis of failure and crack growth on an arc-weld-repaired UIC60 rail to find out the effect of residual stresses on these parameters. They also simulated the arc-weld-surfacing process using FE method in which a semi-elliptical crack was assumed to be initiated at the weld/heat-affected zone boundary in order to simulate the fatigue crack growth. Feng et al. [27] analyzed the pros and cons of on-line welding and post heat treatment of standard rails in China. In Thailand, Srikarun [28] also investigated abrasive wear performance of R260 rails that are repaired by shield metal arc welding (SMAW). Repairing of damaged surface of UIC-54 rails used in Malaysia railway network using SMAW is investigated by SaifulAkmal and Wahab [29]. A numerical model investigating the rolling contact fatigue performance and material defects of a weld-repaired rail is developed by Kabo et al. [30] in Sweden. While these featured studies are devoted to the investigation of arc welding method as a rail repair technique, any study specifically devoted to the submerged arc welding (SAW) as a potential rail repair approach is missing in the open literature. The major difference between SAW and other arc welding processes is that the coverage of the weld joint by flux particles first prevents contamination intrusion and oxidation in the final weld structure, and second minimizes the heat loss during the welding process which increases the travel speed and, subsequently, the productivity rate. It also helps increasing bonding strength between weld beads by developing a secure fusion boundary between welds. Besides, the available literature solely focused on the standard rails used in the railway networks in China, Thailand, Malaysia, and Sweden; no study has yet focused on weld-repairing American standard rails such as 75-lb ASCE and 136RE.

### **1.2.2. Repair via laser powder deposition (LPD)**

Investigation of LPD-repairing of various impaired steel tools such as AISI-SAE 4140H [31], Fe-Mn-Si-Cr-Ni alloys [32], and CoCr1.5FeNiNb0.5 coatings [33] can be found in the open literature. Specifically speaking of industrial application of the LPD-repairing technique, Shepeleva et al. [34] presented a way to increase the wear resistance of the contact surfaces of gas turbine engine blades' shroud shelves through laser cladding. In aerospace industry, Sexton et al. [35] investigated repairing of nickel-based alloys by depositing two different deposition materials on five various substrate materials. Assessment of LPD for repairing high-strength AISI 4340 steels in aeronautical structures is undertaken by Sun et al. [36].

In railway industry, there are several studies where different aspects of LPD application for rail repair are investigated experimentally and numerically. A European project named INFRA-STAR has solely focused on European R260 rails and developed a twin-disk test setup for RCF test to evaluate the wear performance of the deposition materials [37-41]. A numerical simulation of the

twin-disk system was then conducted by Ringsberg et al. in 2005 [42] to investigate laser cladding as a potential preventative approach for R260 rails, and the results were validated based on the reported measurements by INFRA-STAR experiments. A similar experimental investigation on laser clad R260 rails is undertaken by Clare et al. [43,44] where different candidate deposition alloys are investigated based on the output properties. Further recent studies on European R260 and R200 rails in which LPD is utilized as a preventative maintenance technique by cladding a single layer of premium steel on the rail surface to enhance its fatigue and wear life are carried out by Lewis et al. [45], Narayanan et al. [46], and Lu et al. [47]. In Korea, assessment of wear characteristics of LPD-coated KS60 Korean rails is conducted by Seo et al. [41]. They tried depositing a layer of different alloys to attain the lowest achievable wear rate. Exploration of the laser clad U71Mn and U75V standard Chinese rails regarding their wear and fatigue characteristics is performed by Wenjian Wang et al. [49-51], Fu et al. [52], Guo et al. [53], Zhu et al. [54], Ding et al. [55], Zhao et al. [56], Xia et al. [57], and Xinlin Wang et al. [58]. Meng et al. investigated further laser-based approaches, i.e., laser-induction hybrid cladding (LIHC) [59-62] and laser dispersed quenching [63], as a replacement for the regular LPD in consideration of surface coating the U71Mn Chinese rails. They figured out that LIHC can yield to better strength and fracture properties, and is also able to eliminate sites of crack initiation and martensite nucleation in the deposited materials. An investigation on the wear and rolling contact fatigue of the C-class wheel steels and standard Chinese rails through different hardness ratio and creepages is carried out by Hu et al. [64]. Shariff et al. [65] explored the effect of laser cladding on sliding wear resistance of standard India's T-12 rail steel under two different conditions, i.e., first, laser hardening without any deposition, and second, laser melting by depositing one layer of hardened steel. Aladesanmi et al. [66] tried depositing various mixtures of Titanium ceramics and Titanium boride powders on the standard African rail surface and compared the wear and fatigue performance of different mixture ratios. The impact of different LPD process parameters and different deposition materials on the resulting mechanical, metallurgical, and tribological properties of the laser clad standard Australian hypereutectoid rails is studied by a research group in Monash University [67-72].

Almost all studies thus far have primarily examined laser cladding as a preventative means by surface coating the railhead using a single clad layer or, at most, double clad layers. Every deposition layer has a solid-state transformation and cooling rate that is highly reliant on the bed temperature, where the bed may be the rail or the formerly deposited layer. Also, adding multiple deposition layers will induce frequent reheating cycles to the lower layers, while a single deposition layer will not experience such reheating cycle because no layer is deposited on top of it. Therefore, a thorough repairing of a worn rail by adding multiple deposition layers on the railhead is a quite different scenario from depositing one or two layers only for the preventative purposes. Although LPD is acknowledged as one of the most advanced AM processes, there is still a great chance of developing undesired microstructures and material properties through this procedure. Local solidification parameters and solid-state transformation during cooling of the deposition layers are instances of those parameters that affect the resulting microstructure and materials properties. As the deposition layers are sequentially added in a consecutive manner during LPD, forming every new layer induces a new thermal cycle to the previously deposited layers, resulting in a new solid-state transformation. Therefore, analysis of the concluding microstructure distribution and material properties of the deposited part needs a detailed consideration of the effects of LPD processing parameters and tool path on the thermal history of

every single point of the deposition layers. Hence, a comprehensive theoretical and experimental intuition of all of the involved physical interactions is necessary to optimize the process. Numerical simulation is the most affordable means to analyze the physical interactions during the LPD process and finally find the optimum parameters for a typical LPD rail repair. Development of an optimum process to repair standard U.S. rails needs a thorough assessment of mechanical and metallurgical properties of the repaired rail. Therefore, one of the major motivations of this study is to develop a validated FE model that simulates AM repairing of a rail. This model will provide a reliable backbone for further investigations on different AM process parameters to find the most optimized way for rail repair. In summary, the primary contributions of this study can be listed as follows:

- Literature review showed that all of the studies focused on surfacing the rails with a single or, at most, a couple of deposited layers majorly as a preventative approach to reduce the wear rate and increase the fatigue life of the rail rather than fully repairing the rail. As it was mentioned earlier, investigation of the mechanical and metallurgical properties of a multi-layer deposition structure is a complete different scenario than investigating a single deposition layer because of the different heat accumulation history. This is the first study that explores fully repairing a rail with multiple deposition layers.
- This is the first presented FE model as a beneficial tool for studying various process parameters to figure out the optimized condition for complete repairing of a worn rail via AM. Although Lee et al. [25] and Jun et al. [26] simulated the overlay arc welding process for protective coating of a UIC60 rail and Ringsberg et al. [42] numerically investigated the residual stress distribution in a laser-coated R260 rail with a single clad layer of Co-Cr alloy for preventative maintenance approach, i.e., not for full-repair approach, no numerical model has been developed so far aiming investigation of a fully repaired rail with multiple deposition layers added on top.
- All of the studies available in the open literature investigated the operation of LPD for repairing standard rail grades in Europe, Korea, China, India, Africa, and Australia. There is no study yet focusing on the application of AM for repairing standard rails used in the United States railway system. Therefore, this is the first study stream which focuses on repairing rail grades complying with the standards of the American associations (e.g. AREMA, ASCE, ARA, etc.).

## References for Chapter 1

- [1] E. Mortazavian, Z. Wang, H. Teng, Effect of heat treatment on microstructure and hardness of a worn rail repaired using laser powder deposition, *Int. J. Transp. Sci. Technol.* 11(2) (2022) 406-422. <https://doi.org/10.1016/j.ijst.2021.05.004>.
- [2] E. Mortazavian, Z. Wang, H. Teng, Finite element investigation of residual stresses during laser powder deposition process as an innovative technique to repair worn rails, *Proc. Inst. Mech. Eng. F J. Rail Rapid Transit* (2022). <https://doi.org/10.1177/09544097221089410>.
- [3] E. Mortazavian, Z. Wang, H. Teng, Measurement of residual stresses in laser 3D printed train rail using X-ray diffraction technique, *IMECE2021-69822* (2022) V02AT02A005. <https://doi.org/10.1115/IMECE2021-69822>.
- [4] E. Mortazavian, Z. Wang, H. Teng, Finite element investigation of thermal-kinetic-mechanical evolutions during laser powder deposition as an innovative technique for rail repair, *Int. J. Adv. Manuf. Technol.* 118 (2022) 319-342. <https://doi.org/10.1007/s00170-021-07873-y>.
- [5] E. Mortazavian, Z. Wang, H. Teng, Repair of light rail track through restoration of the worn part of the railhead using submerged arc welding process, *Int. J. Adv. Manuf. Technol.* 107 (2020) 3315-3332. <https://doi.org/10.1007/s00170-020-05208-x>.
- [6] E. Mortazavian, Z. Wang, H. Teng, Thermal-kinetic-mechanical modeling of laser powder deposition process for rail repair, *IMECE2019-10758* (2020) V02AT02A052. <https://doi.org/10.1115/IMECE2019-10758>.
- [7] E. Mortazavian, Z. Wang, H. Teng, Thermal-mechanical study of 3D printing technology for rail repair, *IMECE2018-86315* (2019) V002T02A052. <https://doi.org/10.1115/IMECE2018-86315>.
- [8] A.A. Siddiqui, A.K. Dubey, Recent trends in laser cladding and surface alloying, *Opt. Laser Technol.* 134 (2021) 106619. <https://doi.org/10.1016/j.optlastec.2020.106619>.
- [9] L. Zhu, P. Xue, Q. Lan, G. Meng, Y. Ren, Z. Yang, P. Xu, Z. Liu, Recent research and development status of laser cladding: A review, *Opt. Laser Technol.* 138 (2021) 106915. <https://doi.org/10.1016/j.optlastec.2021.106915>.
- [10] J. Grum, J.M. Slabe, A comparison of tool-repair methods using CO<sub>2</sub> laser surfacing and arc surfacing, *Appl. Surf. Sci.* 208 (2003) 424-431. [https://doi.org/10.1016/S0169-4332\(02\)01427-7](https://doi.org/10.1016/S0169-4332(02)01427-7).
- [11] S. Bharathi, A. Arul, M. Moshi, S.R. Sundara Bharathi, R. Rajeshkumar, R. Kumar, Factors influencing submerged arc welding on stainless steel—a review, *APRN J. Eng. Appl. Sci.* 11(2) (2016) ISSN: 1819-6608.
- [12] P.T. Houldcroft, *Submerged-arc welding*, Abington Publishing (1989) UK. ISBN: 1855730022.
- [13] R.F. Kral, S.A. Mayhill, M.Q. Johnson, M.E. Rovnyak, D.J. Coomer, Method of repairing a rail, US Patent (2004) US7520415B2.
- [14] D.F. Cannon, K.O. Edell, S.L. Grassie, K. Sawley, Rail defects: an overview, *Fatigue Fract. Eng. Mater. Struct.* 26(10) (2003) 865-86. <https://doi.org/10.1046/j.1460-2695.2003.00693.x>.
- [15] R. Masoudi Nejad, M. Shariati, K. Farhangdoost, Effect of wear on rolling contact fatigue crack growth in rails, *Tribol. Int.* 94 (2016) 118-125. <https://doi.org/10.1016/j.triboint.2015.08.035>.
- [16] R.S. Parmar, *Welding processes and technology*, Khanna Publishers, New Delhi (2003) ISBN: 9788174091260, 8174091262.

- [17] J. Grum, R. Kejžar, J.M. Slabe, Submerged arc surfacing of Ni–Co–Mo alloys similar to maraging steels on a structural steel, *J. Mater. Process. Technol.* 155–156 (2004) 2011–2018. <https://doi.org/10.1016/J.JMATPROTEC.2004.04.214>.
- [18] N. Murugan, R.S. Parmar, S.K. Sud, Effect of submerged arc process variables on dilution and bead geometry in single wire surfacing, *J. Mater. Process. Technol.* 37(1–4) (1993) 767–780. [https://doi.org/10.1016/0924-0136\(93\)90135-S](https://doi.org/10.1016/0924-0136(93)90135-S).
- [19] H.L. Tsai, Y.S. Tarnng, C.M. Tseng, Optimisation of submerged arc welding process parameters in hardfacing, *Int. J. Adv. Manuf. Technol.* 12(6) (1996) 402–406. <https://doi.org/10.1007/BF01186928>.
- [20] J. Grum, J.M. Slabe, The use of factorial design and response surface methodology for fast determination of optimal heat treatment conditions of different Ni–Co–Mo surfaced layers, *J. Mater. Process. Technol.* 155–156 (2004) 2026–2032. <https://doi.org/10.1016/J.JMATPROTEC.2004.04.220>.
- [21] V.V. Peremitko, Wear-resistant arc surfacing over the layer of alloying charge, *Pat. Weld. J.* (2014). <https://doi.org/10.15407/tpwj2014.08.09>.
- [22] V.N. Matviyenko, L.K. Leschinsky, V.A. Mazur, Heating and melting of the parent metal in submerged-arc surfacing with a composite strip electrode, *Weld Int.* 29(4) (2015) 291–295. <https://doi.org/10.1080/09507116.2014.921375>.
- [23] X. Wang, J. Wang, Z. Gao, D.H. Xia, W. Hu, Fabrication of graded surfacing layer for the repair of failed H13 mandrel using submerged arc welding technology, *J. Mater. Process. Technol.* 262 (2018) 182–188. <https://doi.org/10.1016/J.JMATPROTEC.2018.06.040>.
- [24] X. Wang, J. Wang, Z. Gao, D.H. Xia, W. Hu, Tempering effects on the microstructure and properties of submerged arc surfacing layers of H13 steel, *J. Mater. Process. Technol.* 269 (2019) 26–34. <https://doi.org/10.1016/J.JMATPROTEC.2019.01.024>.
- [25] S.H. Lee, S.H. Kim, Y.S. Chang, H.K. Jun, Fatigue life assessment of railway rail subjected to welding residual and contact stresses, *J. Mech. Sci. Technol.* 28 (2014) 4483–4491. <https://doi.org/10.1007/s12206-014-1016-3>.
- [26] H.K. Jun, J.W. Seo, I.S. Jeon, S.H. Lee, Y.S. Chang, Fracture and fatigue crack growth analyses on a weld-repaired railway rail, *Eng. Fail. Anal.* 59 (2016) 478–492. <https://doi.org/10.1016/j.engfailanal.2015.11.014>.
- [27] Q. Feng, H. Song, Analysis on the operation methods of rail welding and postweld heat treatment in the track change overhaul of existing railway lines, *J. Phys.: Conf. Ser.* 2152 (2022) 012018. <https://doi.org/10.1088/1742-6596/2152/1/012018>.
- [28] B. Srikarun, S. Petchsang, P. Muangjunburee, Study of abrasive wear of railway welding steel repair, grade R260, *Princess of Naradhiwas University Journal* 13 (1) (2021) 209–255. <https://li01.tci-thaijo.org/index.php/pnujr/article/view/241123>.
- [29] M.N. SaifulAkmal, M.N. Wahab, Characterization of UIC-54 rail head surface welded by hardfacing using flux-cored steel wire, In: M.N. Osman Zahid et al. (eds), *Recent trends in manufacturing and materials towards industry 4.0, Lecture notes in mechanical engineering* (2021). [https://doi.org/10.1007/978-981-15-9505-9\\_68](https://doi.org/10.1007/978-981-15-9505-9_68).
- [30] E. Kabo, A. Ekberg, M. Maglio, Rolling contact fatigue assessment of repair rail welds, *Wear* 436–437 (2019) 203030. <https://doi.org/10.1016/j.wear.2019.203030>.
- [31] C. Molina, A. Araujo, K. Bell, P.F. Mendez, M. Chapetti, Fatigue life of laser additive manufacturing repaired steel component, *Eng. Fract. Mech.* 241 (2021) 107417. <https://doi.org/10.1016/j.engfracmech.2020.107417>.
- [32] J. Tian, P. Xu, Q. Liu, Effects of stress-induced solid phase transformations on residual

- stress in laser cladding a Fe-Mn-Si-Cr-Ni alloy coating, *Mater. Des.* 193 (2020) 108824. <https://doi.org/10.1016/j.matdes.2020.108824>.
- [33] M. Ma, W. Xiong, Y. Lian, D. Han, C. Zhao, J. Zhang, Modeling and optimization for laser cladding via multi-objective quantum-behaved particle swarm optimization algorithm, *Surf. Coat. Technol.* 381 (2020) 125129. <https://doi.org/10.1016/j.surfcoat.2019.125129>.
- [34] L. Shepeleva, B. Medres, W.D. Kaplan, M. Bamberger, A. Weisheit, Laser cladding of turbine blades, *Surf. Coat. Technol.* 125 (2000) 45–48. [https://doi.org/10.1016/S0257-8972\(99\)00603-9](https://doi.org/10.1016/S0257-8972(99)00603-9).
- [35] L. Sexton, S. Lavin, G. Byrne, A. Kennedy, Laser cladding of aerospace materials, *J. Mater. Process. Technol.* 122(1) (2002) 63–68. [https://doi.org/10.1016/S0924-0136\(01\)01121-9](https://doi.org/10.1016/S0924-0136(01)01121-9).
- [36] S.D. Sun, Q. Liu, M. Brandt, V. Luzin, R. Cottam, M. Janardhana, G. Clark, Effect of laser clad repair on the fatigue behaviour of ultra-high strength aisi 4340 steel, *Mater. Sci. Eng. A* 606 (2014) 46–57. <https://doi.org/10.1016/j.msea.2014.03.077>.
- [37] E.J.M. Hiensch, F.J. Franklin, J.C.O. Nielsen, J.W. Ringsberg, G.J. Weeda, A. Kapoor, B.L. Josefson, Prevention of RCF damage in curved track through development of the INFRA-STAR two-material rail, *Fatigue Fract. Eng. Mater. Struct.* 26(10) (2003) 1007–1017. <https://doi.org/10.1046/j.1460-2695.2003.00663.x>.
- [38] F.J. Franklin, G.J. Weeda, A. Kapoor, E.J.M. Hiensch, Rolling contact fatigue and wear behaviour of the Infrastar two-material rail, *Wear* 258(7–8) (2005) 1048–1054. <https://doi.org/10.1016/J.Wear.2004.03.054>.
- [39] M. Hiensch, P.O. Larsson, O. Nilsson, D. Levy, A. Kapoor, F. Franklin, J. Nielsen, J.W. Ringsberg, J.B. Lennart, Two-material rail development: field test results regarding rolling contact fatigue and squeal noise behavior, *Wear* 258(7–8) (2005) 964–972. <https://doi.org/10.1016/J.Wear2004.03.067>.
- [40] S.R. Lewis, R. Lewis, D.I. Fletcher, Assessment of laser cladding as an option for repairing/enhancing rails, *Wear* 330–31 (2015) 581–591. <https://doi.org/10.1016/J.WEAR.2015.02.027>.
- [41] S.R. Lewis, S. Fretwell-Smith, P.S. Goodwin, L. Smith, R. Lewis, M. Aslam, D.I. Fletcher, K. Murray, R. Lambert, Improving rail wear and RCF performance using laser cladding, *Wear* 366–367 (2016) 268–278. <https://doi.org/10.1016/J.Wear.2016.05.011>.
- [42] J.W. Ringsberg, A. Skyttebol, B.L. Josefson, Investigation of the rolling contact fatigue resistance of laser clad twin-disc specimens: FE simulation of laser cladding, grinding and a twin-disc test, *Int. J. Fatigue* 27(6) (2005) 702–714. <https://doi.org/10.1016/J.IJFATIGUE.2004.10.006>.
- [43] A.T. Clare, O. Oyelola, J. Folkes, P.K. Farayibi, Laser cladding for railway repair and preventative maintenance, *J. Laser Appl.* 24(3) (2012) 032004. <https://doi.org/10.2351/1.4710578>.
- [44] A.T. Clare, O. Oyelola, T.E. Abioye, P.K. Farayibi, Laser cladding of rail steel with Co–Cr, *Surf. Eng.* 29(10) (2013) 731–736. <https://doi.org/10.1179/1743294412Y.0000000075>.
- [45] S.R. Lewis, R. Lewis, P.S. Goodwin, S. Fretwell-Smith, D.I. Fletcher, K. Murray, J. Jaiswal, Full-scale testing of laser clad railway track; case study – testing for wear, bend fatigue and insulated block joint lipping integrity, *Wear* 376–377 (2017) 1930–1937. <https://doi.org/10.1016/j.wear.2017.02.023>.
- [46] A. Narayanan, M. Mostafavi, T. Pirling, S. Kabra, S.R. Lewis, M.J. Pavier, M.J. Peel, Residual stress in laser clad rail, *Tribol. Int.* 140 (2019) 105844.



- <https://doi.org/10.1016/j.triboint.2019.105844>.
- [47] P. Lu, S.R. Lewis, S. Fretwell-Smith, D.L. Engelberg, D.I. Fletcher, R. Lewis, Laser cladding of rail; the effects of depositing material on lower rail grades, *Wear* 438–439 (2019) 203045. <https://doi.org/10.1016/j.wear.2019.203045>.
- [48] J.W. Seo, J.C. Kim, S.J. Kwon, H.K. Jun, Effects of laser cladding for repairing and improving wear of rails, *Int. J. Prec. Eng. Manuf.* 20 (2019) 1207–1217. <https://doi.org/10.1007/s12541-019-00115-y>.
- [49] W.J. Wang, J. Hu, J. Guo, Q.Y. Liu, M.H. Zhu, Effect of laser cladding on wear and damage behaviors of heavy-haul wheel/rail materials, *Wear* 311(1–2) (2014) 130–136. <https://doi.org/10.1016/J.WEAR.2014.01.011>.
- [50] W.J. Wang, Z.K. Fu, J. Guo, Y.Q. Zhang, Q.Y. Liu, M.H. Zhu, Investigation on wear resistance and fatigue damage of laser cladding coating on wheel and rail materials under the oil lubrication condition, *Tribol. Trans.* 59(5) (2016) 810–817. <https://doi.org/10.1080/10402004.2015.1107926>.
- [51] W.J. Wang, R. Lewis, B. Yang, L.C. Guo, Q.Y. Liu, M.H. Zhu, Wear and damage transitions of wheel and rail materials under various contact conditions, *Wear* 362–363 (2016) 146–152. <https://doi.org/10.1016/J.Wear.2016.05.021>.
- [52] Z.K. Fu, H.H. Ding, W.J. Wang, Q.Y. Liu, J. Guo, M.H. Zhu, Investigation on microstructure and wear characteristic of laser cladding Fe-based alloy on wheel/rail materials, *Wear* 330–331 (2015) 592–599. <https://doi.org/10.1016/J.Wear.2015.02.053>.
- [53] H. Guo, Q. Wang, W.J. Wang, J. Guo, Q. Liu, M. Zhu, Investigation on wear and damage performance of laser cladding co-based alloy on single wheel or rail material, *Wear* 328–329 (2015) 329–337. <https://doi.org/10.1016/j.wear.2015.03.002>.
- [54] Y. Zhu, Y. Yang, X. Mu, W.J. Wang, Z. Yao, H. Yang, Study on wear and ref performance of repaired damage railway wheels: assessing laser cladding to repair local defects on wheels, *Wear* 430–431 (2019) 126–136. <https://doi.org/10.1016/j.wear.2019.04.028>.
- [55] H. Ding, J. Dai, T. Dai, Y. Sun, T. Lu, M. Li, X. Jia, D. Huang, Effect of preheating/post-isothermal treatment temperature on microstructures and properties of cladding on U75V rail prepared by plasma cladding method, *Surf. Coat. Technol.* 399 (2020) 126122. <https://doi.org/10.1016/j.surfcoat.2020.126122>.
- [56] J. Zhao, H. Miao, Q. Kan, P. Fu, L. Ding, G. Kang, P. Wang, Numerical investigation on the rolling contact wear and fatigue of laser dispersed quenched U71Mn rail, *Int. J. Fatigue* 143 (2021) 106010. <https://doi.org/10.1016/j.ijfatigue.2020.106010>.
- [57] Z. Xia, L. Chen, S. Huang, J. Xu, L. Wang, S. Zhang, Effect of solid and annular laser heat sources on thermal cycle and solid phase transformation in rail steel manufactured by laser directed energy deposition, *J. Laser Appl.* 33 (2021) 012049. <https://doi.org/10.2351/7.0000253>.
- [58] X. Wang, L. Lei, H. Yu, A review on microstructural features and mechanical properties of wheels/rails clad by laser cladding, *Micromachines* 12(2) (2021) 152. <https://doi.org/10.3390/mi12020152>.
- [59] L. Meng, W. Zhao, K. Hou, D. Kou, Z. Yuan, X. Zhang, J. Xu, Q. Hu, D. Wang, X. Zeng, A comparison of microstructure and mechanical properties of laser cladding and laser-induction hybrid cladding coatings on full-scale rail, *Mater. Sci. Eng. A* 748 (2019) 1–15. <https://doi.org/10.1016/j.msea.2019.01.068>.
- [60] L. Meng, X. Zeng, K. Hou, Q. Hu, D. Wang, Effect of laser cladding and laser-induction hybrid cladding coatings on the bending properties and fracture behavior of rails, *Surf.*



- Coat. Technol. 374 (2019) 1038–1050. <https://doi.org/10.1016/j.surfcoat.2019.06.051>.
- [61] L. Meng, B. Zhu, Q. Hu, X. Zeng, D. Wang, Laser-induction hybrid cladding of different coatings on rail surface: Microstructure, wear properties and contact fatigue behaviors, Appl. Surf. Sci. 566 (2021) 150678. <https://doi.org/10.1016/j.apsusc.2021.150678>.
- [62] L. Meng, B. Zhu, R. Yan, X. Zeng, Q. Hu, D. Wang, Effect of induction post-heating temperature on the morphology, microstructure and mechanical performance of the heat affected zone in laser-induction hybrid cladding of full-scale rail, J. Mater. Res. Technol. 13 (2021) 1431–1440. <https://doi.org/10.1016/j.jmrt.2021.05.053>.
- [63] L. Meng, C. Xian, B. Zhu, R. Yan, Q. Hu, X. Zeng, D. Wang, Comparison on the microstructure, bending properties and tribological behaviors of rail materials treated by laser dispersed quenching and induction assisted laser dispersed quenching, Surf. Coat. Technol. 410 (2021) 126936. <https://doi.org/10.1016/j.surfcoat.2021.126936>.
- [64] Y. Hu, L. Zhou, H.H. Ding, G.X. Tan, R. Lewis, Q.Y. Liu, J. Guo, W.J. Wang, Investigation on wear and rolling contact fatigue of wheel-rail materials under various wheel/rail hardness ratio and creepage conditions, Tribol. Int. 143 (2020) 106091. <https://doi.org/10.1016/j.triboint.2019.106091>.
- [65] S.M. Shariff, T.K. Pal, G. Padmanabham, S.V. Joshi, Sliding wear behaviour of laser surface modified pearlitic rail steel, Surf. Eng. 26(3) (2010) 199–208. <https://doi.org/10.1179/174329409X455458>.
- [66] V.I. Aladesanmi, O.S. Fatoba, E.T. Akinlabi, Laser clad Ti + TiB<sub>2</sub> on steel rail microstructural effect, Proc. Manuf. 33 (2019) 709–716. <https://doi.org/10.1016/j.promfg.2019.04.089>.
- [67] Q. Lai, R. Abrahams, W. Yan, C. Qiu, P. Mutton, A. Paradowska, M. Soodi, Investigation of a novel functionally graded material for the repair of premium hypereutectoid rails using laser cladding technology, Compos. Part B Eng. 130 (2017) 174–191. <https://doi.org/10.1016/j.compositesb.2017.07.089>.
- [68] Q. Lai, R. Abrahams, W. Yan, C. Qiu, P. Mutton, A. Paradowska, X. Fang, M. Soodi, X. Wu, Effects of preheating and carbon dilution on material characteristics of laser-clad hypereutectoid rail steels, Mater. Sci. Eng. A 712 (2018) 548–563. <https://doi.org/10.1016/j.msea.2017.12.003>.
- [69] T. Roy, Q. Lai, R. Abrahams, P. Mutton, A. Paradowska, M. Soodi, W. Yan, Effect of deposition material and heat treatment on wear and rolling contact fatigue of laser clad rails, Wear 412–413 (2018) 69–81. <https://doi.org/10.1016/j.wear.2018.07.001>.
- [70] Q. Lai, R. Abrahams, W. Yan, C. Qiu, P. Mutton, A. Paradowska, M. Soodi, X. Wu, Influences of depositing materials, processing parameters and heating conditions on material characteristics of laser-clad hypereutectoid rails, J. Mater. Process. Technol. 263 (2019) 1–20. <https://doi.org/10.1016/j.jmatprotec.2018.07.035>.
- [71] T. Roy, R. Abrahams, A. Paradowska, Q. Lai, P. Mutton, M. Soodi, P. Fasihi, W. Yan, Evaluation of the mechanical properties of laser clad hypereutectoid steel rails, Wear 432–433 (2019) 202930. <https://doi.org/10.1016/j.wear.2019.202930>.
- [72] T. Roy, A. Paradowska, R. Abrahams, M. Law, P. Mutton, M. Soodi, W. Yan, Residual stress in laser clad heavy-haul rails investigated by neutron diffraction, J. Mater. Process. Technol. 278 (2020) 116511. <https://doi.org/10.1016/j.jmatprotec.2019.116511>.

## 2. CHAPTER 2 MATERIALS AND EXPERIMENTAL METHODS

As it was mentioned earlier, two AM processes are employed in this research for rail repair purposes: SAW and LPD. However, due to the inconsistency in numerous involved parameters such as scanning speed, wire/powder feeding rate, deposition materials, temperature, cooling rate, tool path, etc. neither SAW nor LPD will deliver a consistent and desired microstructural and mechanical properties to the repaired rail.

This study aims to achieve a repaired rail with the most desired mechanical and microstructural properties through modifying the SAW/LPD-repair process parameters and also conducting some pre- and post-processes on the rail.

The under-investigation properties for evaluation of the repaired rail are hardness, flexural tensile/compressive strength, yield strength, tensile strength, residual stress, microstructural phase distribution, and distribution of micropores and microcracks. There are four case studies to explore: SAW-repaired light rail (i.e., 75-lb/yd rail), SAW-repaired heavy rail (i.e., 136-lb/yd rail), LPD-repaired light rail, and LPD-repaired heavy rail. Fig. 1 shows photos of the typical worn and repaired light/heavy rails.

In the following, Sec. 2.1 presents materials composition of each of the light and heavy rails and also the utilized deposition materials for each of the SAW and LPD processes. Summarized descriptions about the SAW and LPD processes along with the incorporated tool path are given in Sec. 2.2. Regarding sample preparation and different experimental test methods, Sec. 2.3 provides detailed explanation.



(a)



(b)

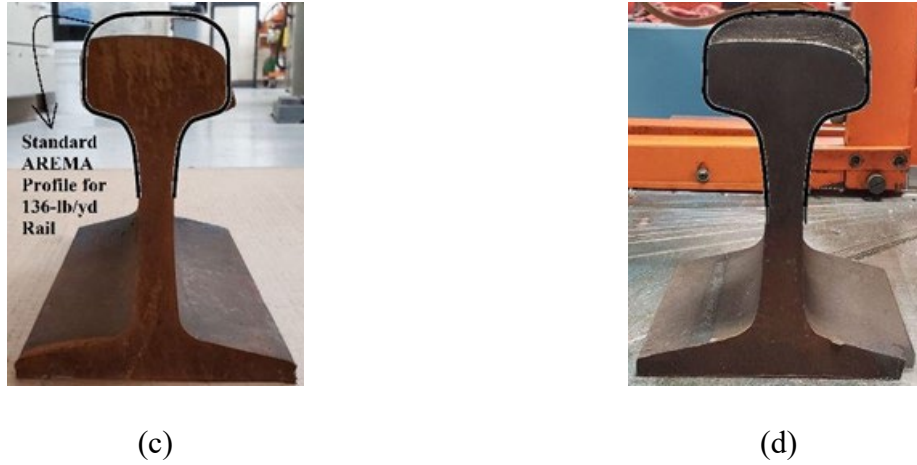


**Fig. 2.1** (a) worn light rail, (b) repaired light rail, (c) worn heavy rail, and (d) repaired heavy rail.

**2.1. Materials**

**2.1.1. Rail**

For light rail case study, a 75-lb/yd worn rail having both the tangential and side wear is used as the sample (Fig. 1a). This rail is a grade-880 C-Mn rail steel following the standards of the American Railway Engineering and Maintenance-of-way Association (AREMA) and is mostly employed for light transit systems [1]. The chemical composition of the rail substrate is determined by chemical analysis and given in Table 1. To resemble a real on-site rail-repair procedure, which is a steady-state heat flow along the continuous longitudinal direction of rail, the available length for the sample should be at least 100 mm [2]. Therefore, a 150-mm cut of the worn rail is utilized in the AM-repair process.

In case of heavy rail, the case study is a 136-lb/yd, i.e. 136RE, worn rail which is typically used in the U.S. heavy-haul railway transportation system [1]. A 150-mm cut of the worn rail, as shown in Fig. 1c, is used as the AM substrate. Based on the AREMA standards, this is an intermediate-strength, low-alloy rail steel of which the chemical composition is presented in Table 1.

The required mechanical properties of the light and heavy rails according to the AREMA standards are given in Table 2.

**Table 1** Chemical composition of the to-be-repaired rail steels (wt.%).

Material	Fe	C	Cr	Mn	Si	Ni	P	S
Light rail	Bal.	0.71	-	1.04	0.21	-	0.022	0.013
Heavy rail	Bal.	0.80	0.03	0.23	0.04	0.14	0.01	0.01

**Table 2** Required mechanical properties for the light and heavy rails

Material	Yield strength (MPa)	Tensile strength (MPa)	Vickers hardness number (HV)	Elongation (%)
Light rail	460	830	222	10
Heavy rail	511	980	318	10

### 2.1.2. Deposition

For SAW-repairing of the light rail, a rutile E71T-1C wire with a diameter of 1.2 mm is adopted. This low-alloy wire is a conventional C-Mn steel weld that has a close chemical composition to the light rail substrate, which allows a chance of a uniform microstructure of the repaired light rail. Table 3 presents the chemical composition of commercial stock material of E71T-1C steel weld wire. A composite MgO-CaF<sub>2</sub>-Al<sub>2</sub>O<sub>3</sub>-SiO<sub>2</sub> agglomerated commercial welding flux is used for the SAW-repairing process of the light rail of which the chemical composition is presented in Table 4, entitled as Light-SAW Flux. Concerning the heavy rail, since the head of the heavy-haul rail requires a much higher hardness, strength, and frictional wear resistance, an 1/8-in Lincore 40-S hard facing submerged arc wire is utilized because of its distinguished rolling and sliding wear properties. This wire is specifically compatible for carbon steel and appropriate for depositing up to 5 layers. Table 3 gives the chemical composition of this utilized SAW wire. The neutral Lincolnweld 801 submerged arc flux is used as the recommended and compatible flux, of which the chemical composition is demonstrated in Table 4, entitled as Heavy-SAW Flux. It is also worth noting that prior to the weld process, the rusts and macro-contaminants on the railhead are removed using sandblasting, and the surface is cleaned thereafter using acetone to remove any remaining micro-contaminant. This cleaning process allows for establishing the best bonding condition.

**Table 3** Chemical composition of the utilized SAW wires (wt.%).

Material	Fe	C	Cr	Mn	Si	Ni	O	N	P	S	Cu	Mo	Al	Ti
E71T-1C	Bal.	0.18	–	1.2	0.8	0.40	0.03	0.030	0.025	0.025	–	–	0.5	0.05
Lincore 40-S	Bal.	0.12	0.50	2.75	3.30	–	–	–	–	–	–	0.85	–	–

**Table 4** Chemical composition of the agglomerated flux used for the SAW-repairing process (wt.%).

Flux	SiO <sub>2</sub>	CO <sub>2</sub>	Al <sub>2</sub> O <sub>3</sub>	CrO	MgO	MoO <sub>3</sub>	CaO	CaF <sub>2</sub>	MnO	TiO <sub>2</sub>	Na <sub>2</sub> O	Fe <sub>2</sub> O <sub>3</sub>
Light-SAW	10.7	–	17.3	–	31.7	–	6.6	24.1	1.1	0.86	0.78	1.9
Heavy-SAW	10.0	21.2	–	8.9	–	18.4	–	–	14.2	–	–	22.7

The initial try for LPD-repairing of both the light and heavy rails is conducted using 304L stainless steel deposition powder, with particle diameter of 45-104  $\mu\text{m}$ , because of its high strength, high corrosion resistance, and great laser compatibility [3]. The chemical composition of 304L can be found in Table 5.

**Table 5** Chemical composition of the utilized LPD steel powders (wt.%).

Material	Co	Fe	C	Cr	Mn	Mo	Si	Ni	P	S	W
304L	-	Bal.	0.03	19.0	2.00	-	1.00	10.5	0.045	0.03	-

## 2.2. Additive manufacturing (AM) repair mechanism

### 2.2.1. Submerged arc welding (SAW)

A distinctive feature of a SAW process is associated with the flux particles; they cover and shield the arc in a way that the wire and the arc are entirely submerged in flux stream. Consequently, unlike most of the common open welding processes, the SAW process is almost free of any extreme heat radiation, which leads to a pretty clean weld. The other substantial advantage of flux coverage is increasing energy transfer efficiency up to more than 90%, as it blocks any radiation loss, convection loss, or energy scattering from wire to the substrate. The specified increased efficiency contributes to a high deposition rate and a favorable weld reliability.

Fig. 2 shows a schematic form of a SAW structure. The wire as the filler material is applied to the substrate surface along with the flux grains that are flown through a hopper. As Fig. 2 shows, the arc is burnt in the covering envelop and the melt pool is solidified on the rail substrate. At the lower layer of flux particle flow, i.e., the top of the envelop, molten flux is formed that is solidified thereafter and develops a thin coating on the weld. This developed coating is called slag and has to be removed afterwards. The SAW process for rail repair in the current work is carried out with an open-circuit welding voltage of 25~36 V, welding current of approximately 150 A, wire feed rate of 21 mm/s, and a travel speed of 23 mm/s.

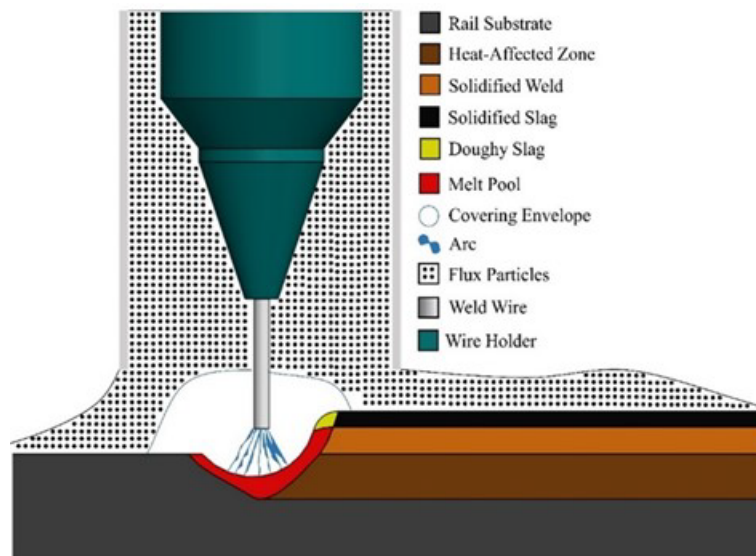


**Fig. 2.2** Schematic illustration of a SAW setup.

### 2.2.2. Laser powder deposition (LPD)

The general function of an LPD process is to develop a melt pool on the substrate surface using laser beam and then blow the powder particles to the developed melt pool by carrier gas. The driven powder particles start to melt once they enter the laser beam threshold. There are two typical LPD setups: off-axis setup, where the powder nozzle is positioned at an angle in relation to the optical laser beam; and coaxial setup, where the powder nozzle is banded around the optical laser beam and both of them, as an integral unit, are positioned perpendicular to the substrate. In coaxial setup, the direction of deposition and tilt of the substrate will not affect the final quality, which is the prevailing advantage of coaxial setup over the off-axis [4]. Therefore, a coaxial LPD setup is used in this research (Fig. 3), which is equipped with a 5-axis computer numerical controlled (CNC) table that shifts, tilts, and rotates. The rail is clamped to the CNC table as the substrate. The coaxial nozzle has a 9 MP Metco powder feeder and a 4 kW IPG fiber laser gun. There is an 11 mm of stand-off distance between the laser beam and railhead surface, which results in a 5 mm laser strike diameter onto the surface. The other LPD parameters include 1.8 kW of laser power, 2 cm<sup>3</sup>/min powder feeding rate, and 6 slpm flow rate of the carrier gas (Argon shielding gas).

### 2.2.3. Tool path

Fig. 4 gives a graphical illustration of the tool path. Due to the rail side wear, the transversal section of the rail does not represent a symmetrical geometry. Therefore, in order to carry out a flat and smooth nozzle travel during depositing every single row and consequently, to avoid continuous elevation changes, the deposition process is conducted along the longitudinal, i.e., x, direction. In the LPD process, the laser scanning speed is 1000 mm/min and the idle time between the deposition of two consecutive deposition rows is 9 s. The SAW process is carried out with an open-circuit welding voltage of 25 ~ 36 V, welding current of approximately 150 A, wire feed rate of 21 mm/s, and a travel speed of 23 mm/s. There is a 50% overlap for two adjacent deposition rows. The deposition layers are built upon one another along the +y direction. The total number of required deposition layers for a complete repair and the required duration for a full repair depend on the repairing process (SAW or LPD), rail size (light or heavy), and depth of wear. For instance, SAW-repairing of the light rail takes a total number of 6 welding layers across the entire build, with 10 to 15 welding passes per layer. LPD-repairing of a 150-mm light rail approximately takes 65 minutes, where a total number of 9 layers are deposited across the entire build. Also, each deposition layer is consisted of 15 to 20 rows. Both the LPD- and SAW-repaired heavy rails contain a total of 5 deposition layers.

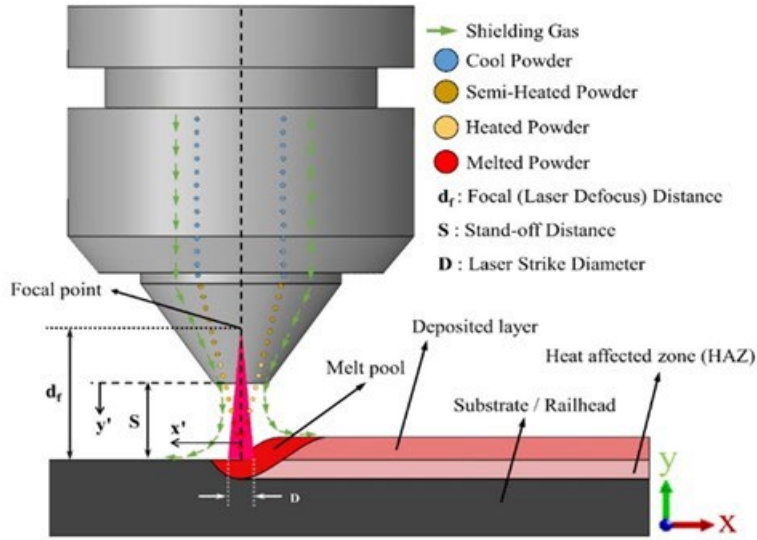


**Fig. 2.3** Schematic illustration of an LPD setup.

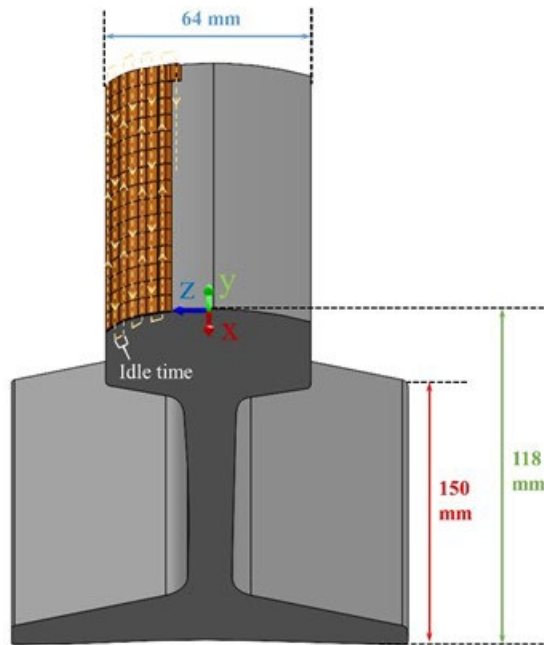


**Fig. 2.4** Graphical illustration of the AM tool path. Every single layer is deposited along +/- x direction, and the layers are built upon one another along +y direction.

### 2.3. Sample preparation

A slice from the head of the repaired rails is used as the specimen for experimental examinations including hardness test, microstructure analysis, residual stress measurement, and flexural and shear strength evaluation. For example, Fig. 5 shows the procedure of specimen extraction from



the LPD-repaired heavy rail.

The sliced sample is first used for the hardness test. Referring to the active standards provided by ASTM E-18 [5] for a mild carbon steel, Rockwell hardness test is executed on B scale using a LECO hardness tester. On this scale, the applied minor and major indentation loads are 10 kgf and 90 kgf, respectively. In case of SAW-repaired heavy rails, where the deposited material is a high-carbon steel, C scale Rockwell hardness is carried out, for which 10 kgf and 150 kgf loads are applied as the minor and major loads, respectively.

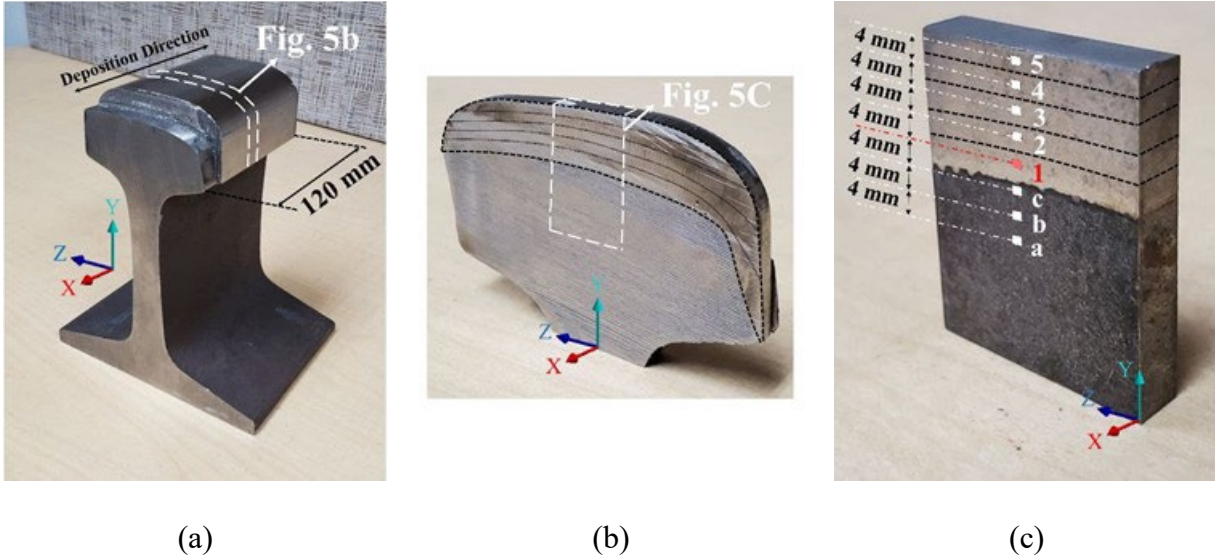


**Fig. 2.5** (a) the LPD-repaired rail, (b) a slice cut from the head of the repaired rail (the boundaries between deposition layers are shown as black dashed lines), and (c) the extracted specimen from the slice cut.

Afterwards, the specimen is polished to 1  $\mu\text{m}$  roughness by pasting diamond on SiC papers. An HCl-based etchant, containing 100 ml HCl, 100 ml ethanol, and 5 g ethylene glycol, is used to etch the sample in order to unveil the micro grains and also to remove the externally induced residual stresses on the specimen surface as a result of the mechanical polishing. The etched specimen is then cleaned in an ultrasonic bath to get prepared for microstructure characterization. A Leica DM750 M is employed for optical microscope (OM) investigation. As a complementary to exploring the microstructure morphology, a scanning electron microscope (SEM) analysis is also performed using a JEOL 7001F FEG. An Oxford ISIS electron-dispersive X-ray spectroscopy (EDS) detector, coupled with the SEM, is utilized to analyze the chemical composition variation from welded/deposited materials to the rail substrate.

For residual stress evaluation, an X-ray diffraction (XRD) stress measurement is done by means of a Bruker D8 Discovery X-Ray diffractometer. This apparatus is equipped with a  $\text{CuK}\alpha$  radiation source with constant wavelength of 1.5406  $\text{\AA}$  and the running parameters of 40 kV and 40 mA for X-ray tube. The sampled area is controlled through a 1-mm pinhole collimator.



Based on the study by Ghasri-Khouzani et al. [6], an X-ray beam, originated from a  $\text{CuK}\alpha$  source and aimed to a steel surface, has an average penetration depth of 5  $\mu\text{m}$ . Accordingly, to mitigate the surface roughness and to ensure that there are no surface spikes taller than 5  $\mu\text{m}$  to interrupt the X-ray beams, pasted diamond suspensions on SiC papers are used to polish the specimen down to 1  $\mu\text{m}$ . A thickness of 750  $\mu\text{m}$  is removed from the sample surface as a result of polishing.

To remove the relaxed residual stresses on the polished sample surface as a result of cutting and polishing, the sample is etched. The typical etched sample can be seen in Fig. 5c. Each course of 30-second etching removes around 50  $\mu\text{m}$  of the sample thickness. This course of etching is repeated over and over until the XRD-measured stress on the surface is stabilized, which subsequently indicates that all the externally-induced residual stresses are fully removed. The related graphs of this step of testing validation will be presented and discussed later on. The common locations where residual stress is measured using XRD are shown in Fig. 5c as numbered white spots on the etched sample, except for the spot 1 that is shown in red. Spot 1 is the location at which the stress is frequently measured at each step of sample preparation, i.e., before polishing, after polishing, and after each course of etching, to make sure that the existing factors of error, i.e., surface roughness and externally-induced residual stresses, are completely eliminated. Once the sample is etched enough that the measured stress at spot 1 is stabilized, stress at the other spots is measured.

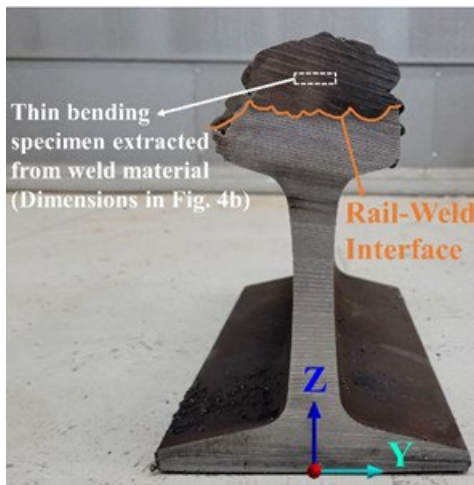
In order to improve the hardness and microstructural properties of the repaired rails, the specimens are heat treated afterwards. A post-process quenching is performed on the SAW-repaired light rail, where a sliced etched sample is heated up to 1100°C, above the austenization temperature of the weld materials, in an FO110CR muffle furnace and soaked for 40 min to ensure homogeneous transformation across the entire specimen. The furnace is then shut off and the furnace was left open to let the red signs of heat disappear. After that, the heated sample is cooled down immediately by submerging into water and quenching to room temperature. The as-quenched (AQ) specimen was milled and polished again according to the same procedure described earlier to prepare for microstructure analysis and hardness test. In case of the LPD-repaired light rail, where 304L stainless steel is used as the deposition material, although quenching generally is recommended as the best available heat treatment method to enhance the hardness and strength properties of steel, for stainless steels the quenching should be followed by a second-step heat treatment to dissolve the grain-boundary precipitated carbides, thereby avoiding any sensitization or excessive brittleness. Accordingly, in line with the results presented by Essoussi et al. [7], the post-processing heat treatment used for the LPD-repaired light rail consists of two steps, i.e., 1) a solution treatment for 1 hour at 1150°C followed by water quenching and 2) isothermal tempering at 350°C for 30 minutes followed by cooling in still air. Therefore, the as-built specimen was placed into an FO110CR muffle furnace that was heated up to 1150°C. After 1 hour of soaking into 1150°C, the specimen was removed from the furnace and immediately quenched into the water. Then, the quenched sample was placed again into the furnace, but this time for 30 minutes long and at 350°C. It was then removed from the furnace and put outside in the still air to be cooled down naturally. Finding and conducting the most appropriate post-heat-treatment method for the repaired heavy rails is under investigation at this time.

Three-point bending test is accomplished for two sets of specimen.

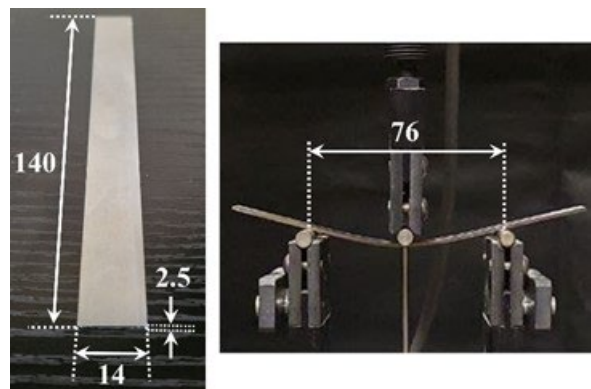
The thin specimen is used to assess the static flexural tensile/compressive strength of the weld, i.e., deposited, materials. The typical location from where the thin specimen is extracted is illustrated in Fig. 6a. The dimensions of a typical thin bending sample are given in Fig. 6b, where all the dimensions are in millimeters. It is also shown in Fig. 6b that the distance between the supports for 3-point bending test is 76 mm. This distance is chosen large enough to make sure that the thin sample will fail due to bending, and not due to shear, to let us evaluate the flexural strength of the materials rather than their shear strength.

The thick specimen is for evaluating the static shear strength, i.e., bonding strength, between the rail and the deposited weld. Therefore, the thick specimen is extracted from the rail-weld interface region, as shown in Fig. 6c. The dimensions of the extracted thick specimen can be found in Fig. 6d. As it is evident in Fig. 6d, the 5-mm-thick specimen is tried to be extracted in a way that it contains almost equal fraction of the weld and rail materials, i.e., 2.5 mm thickness from the weld area and 2.5 mm thickness from the rail zone. Another visible fact in Fig. 6d is that the support distance is chosen small enough, i.e., 30 mm, to ensure that the specimen fails as a result of shear and not bending. This helps us to assess the shear strength at the rail-weld interface. More details about the effect of support distance on the failure mode are given in the results in Chapter 8.

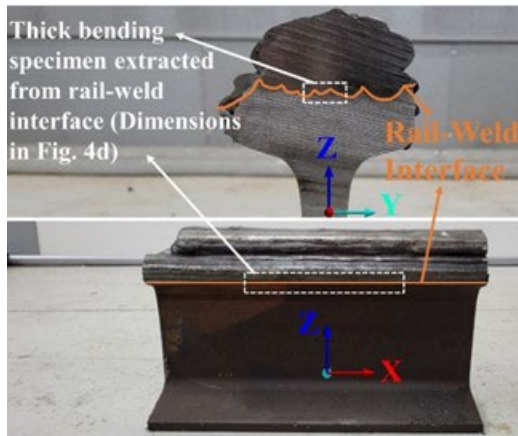
For instantaneous and precise recording of displacements along both directions, moiré diffraction method is used. The samples are considered to fail at a 50% load drop from the maximum reached load, i.e., failure load. The failure load is used for calculating the bending strength. The fracture surfaces of the failed samples are then examined using SEM to analyze and discuss failure modes.



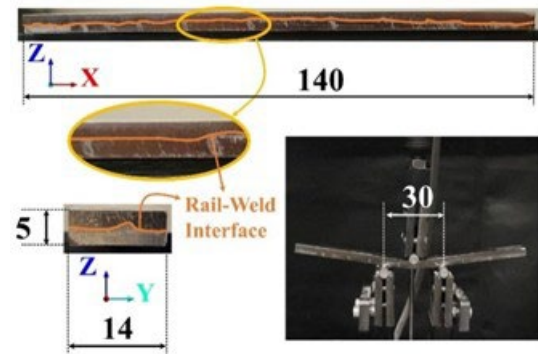
(a)



(b)



(c)



(d)

**Fig. 2.6** (a) Locations of extracting thin bending specimen from weld materials for flexural tensile/compressive strength evaluation, (b) typical thin bending specimen dimensions, (c) location of extracting thick bending specimen for shear strength evaluation at the rail-weld interface, and (d) typical thick bending specimen dimensions (all dimensions are in millimeters)

## References for Chapter 2

- [1] M.P. Hughes-Cromwick, M. Dickens, Public Transportation Fact Book. 71st edition, American Public Transportation Association, Washington, DC (2020).  
<https://www.apta.com/wp-content/uploads/APTA-2020-Fact-Book.pdf>.
- [2] Q. Lai, R. Abrahams, W. Yan, C. Qiu, P. Mutton, A. Paradowska, X. Fang, M. Soodi, X. Wu, Effects of preheating and carbon dilution on material characteristics of laser-cladded hypereutectoid rail steels, *Mater. Sci. Eng. A* 712 (2018) 548–563.  
<https://doi.org/10.1016/J.MSEA.2017.12.003>.
- [3] X.Y. Wang, D.Y. Li, Mechanical, electrochemical and tribological properties of nanocrystalline surface of 304 stainless steel, *Wear* 255(7–12) (2003) 836–845.  
[https://doi.org/10.1016/S0043-1648\(03\)00055-3](https://doi.org/10.1016/S0043-1648(03)00055-3).
- [4] M. Dias da Silva, K. Partes, T. Seefeld, F. Vollertsen, Comparison of coaxial and off-axis nozzle configurations in one step process laser cladding on aluminum substratem *J. Mater. Process. Technol.* 212(11) (2012) 2514–2519.  
<https://doi.org/10.1016/j.jmatprotec.2012.06.011>.
- [5] ASTM E18-15, Standard test methods for Rockwell hardness of metallic materials, ASTM international (2015). <https://doi.org/10.1520/E0018-15>.
- [6] M. Ghasri-Khouzani, H. Peng, R. Rogge, R. Attardo, P. Ostiguy, J. Neidig, R. Billo, D. Hoelzle, M.R. Shankar, Experimental measurement of residual stress and distortion in additively manufactured stainless steel components with various dimensions, *Mater. Sci. Eng. A* 707 (2017) 689-700. <https://doi.org/10.1016/j.msea.2017.09.108>.
- [7] H. Essoussi, S. Elmouhri, S. Ettaqi, E. Essadiqi, Heat treatment effect on mechanical properties of AISI 304 austenitic stainless steel, *Proc. Manuf.* 32 (2019) 883–888.  
<https://doi.org/10.1016/j.promfg.2019.02.298>.

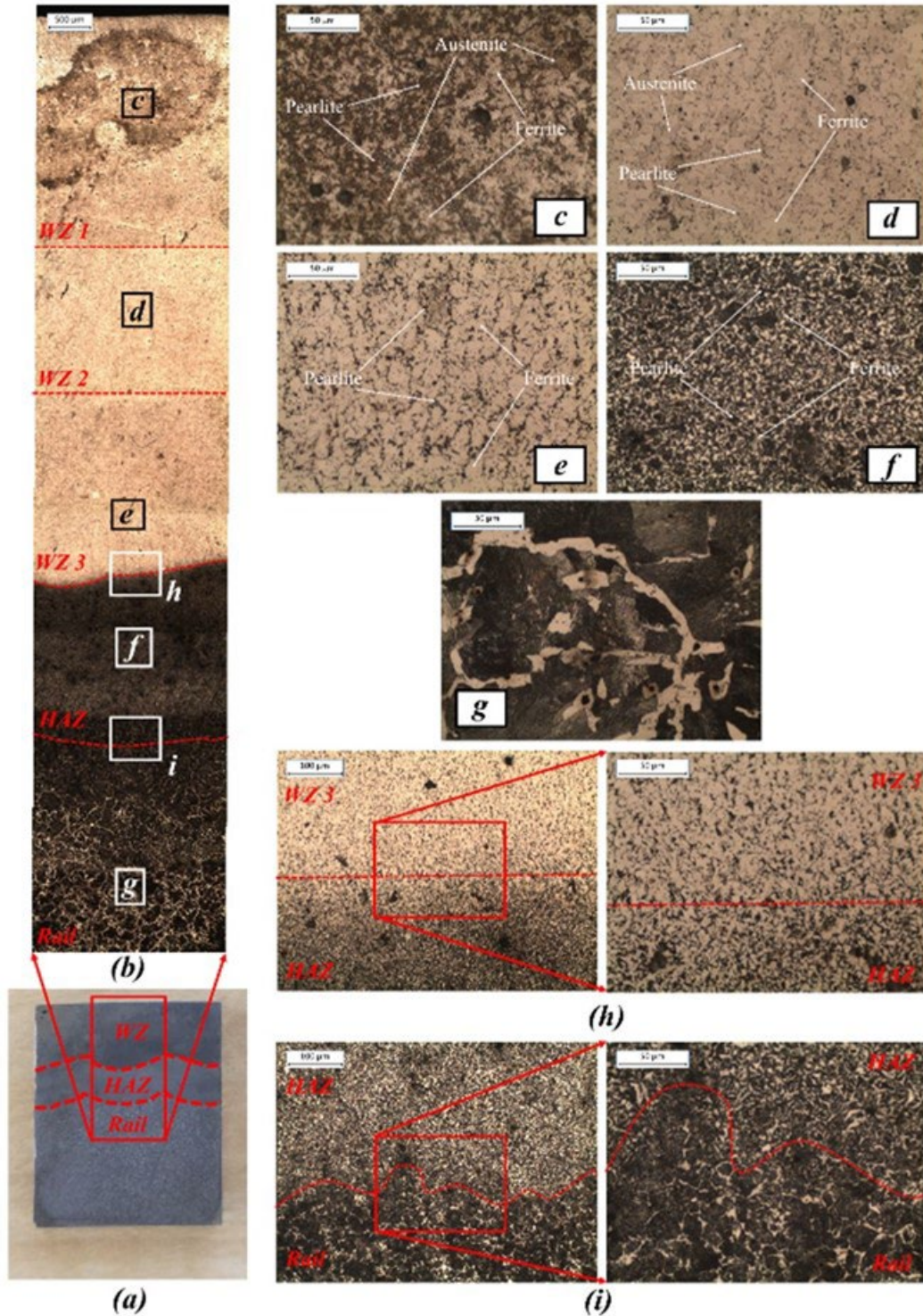
### **3. CHAPTER 3 MICROSTRUCTURAL ANALYSIS OF THE REPAIRED RAIL**

#### **3.1. Light rail**

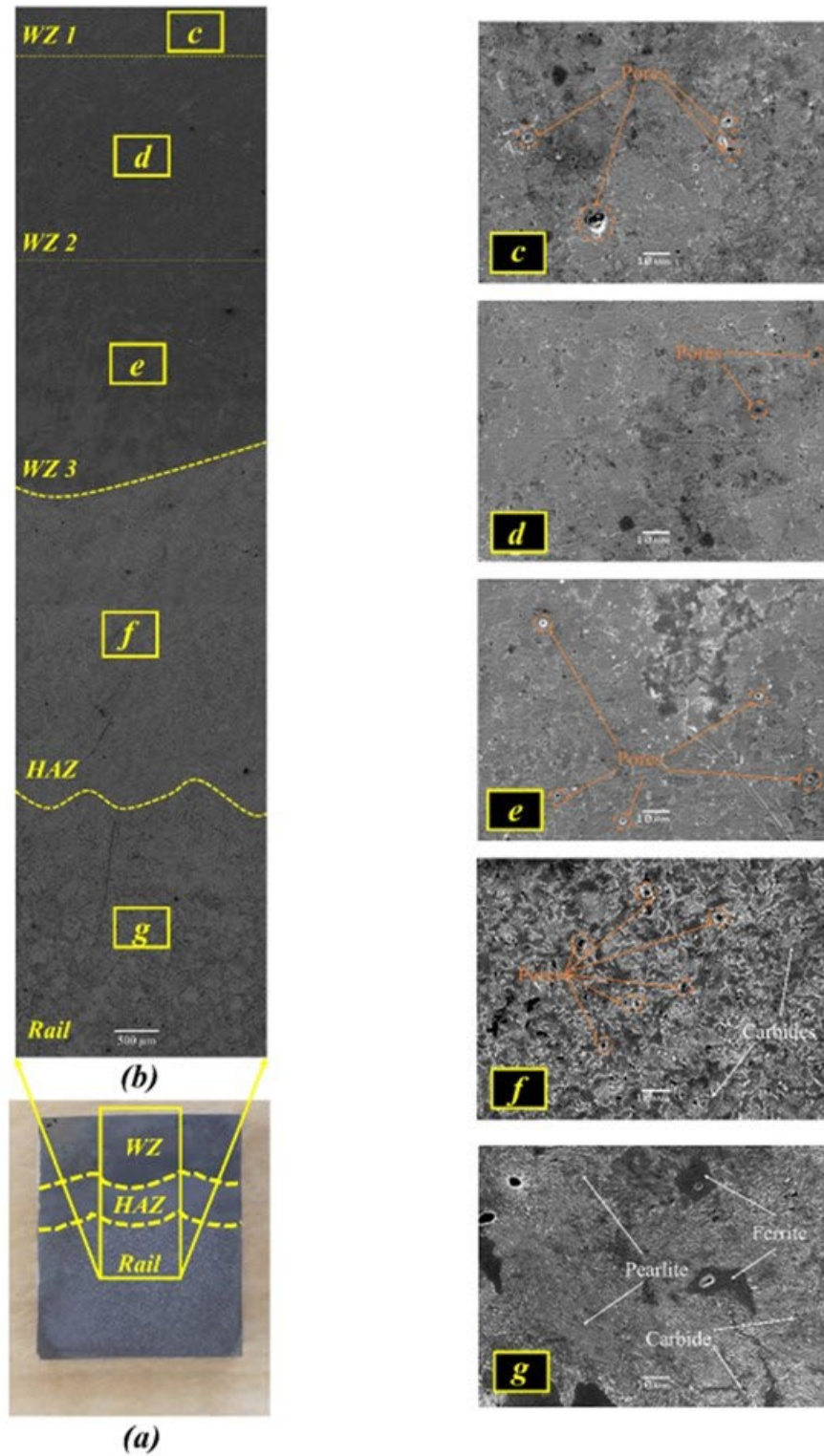
##### **3.1.1. SAW-repaired light rail**

Fig. 1 illustrates optical microscope (OM) micrographs of the cross section of the as-built (AB) metallographic specimen extracted from the SAW-repaired heavy rail. The sample extraction procedure was fully described in Sec. 2.3. According to Fig. 1a, the SAW-repaired specimen is partitioned into three zones: (1) weld zone (WZ), which represents the added weld materials on top of the railhead; (2) heat-affected zone (HAZ), the fusion zone connecting WZ to the rail; and (3) rail zone that is the worn rail substrate. The WZ, as shown in Fig. 1b, is subdivided into three zones with varying microstructure distribution along the depth of the WZ cross section. Fig. 1c corresponds to the WZ1—the top portion of the WZ; WZ2 is the middle portion of the WZ that is illustrated in Fig. 1d, and Fig. 1e shows WZ3—the lower part of the WZ that is adjacent to the HAZ. The OM micrographs of the HAZ and rail are also presented in Figs. 1f and 1g, respectively. Figs. 1h and 1i stand for the WZ/HAZ and the HAZ/rail fusion boundary, respectively, where the mentioned fusion boundary is shown in dashed red line. Subsequently, scanning electron microscope (SEM) micrographs of WZ1, WZ2, WZ3, HAZ, and rail are given in Figs. 2c to 2g, respectively. Table 1 lists chemical composition of different zones of the AB specimen.





**Fig. 3.1** (a) a chopped piece from the metallographic as-built (AB) specimen; (b) Optical macrograph covering weld zone (WZ), heat-affected zone (HAZ), and rail zone; OM micrographs of (c) WZ1, (d) WZ2, (e) WZ3, (f) HAZ, (g) rail, (h) WZ/HAZ fusion boundary, and (i) HAZ/rail fusion boundary are also illustrated.



**Fig. 3.2** (a) a chopped piece from the metallographic specimen of the as-built (AB) specimen; (b) Optical macrograph covering weld zone (WZ), heat-affected zone (HAZ), and rail zone; SEM micrographs of (c) WZ1, (d) WZ2, (e) WZ3, (f) HAZ, and (g) rail are also illustrated.

**Table 6** Chemical composition of different zones of the as-built (AB) SAW-repaired light rail specimen (wt.%).

Zone	Fe	C	Mn	Si	Al	Ti	O	N	P	S
<b>WZ 1</b>	Bal.	0.056	1.30	0.46	0.082	0.0040	0.018	0.0094	0.0092	0.011
		±0.002	±0.24	±0.13	±0.003	±0.0001	±0.003	±0.0007	±0.0001	±0.008
<b>WZ 2</b>	Bal.	0.052	1.18	0.52	0.23	0.0048	0.012	0.0081	0.011	0.010
		±0.003	±0.19	±0.13	±0.01	±0.0003	±0.001	±0.0007	±0.004	±0.008
<b>WZ 3</b>	Bal.	0.055	1.04	0.54	0.120	0.0039	0.032	0.0030	0.010	0.012
		±0.003	±0.24	±0.10	±0.006	±0.0003	±0.005	±0.0009	±0.002	±0.007
<b>HAZ</b>	Bal.	0.255	1.10	0.35	0.023	0.00032	0.0093	0.0001	0.018	0.031
		±0.012	±0.19	±0.10	±0.009	±0.00001	±0.0006	±0.00005	±0.002	±0.001
<b>Rail</b>	Bal.	0.790	1.14	0.230	-	-	-	-	0.043	0.035
		±0.053	±0.28	±0.023	-	-	-	-	±0.022	±0.020

The dendritic pearlite microstructure of the rail substrate is displayed in Figs. 1(g) and 2(g). The corresponding microstructure contains coarse trails of acicular ferritic colonies and a considerable number of fine carbides that are spread throughout the partially and fully pearlitic matrix. The existing acicular ferrite along the grain-boundary pearlite is known as Widmanstätten ferrite [1]. Therefore, the rail substrate microstructure is generally consisted of pearlite, blended with ferrite and carbide.

According to quasi-binary Fe-Al diagram in Fig. 3, for the low-aluminum weld wire used in this study—which contains approximately 0.5 wt.% of aluminum—the microstructure of the WZ is found to be majorly consisted of  $\alpha$ -ferrite and the mixture of  $\alpha$ -ferrite and cementite (i.e., pearlite) at room temperature [2]. Ferrite and pearlite are distinctive in Fig. 1, as they appeared in light-etched and dark-etched grain structure, respectively. Referring to Table 1, the trend of aluminum content concentration shows that it increases from WZ1 to WZ2 and then decreases towards WZ3. Li et al. [3] showed that the surfacing weld layer becomes more pore-sensitive as the aluminum content decreases. Thus, the presence of low aluminum content (< 1.45 wt%) in steel welds along with the resided aluminum oxide from flux particles contribute to formation of non-metallic inclusions containing  $Al_2O_3$  and AlN, which are the fundamental motivation of pore formation. In spite of the detrimental consequence of pore development in low-aluminum steel welds that can subsequently lead to cleavage fracture and cracks, the nucleation of ferrite is the beneficial effect of such inclusions. The ferrite aggregation is directly correlated with aluminum content, whereas the pearlite amount is adversely correlated. Therefore, it can be seen that as the aluminum content increases from WZ1 to WZ2 (see Table 1), the size and concentration of pores is decreased from WZ1 (Fig. 2c) to WZ2 (Fig. 2d), while decreasing aluminum content from WZ2 (Fig. 2d) to WZ3 (Fig. 2e) leads to an increase in pore size and concentration.



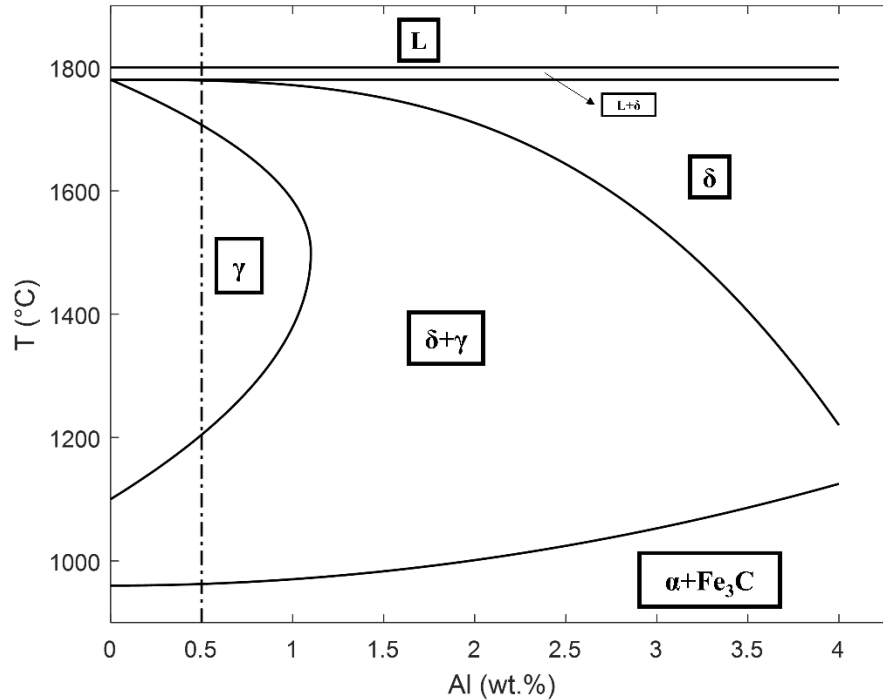


**Fig. 3.3** Fe-Al quasi-binary phase diagram for the low-aluminum (0.5 wt.% of Al content) E71T-1C weld wire used for SAW-repair process [2];  $\delta$ :  $\delta$ -ferrite,  $\alpha$ :  $\alpha$ -ferrite,  $\gamma$ : austenite, and  $\text{Fe}_3\text{C}$ : cementite.

An analogy between WZ1 (Fig. 2c) and WZ3 (Fig. 2e) also shows the coarser pore size in WZ1 as a result of lower aluminum content in this zone rather than WZ3 (Table 1). The preceding decrease-increase trend of pore concentration is also distinctive in Fig. 1b. With regard to microstructure distribution, OM morphologies in Fig. 1 show a fine equiaxed grain structure with uniform distribution in weld zone. Nevertheless, the low aluminum content in WZ1 (Table 1) has resulted in a high portion of pearlite, a moderate fraction of grain-boundary ferrite, and a minor amount of austenite in this zone (Fig. 1c). The presence of residual austenite can be caused by the high cooling rate at the top portion of the WZ, where the arc as the heat source is rapidly removed after finishing the SAW process; hence, as shown in the phase diagram in Fig. 3, a tiny fraction of austenite may remain in the weld microstructure as a result of fast cooling to room temperature. The WZ2 is predominantly consisted of ferrite and austenite that are evenly spread all over the zone, along with a sparse fraction of pearlite (Fig. 1d) in virtue of the ascending trend of aluminum content from WZ1 to WZ2 (see Table 1). The pearlite fraction aggregates in WZ3 compared to WZ2 according to Figs. 1e and 1d, respectively, although it still has lower fraction rather than that in WZ1 (Fig. 1c). Further, as Fig. 1e shows, there are no signs of austenite in WZ3, the lowest zone that is cooled down more gradually rather than the upper zone as it remains exposed to the heat source for a longer time during depositing the upper zones in the SAW process; hence, there have been enough time for austenite to be fully transformed to ferrite and not resided in the microstructure. There may be a deficient amount of fine carbide particles dispersed in the WZ that may not be visible at the provided magnifications. Hence, the primary phases that developed the WZ microstructure are ferrite, pearlite, residual austenite, and a descending amount of carbide that can probably lead to high hardness in this region.

Shen et al. [4] studied the microstructure transformation along with mechanical properties of different surfacing materials before and after processing. According to their findings, a combination of the substrate and surfacing zone builds up the HAZ microstructure. Likewise, the HAZ microstructure in the current sample is a mixing of the microstructure of WZ3 and rail, the abutting zones. It can be observed from Figs. 1h and 1i that moving from WZ3 and rail substrate to the HAZ and trespassing the depicted fusion boundary, the grain size and fraction of various phases are evolved significantly. As Fig. 1h shows, approaching from WZ3 downwards to the HAZ, pearlite concentration increases and a ferrite segregation occurs which then diffuses among pearlite grains. Conversely, a close look at Fig. 1i shows a grain refined zone in HAZ adjacent to the coarsened grain zone of the rail substrate, where the pearlite phase has been segregated gradually from the rail zone upwards to the HAZ and then dispersed throughout the ferrite matrix. In this way, as it is evident in Fig. 1f, the HAZ is consisted of a uniform fine-grained non-dendritic microstructure of ferrite and pearlite. Fig. 2f shows that carbides are also developed all over the HAZ. The corresponding fine and uniform microstructure promises a great hardness and satisfactory mechanical properties and, subsequently, a durable bonding between rail and weld materials. However, it can be seen in Fig. 2f that a great amount of micro pores is breached throughout the HAZ, which can be the basic sites of crack initiation and propagation and consequently material rupture. Such a condensed concentration of micro pores at HAZ can be described as a result of fluctuation of liquid particles at the fusion zone during welding and also various cooling rates in different locations that can finally result in forming defects. Besides, the C-Mn rail substrate is a high carbon steel, which makes it a low-grade substrate in the matter of weldability. As a result, submerged arc surfacing process on such a high carbon steel may lead to pore and crack development at the fusion zone that can be mitigated through heat treatment process later on.

Mori et al. [5] figured out that the present titanium during welding takes part in the de-oxidation process and develops fine titanium-coated oxides that help inter-granular nucleation of ferrites. In addition, Fleck et al. [6] reported that the oxygen element in welding process contributes in establishing fine oxides that attach to the austenite and pearlite grain boundaries and release more space for nucleation of ferrite. Table 1, moving from WZ3 towards HAZ, exhibits losses in titanium and oxygen, the helpful elements for nucleation of ferrite, according to the previous studies mentioned earlier. This descending trend in titanium and oxygen correlates the decreasing in ferrite volume fraction from WZ3 to HAZ, as shown in Fig. 1h. Fleck et al. [6] demonstrated the effect of oxygen in decreasing grain boundary of ferrite that ultimately tends to finer lath size and higher density of ferrite. Also Table 1, moving from rail zone to HAZ, shows an amount of oxygen intrusion, which resulted in refined lath size of ferrite phase, the fact that can be observed in Fig. 1i as well. The carbon dilution phenomenon, which leads to penetration of carbon from high-carbon rail substrate through to the HAZ, causes a sudden rise in carbon percentage in HAZ compared to WZ (Table 1). This abrupt increase in carbon fraction is the basic argument of carbide volume fraction growth in HAZ over against the WZ. It can be seen in Table 1 that the content of manganese, as an austenite-forming element, is decreased gradually from WZ1 to WZ3, just like gradual descending of austenite fraction through the same path, from WZ1 (Fig. 1c) to WZ3 (Fig. 1e). On the other hand, increasing ferrite-forming silicon element helps the ferrite aggregation in the path from WZ1 to WZ3, as shown from Figs. 1c to 1e. According to Fonstein [7], the ferrite-forming elements, like silicon here, are beneficial for boosting mechanical properties like hardness

and cracking resistance. The analysis of the effect of chemical composition on the formation rate of ferrite, pearlite, and austenite phases has shown the influence of alloying element proportion on microstructure phase morphology. It was demonstrated that inclusion of aluminum oxide causes creation of detrimental micro pores, although it can slightly help ferrite formation. It could also be inferred how the loss of austenite-forming elements and inclusion of ferrite-forming elements can substantially improve nucleation of ferrite that conclusively benefits the hardenability and yield strength of the material.

In the next step, the AB specimen is quenched following the procedure described in Sec. 2.3. The optical and scanning electron microstructure of the as-quenched (AQ) specimen are shown in Figs. 4 and 5, respectively. Comparing the AQ sample (Fig. 4a) with the AB (Fig. 1a), the HAZ is vanished in the AQ specimen and is no longer distinguishable with the naked eye. It can be construed that the residing elements in HAZ have been dispersed throughout the sample during the quenching process. The general macrograph of the AQ sample in Fig. 4b shows that the weld zone has been transformed into a dark-colored, fine-grained structure, and the HAZ/rail boundary is not as clear as what it was in the AB case. Table 2 shows the resulting chemical composition of different zones of the AQ sample.

Comparing Figs. 1g and 4g, the rail zone has been transformed from a pearlitic microstructure into a bainitic microstructure. Bainitic ferrite plates consisting of retained austenite and untempered martensite appeared in dark-colored islands, and bainite in light color with finer grain structure are observable in the rail zone in Fig. 4g. Although austenite and untempered martensite are not distinguishable in Fig. 4g, they are distinct as medium-dark-colored and deep-dark-colored areas, respectively, in the SEM morphologies in Fig. 5g. Also, moderate amounts of precipitated carbides are dispersed throughout the ferritic matrix. This bainitic microstructure for a heat-treated rail steel comprising carbides inside ferrite laths is classified as lower bainite by Singh et al. [8].

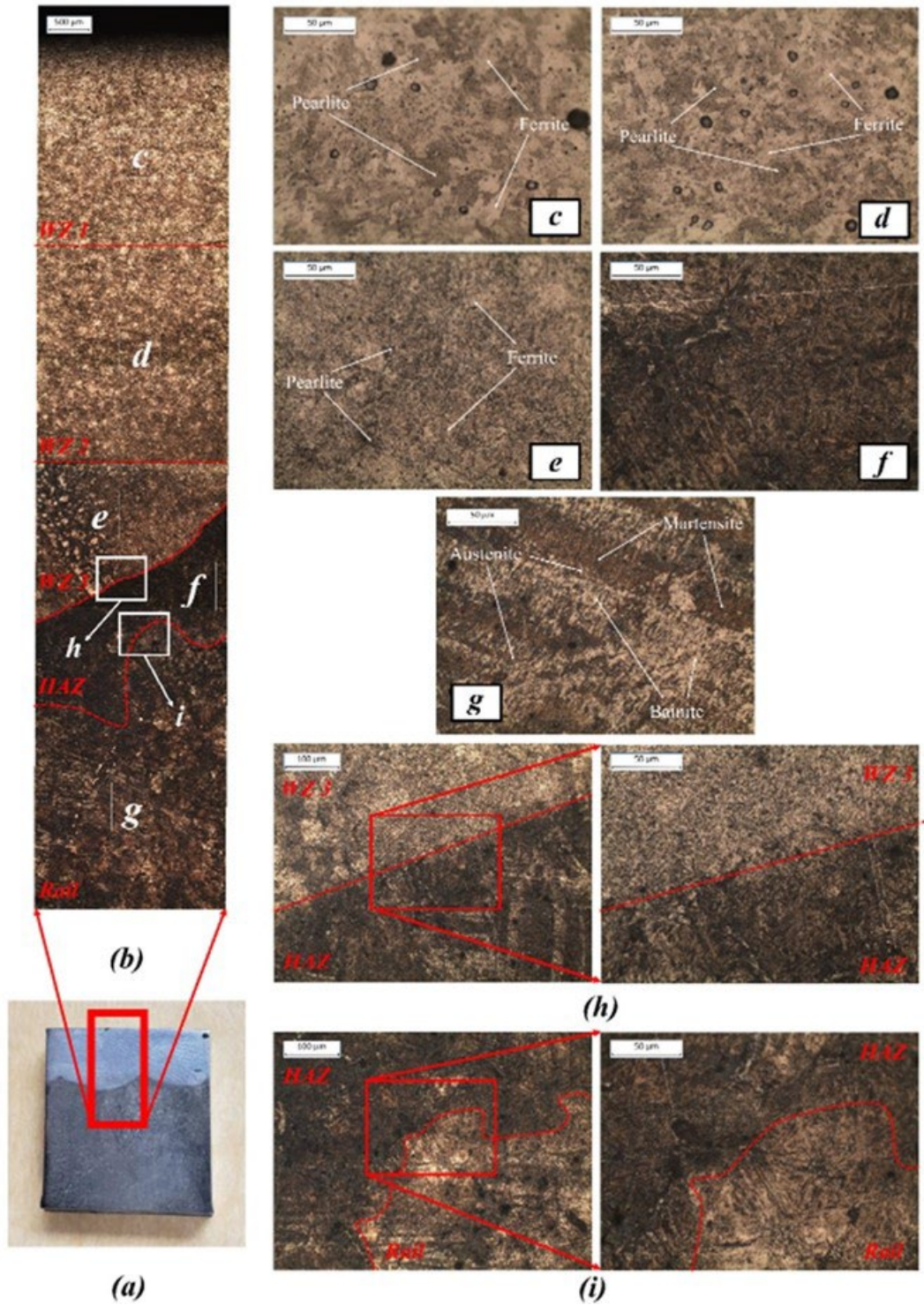


**Fig. 3.4** (a) a chopped piece from the metallographic as-quenched (AQ) specimen; (b) Optical macrograph covering weld zone (WZ), heat-affected zone (HAZ), and rail zone; OM micrographs of (c) WZ1, (d) WZ2, (e) WZ3, (f) HAZ, (g) rail, (h) WZ/HAZ fusion boundary, and (i) HAZ/rail fusion boundary are also illustrated.



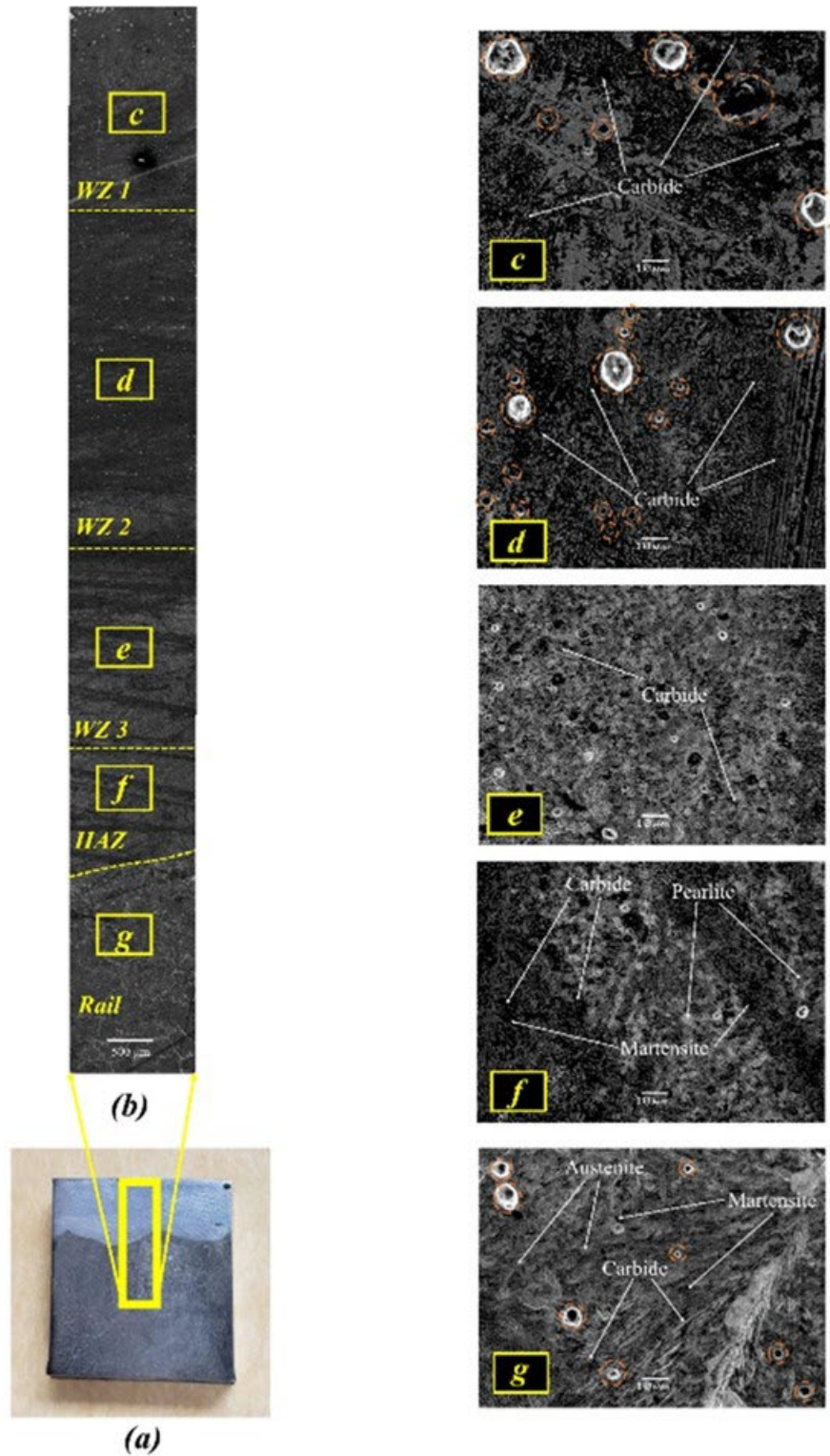


**Fig. 3.5** (a) a chopped piece from the metallographic as-quenched (AQ) specimen; (b) Optical macrograph covering weld zone (WZ), heat-affected zone (HAZ), and rail zone; SEM micrographs of (c) WZ1, (d) WZ2, (e) WZ3, (f) HAZ, and (g) rail are also illustrated.

**Table 7** Chemical composition of different zones of the as-quenched (AQ) SAW-repaired light rail specimen (wt.%).

Zone	Fe	C	Mn	Si	Al	Ti	O	N	P	S
<b>WZ 1</b>	Bal.	0.140	0.166	0.057	0.012	0.0005	0.953	0.0016	0.0004	0.0005
		±0.030	±0.010	±0.005	±0.001	±0.0001	±0.080	±0.0009	±0.0002	±0.0002
<b>WZ 2</b>	Bal.	0.120	0.548	0.066	0.033	0.0006	0.895	0.0014	0.0010	0.0005
		±0.020	±0.039	±0.005	±0.003	±0.0001	±0.052	±0.0008	±0.0001	±0.0002
<b>WZ 3</b>	Bal.	0.180	0.230	0.086	0.017	0.0004	1.010	0.0005	0.0009	0.0005
		±0.030	±0.022	±0.005	±0.003	±0.0001	±0.075	±0.0002	±0.0001	±0.0001
<b>HAZ</b>	Bal.	0.310	0.403	0.010	0.0090	0.000040	0.830	-	0.0023	0.0044
		±0.020	±0.076	±0.004	±0.0003	±0.000006	±0.080	-	±0.0001	±0.0007
<b>Rail</b>	Bal.	0.320	0.110	0.065	-	-	0.796	-	0.012	0.010
		±0.016	±0.019	±0.007	-	-	±0.033	-	±0.005	±0.005

The presence of coarse pores, which are located with dashed orange circles in Fig. 5g, can be attributed to dissolution of CO<sub>2</sub>, due to the exposure to water phase and subsequently intrusion of H<sub>2</sub>CO<sub>3</sub> and FeCO<sub>3</sub> that leads to formation of porous microstructure with precipitated cementite lamellae (Fe<sub>3</sub>C) along pore boundaries [9]. The high wt.% of oxygen in rail zone that is shown in Table 2 confirms the chain of oxidation procedure during water quenching.

With regard to the weld zone, Figs. 4c and 4d shows that WZ1 and WZ2 have become almost identical in microstructure topography, in a way that they can be assigned with one integral zone. Since the AB sample has been heated up to 1100 °C, according to the quasi-binary diagram in Fig. 3, the sample has been partially austenized and no primary austenite has been initiated during the heat treatment process. Accordingly, no retained austenite is visible in microstructure of WZ1 and WZ2 shown in Fig. 4c and 4d. The dominant visible element in WZ1 and WZ2 microstructure is the carbide precipitations that are visible all over the region (see Figs. 5c and 5d). Based on Santofimia et al. [10], carbide precipitations are the lands of sinking carbon that draw the carbons in and do not let them to participate in austenite stabilization, which again explains why austenite is absent in the upper two weld zones. The high density of carbide particles as carbon inhalation lands has considerably led to an increase in carbon weight percentage in these zones as shown in Table 2 for WZ1 and WZ2. The volume fraction of pearlite, which appeared in dark-etched color, has been increased in the AQ sample for the upper weld zones, especially for WZ2, which, along with the carbides, can substantially help increasing hardness in these zones. It is noted, however, that density and size of the pores in WZ1 and WZ2 in the AQ sample increase, which can be associated with the immense oxygen infiltration in this area. This aggression of oxygen helps commencing Al<sub>2</sub>O<sub>3</sub> inclusion that is the main reason of pore creation in microstructures; it can be observed by comparing Figs. 2c and 2d with Figs. 5c and 5d. The same pearlite, ferrite, and carbide are the fundamental elements of WZ3, but with exceptionally finer grain structure (Fig. 4e), which can potentially guarantee great hardness values in this region. According to Table 2, WZ3 presents the highest wt.% of oxygen, which, according to the assertion of Fleck et al. [6], describes the fine-grain structure of the WZ3. The percentage of pearlite in this section has also been markedly increased compared to the AB sample, before quenching. Such growth in pearlitic microstructure can be explained based on the Fe-Al quasi-binary diagram in Fig. 3. At the time that the sample is heated up to 1100 °C, the primary phases consisting weld materials are austenite and δ-ferrite. If the sample would cool down gradually, there was enough time for microstructures to be fully transferred to α-ferrite and cementite. However, as the sample is immediately water-quenched, there will not be enough time for the complete transformation, and hence, a portion of austenite

and  $\delta$ -ferrite will be resided in the microstructure. Due to the presence of carbides, as discussed earlier, there are not enough carbon to stabilize the residual austenite, and thus, the unstable austenite transfers either to  $\alpha$ -ferrite or  $\delta$ -ferrite. On the other hand, due to a great amount of carbon penetration in weld zone, according to the chemical analysis in Table 2, nucleation of cementite ( $\text{Fe}_3\text{C}$ ) starts to grow dramatically, which, with the presence of the ferrite, nucleates more pearlite.

The deep dark etching of the HAZ has made the microstructure slightly invisible. According to the SEM micrograph in Fig. 5f, the HAZ seems to be dominantly consisted of untempered martensite and pearlite. On one hand, Fig. 4h, from WZ3 towards the HAZ, shows that the light-colored island has disappeared and the dark-colored region, which is pearlite, has remained. On the other hand, moving upward from rail zone to HAZ in Fig. 4i, the bainite phase that is light-etched vanishes and the dark-etched area of austenite and untempered martensite remains. Based on the study by Shen et al. [4], this observation confirms the presence of martensite and pearlite in HAZ, and also the numerous carbides that are detectable in the HAZ in Fig. 5f.

### **3.1.2. LPD-repaired light rail**

Fig. 6 shows the OM morphology of the as-built (AB) specimen. Based on Fig. 6a, the AB sample technically can be divided into three zones, i.e., the deposition zone (DZ), the heat-affected zone (HAZ), and the rail zone. Figs. 6c and 6d show magnified micrographs of the rail and the HAZ, respectively. Figs. 6e to 6j show the enlarged OM micrographs of the first to sixth deposition layers. Fig. 7 shows the corresponding SEM micrographs of the different zones. Table 3 provides the chemical compositions of the different zones of the AB specimen.

The authentic microstructure of the C-Mn rail steel is thin lamellar pearlite. Accordingly, as shown in Fig. 6c, the rail material primarily is constituted of dendritic pearlite with random lamellae orientation and pro-eutectoid ferrite. The SEM micrograph in Fig. 7c shows that there are abundant carbides distributed throughout the pearlitic matrix. Hence, the microstructure of the rail zone in the AB specimen typically is composed of a pearlitic-ferritic microstructure that contains thoroughly-dispersed fine carbides.



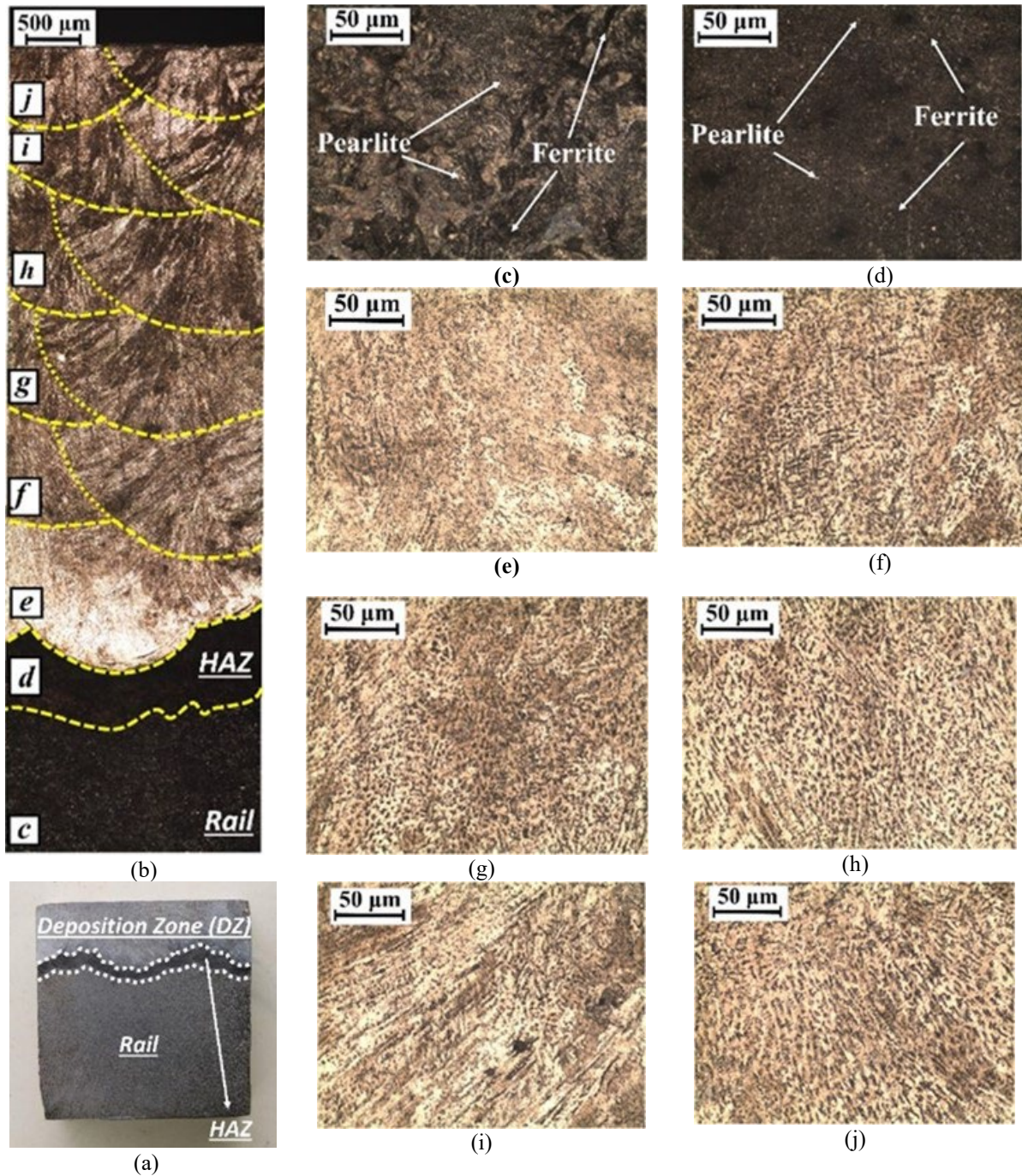


**Fig. 3.6** (a) The metallographic sample chopped from the AB specimen; (b) A comprehensive OM macrograph covering DZ, HAZ, and rail; (c) OM micrograph of the rail and (d) HAZ; OM micrographs of DZ are separated layer-wise in (e), (f), (g), (h), (i), and (j), representing first, second, third, fourth, fifth, and sixth deposition layers, respectively.



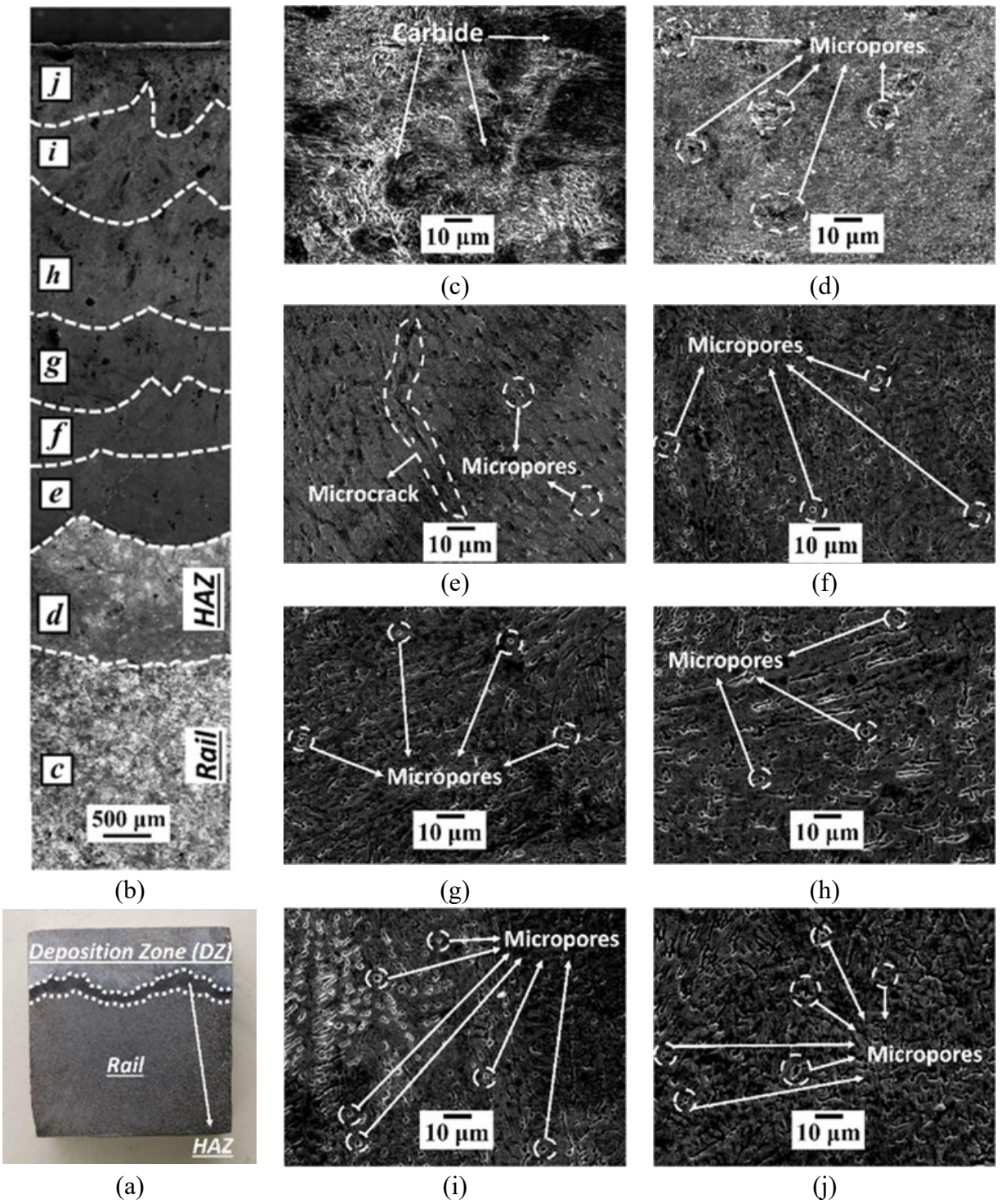


**Fig. 3.7** (a) The metallographic sample chopped from the AB specimen; (b) A comprehensive SEM macrograph covering DZ, HAZ, and rail; (c) SEM micrograph of the rail and (d) HAZ; SEM micrographs of DZ are separated layer-wise in (e), (f), (g), (h), (i), and (j), representing first, second, third, fourth, fifth, and sixth deposition layers, respectively.

**Table 8** Chemical composition of the as-built (AB) LPD-repaired light rail specimen at different zones (wt.%).

Material	Fe	C	Cr	Mn	Si	Ni	O	N	P	S	Cu	Mo
<b>DZ-6*</b>	Bal.	0.0179	16.47	1.86	0.20	8.84	0.0136	0.079	0.009	0.007	0.036	0.039
		±0.0021	±1.32	±0.17	±0.05	±0.57	±0.0029	±0.001	±0.0006	±0.0002	±0.003	±0.60
<b>DZ-5</b>	Bal.	0.0113	16.01	1.79	0.19	8.12	0.0103	0.078	0.010	0.007	0.027	0.042
		±0.0014	±1.18	±0.15	±0.03	±0.54	±0.0027	±0.001	±0.006	±0.24	±0.002	±0.005
<b>DZ-4</b>	Bal.	0.0079	17.82	1.50	0.25	7.21	0.0176	0.082	0.008	0.008	0.048	0.041
		±0.0008	±1.44	±0.11	±0.05	±0.56	±0.0026	±0.004	±0.0009	±0.0003	±0.001	±0.006
<b>DZ-3</b>	Bal.	0.0073	17.67	1.46	0.28	7.19	0.0101	0.080	0.009	0.008	0.031	0.042
		±0.0005	±1.24	±0.17	±0.01	±0.63	±0.0031	±0.007	±0.0005	±0.0005	±0.001	±0.004
<b>DZ-2</b>	Bal.	0.0061	17.24	1.43	0.30	7.22	0.0147	0.079	0.009	0.006	0.043	0.045
		±0.0005	±1.05	±0.16	±0.03	±0.52	±0.0027	±0.003	±0.0001	±0.0008	±0.003	±0.001
<b>DZ-1</b>	Bal.	0.0040	15.29	1.50	0.36	8.09	0.0147	0.084	0.012	0.009	0.031	0.033
		±0.0003	±1.12	±0.16	±0.05	±0.49	±0.0026	±0.003	±0.007	±0.0003	±0.001	±0.006
<b>HAZ</b>	Bal.	0.270	9.94	1.16	0.27	0.062	0.0016	0.00074	0.011	0.007	0.0014	0.0010
		±0.051	±0.17	±0.18	±0.07	±0.001	±0.0008	±0.00004	±0.007	±0.0005	±0.0001	±0.0003
<b>Rail</b>	Bal.	0.790	-	1.14	0.230	-	-	-	0.043	0.035	-	-
		±0.053	-	±0.28	±0.023	-	-	-	±0.022	±0.020	-	-

\* DZ – 6 means “deposition zone – sixth deposited layer”. Same description applies to the other terms listed in this Table with the same format.

To render a crack-resistant structure for a welded/deposited alloy, a microstructure consisting of 5 to 10 vol.% of  $\delta$ -ferrite must be developed. To attain this goal, the ratio of ferrite stabilizers (Cr, Si, Mo) to austenite stabilizers (Ni, C, Mn, N) must be fine-tuned. Fu et al. [11] identified the solidification trend of 304L as a ferritic-austenitic mode, which is demonstrated specifically as a dash-dot vertical line in the Fe-Cr-Ni pseudobinary phase diagram in Fig. 8. Referring to Fig. 6e, the primary austenitic microstructure of the first deposited layer (DZ-1) has three regions in the matter of the color spectrum, i.e., dark-etched, light-etched, and semi-dark-etched. The light-etched austenite is essentially surrounded by the dark-etched area that represents vermicular delta ferrite. At the time of the deposition of DZ-1, the rail initially was at the ambient temperature, so DZ-1 underwent rapid cooling due to the low bed temperature. As a result, referring to Fig. 8, cooling through the  $\delta+\gamma$  domain, i.e., from the ferrite solvus temperature,  $T_{\delta\text{-solvus}}$ , to the austenite solvus temperature,  $T_{\gamma\text{-solvus}}$ , occurs so rapidly that the diffusion of Cr and Ni was eliminated. Thus, the hypothesis is that fast cooling below  $T_{\gamma\text{-solvus}}$  causes a massive  $\delta\rightarrow\gamma$  transformation, and, as a consequence,  $\delta$ -ferrite becomes supersaturated compared to austenite [12]. Hence, the semi-dark network in Fig. 6e resolutely offers the part of  $\delta$ -ferrite that is transformed to austenite via the massive  $\delta\rightarrow\gamma$  transformation process during the first step of fast cooling. Referring to Fig. 8, a critical note to mention is that, after prolonged exposure of  $\delta$ -ferrite to temperatures around 600°C, it is transformed to the brittle sigma phase [13,14]. The DZ-1 has been periodically exposed to newly-induced thermal cycles when the subsequent layers were deposited, and this has kept this layer at elevated temperatures long enough to allow the  $\delta\rightarrow\sigma$  transformation. Thus, one can say that part of the semi-dark region, i.e., the part that is nearer to the dark-etched retained ferrite cellular boundaries, indeed is representing the sigma phase. The SEM micrograph of the DZ-1 in Fig. 7e shows several micropores dispersed all over the structure, and there also are signs that microcracks have developed. The gas that is entrapped in the melt pool during LPD is the main cause of the formation of near-spherical micropores. Suutala and Moisio [15] showed the extent to which the cracking sensitivity of conventionally-welded, stainless steel alloys depend on their chemical compositions, specifically the total weight percentage (wt.%) of sulfur and phosphorus (P+S). Later, Pacary et al. [16] established an improved version of the Suutala diagram specifically

for laser welding. Based on their findings, cracking begins in the microstructure of a laser-deposited 304L austenitic stainless steel only when  $(P+S) \geq 0.018$ . Table 3 shows that the total wt.% of P + S for DZ-1 is greater than 0.018.

Fig. 6f shows a primary  $\delta$ -ferrite microstructure for DZ-2. Since the deposition bed of DZ-2 was the high-temperature DZ-1, it has experienced a much slower cooling rate than DZ-1. Hence, no massive  $\delta \rightarrow \gamma$  transformation has occurred during the deposition of DZ-2, which is the reason the semi-dark area has been diminished in this layer (Fig. 6f) compared to DZ-1 (Fig. 6e). The ferrites in Fig. 6f appeared mostly to be in the shape of thin, dark lines that have been laid at the cores of the subgrains. These lines represent the Cr-enriched and Ni-depleted composition, and they are shaped during the early transient stages of the initial solidification. Table 3 also shows that, when moving from DZ-1 to DZ-2, the wt.% of ferrite-stabilizing chromium is increased, while wt.% values of both the austenite-stabilizing nickel and manganese are decreased. In Fig. 7f, signs of micropores are detectable in DZ-2, but there are no distinguishable symptoms of microcracks in this layer. Table 3 indicates that P+S in DZ-2 is less than 0.018 wt.%, which describes the absence of microcracks in this region.

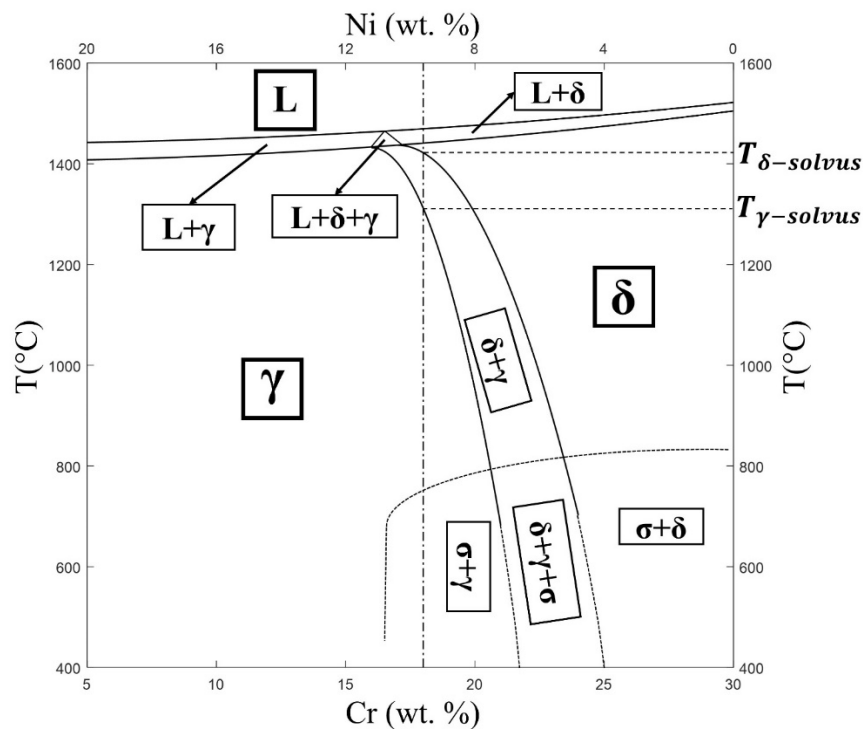


**Fig. 3.8** Phase diagram of the Fe-Cr-Ni pseudobinary system for 304L (70 wt.% Fe) used in powder form for the LPD repair process. L: liquid;  $\delta$ :  $\delta$ -ferrite;  $\gamma$ : austenite;  $\sigma$ : sigma.

Comparing the microstructures of DZ-2 and DZ-3 in Figs. 6f and 6g, respectively, show that they have almost the same phase distribution. Comparing the chemical compositions of DZ-2 and DZ-3 in Table 3 indicates that the wt.% of the ferritizers (Cr, Si, Mo) and the wt.% of the austenizers (Ni, Mn, C, N) are almost equal in these two layers. This provides a strong rationale for the identical microstructures of DZ-2 and DZ-3. This analogy describes that DZ-2 and DZ-3

experienced the same thermal history, i.e., both were deposited on a hot substrate and then exposed to multiple cycles of heating and cooling due to the deposition of the upper layers.

These same reasons explain the microstructural similarity of DZ-4 (Fig. 6h) and DZ-3 (Fig. 6g). The SEM micrographs of DZ-3 and DZ-4 in Figs. 7g and 7h, respectively, show practically the same micropores and microcracks based on size and accumulation, which can be explained by noting that the total P+S wt.% for both layers is less than 0.018, as recorded in Table 3.

Moving from DZ-4 (Fig. 6h) to DZ-5 (Fig. 6i), the general microstructure switches to primary austenite. Fig. 6i resembles a light-etched austenitic matrix that is mixed with a dark-etched ferritic network that is appeared as acicular/lath-like ferrite. An insignificant, semi-dark, supersaturated  $\delta$ -ferrite also is observable in DZ-5. This layer was not cooled as fast as DZ-1, because of higher bed temperature, but it was cooled faster than DZ-2, DZ-3, and DZ-4 because it has been reheated only once, while the lower layers have been reheated at least twice. Hence, DZ-5 has experienced a moderate cooling rate, i.e., a rate that allowed adequate time for the complete  $\delta \rightarrow \gamma$  transformation. However, this time interval was too short to allow for the development of brittle sigma, but it was not short enough to cause a great extent of massive  $\delta \rightarrow \gamma$  transformation. Accordingly, the final microstructure is primarily austenite, but there is still a slight fraction of the semi-dark, supersaturated  $\delta$ -ferrite. Table 3 also shows that the wt.% of Ni and Mn, the most powerful austenizers, is increased dramatically in DZ-5 compared to the former layers. Although the other austenizer, N, is decreased in DZ-5, it is not as much of a determinant as Ni and Mn to be able to downgrade the austenite in this layer. Exploring ferritizers in Table 3 states that Si and Cr, as the most powerful ferrite promoters, are decreased markedly in DZ-5 rather than in the previous layers, which again describes the logic of the primary austenite microstructure in this zone. A sensible increase in the concentration of micropores in DZ-5 in comparison with the former layers is evident in Fig. 7i. The porosity level of the laser-cladded materials is inversely correlated with the laser power. Despite the constant laser power used to deposit all six layers, the lower layers are exposed to laser power multiple times during the deposition of the upper layers, even though the subsequent exposures were not as powerful as the first exposure. Therefore, a fraction of the micropores that developed in every deposited layer has disappeared due to their being reheated. Thus, it is logical that DZ-5, which is reheated only once, has more micropores than the lower layers that are reheated several times.

Based on the observations in Fig. 6j, DZ-6 is composed of a fine-grained microstructure in which the austenite and vermicular  $\delta$ -ferrite have almost the same weight. However, the results in Table 3 indicate that moving from the austenitic DZ-5 to DZ-6, the wt.% values of all of the austenizers, i.e., nickel, manganese, carbon, and nitrogen, have increased, while the ferritizers, including chromium, silicon, and molybdenum, have either increased only slightly, stayed nearly the same, or decreased. Hence, first, since the increment of the austenizers weighs more than that of the ferritizers, and, second, because this new region, i.e., DZ-6, is being compared with an austenitic region, i.e., DZ-5, it is concluded that the DZ-6 region primarily consists of austenite. Also, the semi-dark, supersaturated  $\delta$ -ferrite is reappeared in massive quantities in this region, and the reason this occurred is attributed to this layer's faster cooling rate. The finally deposited layer, i.e., DZ-6, was not reheated and, in addition, its top surface was exposed to free air stream that helped enormously to cool it down faster. However, in contrast to what was discussed for DZ-1 as a result of reheating, since DZ-6 has not been reheated, there was not enough time for the transformation

of  $\delta$ -ferrite to the sigma phase. Thus, there is little chance that the semi-dark region in DZ-6 contains any significant amount of the brittle sigma phase. As shown in Fig. 7j, the DZ-6 layer has a massive distribution of micropores due to the lack of reheating. The final noteworthy observation about DZ-5 and DZ-6 is the lack of microcracks in their microstructures (Figs. 7i and 7j), which occurred for the same reason that the wt.% of P+S in these two regions is still below 0.018 (Table 3). Generally, the DZ microstructure is composed of austenite,  $\delta$ -ferrite, and sigma. DZ-1, DZ-5, and DZ-6 are primary austenite, and DZ-2, DZ-3, and DZ-4 are primary ferrite. The volume fraction of the brittle sigma phase decreases from DZ-1, which has the maximum fraction, to DZ-4, which has the minimum fraction among the first four deposition layers. DZ-5 and DZ-6 contain no sigma. The only layer that contains microcracks is DZ-1. Also, the size and density of the micropores generally increase from DZ-1 up to DZ-6.

The microstructure and mechanical properties of the HAZ always are a mixture of the two adjacent zones. Going from the rail (Fig. 6c) to the HAZ (Fig. 6d), ferrite segregation occurs and a great fraction of pearlite disappears, i.e., the minor fraction of the retained fine-grain, non-dendritic pearlite is diffused into the ferritic network. Due to the adjusted laser power, that can keep the substrate and the developed melt pool in the doughy state and not let it trespass into the diluted state, massive amounts of the deposition materials cannot penetrate through to the substrate materials. Therefore, the HAZ has been, to a great extent, immune from the intrusion of the micrograins of the deposited materials. Thus, the HAZ (Fig. 6d) has inherited only the ferrite phase from DZ-1 (Fig. 6e), which is the only phase that exists in common between rail and DZ-1. Therefore, in Fig. 6d, a uniform primary ferrite microstructure of HAZ is visible in which the fine, non-dendritic pearlite particles are distributed throughout the entire ferritic matrix. Such a consistent microstructure with a ferritic background can yield a satisfactory level of hardness and strength at the rail-deposition joint. Even so, based on the SEM observations in Fig. 7d, this region has an enormous density of coarse micropores, which are the most detrimental sites because they result in the initiation of cracks, eventually resulting in the material rupture. The oscillation of the melted powder particles at the fusion field during the LPD process and the variable local cooling rate lead to the formation of various defects that result in large numbers of micropores in the final microstructure. The other reason for the augmentation of the micropores in HAZ can be attributed to the nature of the C-Mn rail which, due to the high percentage of carbon, typically is poor-weldable steel to act as a substrate. Hence, LPD on this high-carbon steel will breach micropores at the substrate-deposition interface. Also, the chemical composition of the HAZ in Table 3 shows that the total wt.% of P+S in this region is almost equal to 0.018; this fact makes this zone vulnerable to crack initiation, even though no cracks are visible yet in SEM (Fig. 7d). However, the good thing about the HAZ is the dominancy of ferrite, which is a great benefit for increasing the crack resistance and yield strength of the material. Since the HAZ is the bridge between the rail and DZ, this area has to be the pioneer regarding hardness, yield strength, and crack resistance among all three zones to prevent any chance of cracking and delamination. Hence, it seems necessary to heat-treat the AB rail in order to alleviate the micropores and increase the immunity of the final product. In this way, the AB LPD-repaired light rail sample is heat treated following the instructions given in Sec. 2.3. The heat-treated (HT) specimen is analyzed in the following.



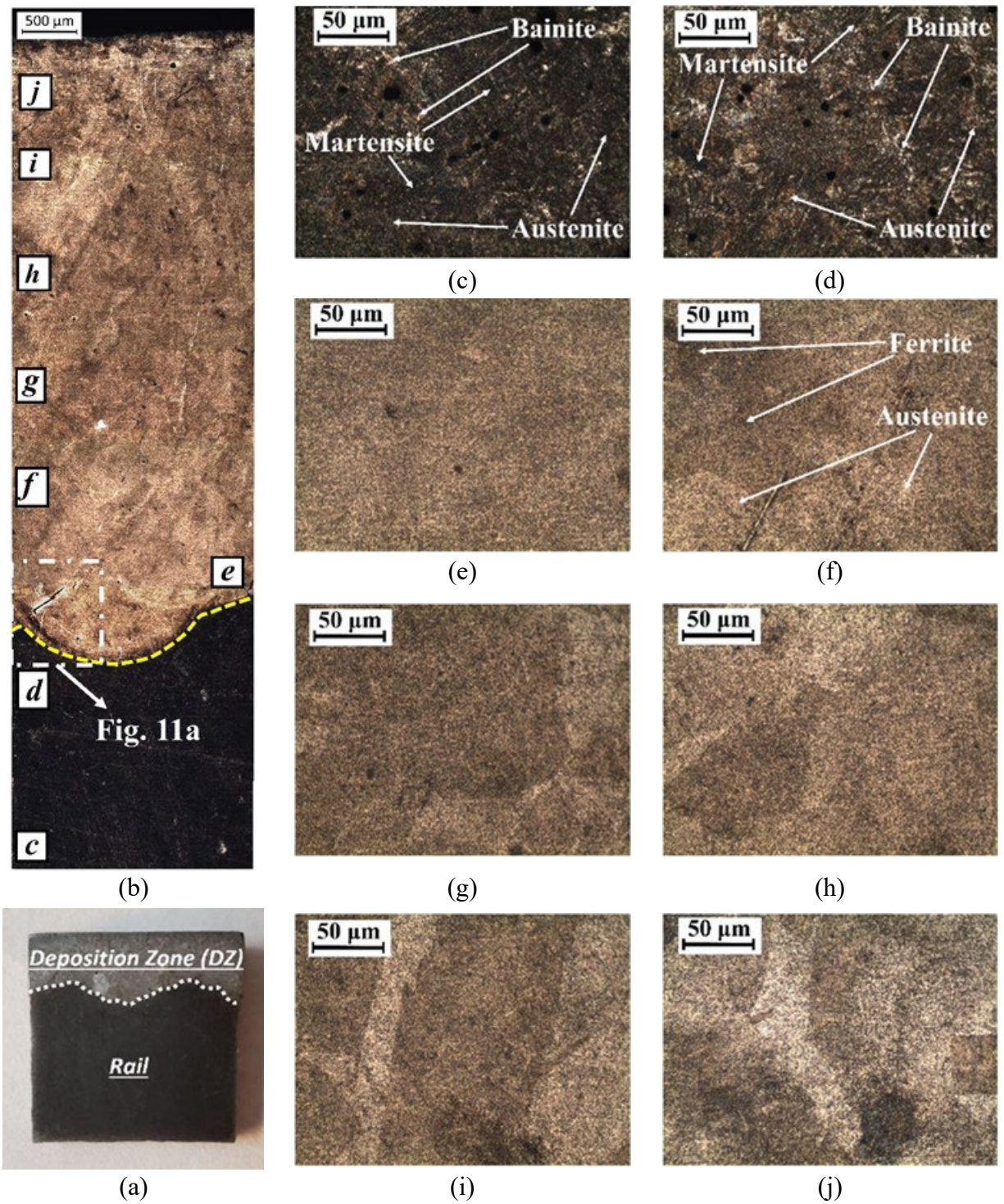


**Fig. 3.9** (a) The metallographic sample chopped from the heat-treated (HT) specimen; (b) A comprehensive OM macrograph covering DZ and rail; (c) OM micrograph of rail and (d) HAZ; due to the disappearance of the interlayer boundaries at the DZ, OM micrographs are taken from the same corresponding locations in Fig. 7 at the (e) first, (f) second, (g) third, (h) fourth, (i) fifth, and (j) sixth deposition layers.



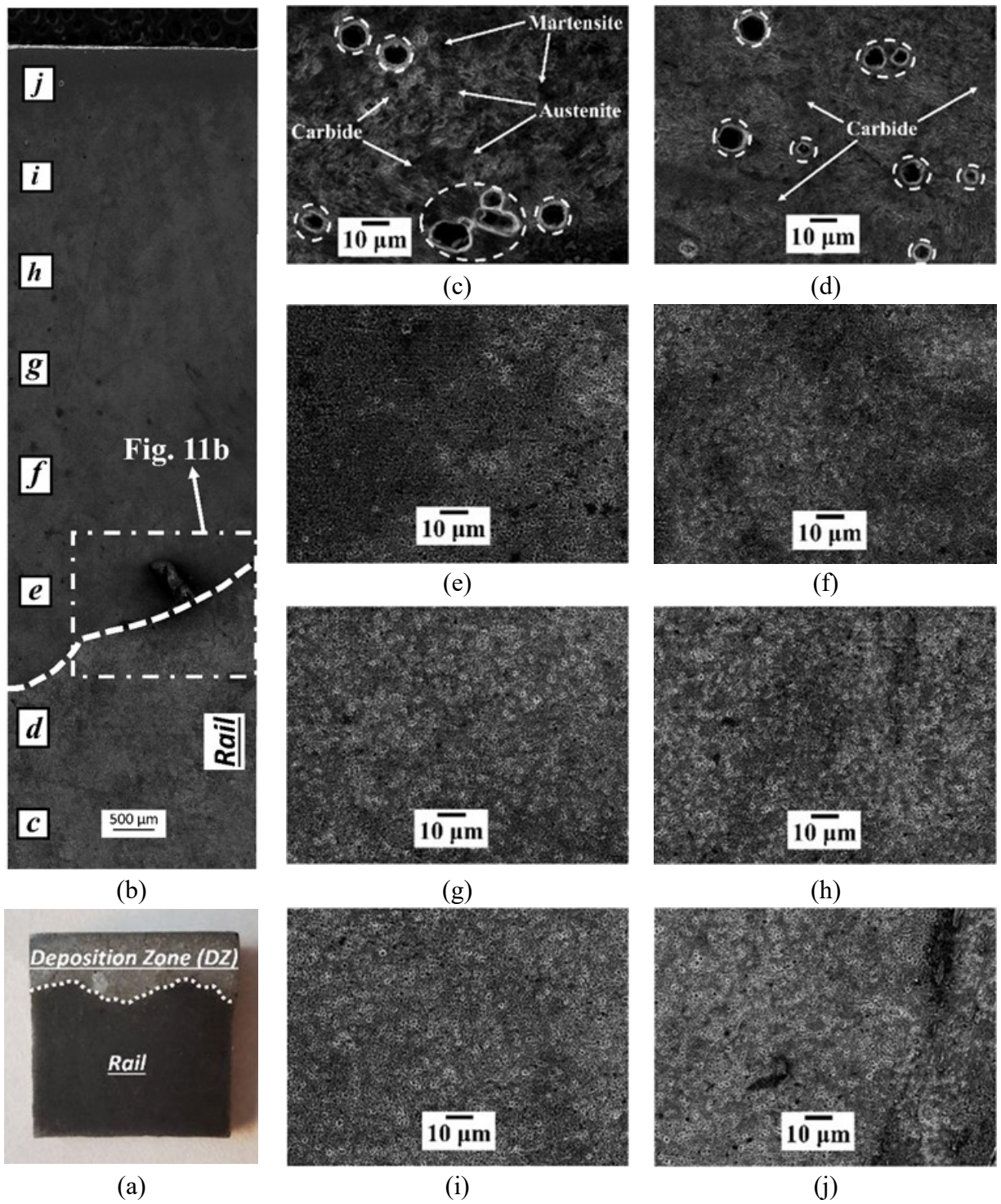


**Fig. 3.10** (a) The metallographic sample chopped from the heat-treated (HT) specimen; (b) A comprehensive SEM macrograph covering DZ and rail; (c) SEM micrograph of rail and (d) HAZ; due to the disappearance of the interlayer boundaries at the DZ, OM micrographs are taken from the same corresponding locations in Fig. 8 at the (e) first, (f) second, (g) third, (h) fourth, (i) fifth, and (j) sixth deposition layers.

**Table 9** Chemical composition of the heat-treated (HT) LPD-repaired light rail specimen at different zones (wt.%).

Material	Fe	C	Cr	Mn	Si	Ni	O	N	P	S	Cu	Mo
<b>DZ-6*</b>	Bal.	0.019	9.74	1.46	0.19	7.62	0.72	0.082	0.0004	0.0002	0.042	0.043
		±0.002	±0.23	±0.22	±0.04	±0.59	±0.05	±0.003	±0.0002	±0.0001	±0.004	±0.005
<b>DZ-5</b>	Bal.	0.023	7.49	1.54	0.27	8.22	0.80	0.071	0.0004	0.0005	0.009	0.036
		±0.002	±0.35	±0.24	±0.03	±0.66	±0.04	±0.006	±0.0001	±0.0002	±0.001	±0.001
<b>DZ-4</b>	Bal.	0.015	10.08	1.48	0.21	7.25	0.67	0.078	0.0009	0.0012	0.015	0.039
		±0.004	±1.16	±0.22	±0.01	±0.56	±0.07	±0.005	±0.0001	±0.0005	±0.001	±0.003
<b>DZ-3</b>	Bal.	0.008	8.01	0.98	0.23	7.15	0.89	0.062	0.0017	0.0023	0.025	0.042
		±0.001	±0.17	±0.07	±0.01	±0.56	±0.05	±0.008	±0.0003	±0.0003	±0.005	±0.001
<b>DZ-2</b>	Bal.	0.080	10.94	1.16	0.31	6.80	0.78	0.043	0.0091	0.0125	0.083	0.036
		±0.003	±1.19	±0.22	±0.02	±0.56	±0.05	±0.001	±0.0008	±0.0013	±0.007	±0.007
<b>DZ-1</b>	Bal.	0.073	10.26	1.10	0.32	5.40	0.97	0.051	0.0102	0.0140	0.011	0.012
		±0.001	±1.98	±0.21	±0.04	±0.47	±0.07	±0.006	±0.0011	±0.0031	±0.005	±0.007
<b>HAZ</b>	Bal.	0.294	3.24	0.57	0.13	0.22	1.28	0.0032	0.017	0.020	0.0028	0.0082
		±0.045	±0.10	±0.17	±0.09	±0.02	±0.80	±0.0002	±0.001	±0.003	±0.0004	±0.0003
<b>Rail</b>	Bal.	0.305	0.92	0.138	0.057	-	1.35	-	0.015	0.011	-	-
		±0.053	±0.23	±0.017	±0.001	-	±0.24	-	±0.009	±0.007	-	-

\* DZ – 6 means “deposition zone – sixth deposited layer”. Same description applies to the other terms listed in this Table with the same format.

Figs. 9 and 10 give OM and SEM morphologies of the HT specimen, respectively, and its chemical distribution is given in Table 4.

Regarding the rail zone, its pearlitic microstructure before heat treatment (Fig. 6c) is switched to a bainitic microstructure (Fig. 9c). The dominant bainitic ferrite plates appear as dark islands and contain untempered martensite along with retained austenite. The minor portion of the light-color, fine-grain bainite also is observable in the rail zone in Fig. 9c. SEM capture from the HT rail zone in Fig. 10c gives a clearer vision of the bainitic ferrite plates, where martensite and austenite are shown as full-dark and semi-dark areas, respectively. The SEM also shows a mild agglomeration of precipitated carbides that are distributed evenly in the entire ferritic network. The bainitic microstructure of the HT rail that contains ferrite laths with interdendritic carbides is categorized as lower bainite. It also is quite obvious the extent to which the rail zone is suffering from the established coarse micropores as they are dash-encircled in Fig. 10c. The aggregation of micropores after water quenching is due chiefly to the dissolution of CO<sub>2</sub>, which occurs as a result of water exposure and, consequently, the intrusion of H<sub>2</sub>CO<sub>3</sub> and FeCO<sub>3</sub>. The dissolute CO<sub>2</sub> forms a porous structure where the cementite lamellae, Fe<sub>3</sub>C, is precipitated along the boundaries of the micropores [17]. The intrusion of a high wt.% of oxygen into the rail zone (Table 4) attests the described oxidation chain during heat treatment.

One of the featured homogenizing effects of heat treatment can be seen in the DZ of the HT sample, where there is almost no microstructural inconsistency among different deposition layers (Fig. 9b) compared to that of the AB specimen (Fig. 6b). The fusion boundaries between the deposition layers have been disappeared entirely, and, after heat treatment, the DZ becomes an integral zone. The residual thermal stresses that are generated in the AB specimen during the LPD heating-cooling cycles will act as the motive force for recrystallization during heat treatment. This phenomenon results in relieving the stress thereby reducing the grain boundary interfacial free energy. As a result, the low-angle boundaries of the AB specimen are switched to high-angle boundaries in the HT sample, which makes them almost parallel to the interlayer crystallographic



orientation, which eliminates the existing misorientation at the fusion boundaries. Thus, due to the lack of interlayer boundaries in the HT sample to help discern the different deposition layers, the OM and SEM micrographs in Figs. 9 and 10 are captured at the same corresponding locations in Figs. 6 and 7 to track the microstructural evolution of each zone.

Fig. 11 shows a cross-section morphology of the microcracks that are developed at the rail-DZ interface. The current microcracks in this zone are now significantly larger after heat treatment than they were before heat treatment (Fig. 7e). Fig. 11 shows the severe oxidation around the microcracks in DZ-1 and the bonding defects at the rail-DZ interface. The cracks and defects, that had already developed, provide accelerated diffusion paths for oxygen and iron, meaning that they expose the adjacent materials to air and consequently facilitate the oxidation to occur there, making it even faster than it is at other potential locations, such as grain boundaries and deformation bands. The oxidation cracks that have propagated in the intergranular boundaries decrease the bonding strength of the grain boundaries by forming a thick oxide film at those bonding defects, thereby producing a considerable degrading effect on the fatigue performance. The chemical compositions of DZ-1 before and after heat treatment are provided in Tables 3 and 4, respectively, and they show a significant increase in the wt.% of oxygen, which explains the acute oxidation that occurred in this zone.

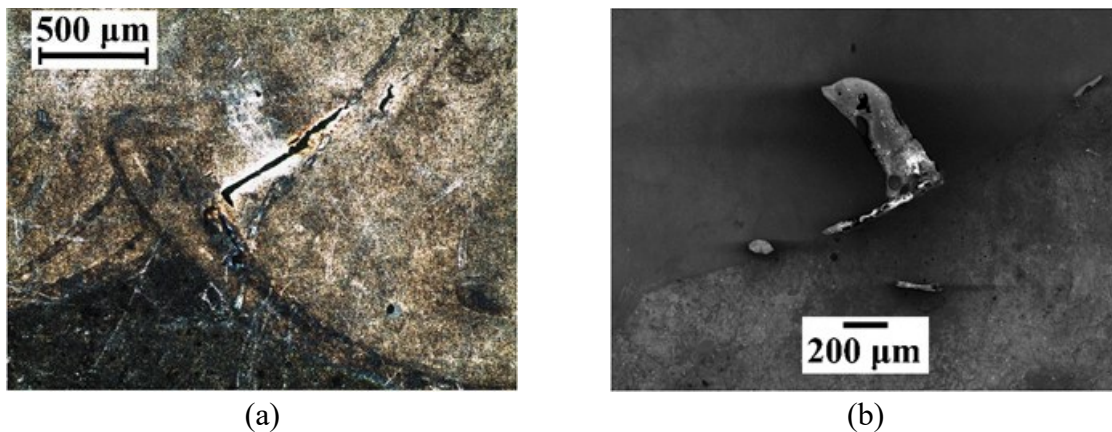


**Fig. 3.11** Close view of the microcracks that are developed in the heat-treated (HT) specimen at the rail-DZ interface through (a) OM and (b) SEM morphology.

A general comparison of Figs. 6e-j with Figs. 9e-j shows that the heat treatment has transformed the heterogeneous, coarse microstructure of the DZ into a homogeneous, fine-grain structure. During the heat treatment of stainless steels, oxide inclusions have a determinant role in forming the steel microstructure by participating as nucleation sites for solidification and phase transformation. It was reported by Takano et al. [18] that heat treatment changes the composition of oxide inclusions in stainless steel, which is highly dependent on the concentration of Mn, Si, and Cr. They showed that the leading cause of the fine grain structure in heat-treated austenitic stainless steel is the dissolution of the coarse MnO-SiO<sub>2</sub> inclusions and the precipitation of fine MnO-Cr<sub>2</sub>O<sub>3</sub> inclusions during heat treatment. They also concluded that this transition occurs only if the initial Si content is sufficiently low, i.e., < 0.3 wt.%, otherwise the oxide inclusions remain as MnO-SiO<sub>2</sub>. Referring to Table 3, the initial values of the wt.% of Si before heat treatment in all

of the deposition layers were kept equal to or below the boundary value of 0.3 except for DZ-1 in which the Si content exceeded 0.3% by a small amount. This fact describes the fine grain structure of the DZ of the HT sample, where the precipitated MnO-Cr<sub>2</sub>O<sub>3</sub> inclusions have suppressed the common grain-coarsening effect of heat treatment. Regarding the phase distribution, despite the visible overall balance between the light-etched austenite and the dark-etched  $\delta$ -ferrite in the DZ micrographs (Figs. 9e-j), tracing from Fig. 9e to 9j shows a gradual intensification of the light lands of austenite. Ren et al. [19] concluded that MnO-Cr<sub>2</sub>O<sub>3</sub> inclusions have a strong pinning effect on the austenite grain boundaries in 304 stainless steel. The descending trend of the wt.% of Si from DZ-1 up to DZ-6 in the AB specimen (Table 3) yields an ascending trend of MnO-Cr<sub>2</sub>O<sub>3</sub> inclusions along the same path for the HT sample. More MnO-Cr<sub>2</sub>O<sub>3</sub> contributes to pinning more austenite grain boundaries, which ultimately contributes to the higher austenite volume fraction after heat treatment. Table 4 also shows that, when moving from DZ-1 to DZ-6, the Cr and Si ferritizers decrease, but the austenizing elements of Ni and N generally increase. The gradual transition from a balanced dark-light microstructure in DZ-1 to a primary light microstructure in DZ-6 also is visible in the SEM micrographs in Figs. 10e-j. Explanation of the intensification of the austenite also can be made based on the pseudo-binary diagram in Fig. 8, in which the solution treatment temperature (1150°C) lies in the austenization area and allows space for austenite expansion. However, the high percentage of ferritizers and MnO-SiO<sub>2</sub> inclusions in some areas do not allow the austenite to grow extensively. It also is important to note that the solution treatment at temperatures above 700°C for long periods will allow sigma to fully transform to  $\delta$ -ferrite. Thus, one can say that the brittle sigma phase almost completely disappeared in the HT specimen. Comparing the SEM macrograph of the AB sample (Fig. 7b) to the SEM macrograph of the HT sample (Fig. 10b) illustrates how heat treatment could help transform a porous, imbalanced DZ into a consistent microstructure with a meager fraction of micropores. As was discussed earlier, reheating helps relieve a considerable fraction of the micropores. Therefore, the isothermal tempering step contributes to a rearranged recrystallization in which a great amount of the micropores are disappeared. In summary, the DZ of the HT sample primarily contains austenite and  $\delta$ -ferrite, and the sigma phase is completely dissolved. Although the two constitutive phases are fairly in balance in DZ-1, the volume fraction of austenite increases gradually when moving towards the upper layers from DZ-1 to DZ-6. Heat treatment, as expected, generally could transform the DZ from a porous medium into a solidified, impermeable region by removing a significant fraction of the existing micropores. Even so, the existing microcracks in DZ-1 are intensified after heat treatment, which can have an adverse effect on the fatigue performance of the repaired rail.

Comparing Figs. 6a and 6b to Figs. 9a and 9b show that there is no discernible HAZ in the HT sample, neither with the naked eye (Fig. 9a) nor when using a microscope (Fig. 9b); it is literally split into two regions of rail and DZ, without any transition region in between. The related OM and SEM micrographs of the former location of HAZ in Figs. 9d and 10d, respectively, show a microstructure that is quite close to that of the HT rail zone (Figs. 9c and 10c). However, in HAZ compared to the rail zone, it clearly can be distinguished that the volume fraction of the deep-dark martensite has decreased and that the volume fraction of the semi-dark austenite has increased. Besides, the light-etched bainite is obviously more condensed in HAZ than it is in the rail region. Precipitated carbide particles throughout the bainitic matrix also are visible in Fig. 10d. Comparing the chemical composition of the HAZ of the HT sample (Table 4) with that of the AB sample (Table 3) shows that the leading ferritizing elements of Cr and Si have decreased, but the

austenizing Ni, C, and N have increased as a result of the heat treatment. Hence, this fact indicates why the primary ferrite HAZ (Fig. 6d) is switched to a bainitic structure that contains a massive amount of austenite (Fig. 9d). Regarding the grain size, the heat treatment has noticeably coarsened the grain structure of the HAZ. The aggregation of micropores also is apparent in this zone (Fig. 10d) as was the case in the rail zone. The reasons for this were discussed earlier when the HT rail area was analyzed.

### 3.2. Heavy rail

#### 3.2.1. SAW-repaired heavy rail

Optical Microscope (OM) captures from the etched specimen, that is extracted from the repaired rail, are shown in Fig. 12. In Fig. 12a, the etched specimen is divided into three areas of weld, heat-affected zone (HAZ), and rail. It is seen in Fig. 12b that the weld area contains four layers with different compositions/orientations in microstructure. A closer look into the microstructure of the fourth, third, second, and first weld layers are shown in Figs. 12c, 12d, 12e, and 12f, respectively. Close-up OM captures from the HAZ and rail can be found in Figs. 12h and 12j, respectively. The interfaces between weld and HAZ and between HAZ and rail are contained in Figs. 12g and 12i, respectively. The distribution of the chemical elements throughout the examined areas in Fig. 12 are given in Table 5.

**Table 10** Chemical composition (wt.%) of different areas of the repaired rail

Area	Fe	C	Cr	Mn	Mo	Si
Layer 4	Bal.	0.067 ± 0.007	0.32 ± 0.05	1.25 ± 0.20	0.82 ± 0.03	3.42 ± 0.40
Layer 3	Bal.	0.028 ± 0.007	0.39 ± 0.05	1.93 ± 0.20	0.80 ± 0.03	3.26 ± 0.40
Layer 2	Bal.	0.016 ± 0.007	0.41 ± 0.05	2.55 ± 0.20	0.73 ± 0.03	3.12 ± 0.40
Layer 1	Bal.	0.017 ± 0.007	0.47 ± 0.05	2.19 ± 0.20	0.73 ± 0.03	2.94 ± 0.40
HAZ	Bal.	0.23 ± 0.06	0.12 ± 0.01	1.01 ± 0.20	0.03 ± 0.01	0.53 ± 0.40
Rail	Bal.	0.80 ± 0.06	0.03 ± 0.01	0.23 ± 0.03	-	0.04 ± 0.01

A dendritic thin lamellar pearlite microstructure is detectable for the rail in Fig. 12j. The rail microstructure obviously contains coarse, light islands of pro-eutectoid ferrite and dark-etched, dendritic pearlite lamellae that are randomly oriented. Sporadic signs of dissipated carbides are also traceable over the pearlitic-ferritic matrix.

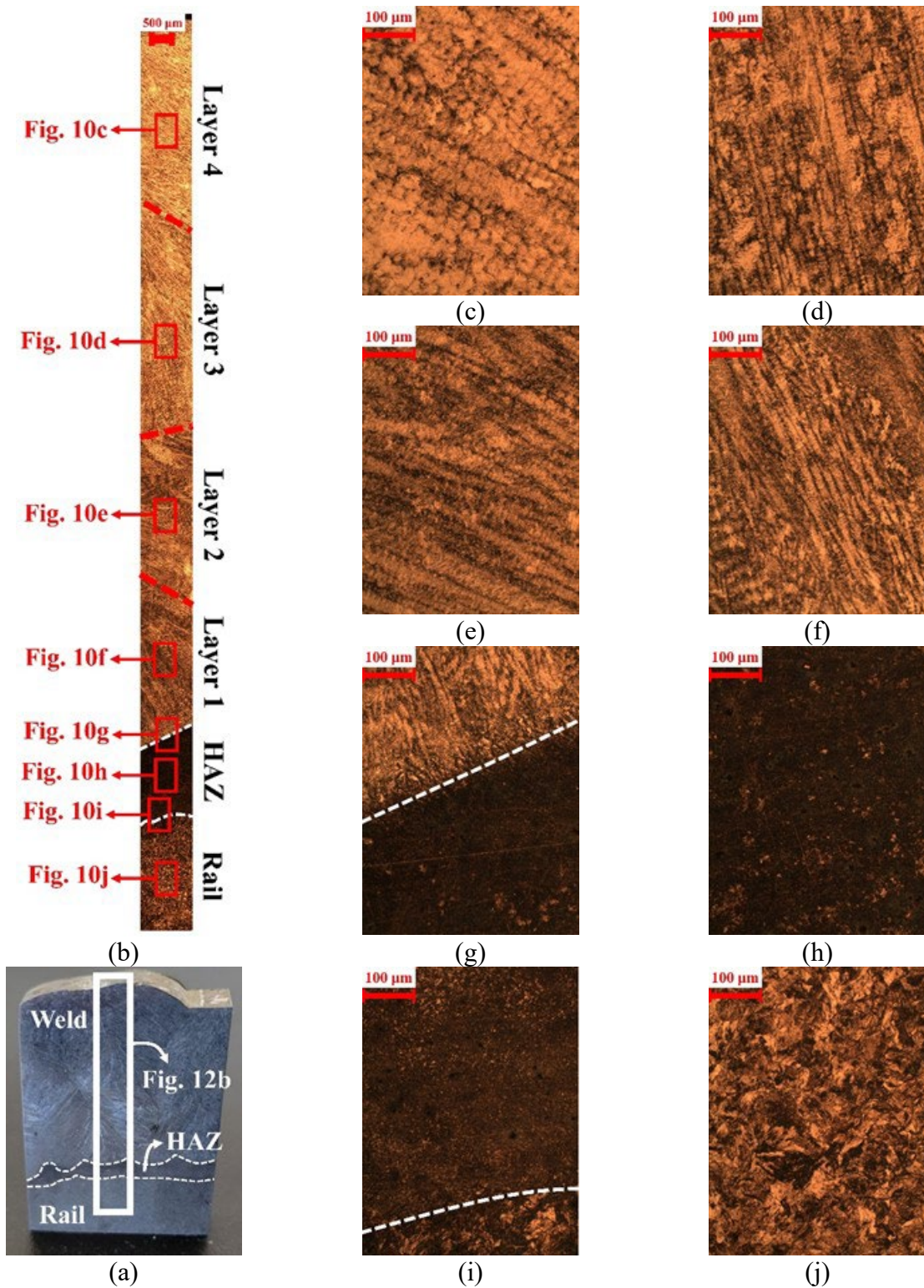


**Fig. 3.12** (a) An etched specimen extracted from the head of the repaired rail, (b) A thorough OM capture from the entire weld zone with the four layers deposited, the heat-affected zone (HAZ), and the rail; closer OM shots are taken from (c) fourth, (d) third, (e) second, and (f) first weld layers, (g) weld-HAZ interface, (h) HAZ, (i) HAZ-rail interface, and (j) rail.

Per Fe-Cr phase diagram shown in Fig. 13, the utilized Lincore 40-S weld wire with around 0.5 weight percentage (wt.%) of chromium (referring to Sec. 2.1.2, Table 3) has a mixture of BCC phases containing Fe-rich (BCC) and Cr-rich (BCC') alloy compounds at room temperature. The general BCC phase of the weld material is observed and approved during the XRD analysis, as will be presented in the Residual Stress Measurement chapter, i.e., Chapter 5. A linked investigation of the Fe-Cr phase diagram in Fig. 13 and the chemical distribution in Table 5 offers the fact that for the four weld layers, with a Cr-wt.% interval of 0.32 to 0.47, there is no chance of austenite ( $\gamma$ ) formation. The  $\gamma$  loop falls between 0 to 0.12 wt.% of Cr content, which is not contained in the interval of current case study. Hence, it is guaranteed that none of the distinguished phases in the OM morphology represent any austenite. A close inspection of the weld layers in Figs. 12c to 12f suggests three discernible regions, primarily categorized based on their brightness appearances. The light region represents the Alpha-ferrite ( $\alpha$ -Fe) phase, the dark network stands for the acicular Alpha-chromium ( $\alpha$ -Cr) phase, and the brittle sigma ( $\sigma$ ) phase is appeared as a semi-dark zone. A general rule of thumb that can be attributed to the Fe-Cr phase diagram is that as the Cr-wt.% increases from 0 to 1, a light-etched to dark-etched transition occurs; the austenite with the lightest appearance in a HCL-etched carbon steel nucleates at  $0 \leq \text{Cr-wt.}\% < 0.12$ , then, at  $\text{Cr-wt.}\% \geq 0.12$ , a combined  $\alpha$ -Fe +  $\alpha$ -Cr phase forms which starts with the dominancy of the light-etched  $\alpha$ -Fe at  $\text{Cr-wt.}\% = 12$  and smoothly transforms to a dark-etched,  $\alpha$ -Cr-dominant compound as the Cr-wt.% leans towards 1. Table 5 shows a declined flow of Cr-wt.% from Layer 1 to Layer 4. As the first layer is welded on the railhead surface – with the liquidus weld drops at 1600-1700°C and the preheated railhead surface at 200-300°C – the weld materials start to experience an initially fast cooling procedure down to 500-700°C; a temperature range in between with closer tendency to the railhead temperature as this is a bigger bulk material. It then remains at that temperature interval for a while. Anyway, once the second layer is started to weld on top of the first layer, Layer 1 is reheated and has a chance for long exposure at a higher temperature range, i.e., 700-1000°C. In the meantime, Layer 2, with a higher initial substrate temperature at the time of starting deposition, i.e., 500-700°C, also remains at elevated temperatures around 700-1000°C until the third layer starts to get welded on top of it. This trend proves the fact that the top layers are exposed to higher ranges of temperature, i.e., higher than 500-800°C. Based on Fig. 13, for the utilized Fe-Cr weld alloy where Cr-wt.% is measured to be in the 0.32-0.47 range, long exposures to 500-800°C gives enough time for a  $\alpha \rightarrow \sigma$  transition. The longer the exposure time, the higher fraction of  $\alpha$  would have the opportunity for transforming to the brittle  $\sigma$ . Besides, higher wt.% of Cr, i.e., closer to 0.47, leads to higher chance of complete  $\alpha \rightarrow \sigma$  transition at 500-800°C, while lower Cr-wt.%, i.e., closer to 0.32, yields to partial  $\alpha \rightarrow \sigma$  transformation. In other words, higher wt.% of Cr results in higher precipitated  $\sigma$ , but lower Cr-wt.% gives lower fraction of the brittle  $\sigma$  phase in the final microstructure. This fact clearly explains why the fraction of the semi-dark  $\sigma$  area decreases as we move from Layer 1 (Fig. 12f), to Layer 2 (Fig. 12e), to Layer 3 (Fig. 12d), and to Layer 4 (Fig. 12c). Layer 1 with higher reheating opportunities had longer available time to stay at 500-800°C and undertake the  $\alpha \rightarrow \sigma$  transformation process. As we move to the upper layers, the number of reheating opportunities decreases, the length of the 500-800°C exposure time decreases, hence the chance of  $\alpha \rightarrow \sigma$  decreases, and therefore lower fraction of brittle  $\sigma$  remains in the final microstructure at room temperature. Another discernible fact is that as the Cr-wt.% decreases from Layer 1 to Layer 4 (see Table 5), the volume fraction of the Cr-rich  $\alpha$ , i.e.,  $\alpha$ -Cr, decreases and that of the Fe-rich  $\alpha$ , i.e.,  $\alpha$ -Fe, increases. Therefore, Layer 1, with the highest Cr-wt.% among the four weld layers, contains the highest dark  $\alpha$ -Cr volume fraction (Fig. 12f), and

Layer 4, with the lowest Cr-wt.% among the four weld layers, includes the lowest dark  $\alpha$ -Cr volume fraction (Fig. 12c). Another contributor to the increment of the ferrite phase in the upper layers is that the wt.% of the ferrite stabilizers (Mo and Si) have an increasing trend from Layer 1 to Layer 4 (Table 5). This hence describes the increasing of the light-etched  $\alpha$ -Fe area from the first layer (Fig. 12f) to the fourth (Fig. 12c).

When layers of materials are welded on the top of a substrate, the sandwiched HAZ, based on the findings of Shen et al. [4], contains a combined mixture of the weld and the substrate materials. On one hand, based on Fig. 12g, as we go down from weld to the HAZ, concentration of  $\alpha$ -Cr increases and  $\alpha$ -Fe is dissipated throughout the dark  $\alpha$ -Cr matrix. It is seen in Table 5 that the ferritizers, i.e., Mo and Si, experience a significant descend from Layer 1 downwards to the HAZ; therefore, in their absence,  $\alpha$ -Fe does not have enough stability and easily dissipates in favor of  $\alpha$ -Cr. On the other hand, referring to Fig. 12i, moving upward from rail to the HAZ, the dark pearlite has been segregated and moved on to the HAZ, but a minor fraction of the pro-eutectoid ferrite could successfully migrate through to the HAZ. Hence, the core of the HAZ, as observable in Fig. 12h, is majorly consisted of pearlite and  $\alpha$ -Cr, with dark appearances, and contains a minor fraction of ferrite with light appearance.

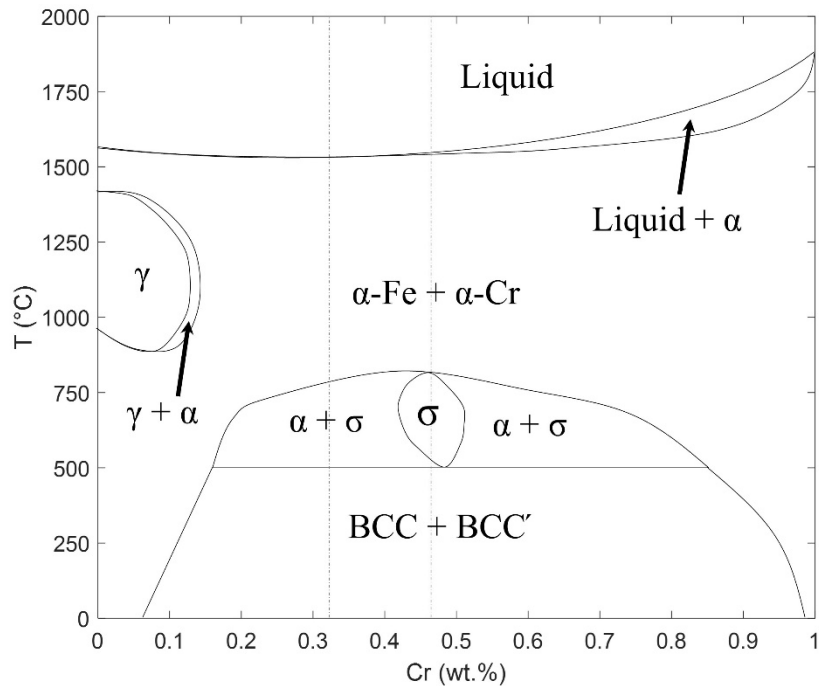


**Fig. 3.13** Fe-Cr phase diagram for the Lincore 40-S hard-facing wire used in the SAW process



### References for Chapter 3

- [1] S. Kou, *Welding metallurgy*, John Wiley & Sons Inc. (2002) ISBN: 978-0-471-43491-7
- [2] S.S. Babu, S.A. David, M.A. Quintana, Modeling microstructure development in self-shielded flux cored arc welds, *Weld J.* 80 (2001) 91–97.
- [3] D. Li, G.Q. Gou, Y. Liu, T.H. Zhu, H. Ji, H. Chen, Effect of Al on microstructure and impact property of surfacing repair layer of rail, *Surf. Eng.* 28(7) (2012) 548–553. <https://doi.org/10.1179/1743294411Y.0000000078>.
- [4] L. Shen, J. Zhou, X. Ma, X.Z. Lu, J.W. Tu, X. Shang, F. Gao, J.S. Zhang, Microstructure and mechanical properties of hot forging die manufactured by bimetal-layer surfacing technology, *J. Mater. Process. Technol.* 239 (2017) 147–159. <https://doi.org/10.1016/J.JMATPROTEC.2016.08.020>.
- [5] N. Mori, H. Homma, S. Okita, M. Wakabayashi, Mechanisms of notch toughness improvements in weld metals containing Ti and B, *J. Japan Weld. Soc.* 50(2) (1980) 174–181. <https://doi.org/10.2207/qjwsw1943.50.174>.
- [6] N.A. Fleck, O. Grong, G.R. Edwards, D.K. Matlock, The role of filler metal wire and flux composition in submerged arc weld metal transformation kinetics, *Welding* (1986) 113s–121s.
- [7] N. Fonstein, *Advanced high strength sheet steels*, Springer (2015) ISBN: 978-3-319-19165-2.
- [8] U.P. Singh, B. Roy, S. Jha, S.K. Bhattacharyya, Microstructure and mechanical properties of as rolled high strength bainitic rail steels, *Mater. Sci. Technol.* 17(1) (2001) 33–38. <https://doi.org/10.1179/026708301101509098>.
- [9] D. López, W. Schreiner, S. de Sánchez, S. Simison, The influence of carbon steel microstructure on corrosion layers: an XPS and SEM characterization, *Appl. Surf. Sci.* 207(1–4) (2003) 69–85. [https://doi.org/10.1016/S0169-4332\(02\)01218-7](https://doi.org/10.1016/S0169-4332(02)01218-7).
- [10] M. Santofimia, L. Zhao, J. Sietsma, Microstructural evolution of a low-carbon steel during application of quenching and partitioning heat treatments after partial austenitization, *Metall. Mater. Trans. A* 40(46) (2008) 46–57. <https://doi.org/10.1007/s11661-008-9701-4>.
- [11] J.W. Fu, Y.S. Yang, J.J. Guo, J.C. Ma, W.H. Tong, Microstructure evolution in AISI 304 stainless steel during near rapid directional solidification, *Mater. Sci. Technol.* 25 (8) (2009) 1013–1016. <https://doi.org/10.1179/174328408X317093>.
- [12] T.B. Massalski, A.J. Parkins, J. Jaklovski, Extension of solid solubility during massive transformation, *Metall. Mater. Trans. B* 3 (1975) 687–694. <https://doi.org/10.1007/BF02642752>.
- [13] M.O. Malone, Sigma and 885°F embrittlement of chromium-nickel stainless steel weld metals, *Weld. J.* 46 (6) (1967) 241–253.
- [14] E. Foroozmehr, R. Kovacevic, Thermokinetic modeling of phase transformation in the laser powder deposition process, *Metall. Mater. Trans. A* 40 (8) (2009) 1935–1943. <https://doi.org/10.1007/s11661-009-9870-9>.
- [15] N. Suutala, T. Moisio, Use of chromium and nickel equivalents in considering solidification phenomena in austenitic stainless steels, *Solidification Technology in the Foundry and Casthouse* (1983) 310–314.
- [16] G. Pacary, M. Moline, J.C. Lippold, A diagram for predicting the weld-solidification-cracking susceptibility of pulsed-laser welds in austenitic stainless steels, *Edison Welding Institute, Research brief* (1990) B9008.
- [17] D. López, W. Schreiner, S. de Sánchez, S. Simison, The influence of carbon steel

- microstructure on corrosion layers: an XPS and SEM characterization, *Appl. Surf. Sci.* 207(1–4) (2003) 69–85. [https://doi.org/10.1016/S0169-4332\(02\)01218-7](https://doi.org/10.1016/S0169-4332(02)01218-7).
- [18] K. Takano, R. Nakao, S. Fukumoto, T. Tsuchiyama, S. Takaki, Grain size control by oxide dispersion in austenitic stainless steel, *Tetsu to Hagane – J. Iron Steel Inst. Jpn.* 89(5) (2003) 616–622. [https://doi.org/10.2355/tetsutohagane1955.89.5\\_616](https://doi.org/10.2355/tetsutohagane1955.89.5_616).
- [19] Y. Ren, L. Zhang, P.C. Pistorius, Transformation of oxide inclusions in type 304 stainless steels during heat treatment, *Metall. Mater. Trans. B* 48(5) (2017) 2281–2292. <https://doi.org/10.1007/s11663-017-1007-8>.



## 4. CHAPTER 4 HARDNESS MEASUREMENT OF THE REPAIRED RAIL

### 4.1. Light rail

#### 4.1.1. SAW-repaired light rail

To evaluate hardness distribution at different zones including weld zone (WZ), heat-affected zone (HAZ), and rail, hardness measurement is taken on the cross section of the rail sample along three lines. Major and minor loads of 90 kgf and 10 kgf are incorporated, respectively, for the B-scale Rockwell hardness test in this study. The three aforementioned lines are employed based on AREMA test plan recommendation [1], as shown in Fig. 1a.

The hardness distribution for the as-built (AB) sample along left gauge line (Line 1), right gauge line (Line 2), and the middle line (Line 3) are shown in Fig. 1b. The minimum required hardness given by AREMA for light-duty rails [1] is also depicted as a red dashed line in Figs. 1b to 1d. The different zones of the AB rail are apparent based on the variation of hardness along the corresponding lines. The average hardness for Lines 1, 2, and 3 in the WZ area are 80.4 HRB, 78.5 HRB, and 81.5 HRB respectively. It can be seen that the gauges are slightly harder than the middle section. Similarly, the average measured hardness along Lines 1, 2, and 3 in the HAZ area are 93.1 HRB, 91.2 HRB, and 94.92 HRB, respectively. The unaffected rail substrate shows an average hardness value of 95 HRB. As it is evident in Fig. 1b, the hardness in the WZ increases gradually from top of the AB railhead down to the WZ/HAZ interface. Sec. 3.1.1, Fig. 1 shows a descending trend of austenite from WZ1 downwards to WZ3, which justifies the rising trend of hardness from top of the weld zone down to the WZ/HAZ interface. Sec. 3.1.1, Fig. 1 also presents the increase of pearlite volume fraction from WZ2 to WZ3, which again confirms the higher hardness value in WZ3. It can be observed from Sec. 3.1.1., Fig. 1 that the HAZ has a considerable finer grain structure compared to both the WZ and the rail. This fact along with the great density of carbide precipitations in this zone makes the HAZ the hardest zone among all the areas of the AB sample as shown in Fig. 1b. The coarse-grain pearlitic-ferritic microstructure of the rail zone with moderate mass of carbides gives a medium hardness value for this region. It is clearly observable in Fig. 1b that the overall hardness of the AB rail is below the minimum AREMA requirement.

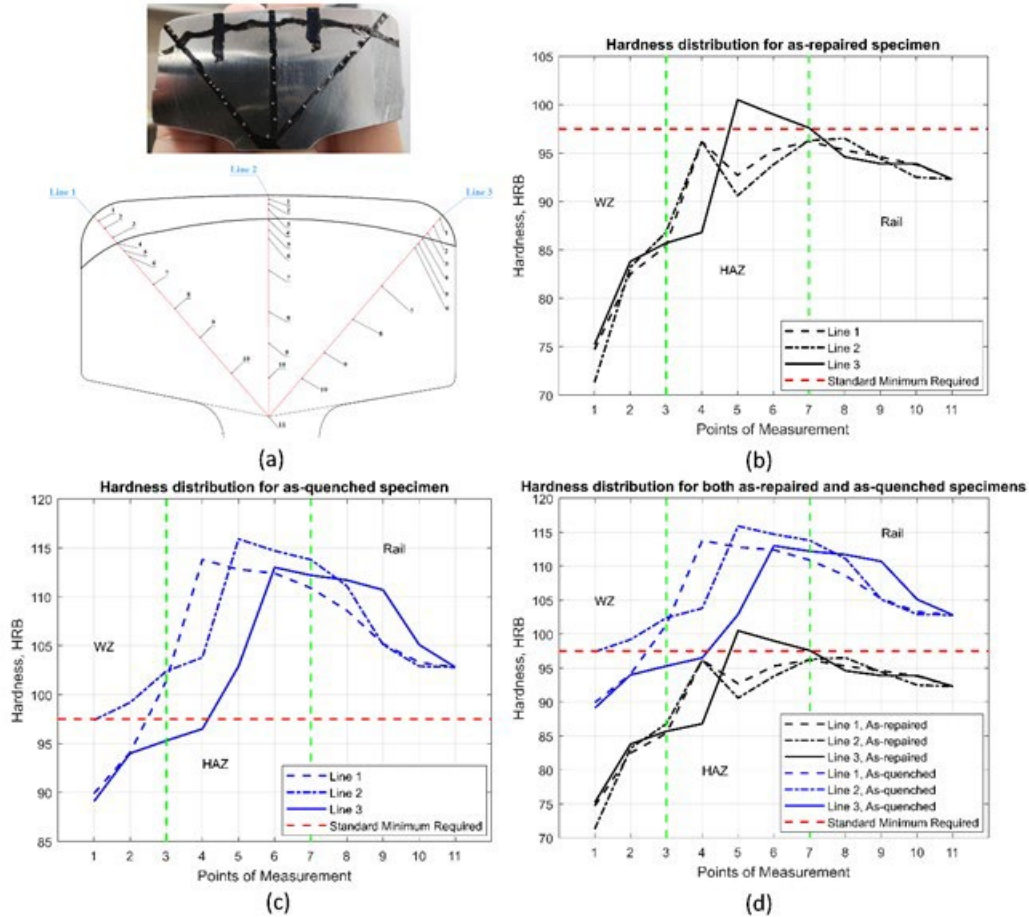


**Fig. 4.1** (a) Hardness test plan showing the lines along which hardness is measured on the demonstrated points; (b) hardness distribution for the as-built (AB) sample; (c) hardness distribution for the as-quenched (AQ) sample; (d) putting both the AB and AQ hardness distribution results together (the red dashed line represents the minimum acceptable hardness for light-duty rail, assigned according to AREMA’s standards [1]).

Fig. 1c illustrates hardness distribution of the AQ specimen. The average hardness in the WZ area varies from 95.1 HRB to 99.6 HRB, and then to 92.8 HRB for Lines 1, 2 and 3, respectively. With regard to the HAZ, the hardness is measured as 110.3 HRB, 110.1 HRB, and 103.9 HRB for Lines 1, 2, and 3, respectively. The average hardness of the rail is increased to 106 HRB. Therefore, heating up the AB rail sample to 1100 °C and water-quenching causes a noticeable increase in hardness in all areas of the sample (about 26%).

Comparing the AB and AQ samples zone-by-zone, it can be observed that residual austenite in WZ1 in the AB sample (Sec. 3.1.1., Fig. 1c) has disappeared and a massive amount of carbides are precipitated in this region (Sec. 3.1.1, Figs. 4c and 5c). The same observation can be attributed to WZ2. In addition, the ferrite volume fraction has been remarkably increased in WZ2 in the AQ sample (Sec. 3.1.1, Fig. 4d) compared to the AB sample (Sec. 3.1.1, Fig. 1d). The removal of austenite, the exceptional increase in carbide particles, and the growth in pearlite volume fraction are the major contributors of increasing hardness in WZ1 and WZ2 as a result of quenching. A

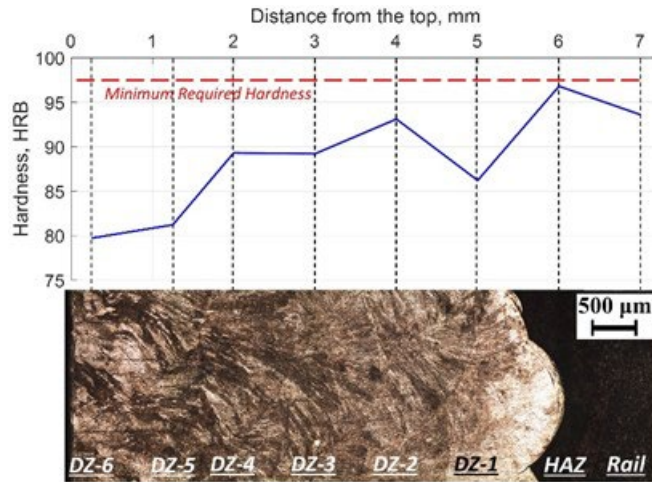
transformation from coarse-grain (Sec. 3.1.1, Fig. 1e) to a fine-grain microstructure (Sec. 3.1.1, Fig. 4e) plus carbide precipitation and additional pearlite nucleation in WZ3 (Sec. 3.1.1, Figs. 4e and 5e) made this zone harder after quenching. Regarding HAZ, the nucleation of martensite in this area after quenching (Sec. 3.1.1, Figs. 4f and 5f) that did not exist in the same area in the AB sample (Sec. 3.1.1, Fig. 1f) and the growth of carbide precipitations in this area after quenching (Sec. 3.1.1, Fig. 5f) rather than before quenching (Sec. 3.1.1, Fig. 2f) justifies the excessive increase of hardness in this zone. The same justification for hardness raise in HAZ can be applied for the rail zone.

The achieved hardness for the AQ sample is still below the minimum required hardness which is equal to 97.5 HRB and is illustrated in a dashed red line in Fig. 6d, where all the results of the quenched and non-quenched samples are put together for comparison purposes. To improve the hardness, the current weld wire can be substituted with a homemade one containing more carbon content. The average hardness at the gauges was lower than the middle zone before quenching, but then increased to higher than that of the middle zone. This can be caused by the faster cooling rate at the gauges during the quenching process due to the greater area of exposure.

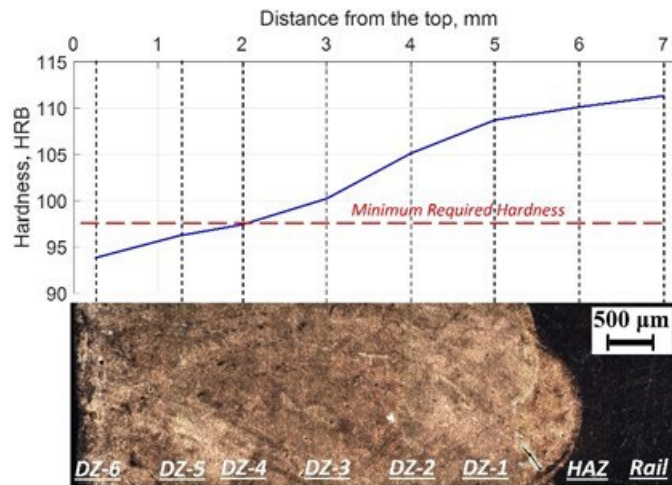
There is an inversed correlation between hardness and wear rate: higher hardness gives lower wear rate [2,3]. Although increasing hardness desirably reduces the wear rate, superior hardness leads to brittleness and cracking. Initiation of martensitic phase in the microstructure of the deposited surface brings crack propagation in virtue of the brittle nature of martensite micro-constituent compared to any other materials with the same carbon content [4,5]. In this way, despite the fact that a homemade high-carbon flux-cored arc wire using SAW process for rail repair is encouraged, it is not recommended to use martensitic wire. The other concern is the increasing of pore concentration in the microstructure which could cause crack initiation and early failure. To mitigate this problem, tempering or quenching and processing (Q&P) are recommended. Nonetheless, it should be noted that these processes can lead to a decreased hardness and make the rail more susceptible to wear.

#### **4.1.2. LPD-repaired light rail**

Hardness is evaluated from the topmost deposited layer in the deposition zone (DZ) which is the sixth deposition layer (DZ-6) downwards to a depth of 7 mm in a way to cover all of the studied zones, including DZ, HAZ, and rail. Figs. 2a and 2b, respectively, show the measured hardness distribution for the as-built (AB) and heat-treated (HT) samples. The hardness of each zone is measured nine times at nine different sampled locations of the repaired rail, and the presented values in Fig. 2 are the average measured hardness at each zone. The red dashed line in Fig. 2 shows the minimum required hardness for standard U.S. light rails, 97 HRB, as assigned by AREMA [1].



(a)



(b)

**Fig. 4.2** Hardness distribution: (a) in the as-built (AB) rail; (b) in the heat-treated (HT) rail. The red dashed lines represent the minimum required hardness for standard U.S. light rails assigned by AREMA [1].

Fig. 2a clearly shows that the hardness of the AB sample is thoroughly below the minimum requirement. The minimum hardness (~80 HRB) occurs in DZ-6 and DZ-5, which have a primary austenite microstructure. Based on Fig. 2a, going from DZ-5 to DZ-4, the hardness is increased dramatically, from 80 to around 90 HRB (about a 12.5% increase), which, for the most part, can be attributed to the transition of the microstructure from primary austenite (Sec. 3.1.2, Fig. 6i) to primary ferrite (Sec. 3.1.2, Fig. 6h). The intrusion of the brittle sigma phase in DZ-4 is the second determining factor for such a considerable increment. The hardness continues to increase from DZ-4 to DZ-2 due to the increase of the sigma volume fraction along this path (Sec. 3.1.2, Fig. 6h to 6g to 6f). Although sigma also continues to increase from DZ-2 (Sec. 3.1.2, Fig. 6f) to DZ-1 (Sec. 3.1.2, Fig. 6e), the primary microstructure switches back from ferrite to austenite, which has

a more decisive effect on the value of hardness than the effect of sigma growth. This ultimately results in a 6% reduction of hardness from 93 HRB in DZ-2 to 87 HRB in DZ-1. The austenite-to-ferrite changeover and also the increase in the value of sigma from DZ-5 to DZ-4 both contributed to the increased hardness. But, from DZ-2 to DZ-1, while the ferrite-to-austenite transition reduces the hardness somewhat, the sigma volume fraction increment tries to increase the hardness, although not as strong as the hardness reducer parameter. Therefore, the decrease in the hardness from DZ-2 to DZ-1 is not as sharp as the increase in the hardness from DZ-5 to DZ-4. The maximum hardness is reached at HAZ, where an alteration occurs from primary austenite at DZ-1 to a fine pearlitic-ferritic network at HAZ, so the hardness increases from 87 to 96 HRB. Fig. 2a shows that there is no significant difference between the hardness of the rail zone and the hardness of HAZ. Both of them consist of a ferrite-pearlite network (Sec. 3.1.2, Figs. 6c and 6d), but the rail has a coarse-grain microstructure and consequently has a relatively lower hardness than the fine-grain HAZ.

The hardness distribution of the HT sample in Fig. 2b shows how effectively the employed heat treatment increased the hardness throughout the repaired rail. The hardness values generally are shifted to higher amounts than the minimum required, except for the two upper deposition layers of DZ-5 and DZ-6. The major reason for such an enhancement of hardness is the evolution from a coarse, inhomogeneous grain structure (Sec. 3.1.2, Figs. 6e-j) to a fine, homogenous structure (Sec. 3.1.2, Figs. 9e-j). All of the HT deposition layers have an austenite-ferrite microstructure. A clear conclusion from Fig. 2b is that there is an inverse correlation between the volume fraction of austenite and the hardness values; DZ-6 with the highest austenite volume fraction (Sec. 3.1.2, Fig. 9j) has the lowest hardness of 94 HRB, and DZ-1, with the minimum volume fraction of austenite (Sec. 3.1.2, Fig. 9e) has the maximum hardness, i.e., 108 HRB, among the deposition layers. In more general terms, the gradual deterioration of austenite from DZ-6 downwards to DZ-1 has led to a steady increase in hardness along the same path. Another affirmation of the homogenizing effect of heat treatment is the uniform distribution of hardness between DZ-1, HAZ, and the rail zone in the HT sample in Fig. 2b without any sign of harsh fluctuations such that occurred for the AB sample in Fig. 2a. HAZ and rail zone in the HT specimen are slightly harder than DZ because of the martensitic microstructure (Sec. 3.1.2, Figs. 9c and 9d) and the precipitated carbides (Sec. 3.1.2, Figs. 10c and 10d).

There is an inverse relationship between hardness and wear rate, which means that the higher the hardness becomes, the lower the wear rate becomes. However, excessive hardness will result in brittleness, which increases the cracking susceptibility. Therefore, the existence of martensite in the final rail microstructure is banned by AREMA standards because of the brittle characteristic of this constituent, which would result in the early initiation and propagation of cracks. The promising result of the current case study is that the deposition materials on the top of the rail are free of martensite. Also, although the hardness of the upper deposition layers is slightly lower than the minimum required (~2%), the overall hardness of the deposition materials is at an acceptable level. The heat treatment could deliver a fine grain structure in the deposition area with a minimum concentration of micropores. Even so, the HT substrate has two adverse characteristics, i.e., 1) its martensitic microstructure (Sec. 3.1.2, Fig. 9c) and 2) a considerable accumulation of coarse micropores (Sec. 3.1.2, Fig. 10c). Although the rail substrate will not be in direct tribological contact with the wheels of the train and, hence, is not a primary matter of concern, a porous, brittle microstructure is significantly susceptible to early cracking under dynamic train loads. Aside from

all of these concerns, the major concern about the final product is the presence of detrimental cracks at the rail-deposition interface. Propagation of these cracks under dynamic loads will lead to premature failure and delamination of the deposited steel.

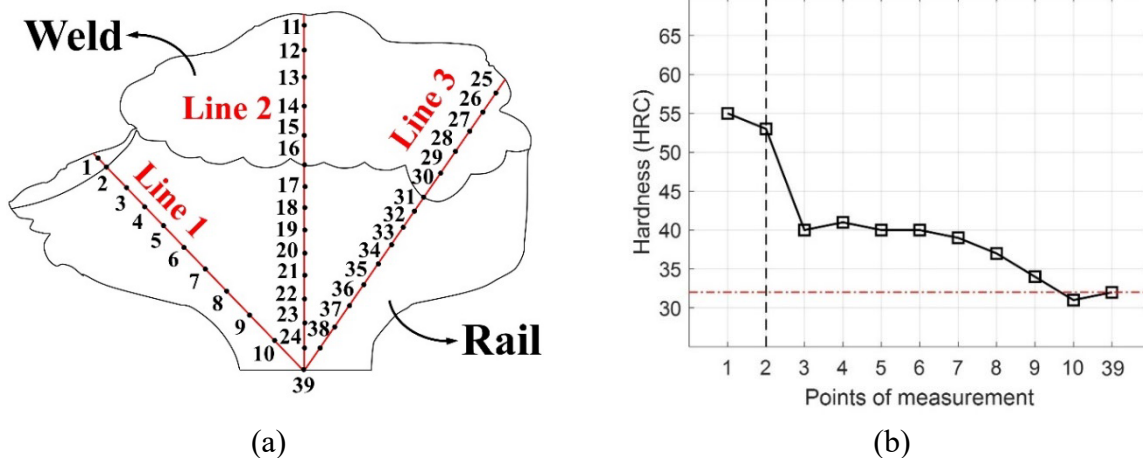
To conclude, the ultimate outputs of LPD repairing the standard 75-lb U.S. light rail using the austenitic 304L stainless steel seem promising regarding the microstructure and hardness properties. However, the developed martensite in the rail substrate and the initiated cracks at the rail-deposition interface are adverse occurrences. Prevention of the nucleation of martensite in the rail material can be achieved by isolating the rail substrate so that it is not heated during the post-heat treatment of the repaired rail. The crack initiation at the rail-deposition interface can be alleviated or eliminated by preheating the head of the worn rail as the LPD substrate. Evaluation of the recommended pre- and post-processing requires additional experimental studies to ultimately achieve a promising LPD rail repair process with minimum defects in the final product.

## 4.2. Heavy rail

### 4.2.1. SAW-repaired heavy rail

Per AREMA regulations [1], distribution of hardness along the three lines, shown in Fig. 3a, should be maximum at the surface of the railhead, i.e., points 1, 11, and 25 in Fig. 3a, and then undergo a smooth declination towards the minimum hardness at the root of the railhead, i.e., point 39 in Fig. 3a.

Fig. 3 gives the hardness distribution along the left gauge, middle, and right gauge of the repaired railhead, i.e., Lines 1, 2, and 3, respectively, in Figs. 3b, 3c, and 3d, respectively. The minimum required hardness assigned by AREMA [1] for heavy 136RE rails, which is equal to 32 HRC, is shown as a horizontal dash-dot line in all the graphs. The vertical dashed line in each graph locates the rail-weld interface. Therefore, the areas at the left side of the vertical dashed lines in Figs. 3b, 3c, and 3d represent the weld area, and the areas at the right stand for the rail area.



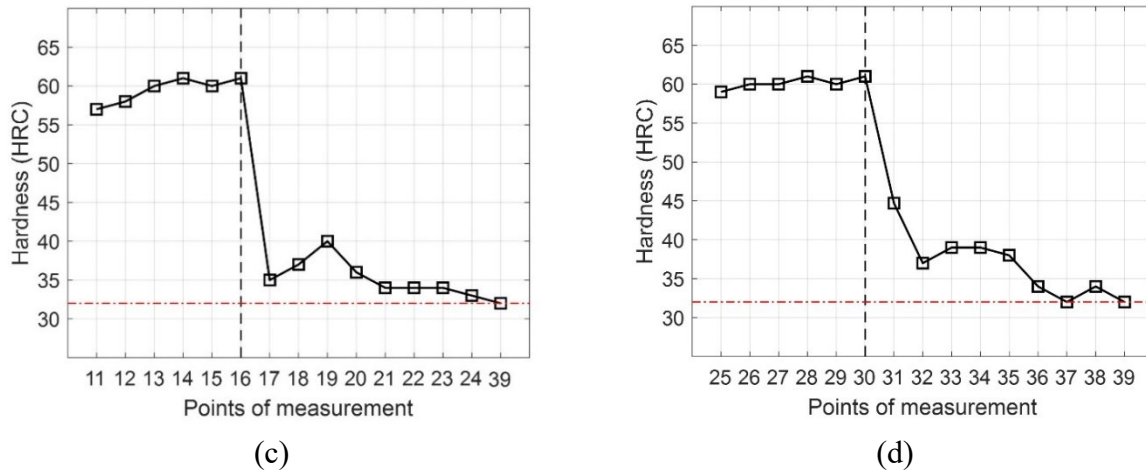


**Fig. 4.3** Hardness distribution on the head of the repaired rail showing the (a) hardness test plan and hardness distribution along (b) Line 1 (c) Line 2, and (d) Line 3; the vertical dashed line in all of the graphs located the rail-weld interface and the horizontal red dash-dot line shows the minimum acceptable hardness based on AREMA standards [1].

It is evident in Figs. 3b-d that the average measured hardness at the weld zone along Lines 1, 2, and 3 are 54, 59.5, and 60 HRC, respectively. The mean hardness measured in the rail section along Lines 1, 2, and 3 are 37, 35, and 36 HRC, respectively. Therefore, the overall hardness in the weld area is estimated as 58 HRC, and that of the rail area is 36 HRC. The results then imply that the hardness results meet the standard AREMA requirement in a way that the maximum occurs at the head and minimum occurs at the root of the repaired railhead, and the hardness of the repaired rail in almost all the regions is higher than the minimum required 32 HRC. However, it fails to meet the AREMA standards in the matter of a smooth declination from the maximum at the head to the minimum at the root; as the results tell and the graphs show in Figs. 3b-d, a sharp, step decrease of hardness happens at the rail-weld interface, moving from the weld area to the rail zone.

As it was shown and discussed in Sec. 3.2.1, the hardest phase present in the weld material is the brittle  $\sigma$  phase. Although the sigma phase can significantly contribute to increasing the hardness and, unlike martensite, is not against AREMA regulations to possess part of the railhead microstructure, it substantially affects the material ductility by increasing the brittleness, which raises the chance of premature cracking and failure of the rail under dynamic wheel-rail load. Therefore, while the quite higher hardness of the weld material than the minimum required (about 80% higher) seems satisfying, it might make the deposited weld too brittle and hence require some post-heat-treatment (e.g. tempering) to alleviate the hardness down to some values closer to the minimum 32 HRC. In this way, while the hardness still meets the minimum standards, the material becomes more ductile and decreases the chance of early cracking and premature failure. Another contributor phase to a high hardness in the weld zone is the  $\alpha$ -Fe phase. It was discussed in Sec. 3.2.1 that as we move from lower weld layers close to the rail to upper weld layers at the top surface of the repaired rail, the volume fraction of  $\sigma$  decreases and that of the  $\alpha$ -Fe increases. It can be then inferred that as one of the hardness-increment-contributors, i.e.,  $\sigma$ , decreases in the upper layers, the other contributor, i.e.,  $\alpha$ -Fe, increases in volume fraction. This hence explains the almost constant, high hardness in the whole weld area, as visible in Fig. 3; the hardness of the weld zone remains between 55 to 60 HRC and no considerable fluctuation occurs.



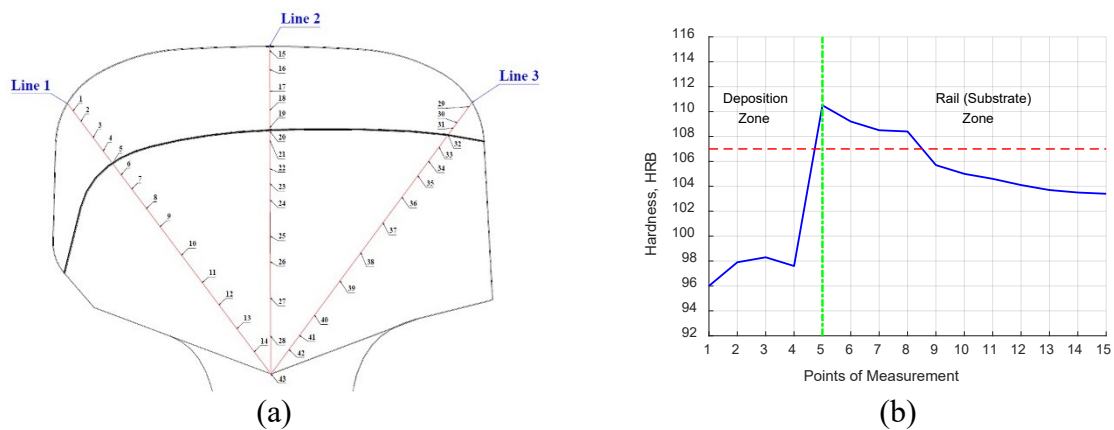
As the hard  $\alpha$ -Fe and the brittle  $\sigma$  phases disappear in the HAZ while the mild-hardness  $\alpha$ -Cr increases, the hardness suddenly descends from 55-60 HRC to around 40 HRC. Thereafter, in the rail area with the standard pearlitic-ferritic phase, the hardness values match the standard expected values between 32 to 42 HRC, converging to 32 HRC at the root of the repaired rail (Fig. 3).

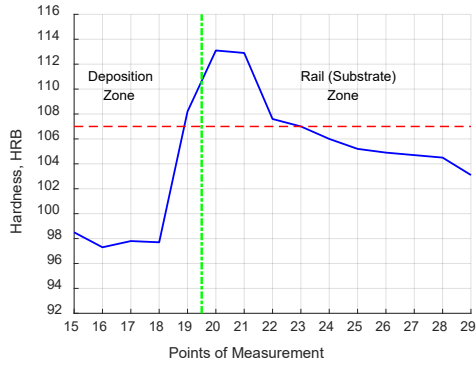
Thus, a proper choice of heat treatment, such as tempering, can dissolve the brittle  $\sigma$  phase and help towards augmentation of the ferrite phase in the weld zone. This microstructural transformation not only could make a consistent hardness distribution all over the repaired railhead, but it also could aid the hardness of the weld material to reduce to the standard 32-40 HRC interval.

#### 4.2.2. LPD-repaired heavy rail

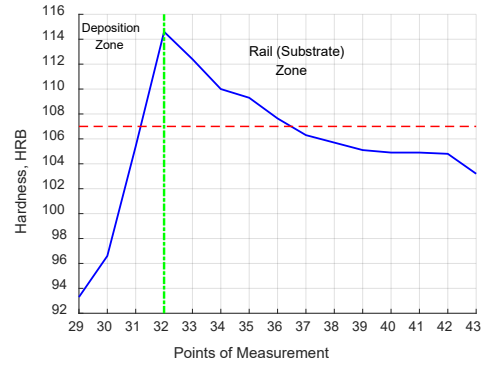
To evaluate hardness distribution at different zones including deposition zone, HAZ, and rail, hardness measurement is taken on the cross section of the AB sample along three lines. Major and minor loads of 90 kgf and 10 kgf are incorporated, respectively, for the B-scale Rockwell hardness test. The three aforementioned lines are employed based on AREMA test plan recommendation [1], as shown in Fig. 4a. The horizontal red dashed line in Figs. 4b, c, and d shows the minimum required hardness for standard U.S. heavy rails, 107 HRB, as assigned by AREMA [1]. The rail-deposition interface is located using a vertical green line in Figs. 4b, c, and d.

The average hardness for Lines 1, 2, and 3 in the deposition zone are 100 HRB, 99 HRB, and 102 HRB, respectively. It can be seen that the hardness of all of the areas of the deposited materials is considerably lower than the minimum required, i.e., 107 HRB. This is not a satisfactory result, and the repaired rail will definitely undergo a premature failure under the train load. In this way, this LPD-repaired heavy rail will certainly need a post-heat-treatment to increase the hardness at the deposition zone. Since the same 304L stainless steel that was used for LPD-repairing the light rail is used for the heavy rail as well, the same heat treatment will also be employed for increasing the hardness here. The heat-treatment process and measuring the results is under investigation at this time.





(c)



(d)

**Fig. 4.4** Hardness test results from the as-built (AB) LPD-repaired heavy rail; (a) schematic map of the points and lines on which the hardness is measured; (b) hardness distribution along line 1, (c) line 2, and (d) line 3; the horizontal red dashed line represents the minimum acceptable hardness for heavy rails, assigned according to AREMA’s standards [1], and the vertical green line represents the location of the rail-deposition interface.

## References for Chapter 4

- [1] AREMA Manual for Railway Engineering, Chapter 4: Rail, American Railway Engineering and Maintenance-of-way Association (2020).
- [2] Y. Jin, M. Ishida, A. Namura, Experimental simulation and prediction of wear of wheel flange and rail gauge corner, *Wear* 271 (2010) 259–267.  
<https://doi.org/10.1016/j.wear.2010.10.032>.
- [3] U. Tayfun, B. Witold, G. İbrahim, Wear and friction of composites of an epoxy with boron containing wastes, *Polímeros* 25 (2015). <https://doi.org/10.1590/0104-1428.1780>.
- [4] W.D.Jr. Callister, *Materials science and engineering: an introduction*, 6th Edition, JohnWiley & Sons, Inc. (2002) ISBN 978-0-471-13576-0.
- [5] G. Lacroix, T. Pardoën, P.J. Jacques, The fracture toughness of TRIP-assisted multiphase steels, *Acta Mater.* 56(15) (2008) 3900–3913.  
<https://doi.org/10.1016/J.ACTAMAT.2008.04.035>.

## 5. Chapter 5 RESIDUAL STRESS MEASUREMENT OF THE REPAIRED RAIL

### 5.1. Light rail

#### 5.1.1. LPD-repaired light rail

In this section, the measured residual stresses will be presented based upon the coordinate system shown in Fig. 1. The dashed lines in Fig. 1 along x and z directions are seated at the rail-deposition interface. The origin is located at the center of the railhead surface; y = 0 plane intersects with the rail-deposition interface, and the top surface of the deposition part is located at y = 4 mm plane.

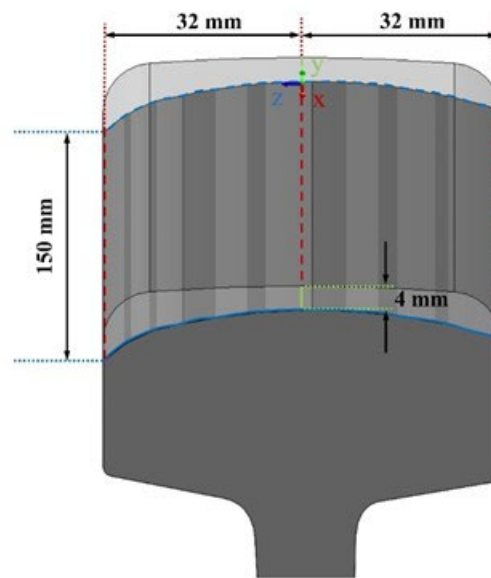


**Fig. 5.1** Coordinate system upon which the results are presented for the LPD-repaired light rail.

The measurement of the residual stresses is conducted via XRD stress measurement technique. The running parameters of the XRD stress measurement setup are described in Sec. 2.3. To determine the proper  $2\theta$  angle for stress measurement, phase scan analysis is carried out to acquire the diffraction peak patterns of both the deposition and rail materials. The resulting diffraction peak patterns of the 304L deposition steel and C-Mn rail are shown in Figs. 2a and 2b, respectively. It is preferred to measure the residual stresses at high  $2\theta$  values, because the applied minor changes to the d-spacing, as a result of strain, are measured more precisely at higher angle range of  $2\theta$  [1]. Therefore, the FCC (3 3 1) peak at  $2\theta = 117.5^\circ$  (Fig. 2a) for the deposition area and the BCC (2 2 2) peak at  $2\theta = 137.1^\circ$  (Fig. 2b) for the rail area is picked for measuring the stress using the  $\sin^2\psi$  method. The angular rotation of  $\psi$  angle for each stress measurement is started from  $\psi = 0^\circ$ , and successive  $\psi$  offsets are added in a way to cover the  $0^\circ \leq \psi \leq 45^\circ$  range with 5 equal intervals and a total number of 6 points of  $\psi$ . The  $2\theta$  measurement range for the deposition zone is from  $115.1^\circ$  to  $119.9^\circ$  and for the rail zone is from  $135.1^\circ$  to  $139.1^\circ$ . Sliding gravity technique is used for peak evaluation, and data correction is performed for background, absorption, and Lorentz polarization. The  $2\theta$  scans are operated with 0.02 increment, and a counting accumulation of 0.8 s/step is

incorporated.

In order to verify the XRD stress measurement accuracy, horizontal line profiles are taken from the specimen at its different stages, i.e., as-built (AB), as-polished (AP), and as-etched 1 (AE1). In the depicted profiles in Fig. 3, the horizontal dashed lines are the location of the median plane. As it can be seen in Fig. 3, the AB sample has a high roughness with around  $\pm 50 \mu\text{m}$  height/depth of the peaks/pits. For the AP sample, the distance of the peaks/pits from the median plane is considerably decreased to  $\pm 0.8 \mu\text{m}$ , which indicates a much smoother surface of the sample at the AP stage. The captured line profile from the AE1 sample shows almost the same roughness pattern and magnitude as that of the AP sample.

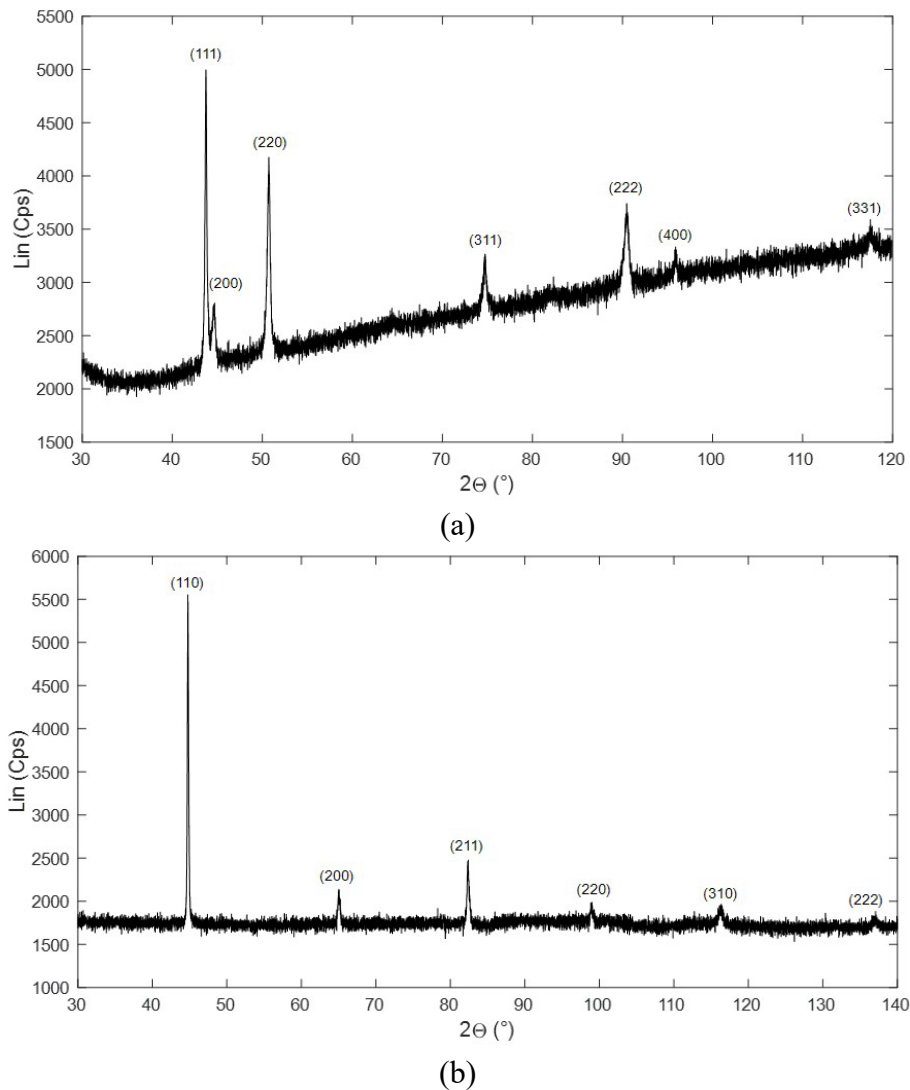


**Fig. 5.2** Diffraction Peak Pattern through the full range of  $2\theta$  for (a) 304L deposition steel and (b) C-Mn light rail.

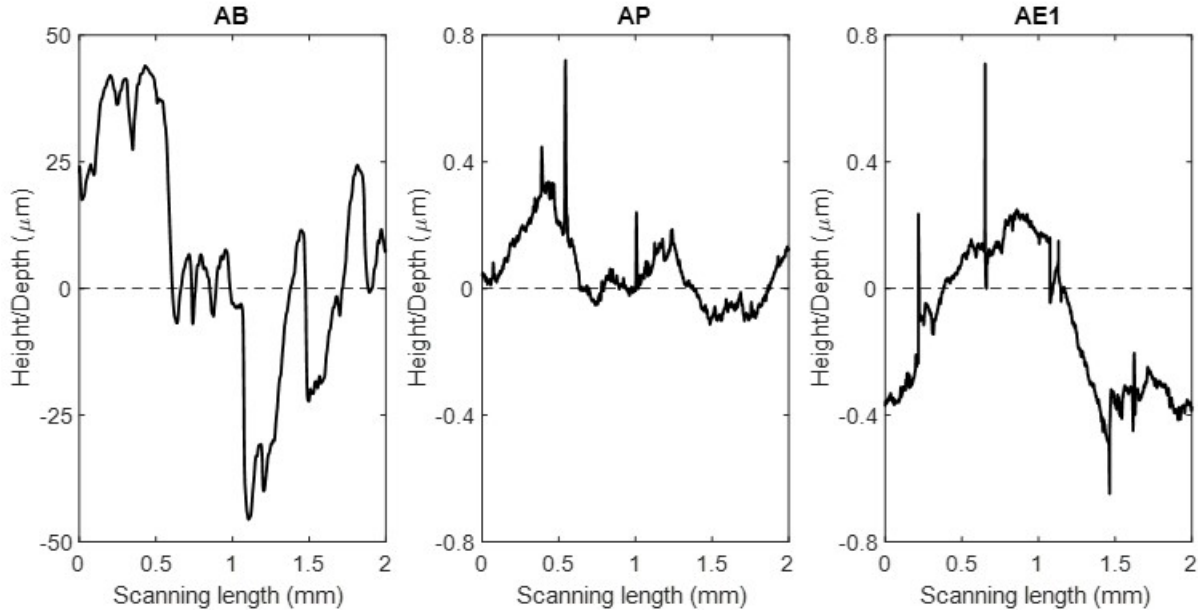


**Fig. 5.3** Horizontal line profile from the surface of the repaired rail specimen at three different stages of as-built (AB), as-polished (AP), and as-etched 1 (AE1).

In conjunction with the line profile acquisition, residual stress of the specimen at its different stages, i.e., AB, AP, and AE1, is measured using XRD to ascertain that all of the measurement errors associated with the rough surface and the relaxed residual stresses on the surface as a consequence of polishing are eliminated. The measurement is continued to carry out on the further etched samples, i.e., AE2, AE3, AE4, and AE5. All of the measurements are conducted at the  $(x,y,z) = (20,3,13)$  mm (refer to Fig. 1 for configuration of the coordination system). The measurement results are shown in Fig. 4. It is also worth mentioning that mechanical polishing removed 750- $\mu\text{m}$  thickness of the specimen materials, and every step of etching removed 50  $\mu\text{m}$  of the specimen thickness. Fig. 4 shows the considerable effect of polishing on the measured stress values. For a  $\text{CuK}\alpha$  radiation into the stainless steel, the X-ray beam penetration depth is about 5 $\mu\text{m}$  [2,3]. Therefore, for the rough AB sample with  $\pm 50$   $\mu\text{m}$  peaks/pits (Fig. 3 AB) where the surface contains spikes to a level of about 10 times higher than the X-ray penetration depth, interruption of the X-ray beam by those spikes will lead the XRD measurement to yield lower stress values than the actual. While it visually seems that consecutive layer removal through etching does not act as effectively as the polishing did in stabilizing the measured stress, there is about 8–16% difference in the measured stresses between the AP and the AE5 samples. According to Figs. 4a, 4b, and 4c, the  $\sigma_l$ ,  $\sigma_t$ , and  $\sigma_n$  values keep on modifying until the fourth, third, and fourth steps of etching, respectively. Hence, it is concluded that after mechanical polishing and five steps of chemical etching, the acquired XRD stress profile is accurate enough, and all of the existing errors mentioned earlier are now eliminated. In this way, the AE5 specimen will be used for the rest of the XRD stress measurements.

Each of the longitudinal and transversal residual stresses is measured at four different points along x and z directions, respectively, at the rail-deposition interface. Normal residual stress measurement is taken along y direction at two points in the deposition zone, i.e.,  $y = 1$  mm and  $y = 3$  mm, and two points in the rail zone, i.e.,  $y = -3$  mm and  $y = -5$  mm (refer to Fig. 1 for



configuration of the coordinate system). The inter-planar spacing,  $d$ , versus  $\sin^2\psi$  values is plotted for all the measuring points and is given in Fig. 5. The employed elastic constants for 304L deposition steel are  $E = 190$  GPa and  $\nu = 0.3$ , and those for C-Mn rail are  $E = 203$  GPa and  $\nu = 0.3$ . Evaluation of stress amounts is carried out using the assigned elastic constants along with the gradient of the curve fitting line from the  $d$ - $\sin^2\psi$  plots in Fig. 5. The resulting stress is given by the following equation [1]:

$$\sigma = m \left( \frac{E}{\nu + 1} \right) \quad (1)$$

where  $m$  is the gradient of the curve fitting line of the  $d$ - $\sin^2\psi$  plot. As it can be seen in Fig. 5c for  $y = -3$  mm, the curve fitting line of this plot has a descending gradient, which gives a negative value to  $m$  and subsequently gives a negative (compressive) stress. All the measured stresses from the  $\sin^2\psi$  analysis are given in Table 1.

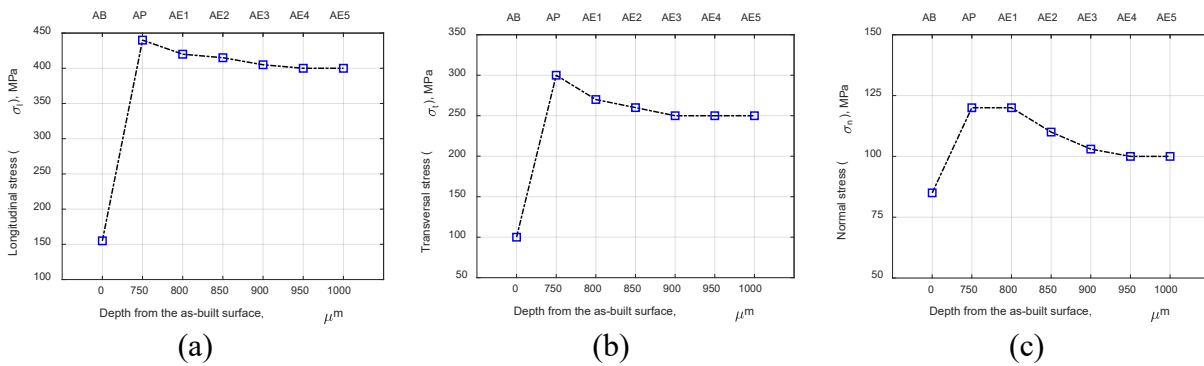


**Fig. 5.4** The measured (a) longitudinal,  $\sigma_l$ , (b) transversal,  $\sigma_t$ , and (b) normal,  $\sigma_n$ , residual stresses via XRD at point  $(x,y,z) = (20,3,13)$  (See Fig. 1 for configuration of the coordination system) for different stages of sample preparation, i.e., as-built (AB), as-polished (AP), and five etching steps (AE1 to AE5).

**Table 11** Measured residual stress values at different locations of the as-etched 5 (AE5) LPD-repaired rail sample (Refer to Fig. 1 for configuration of the coordinate system).

Location (x,y,z) (mm)	$\sigma_l$ (MPa)	Location (x,y,z) (mm)	$\sigma_t$ (MPa)	Location (x,y,z) (mm)	$\sigma_n$ (MPa)
(20,0,0)	400	(0,0,-24)	200	(0,3,0)	96
(55,0,0)	320	(0,0,-12)	240	(0,1,0)	91
(95,0,0)	380	(0,0,12)	250	(0,-3,0)	-25
(130,0,0)	420	(0,0,24)	248	(0,-5,0)	12

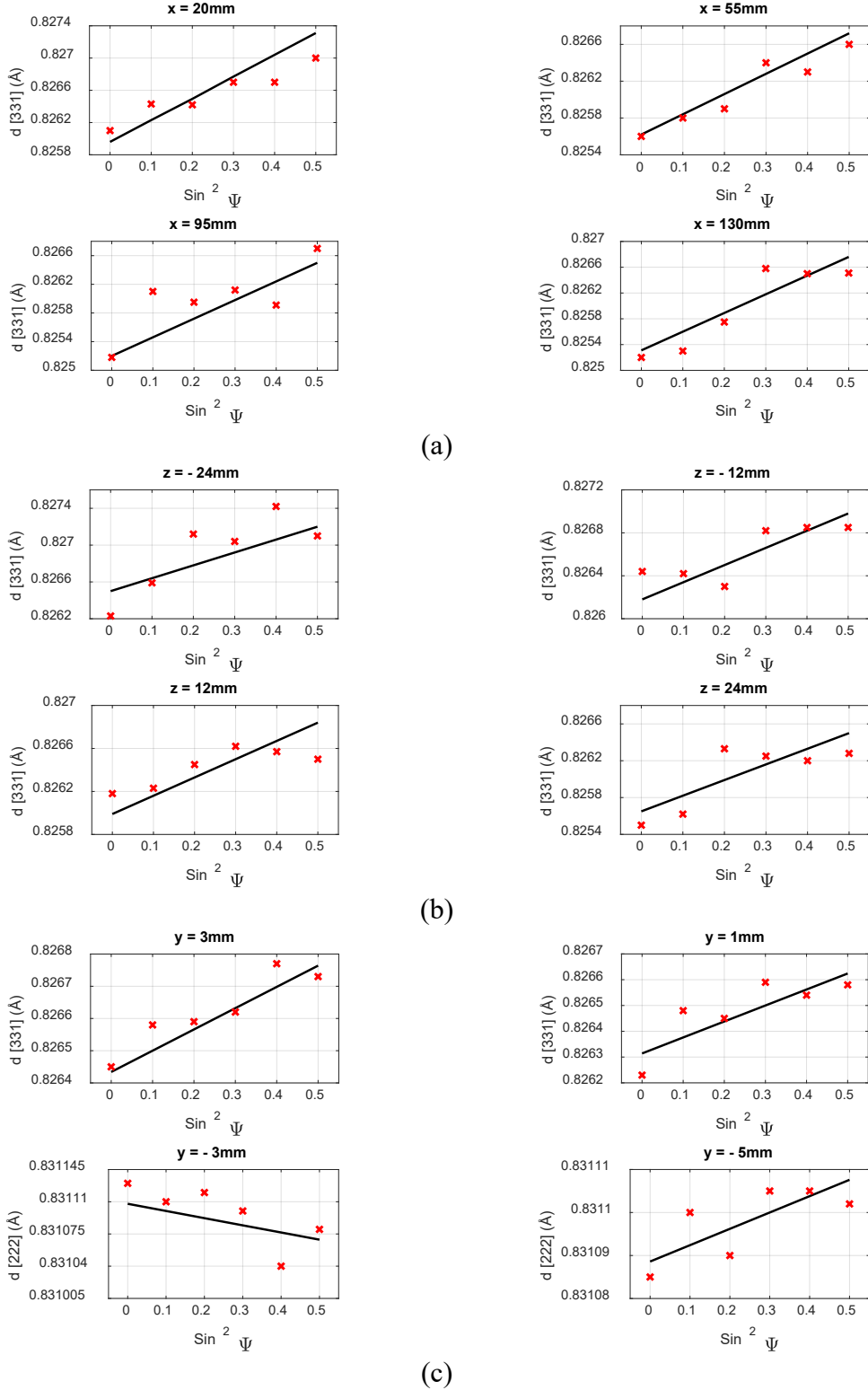


**Fig. 5.5** Obtained plots of inter-planar spacing,  $d$ , versus  $\sin^2\psi$  from XRD measurement of (a)  $\sigma_I$  at  $(z, y) = (0, 0)$ , (b)  $\sigma_I$  along rail-deposition interface at  $x = 0$  plane, and (c)  $\sigma_n$  at  $(x, z) = (0, 0)$ . Refer to Fig. 1 for configuration of the reference coordination system.

## 5.2. Heavy rail

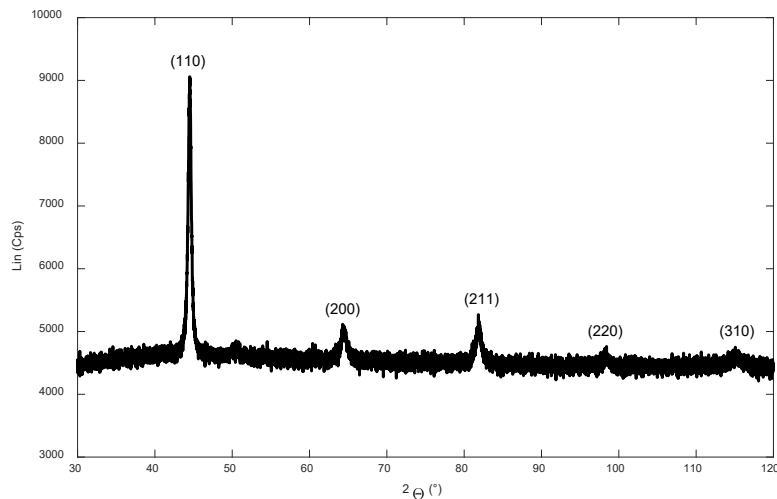
### 5.2.1. SAW-repaired heavy rail

Just as presented in Sec. 5.1.1, surface roughness of the sample is measured to make sure that it is less than  $5\ \mu\text{m}$ , i.e., X-ray penetration depth. This process will not be described here again.

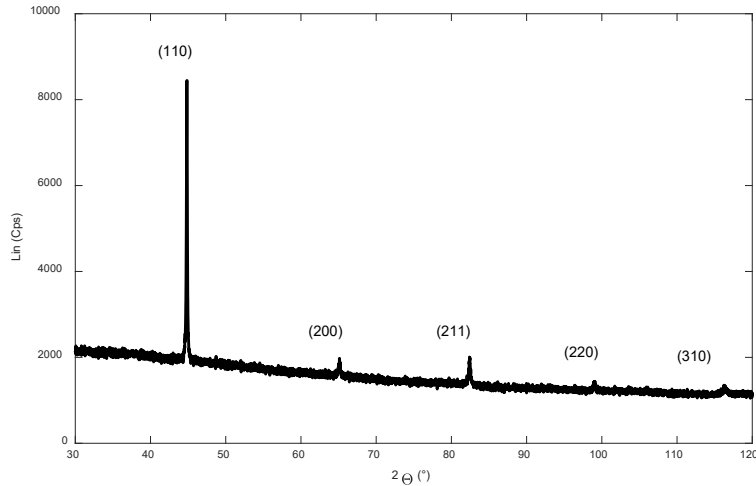
A typical XRD phase scan analysis from the weld and rail materials are given in Figs. 6a and 6b, respectively. As it is intended to obtain a precise measurement of strain owing to lattice spacing variations, the residual stresses are recommended to be measured at the highest possible diffraction angles as long as it does not considerably affect the measurement accuracy [1].

In this way, stress in the weld section, i.e., at points 1 to 5 as per Sec. 2.3, Fig. 5c, is measured at the BCC (3 1 0) diffraction peak, i.e., diffraction angle ( $2\theta$ ) of  $115.1^\circ$  referring to Fig. 6a. Measurement of residual stresses in the rail section at points a and b in Sec. 2.3, Fig. 5c is also conducted at the diffraction peak of BCC (3 1 0) which, based on Fig. 6b, is located at the diffraction angle of  $116.2^\circ$ .

$\text{Sin}^2\psi$  method is utilized for stress calculation. Starting from  $\psi=0^\circ$  and stepwise adding of five equal offsets up to  $\psi=45^\circ$ , a total of six  $\psi$  points are taken into account. The assigned range of diffraction angle for the XRD measurements is  $114^\circ \leq 2\theta \leq 118^\circ$  with a stepwise increment of 0.02, where an 0.8 second per step of counting accumulation is employed. Sliding gravity is used for the peak evaluation, and data correction for Lorentz-polarization background and absorption is undertaken.



(a)



(b)

**Fig. 5.6** XRD phase scan analysis at the (a) weld section, and (b) rail section of the repaired rail.

To ensure the validity of the measured residual stresses using XRD, where no additional residual stresses would affect the results, the Polished sample is etched in several steps until the measured stress is stabilized and any further layer removal would not result in any sensible changes in the measured stresses.

Per Sec. 2.3, Fig. 5c, spot 1 (shown in red) is picked as the base point at which stress measurement is performed at different stages of the specimen. The different stages of the specimen include the As-built stage (indicated as A-B in Fig. 7), Polished (indicated as P in Fig. 7), and Etched. After polishing, the sample is etched for 5 times, indicated as E-1 after first time of etching in Fig. 7, E-2 after second time of etching, and so on. The Depth parameter in Fig. 7 represents the distance of the current surface of the specimen from the base surface in the As-built condition. Polishing removed 750  $\mu\text{m}$  from the As-built surface, and each step of etching removes another 50- $\mu\text{m}$  layer from the specimen surface.

The measured in-plane longitudinal and transversal stresses, i.e.,  $S_{xx}$  and  $S_{yy}$  (refer to Sec. 2.3, Fig. 5 to configure the x and y coordination), are shown in Figs. 7a and 7b, respectively. It is evident that polishing could cause a shifting around 45-50% in the measured stress value. The reason of such an intensive increase in the measured stress can be attributed to, first, removing the interrupting surface spikes and letting the X-ray beams to penetrate enough to the surface and measure the existing residual stresses instead of scattering around, and second, the extra residual stresses on the surface induced during the polishing process. To remove that extra portion of the residual stresses, i.e., the portion applied through polishing, the sample is etched.

Fig. 7 shows that five steps of etching could decrease the measured  $S_{xx}$  and  $S_{yy}$  by 7% and 20%, respectively. The difference between the measured stress value in the P and E-5 stages in Fig. 7 technically stands for the induced residual stresses due to polishing that are now removed in the E-5 specimen. It can be interpreted from Figs. 7a and 7b that there is no difference between the measured stress in the E-4 and E-5 stages for both the  $S_{xx}$  and  $S_{yy}$ . Hence, the E-5 specimen is used

hereafter for measuring stress at the rest of the spots shown in Sec. 2.3, Fig. 5c.

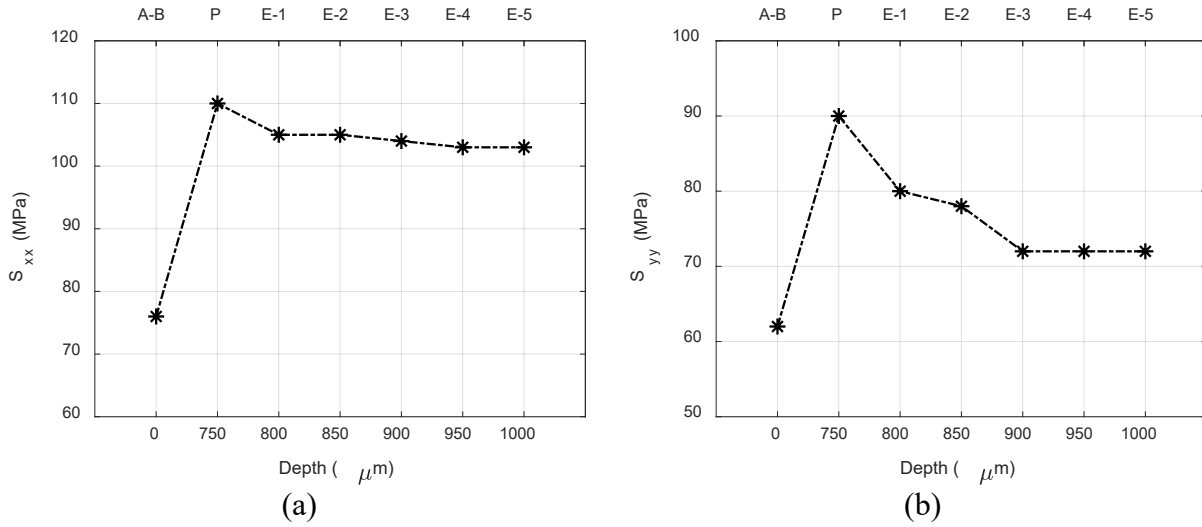


**Fig. 5.7** Measured residual stresses using XRD method at spot 1 (shown in red in Sec. 2.3, Fig. 5c) along the (a) longitudinal and (b) transversal directions at different stages of the specimen; As-built (A-B), Polished (P) and first to fifth time of etching (E-1 to E-5).

Longitudinal and transversal residual stresses, i.e.,  $S_{xx}$  and  $S_{yy}$ , are measured on the E-5 specimen at all the spots shown in Sec. 2.3, Fig. 5c and the results are given in Fig. 8. The lower x axis shows the distance of each spot from spot 5 (based on Sec. 2.3, Fig. 5c), and the upper x axis marks the corresponding spot number. It should be noted that spots 1 to 5 are located in the weld zone, with spot 5 the farthest and spot 1 the closest spot to the rail-weld interface, and spots a and b are in the rail zone, where spot b is the closer spot to the rail-weld interface. From the graphs shown in Fig. 8, the rail-weld interface falls somewhere between 16 to 20 mm from spot 5, i.e., between spots 1 and b.

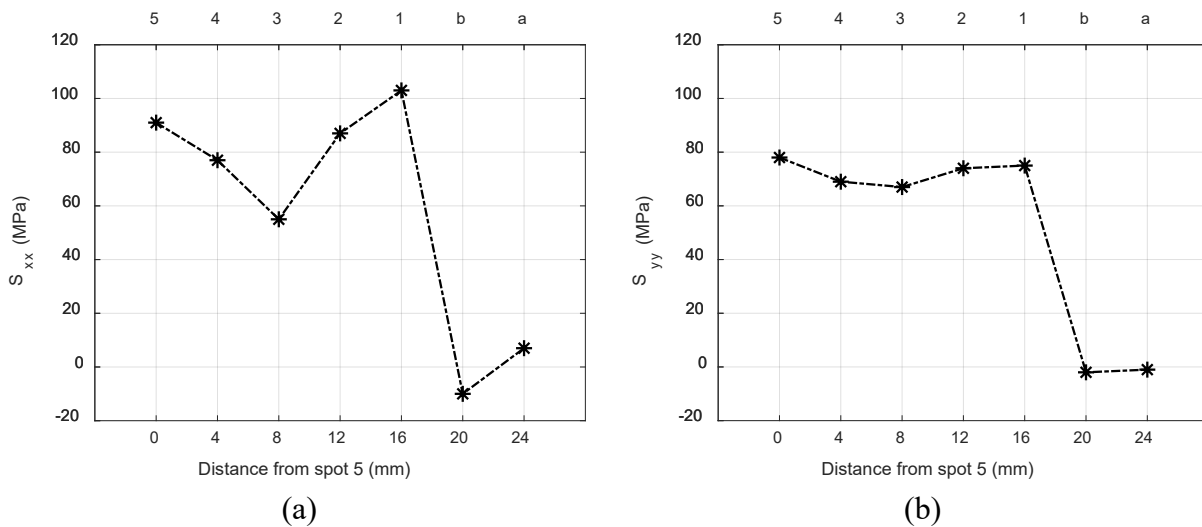


**Fig. 5.8** Measured (a) longitudinal and (b) transversal residual stresses using XRD on the E-5 specimen at all the spots shown in Sec. 2.3, Fig. 5c; the upper  $x$  axis shows the spot numbers and the lower  $x$  axis shows their distance from spot 5.

According to Fig. 8a, the weld zone carries only tensile  $S_{xx}$  with the maximum values of 91 and 103 MPa located at spots 5 and 1, respectively, which represent the top surface of the weld and the area near the rail-weld interface, respectively. The minimum tensile  $S_{xx}$  of 55 MPa in the weld area is found in the middle section at spot 3. A tensile-to-compressive transition of stress happens at the rail-weld interface, i.e., from spot 1 to b, where the maximum tensile  $S_{xx}$  of 103 MPa in the weld section transforms to maximum compressive  $S_{xx}$  of 10 MPa in the rail section. It is seen that  $S_{xx}$  in the lower areas of the rail, i.e., point a, switches back to tensile, but stays at low and relatively negligible values.

Regarding the transversal stress ( $S_{yy}$ ) in Fig. 8b, almost the same pattern can be figured out. The maximum tensile  $S_{yy}$  values of 78 and 75 MPa in the weld materials is found at spots 5 and 1, respectively. A compressive stress of 2 MPa is located at spot b, which is in the rail area close to the rail-weld interface. A near-zero  $S_{yy}$  happens in lower areas of the rail at spot a.

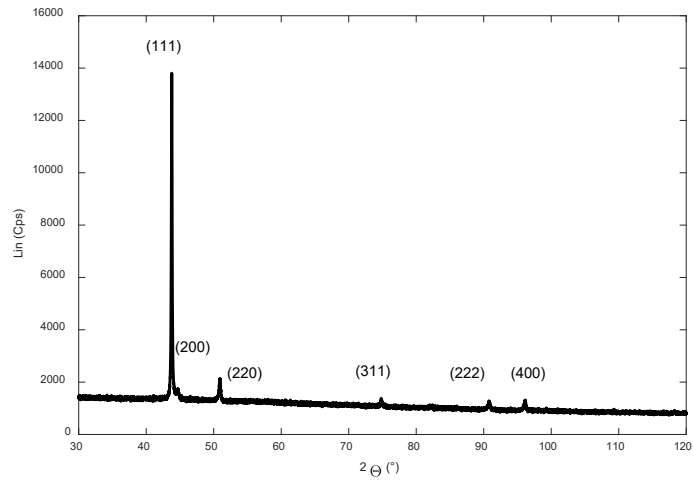
At the time of starting the SAW process, on one hand, a sudden temperature rise happens which leads to a rapid expansion of the rail surface. On the other hand, the deposited weld layer tends to shrink as a result of fast cooling through convection with the air and conduction with the bulk rail substrate. The collision of these two phenomena concludes to an applied tensile stress from rail to weld (found in spot 1 in Fig. 8) and an applied compressive stress from weld to rail (found in spot b in Fig. 8). After depositing the first weld layer, the substrate is already at a high temperature and depositing the subsequent layers will not experience a high tensile stress due to expansion-shrinkage interactions as much as the first layer did. This explains the lower tensile stresses in the middle layers, i.e., spots 2 to 4. However, the last weld layer, i.e., the top layer, cools down faster than the lower layers as a result to direct exposure to the air. Besides, unlike the lower weld layers, the top layer does not have a chance of relieving a portion of its residual stress by getting reheated owing to depositing a new layer on the top. That is why the tensile stress grows again in the upper areas of the weld, i.e., spot 5.

### 5.2.2. LPD-repaired heavy rail

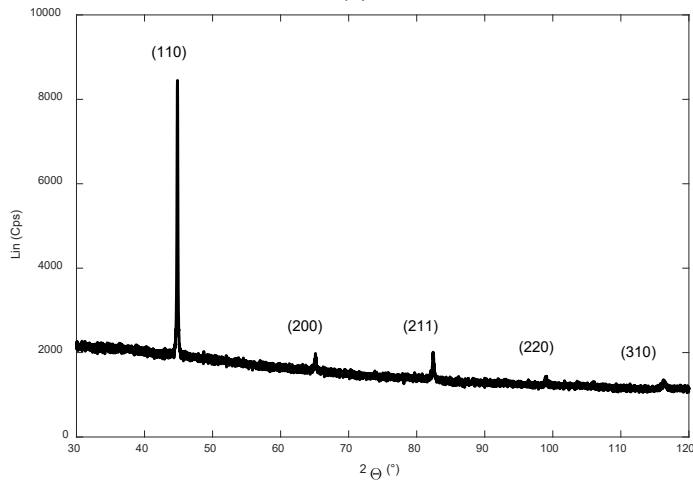
The measured results are presented based upon the coordinate system and the assigned points shown in Sec. 2.3, Fig. 5. The XRD measurement points are illustrated in Sec. 2.3, Fig. 5c. Measurements at point 1, that is shown as a red point in Sec. 2.3, Fig. 5c, are conducted before and after every single step of sample development to ensure that the contributing errors owing to the surface roughness and externally induced residual stresses are eliminated. Stress measurement at other given points (white points in Sec. 2.3, Fig. 5c) are performed on the ultimately finished specimen, i.e., after all the polishing and chemical etching steps.

Surface roughness measurement is conducted here to ensure the measurement accuracy. However, since the results and the measurement process are quite the same as what was presented in Sec. 5.1.1, the descriptions are not repeated here.





(a)



(b)

**Fig. 5.9** Diffraction Peak Pattern through the full range of  $2\theta$  for (a) 304L deposition steel and (b) heavy rail.

Figs. 9a and 9b show a general phase scan analysis of the deposition and rail materials, respectively. In order to gain accurate strain values due to minor changes in lattice spacing, it is preferred to measure residual stresses at high diffraction angles to capture those slight variations [1]. Thus, XRD stress measurement at points 1, 2, 3, 4, and 5, that are located in the deposition area (see Fig. 5c), is carried out at the diffraction angle of  $2\theta = 96.2^\circ$  where, referring to Fig. 9a, FCC (4 0 0) diffraction peak occurs. Residual stresses at the rail zone, i.e., points a, b, and c in Sec. 2.3, Fig. 5c, are evaluated at the diffraction angle of  $2\theta = 116.2^\circ$  corresponding to BCC (3 1 0) peak in Fig. 9b. Stress measurement at these points is performed using  $\sin^2\psi$  method. A total number of six points of  $\psi$  are employed at each measurement point, starting from  $\psi = 0^\circ$  followed by successive adding of  $\psi$  offsets up to  $\psi = 45^\circ$  with five equal intervals. The incorporated diffraction angle measurement range in the deposition area is  $94.2^\circ \leq 2\theta \leq 98.2^\circ$  and in the rail area is  $114.6^\circ \leq 2\theta \leq 117.8^\circ$ , with a 0.02 increment of  $2\theta$  and a counting accumulation of 0.8 seconds per step. Peak evaluation is conducted using sliding gravity method, and data correction

is used for Lorentz-polarization, background, and absorption.

Measurement verification is also conducted just like what was done for the LPD-repaired light rail in Sec. 5.1.1 and hence, will not be described here again. It is just worth noting that the AE5 specimen will be used for the stress measurement.

The measured  $\sigma_{xx}$  and  $\sigma_{zz}$  stress components at different measuring locations, i.e., the depicted points in Fig. 5c, are shown in Fig. 10. All of the presented measurements are performed on the AE5 specimen. As it was mentioned earlier in Section 2.2.3, a total number of five layers are deposited on the worn head of the heavy rail. Accordingly, residual stresses at the first, second, third, fourth, and fifth deposition layers are measured by XRD profiling at points 1, 2, 3, 4, and 5 (as shown in Sec. 2.3, Fig. 5c), located at 2 mm, 6 mm, 10 mm, 14 mm, and 18 mm below the top surface of the deposition materials, respectively. Residual stress evaluation continues down to the rail zone at points c, b, and a (as shown in Sec. 2.3, Fig. 5c) that are located at 22 mm, 26 mm, and 30 mm below the top surface of the deposition materials, respectively. The measuring points along with their corresponding distance from the deposition top surface are given in Fig. 10 as the upper x-axis and lower x-axis components, respectively.

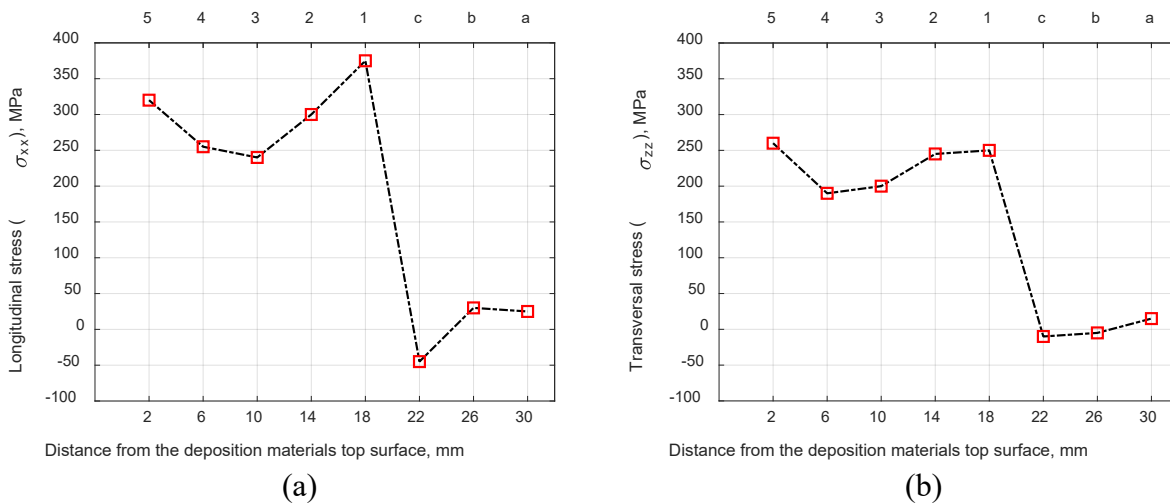


**Fig. 5.10** The XRD measured (a) longitudinal ( $\sigma_{xx}$ ) and (b) transversal ( $\sigma_{zz}$ ) residual stress distribution in the repaired rail. the upper x-axis denotes the corresponding measuring point (refer to Sec. 2.3, Fig. 5c for configuration of the points).

Regarding the longitudinal stress ( $\sigma_{xx}$ ) distribution in Fig. 10a, the maximum tensile stress of 375 MPa occurs at the first deposition layer (point 1). The topmost deposition layer (point 5) carries the second-maximum residual stress, i.e., 320 MPa. The deposition layer carrying the minimum tensile stress of 240 MPa is the third layer (point 3). Maximum compressive stress of 45 MPa can be found in the rail zone at point c.

Speaking of the distribution of transversal residual stresses ( $\sigma_{zz}$ ) in Fig. 10b, maximum tensile stress of 260 MPa is found at the fifth deposition layer (point 5), and the second maximum tensile of 250 MPa happens at the first deposition layer (point 1). Minimum tensile stress in the deposition zone is around 190 MPa in the fourth deposition layer (point 4). In the rail zone, the nearest point

to the rail-deposition interface (point c) carries the maximum compressive stress of 10 MPa.

According to Fig. 10, both stress components ( $\sigma_{xx}$  and  $\sigma_{zz}$ ) undergo almost similar stress distribution pattern. Maximum stress values occur at the first and fifth deposition layers (points 1 and 5). The third and fourth deposition layers (points 3 and 4) contain minimum residual stresses in the deposition zone. Moving from point 1 in the deposition zone down to point c in the rail zone, the maximum tensile residual stress transforms to maximum compressive stress in the rail zone. The area between point 1 and point c, where the rail-deposition layer is also located, may be called the heat-affected zone. The maximum compressive stress takes place in point c, and then the residual stresses decay to near-zero values in points b and a.

The given residual stress distribution in Fig. 10 shows that the maximum tensile stresses happen in the first and last deposition layers, i.e., points 1 and 5, respectively. Lower tensile stresses are found at the middle layers (points 2, 3, and 4). A maximum compressive stress can be discovered in the rail zone near the rail-deposition interface (point c).

The LPD process starts with no bed preheating, meaning that the railhead as the LPD substrate is at the room temperature at the start of depositing the first deposition layer. This fact, on one hand, causes the rail to start a fast expansion during the deposition of the first layer as a result of an accelerated temperature rise, and on the other hand, makes the first deposition layer to undergo a rapid shrinkage since the rail acts as a giant, cold substrate that absorbs a large amount of the induced heat from the LPD process. Hence, the rapid expansion and shrinkage of the rail and deposition steel, respectively, along with the fact that the high-carbon rail has a higher yield strength and higher thermal expansion coefficient than the austenitic deposition materials [4,5], ultimately makes the rail to apply a high tensile stress to the deposition layer to freeze its fast shrinkage. This explains the high tensile stress at the first deposition layer (point 1). The deposition layer also applies back a minor compressive load to harness the thermal expansion of the rail. This causes a low compressive stress to be applied to the railhead, as can be seen in point c in Fig. 10.

The second layer deposits on a high-temperature bed, where the bed for this layer is the worn rail and the first layer that is already deposited. Hence, second layer will not experience a huge thermal shock as the first layer did. Also, there is not any thermal expansion and yield strength mismatch between this layer and the first deposited layer, since both of them are of the same material. These evidences, which can be given for the third and fourth layers as well, justify the lower residual stress in these layers (points 2, 3, and 4) compared to the first layer (point 1).

The topmost deposition layer, i.e., fifth layer, will not be reheated as a result of depositing a further layer on top of it. This causes this layer to cool down much faster than the lower layers. All of the lower layers are reheated at least once as a result of depositing a new layer on the top. This reheating will cause them to cool down much slower than the top layer. Also, all of the lower layers are bounded by high-temperature materials on both sides, but the top layer is exposed to the ambient air on its upper side and starts losing heat rapidly to the environment through both convection and radiation. The other advantage of reheating for the lower layers is that it will cause a part of their residual stresses to get relieved, but the last deposition layer does not have this opportunity to relieve a part of its residual stresses. Relying on the presented reasons, the top deposition layer (point 5) has higher residual stresses than the lower layers, especially the middle

layers (points 2, 3, and 4).

The 304L stainless steel that is used as the deposition material has a room-temperature yield strength of around 215 MPa. According to Fig. 10, it is seen that almost all of the deposition layers have exceeded the material yield strength, i.e., 215 MPa. This means a great risk of early cracking and failure of the deposition steel under the dynamic load of train. In order to ease off the residual stresses, preheating the railhead before LPD repairing and also reheating the whole deposition area after LPD repairing are recommended. The pre- and post-heating methods are currently under investigation.

## References for Chapter 5

- [1] M.E. Fitzpatrick, A.T. Fry, P. Holdway, F.A. Kandil, J. Shackleton, L. Suominen, Determination of residual stresses by X-ray diffraction, National Physical Laboratory (2002) Measurement good practice guide no. 52.
- [2] M. Ghasri-Khouzani, H. Peng, R. Rogge, R. Attardo, P. Ostiguy, J. Neidig, R. Billo, D. Hoelzle, M.R. Shankar, Experimental measurement of residual stress and distortion in additively manufactured stainless steel components with various dimensions, Mater. Sci. Eng. A 707 (2017) 689–700. <https://doi.org/10.1016/j.msea.2017.09.108>.
- [3] V.V. Lider, X-Ray diffraction topography methods, Phys. Solid State 63 (2021) 189–214. <https://doi.org/10.1016/j.msea.2017.09.108>.
- [4] ASM Handbook, Properties and selection: irons, steels, and high-performance alloys, in: Elevated-temperature properties of stainless steels, ASM International 1 (1990) 930-949. <https://doi.org/10.31399/asm.hb.v01.a0001048>.
- [5] G. Li, H. Lyu, L. Huang, X. Wang, 5 - Properties of high-strength steels at and after elevated temperature, In: Behavior and design of high-strength constructional steel, Woodhead Publishing (2021) 153-204. <https://doi.org/10.1016/B978-0-08-102931-2.00005-X>.

## **6. Chapter 6 SIMULATING THE RAIL-REPAIR PROCESS USING FINITE ELEMENT ANALYSIS (FEA)**

The repetitive experimental evaluation of all of the involved parameters until finding the optimum condition will cost a lot of materials and time. Therefore, to avoid considerable costs associated with the experimental lab tests, a finite element (FE) model is developed in which the full LPD rail repair process is simulated; further investigations on the process parameters can be conducted numerically after the thorough validation of the model.

Sec. 6.1 will describe the established FE model regarding the geometry, solution domain, and the incorporated elements and equations. Then, in Sec. 6.2, the developed FE model for repairing the light rail will be validated by comparing the calculated results against the experimental results of an LPD-repaired light rail using 304L, i.e., the results that were presented in Secs. 3.1.2, 4.1.2, and 5.1.1. At this time, the developed FE model is considered for LPD-repairing of the light rails only. The process simulation of SAW-repairing and also that for the heavy rails will be carried out in the near future.

### **6.1. Finite element (FE) model development**

A coupled thermal-kinetic-mechanical FE model that simulates the AM rail repair process is developed. A flowchart representing the general work plan of the FE model is given in Fig. 1. For the sequential thermal-mechanical calculation, thermal calculation feeds its output to the mechanical calculation as the initial nodal thermal loads. On one hand, calculation of the thermal field for every single time step is reliant on the material properties, and on the other hand, material properties calculation at any time is dependent on the thermal field. This fact necessitates adding a thermal-kinetic calculation chain to the model, which is schematically shown as the connection between thermal and kinetic calculation in Fig. 1. The hardness and microstructure properties are updated at every time step through the user-defined relationships for microstructures and material properties. Thermal-kinetic analysis accounts for heat and mass transfer and also phase transformation, which are given to the model through a set of conjugate equations. It is indeed obvious that these equations cannot get solved via analytic methods. To attain more accurate numbers out of thermal calculation, a set of mathematical expressions are given to the model as an external user-defined subroutine, where the element activation temperature, phase transformation latent heat, and laser power attenuation are considered.



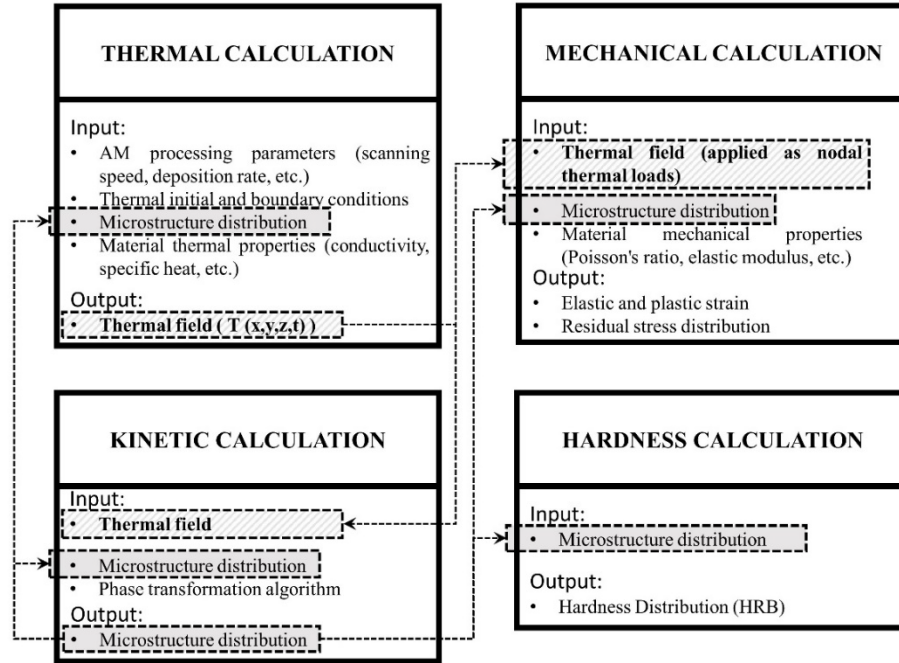


**Fig. 6.1** A flowchart illustrating the designated work plan for coupled thermal-kinetic-mechanical calculations in the developed FE model for simulating AM rail repair process.

Referring to Fig. 1, the analysis cycle starts with thermal calculation. The problem solution domain along with all the initial and boundary conditions are fed to the thermal model to give the resulting  $T(x,y,z,t)$  as the output file. The thermal field outcome is inserted into the kinetic model for every single time step in order to predict the microstructure distribution. The microstructure outcome is: first, imported to the thermal model input to update the thermal problem initial values; second, given back to the kinetic calculation itself to update the input; third, put into the developed equations for hardness calculation; and fourth, along with the thermal output, is fed to the mechanical calculation input. It is evident in Fig. 1 that mechanical and hardness calculation give residual stress and hardness distribution, respectively, in the output file. All the mentioned calculations above repeat for each time step.

### 6.1.1. Thermal calculation

All the involved heat transfer mechanisms during the AM process should be considered in the model to attain an accurate thermal field.

The following equation calculates the conduction heat transfer:

$$\rho c \frac{\partial T}{\partial t} = \nabla \cdot (k \cdot \nabla T) + \Gamma \quad (1)$$

where  $\rho$ ,  $c$ , and  $k$  represent the density, specific heat, and conductivity, respectively, and  $T$  represents the local temperature at any specific time of  $t$ . An amount of 260 kJ/kg is considered for the latent heat of phase transformation ( $\Gamma$ ) [1].

The bulk rail and deposition materials, as the solid domain, lose and gain heat through their interfaces with ambient. This loss/gain of heat is carried out via convection and radiation heat transfer mechanisms. Hence, the convection and radiation equations are applied as problem boundary conditions, because they occur as a result of the surface-ambient interactions.

The most important surface-ambient interaction to consider is the ultimate laser power that strikes on the surface. The ultimate laser power that reaches the substrate to create the molten pool is lower than the laser source power due to the laser power attenuation. To take this effect into consideration, the laser beam is regarded to be distributed in Gaussian form. Utilizing the analytical CFD model of Taberero et al. [2], the ultimate laser power is expressed as:

$$P_u = \frac{2P_s}{\pi R_t^2} \times \exp\left(-2\left(\frac{R_l}{R_t}\right)^2\right) \quad (2)$$

where  $P_u$  and  $P_s$  give the laser ultimate and source power, respectively. The parameter  $R_t$  is the total beam radius, while  $R_l$  gives the local radius through the following definition:

$$R_l = ((x - Vt)^2 + y^2)^{1/2} \quad (3)$$

where  $V$  is the laser travel speed. The following assumptions are made for deriving the attenuated power of the laser source:

- The powder particles shadow effect is neglected.
- Powder particles are assumed as perfect sphere of 75  $\mu\text{m}$  diameter that hit the melt pool with a blowing velocity of 4 m/s.
- Based on the published data by Liu and Lin [3], for a laser power of 1.8 kW, powder diameter of 75  $\mu\text{m}$ , and 4m/s blowing velocity, the percentage of the evaporated mass of powder is low enough to be neglected. Accordingly, particle evaporation is not considered here.
- Heat transfer through the carrier gas is low enough to be omitted.
- The powder distribution profile is also considered to be Gaussian based on the Lin's suggestion [4].

According to the recommended methods in [5,6], Beer-Lambert method is employed to calculate the attenuated laser power,  $P_a$ . By integrating along the stand-off distance of the laser beam, from laser aperture  $((x', y') = (0, 0)$  in Sec. 2.2.2, Fig. 3) down to the railhead surface  $((x', y') = (0, S)$  in Sec. 2.2.2, Fig. 3, where  $S = 11$  mm), the following expression is established:

$$\int_{P_0}^{P_s} \frac{dP}{P} = -\epsilon \int_0^{11} \left(\frac{C_m}{\pi R_{jt}^2}\right) \exp\left(-2\left(\frac{R_{jl}}{R_{jt}}\right)^2\right) dy' \quad (4)$$

where  $R_{jl}$  and  $R_{jt}$  are local and total powder jet radius, respectively. The Mie's optical factor,  $\epsilon$ , is equal to  $\pi d_p^2/4$  ( $d_p$  is powder particle diameter), based on the recommendation from Frenk et al. [7].  $C_m$  is the maximum powder concentration, which is formulated as:

$$C_m = \left( \frac{6\sqrt{2}}{\pi^{3/2}} \right) \left( \frac{\dot{m}}{\rho_p v_p d_p^3 R_{jt}} \right) \quad (5)$$

where  $\rho_p$  and  $v_p$  represent the powder density and velocity, respectively. Powder density is considered to be of the constant value of 7955 kg/m<sup>3</sup> [3]. Powder feeding rate,  $\dot{m}$ , is defined as:

$$\dot{m} = \frac{\pi}{6} (d_p^3 \rho_p v_p) \int_{-\infty}^{\infty} \left( \frac{C_m}{\pi R_{jt}^2} \right) \exp \left( -2 \left( \frac{R_{jl}}{R_{jt}} \right)^2 \right) dR_{jl} \quad (6).$$

Relying on the outcomes of Liu and Lin [3], it can be logically assumed that the powder particles will not melt before joining the melt pool. Another presumed fact is that if any powder particle does not successfully enter the melt pool, it will be rebounded or driven away, i.e., none of the powder particles will adhere on the bed surface. Melt pool temperature is estimated as equal to the railhead's liquidus temperature,  $T_{liq}$ . Thus, the powder particles melt and reach  $T_{liq}$  right at the moment of their entrance into the melt pool. Consequently, the ultimate laser power that hits the substrate is developed as follows:

$$P_u = \alpha_{sub} \left( \frac{2P_s}{\pi R_t^2} \times \exp \left( -2 \left( \frac{R_l}{R_t} \right)^2 \right) - P_a \right) - \frac{\eta \dot{m}}{\pi R_t^2} (\Gamma + \bar{c}(T_{liq} - T_p)) \quad (7)$$

where  $\alpha_{sub}$  stands for the substrate absorptivity,  $\eta$  gives the powder efficiency, and  $\bar{c}$  represents the average specific heat of the powder particles, which is considered equal to 740 J/kg°C. For the immediate temperature of powder particles before entering the molten pool,  $T_p$ , an average value of 224°C is taken into account [6]. Solution of the numerical integrals in Eqs. 4 and 7 gives the Gaussian power distribution of both the laser source and ultimate laser power, which is shown in Fig. 2. It is hence concluded based on the figure that an average amount of 130 W of the laser source power is attenuated, i.e.,  $P_a = 130$  W. In this way, thermal problem boundary condition can be defined as:

$$-k(\nabla T \cdot \vec{n}) = P_u - U(T - T_a) \quad (8).$$

The term  $U(T-T_a)$  expresses the total heat loss from the solid body to the ambient through convection and radiation mechanisms. The overall film coefficient,  $U$ , is equal to  $2.4 \times 10^{-3} \epsilon T^{1.6}$ , where the value of the radiative emissivity,  $\epsilon$ , is taken as 0.85 [6]. The ambient temperature,  $T_a$ , is 25°C.

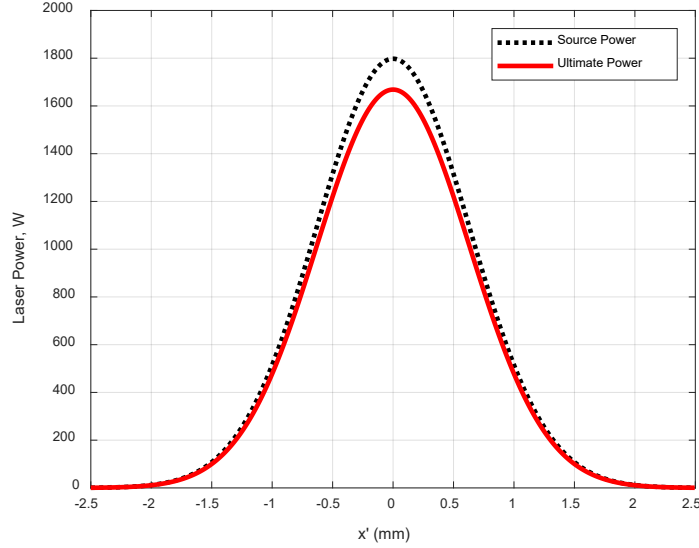


**Fig. 6.2** Distribution of laser source power and laser ultimate power along the laser strike diameter at  $y' = S = 11$  mm (refer to Sec. 2.2.2, Fig. 3 for  $(x',y')$  coordination).

In order to build up the worn part of the railhead in the FE model based on the defined LPD strategy, the element birth-and-kill technique is incorporated. The steps involved in this technique are described as follows:

- a) Modeling the solution domain, including worn rail geometry and the deposition part (Fig. 3a).
- b) Discretizing the solution domain into finite elements (Fig. 3b). The employed three-dimensional solid element is the 10-node coupled field type, referred to as "SOLID227" in ANSYS. The element mesh mapping of the deposition domain is done manually in order to scrutinize the 50% overlap of the adjacent clads.
- c) Deactivating, i.e., killing, the deposition domain at the beginning (Fig. 3c). In this step, all of the elements of the deposition domain are deactivated at  $t = 0$ . Therefore, the problem is initiated with a sole worn rail, the initial temperature of which is defined as:

$$T(x, y, z, t = 0) = T_i \quad (9a)$$

where, based on the selected preheating case,  $T_i$  has various values. In this study, in order to investigate the effect of bed preheating on residual stresses, five different cases are examined, i.e.,  $T_i = 25^\circ\text{C}$  (no preheating),  $400^\circ\text{C}$ ,  $600^\circ\text{C}$ ,  $800^\circ\text{C}$ , and  $900^\circ\text{C}$ . The model will be verified based on the no-preheating condition ( $T_i = 25^\circ\text{C}$ ). Investigation of the effect of preheating will be analyzed and discussed in great details in Chapter 7.

- d) Stepwise activating, i.e., bearing, the deactivated deposition elements (Fig. 3d). Here, the elements of the deposition domain start to activate at the same pace as the actual powder feeding rate. Technically, the laser power has to be high enough to melt the deposition bed, i.e., the railhead, and ensure perfect bonding. Thus, the second initial condition is to set the initial temperature of the activated elements at the melting temperature of the railhead:

$$T(x, y, z, t = t_{activation}) = T_{melt} = 1500^{\circ}\text{C} \quad (9b).$$

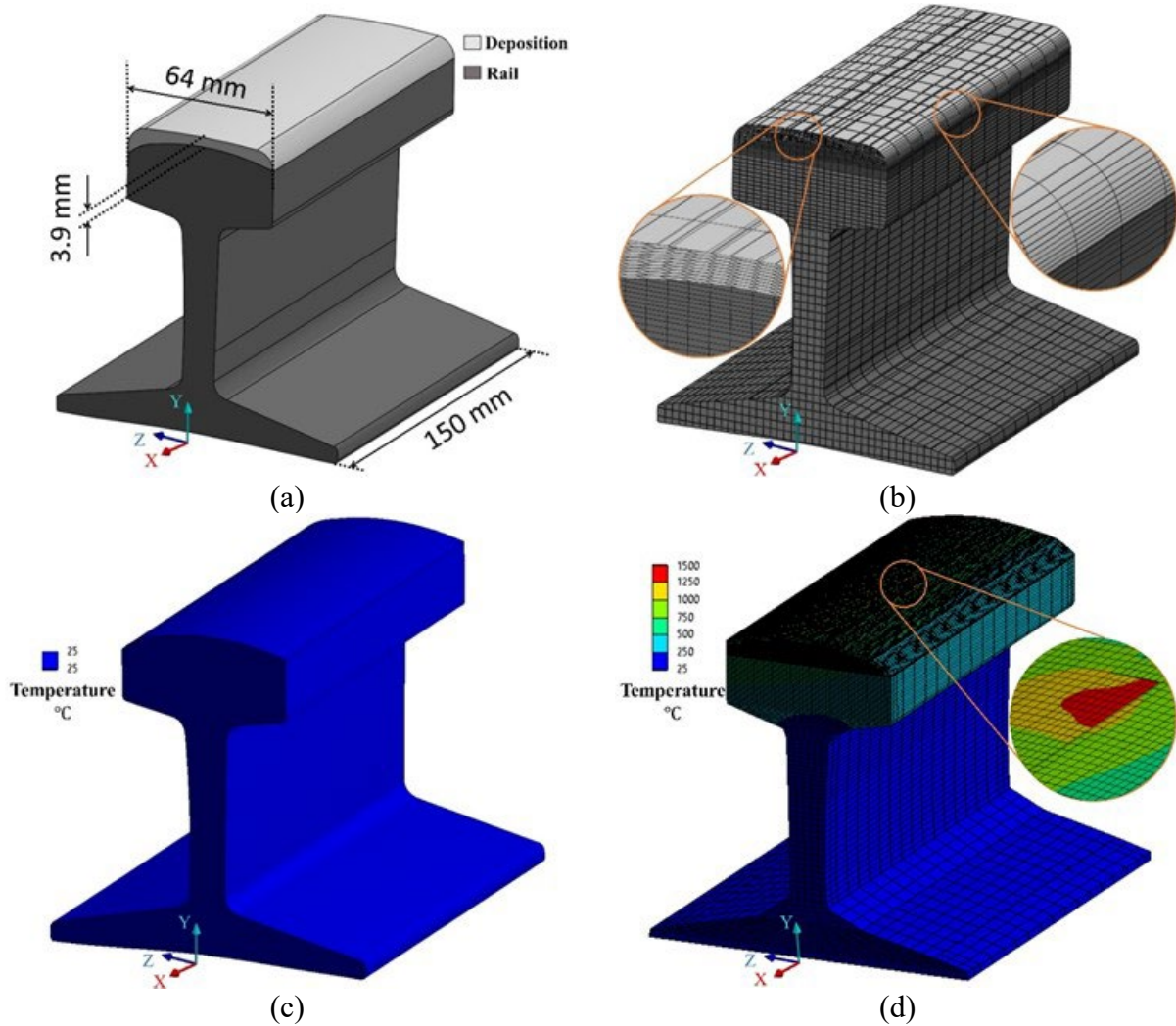


**Fig. 6.3** Graphical illustration of the element-birth-and-kill method that is used to simulate the LPD process in the FE model in 4 steps, i.e., (a) modeling the solution domain, (b) discretizing the solution domain into finite elements, (c) killing the deposition elements at the beginning (here shown for the  $T_i = 25^{\circ}\text{C}$ ), and (d) bearing the killed deposition elements step by step.

Regarding the tool path, the laser heat source, in tandem with the element activation process, travels back and forth along the  $\pm x$  axis. There is 9s of idle time between finishing the activation of the last element of a completed deposition row and starting the activation of the first element of the consecutive row. The deposition layers are built upward along the  $+y$  axis.

As regards to guarantee the calculation accuracy with minimum computational time, a grid independence test is carried out for the thermal model. To perform this test, five grid densities are tested and the temperature parameter,  $T(x,y,z,t)$ , at the very last time step right after the activation of the last deposition element ( $t_{final}$ ) and two selected locations, i.e.,  $(x,y,z) = (-50,2,0)$  mm and

$(x,y,z) = (-100,-100,0)$  mm (refer to Sec. 5.1.1, Fig. 1 for configuration of the coordination system), is used as the test criteria. Table 1 lists the results of the grid independence test. The Grid no. 4 with 475,646 elements and 586,592 nodes is finally picked for the numerical model. Selecting the denser Grid no. 5 with 868,023 elements and 954,825 nodes results in only  $\leq 2\%$  modification in the predicted temperature values. In the matter of the dependent variables, their residual sum are monitored after each iteration. Based on the assigned convergence criterion, the maximum relative mass residual depending on the input mass has to be lower than  $10^{-4}$ .

**Table 12** Grid Independence Test.

Grid no.	Elements	Nodes	$T(-50,2,0,t_{final})$ (°C)	$T(-100,-100,0,t_{final})$ (°C)
1	12,334	20,628	449	147
2	142,018	215,553	489	159
3	229,055	302,515	548	183
4	475,646	586,592	573	194
5	868,023	954,825	579	197

### 6.1.2. Kinetic calculation

Four candidate steels, including 304L stainless steel, 410L stainless steel, Stellite 6, and Stellite 21, are chosen to investigate the best option, i.e., the option in which the lowest residual stress and highest strength are attained simultaneously. The leading motivation for choosing 410L, Stellite 6, and Stellite 21 is their remarkable tribological and mechanical properties based on the reports in [8,9], which make them notably applicable for rail repair. Since the guidelines of the AREMA [10] have restricted the martensite occupation in the microstructure of any standard U.S. rail, the selection of 304L is made mainly due to its austenitic nature, which essentially allows the avoidance of martensite in the finally established microstructure of the repaired rail. It also should be noted that the other reason for selecting these four materials is that they are commercially available as powders that are specifically intended for LPD applications.

A phase-transformation paradigm for each of the four tool steels is developed and applied to the model in a way to predict the microstructural phase evolutions during the heating-cooling cycles of the LPD process. Fig. 4 shows these paradigms in the form of schematic diagrams. A brief description of the analytical procedure, through which each of the phase-transformation diagrams and the reciprocal phase-volume-fraction equations were obtained, is presented in the following.

Since 304L is an austenitic stainless steel, its  $Ni_{eq}$ - $Cr_{eq}$  system must be authenticated first in order to determine its phase transformation procedure [11]:

$$\begin{aligned} Ni_{eq} &= 0.5(Mn) + (Ni) + 30(C + N) \\ Cr_{eq} &= 0.5(Nb) + (Cr + Mo) + 1.5(Si) \end{aligned} \quad (10)$$



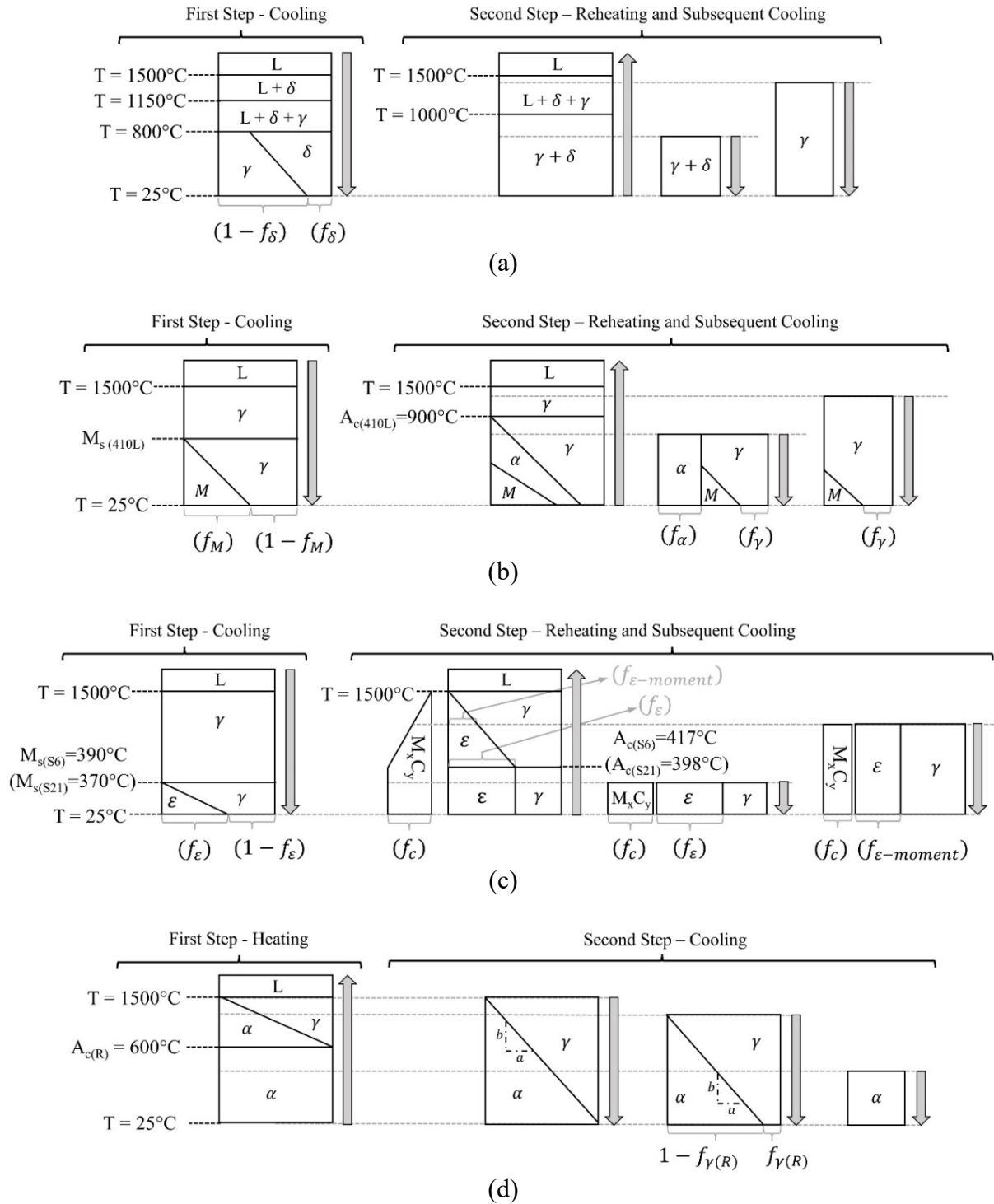
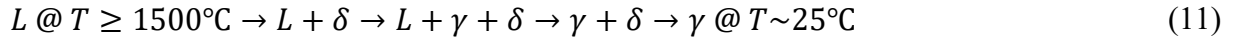


**Fig. 6.4** Schematic diagrams showing the defined phase-transformation paradigms applied to the kinetic analysis of the FE model for each of the deposition tool steels, i.e., (a) 304L stainless steel and (b) 410L stainless steel, (c) Stellite 6 and Stellite 21 ( $M_{s(S6)}$  and  $A_{c(S6)}$  correspond to the Stellite 6 case, and  $M_{s(S21)}$  and  $A_{c(S21)}$  correspond to the Stellite 21 case), and (d) rail.

where every element mentioned in the equations represents the corresponding weight percentage.

For the powder 304L deposition steel, where  $1.5 < Cr_{eq}/Ni_{eq} < 2.0$ , the phase transformation process is proposed as follows:



where L,  $\delta$ , and  $\gamma$  are the liquid phase, the  $\delta$ -ferrite phase, and the austenite phase, respectively. Fig. 4a shows a schematic depiction of the aforementioned phase transformation prediction. A combination of austenite and  $\delta$ -ferrite is the main product of 304L solidification. The final volume fraction of  $\delta$ -ferrite is correlated directly with the solidification rate. The lower the solidification rate, the longer time the  $\delta \rightarrow \gamma$  transformation takes, which subsequently leads to a lower volume fraction of  $\delta$ -ferrite. The cooling rate of every deposition layer is related to the bed temperature, where the bed refers to the railhead and the formerly deposited layer for the first deposition layer and successive deposition layers, respectively. Considering the bed temperature, defined as parameter T, and the standards developed by ASTM A800 [12], the  $\delta$ -ferrite volume fraction for 304L tool steel is expressed as:

$$f_{\delta} = \begin{cases} 1 - \exp(6.65 \times 10^{-5} \times T - 0.1142), & T \leq 800 \\ 0, & T > 800 \end{cases} \quad (12)$$

where  $f_{\delta}$  is the volume fraction of retained  $\delta$ -ferrite after complete cooling to room temperature. Also, Fig. 4a shows that when the reheating exceeds  $1000^{\circ}\text{C}$ , the subsequent cooling to room temperature results in a pure austenite microstructure.

Fig. 4b shows a phase transformation diagram of 410L stainless martensite steel, which technically undergoes an  $\gamma \rightarrow \alpha \rightarrow \gamma \rightarrow L$  transformation during the first heating and a  $L \rightarrow \gamma \rightarrow \gamma + \alpha + M$  transformation during the cooling that follows [13]. Therefore, as can be seen in Fig. 4b, the initial cooling process starts with a  $L \rightarrow \gamma$  transition process, where, at the given range of cooling rates ( $0.5\text{-}100^{\circ}\text{C/s}$ ), the diffusion of austenite essentially is restrained with the only exception being a minor  $\gamma \rightarrow M$  transformation that starts at the  $M_{s(410L)}$  temperature. Depending on the rate of cooling,  $M_{s(410L)}$  may vary over a wide range of temperatures, i.e.,  $245\text{-}375^{\circ}\text{C}$  [14]. Based on the findings of Lima et al. [14],  $M_{s(410L)}$  has an inverse correlation with the cooling rate and its austenitization temperature ( $A_{c(410L)}$ ). In consonance with the dilatometry findings of Deev et al. [13], the  $A_{c(410L)}$  is considered equal to  $900^{\circ}\text{C}$  in the ongoing calculations. Thus, for a constant  $A_{c(410L)}$ , the variation of  $M_{s(410L)}$  as a function of cooling rate can be formulated as follows:

$$M_{s(410L)} = 375 - 0.56(CR) \quad (13)$$

where CR is the cooling rate ( $^{\circ}\text{C/s}$ ). The Koistinen and Marburger equation [15], which is applicable to an extensive selection of ferrous alloys, is used in the kinetic model in order to predict the volume fraction of the martensite being formed below  $M_{s(410L)}$ :

$$f_M = \begin{cases} 1 - f_{\gamma_1}, & T \geq M_{s(410L)} \\ 1 - f_{\gamma_1} \times \exp\left(-0.011(M_{s(410L)} - T)\right), & T < M_{s(410L)} \end{cases} \quad (14)$$

where  $f_M$  is the martensite volume fraction at temperature T, and  $f_{\gamma_1}$  is the initial volume fraction

of austenite. Fig. 4b shows that after the initial cooling of 410L and during the reheating process, the volume fractions of austenite and  $\alpha$ -ferrite are increased and decreased linearly with the temperature, respectively, until the  $\alpha$ -ferrite is completely transformed to austenite at  $A_{c(410L)}$ . Fig. 4b shows that if the subsequent cooling occurs before reaching  $A_{c(410L)}$ , there will be a partially or fully  $\gamma \rightarrow M$  transformation, along with the formation of  $\alpha$ -ferrite. The formulated volume fraction of the retained austenite for 410L steel is expressed and inserted into the model:

$$f_{\gamma} = f_{\gamma_1} \times \exp(-(M_{s(410L)} - T)/91) \quad (15)$$

where  $f_{\gamma}$  is the retained austenite volume fraction at temperature  $T$ . Accordingly, the  $\alpha$ -ferrite volume fraction is equal to:

$$f_{\alpha} = 1 - f_M - f_{\gamma} \quad (16).$$

However, if the cooling process starts after exceeding  $A_{c(410L)}$ , there would be only an  $\gamma \rightarrow M$  transformation, and no formation of  $\alpha$ -ferrite would occur.

The phase-transformation paradigm in Fig. 4c illustrates the microstructural evolutions of Stellite 6. The Co-based Stellite 6 alloy generally consists of two allotropes, i.e., 1) a high-temperature  $\gamma$  allotrope that has a face-centered-cubic (fcc) crystal structure and is strongly stable up to the melting temperature of 1500°C and 2) a low-temperature allotrope,  $\epsilon$ , with hexagonal-close-packed (hcp) crystallite, which gains stability at temperatures lower than 417°C [16]. Under various circumstances, these two allotropes can transform into each other. The  $\gamma \rightarrow \epsilon$  is referred to as the martensitic transformation. At the cooling step, it undergoes an  $\gamma \rightarrow \epsilon$  transition starting at  $M_{s(S6)} = 390^\circ\text{C}$ , as shown in Fig. 4c, during the first step of cooling. The martensite starts to develop linearly below  $M_{s(S6)}$  until its volume fraction reaches  $f_{\epsilon}$  at room temperature, i.e., 25°C. When the bed temperature,  $T$ , and the cooling rate,  $CR$ , are known, the equations developed by Yang et al. [16] can be used to calculate the volume fraction of the transformed martensite at each time step by solving the following equation for  $f_{\epsilon}$ :

$$\frac{CR}{\vartheta \cdot \exp(-Q/RT)} = \left( \frac{1}{s_g^2 \cdot a_{hcp}} + (10^{15.532 - 3.897 \cdot f_{\epsilon}}) \cdot f_{\epsilon} \right) \cdot (1 - f_{\epsilon}) \quad (17)$$

where  $Q$  is the active energy required for nucleation, which, according to the results of Turrubiates-Estrada et al. [17], is 164 kJ/mol;  $R$  is the gas constant, i.e., 8.314 J/mol.K;  $s_g$  is the grain size of the matrix, i.e., 18.3  $\mu\text{m}$  [16]; and  $a_{hcp}$  is the lattice constant of the hcp crystal structure, which is set equal to 4.113 Å [16]. During the reheating, the reverse transition of  $\epsilon \rightarrow \gamma$  occurs at  $A_{c(S6)} = 417^\circ\text{C}$ . Regarding the precipitated  $M_xC_y$  carbides, there is a linear relationship between the martensitic transformation and carbide precipitation. Hence, the kinetic calculations of the current model for Stellite 6 are set such that the momentary volume fraction of the precipitated carbides,  $f_c$ , at any given time is equal to:

$$f_c = 0.15(f_{\epsilon\text{-moment}}) \quad (18)$$

where, according to Fig. 4c, during the reheating process,  $f_{\epsilon\text{-moment}}$  is equal to  $f_{\epsilon}$  at temperatures below  $A_{c(S6)}$ , and then begins to decrease linearly from  $f_{\epsilon}$  at  $A_{c(S6)} = 417^{\circ}\text{C}$  to 0 at  $T_{\text{melt}} = 1500^{\circ}\text{C}$ . Fig. 4c shows that the retained volume fraction of each phase during the subsequent cooling after reheating is defined to remain exactly the same as the momentary volume fraction at the time step when reheating is finished and subsequent cooling begins.

The other Co-based deposition alloy is Stellite 21, which has the same phase-transformation protocol as that defined for Stellite 6 [18]. However, conforming to the calculations for the Co-Cr binary system [19], there is a slight shifting of the  $M_s$  and  $A_c$  temperatures for Stellite 21, compared to those for Stellite 6. Therefore, the phase-transformation paradigm presented in Fig. 4c for Stellite 6 is repeated almost identically for Stellite 21, with the only exception being that  $M_{s(S21)} = 370^{\circ}\text{C}$  and  $A_{c(S21)} = 398^{\circ}\text{C}$ . This will cause changes to the amounts that are calculated for  $f_{\epsilon\text{-moment}}$ , and subsequently,  $f_c$ .

In accordance with the phase-transformation diagram shown for the rail material in Fig. 4d, for the upper regions of the railhead that are close to the deposition area and that heat up to  $1500^{\circ}\text{C}$ , the subsequent cooling process undergoes a full  $\gamma \rightarrow \alpha$  transformation and revives the complete pearlite structure at room temperature [20]. In this way, the volume fraction of austenite,  $f_{\gamma(R)}$ , is designed to decrease linearly from 1 at  $T = 1500^{\circ}\text{C}$  to 0 at  $T = 25^{\circ}\text{C}$ , a slope that is shown as  $b/a$  in Fig. 4d. For the regions of the rail that are heated initially to temperatures lower than  $1500^{\circ}\text{C}$ , but higher than the rail's austenization temperature, i.e.,  $A_{c(R)} = 600^{\circ}\text{C}$ , a partial  $\gamma \rightarrow \alpha$  transition occurs, and a portion of the austenite remains in the microstructure after cooling to room temperature. In Fig. 4d, at any temperature between  $600^{\circ}\text{C}$  and  $1500^{\circ}\text{C}$  that the cooling starts,  $f_{\gamma(R)}$  decreases linearly with the same slope as  $b/a$  until it intercepts the  $T = 25^{\circ}\text{C}$  line, where the right side of the intercepted  $T = 25^{\circ}\text{C}$  line gives the amount of  $f_{\gamma(R)}$ . For the regions that are quite far from the deposition area and heat up only to temperatures below  $600^{\circ}\text{C}$ , the subsequent cooling produces pure  $\alpha$ -ferrite without any austenite. It is worth mentioning that the presence of cementite in the pearlitic rail steel was low enough to be neglected.

### 6.1.3. Mechanical calculation

The element network in mechanical calculation is identical to that used for thermal calculation. According to the developed model in [21], a feed-forward artificial neural network (ANN) model of the back-propagation learning algorithm for training set with mean square error criteria is engaged for modeling elastic-plastic constitutive material to predict residual strain and stress. This model represents a combined isotropic-kinematic model of the infinitesimal theory of plasticity that is extended to large ranges of strain at elevated temperatures. It technically consists of three input variables of ANN including strain, strain rate, and temperature. The output variable is flow stress with eight neurons in the intermediate layers. More details regarding this utilized model can be found in the comprehensive study by Gupta et al. [21]. Table 2 gives the temperature- and microstructure-dependent mechanical and thermal properties of the deposition and rail materials for different microstructural phases and different temperatures that are inserted into the FE model.

The same element-birth-and-kill technique with equivalent activation rate in thermal calculation is employed here. Activation of each element occurs when the element's temperature drops below  $T_{\text{liq}}$ , and the corresponding thermal field is applied on the element as the initial thermal load. The

activated element then starts to cool down while residing some elastic and plastic strain. Nevertheless, even the deactivated elements are technically alive but with a degrading stiffness. The stiffness starts to recover once the element is activated. Boundary conditions are applied only as to restrain the solid body from any probable rigid body motion.

**Table 13** Temperature/microstructure-dependent mechanical and thermal properties of the rail and deposition tool steels used in FE modeling of the LPD-rail-repair process.

Material		T (°C)	E (GPa)	$\nu$	Yield Strength, $Y_s$ (MPa)	$\alpha$ ( $10^{-5}/^{\circ}\text{C}$ )	$c_p$ (J/kg $^{\circ}\text{C}$ )	k (W/m $^{\circ}\text{C}$ )	
Rail (880-grade steel) [20]	$\alpha$	25	203	0.26	460	1.20	434	60.5	
		600	110	0.33	308	1.40	638	41.6	
		1000	-	-	156	-	-	-	
		1500	-	-	66	-	-	-	
	$\gamma$	25	-	-	511	-	-	-	
		600	-	-	358	-	-	-	
		1000	19	0.40	204	1.47	886	12.6	
		1500	19	0.40	61	1.47	886	12.6	
		25	-	-	215	-	-	-	
304L stainless steel [22]	$\delta$	600	134	0.34	144	1.73	745	18.9	
		1000	19	0.41	90	1.82	984	15.5	
		1500	19	0.41	31	1.82	971	13.2	
	$\gamma$	25	200	0.29	276	1.73	510	15.5	
		600	141	0.37	211	1.87	687	22.4	
		1000	19	0.45	94	1.97	953	28.7	
		1500	-	-	39	-	-	-	
		25	172	0.21	275	1.01	420	56.5	
		600	-	-	211	-	-	-	
410L stainless steel [22,23]	M	1000	-	-	93	-	-	-	
		1500	-	-	28	-	-	-	
		25	207	0.29	415	1.58	502	20.5	
	$\gamma$	600	152	0.35	279	1.62	668	24.2	
		1000	20	0.45	174	1.66	863	26.6	
		1500	20	0.45	70	1.66	863	26.6	
		25	200	0.27	360	1.08	460	18.2	
		600	129	0.30	252	1.11	619	14.4	
		1000	-	-	140	-	-	-	
	Stellite 6 [23,24]	$\epsilon$	1500	-	-	49	-	-	-
			25	210	0.26	483	0.73	400	13.1
			600	152	0.29	370	0.93	553	21.6
		$\gamma$	1000	21	0.36	203	1.12	565	24.7
			1500	21	0.36	69	1.12	565	24.7
			25	237	0.28	750	1.14	444	14.8
600			172	0.32	504	1.45	615	24.3	
1000			24	0.39	255	1.65	628	27.8	
1500			24	0.39	82	1.65	628	27.8	
$M_xC_y$ (Carbides)	25	190	0.20	313	0.68	373	40.8		
	600	137	0.22	218	0.87	517	57.1		
	1000	19	0.27	124	1.05	527	61.7		
	1500	19	0.27	60	1.05	527	61.7		
	25	217	0.26	565	0.70	384	11.4		
	600	160	0.30	379	0.89	512	19.5		
Stellite 21 [18,25]	$\epsilon$	1000	21	0.34	192	1.08	553	22.7	
		1500	21	0.34	58	1.08	553	22.7	
		25	245	0.28	650	1.10	427	13.0	
	$\gamma$	600	181	0.32	422	1.36	569	22.2	
		1000	24	0.40	195	1.52	615	25.8	
		1500	24	0.40	66	1.54	615	25.8	

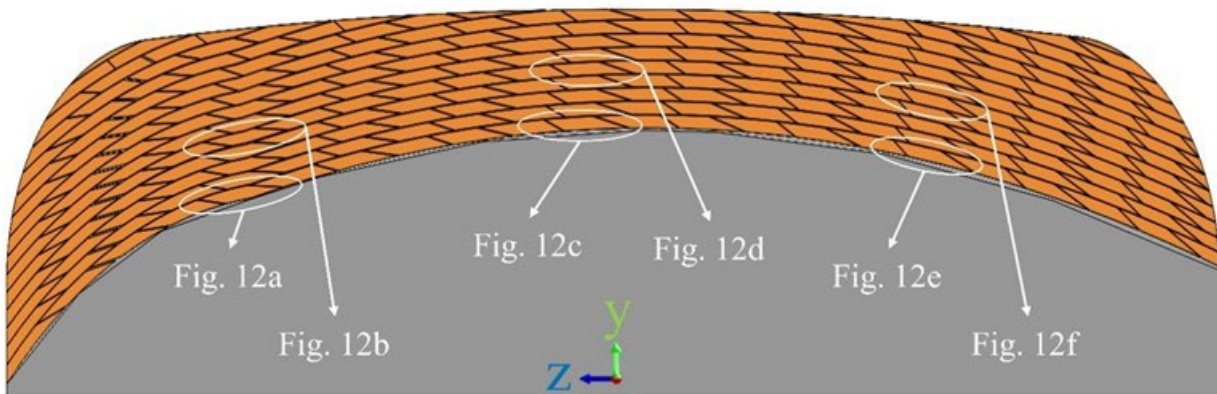
$M_xC_y$ (Carbides)	25	196	0.19	517	0.66	359	35.9
	600	145	0.21	310	0.82	478	50.3
	1000	19	0.25	176	0.91	517	54.3
	1500	19	0.25	56	0.92	517	54.3

## 6.2. FE model validation

The predicted temperature, microstructure, hardness, and residual stress distribution in the LPD-repaired light rail are presented based upon the coordinate system shown in Sec. 5.1.1, Fig. 1. The predicted numerical results are analyzed and also compared against the measured experimental data to validate the developed FE model.

### 6.2.1. Thermal field

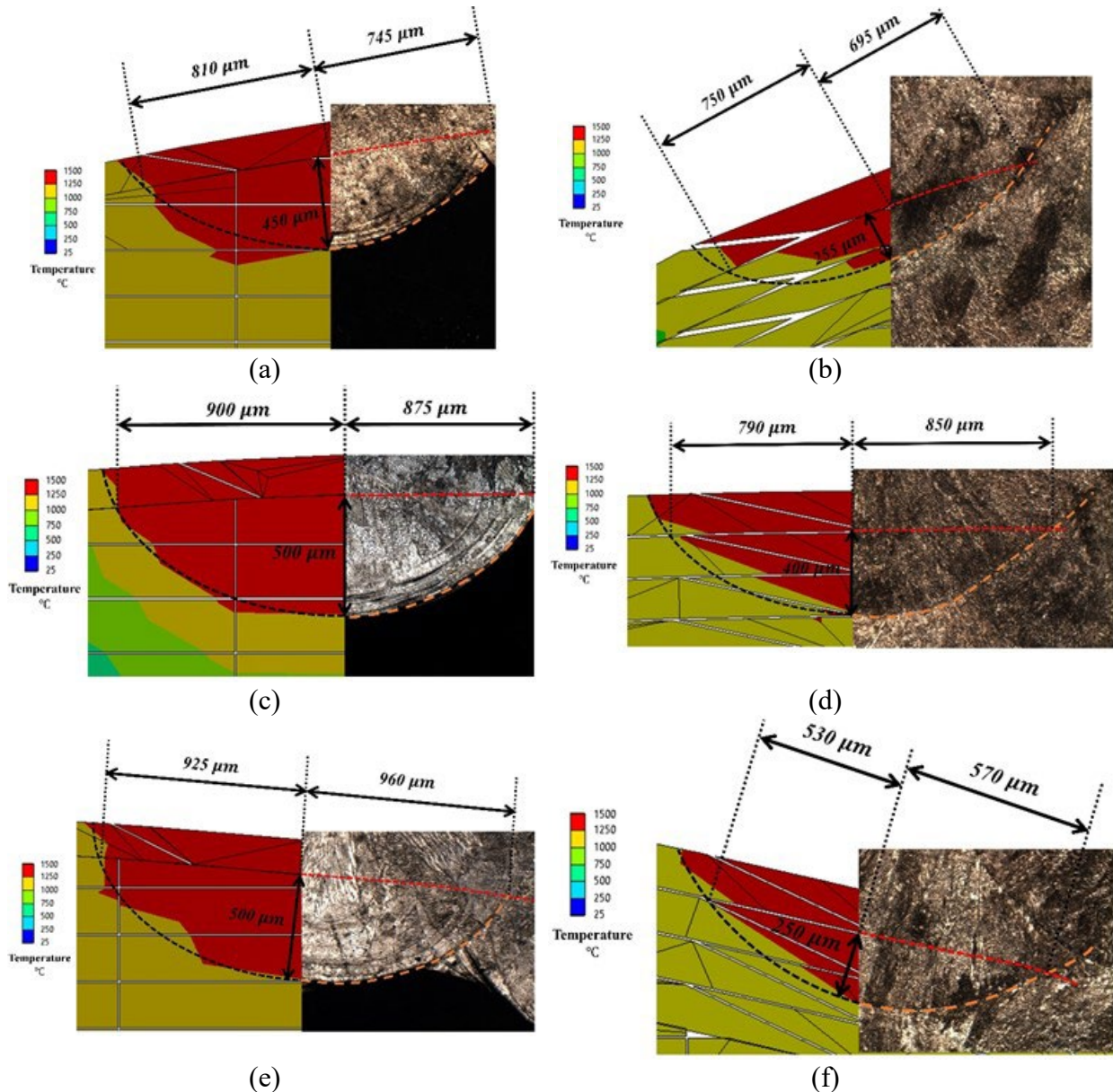
Validation of thermal calculation is executed through comparing the measured and predicted dilution region size. Optical microscope (OM) macrographs from the etched sample are used for measuring the dilution depth at different regions. In numerical regard, the immediate depth of the  $\geq 1500^\circ\text{C}$  thermal contours at the end of the activation course of a single element gives the predicted depth of the melted substrate, i.e., dilution depth. The OM macrographs from different locations of the deposition materials are put against the captured thermal contour at the corresponding location for comparison purposes. Fig. 5 maps the regions where the dimensional correlation between the measured and predicted dilution depth is performed; close-up inspection of these areas is depicted in Fig. 6. Despite a slight dimensional deviation, a fairly great coherence is observable between the numerical and experimental results. The reason of the resulting minor mismatch may be attributed to a few effective parameters on dilution depth, e.g., specific energy, local iron contamination, and local powder concentration, that are not considered in the FE model. Nonetheless, since none of the dimensional deviations does not exceed 10%, the accuracy of the thermal model is reliably insured.



**Fig. 6.5** General mapping of the areas where the dimensional comparison of the dilution depth between the predicted and measured results is performed. Referring to Sec. 5.1.1, Fig. 1, this figure shows the rail transversal cross section at  $x = 75$  mm.

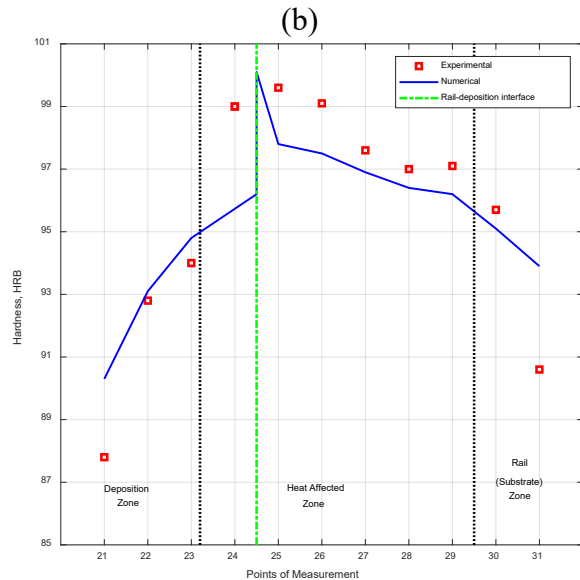
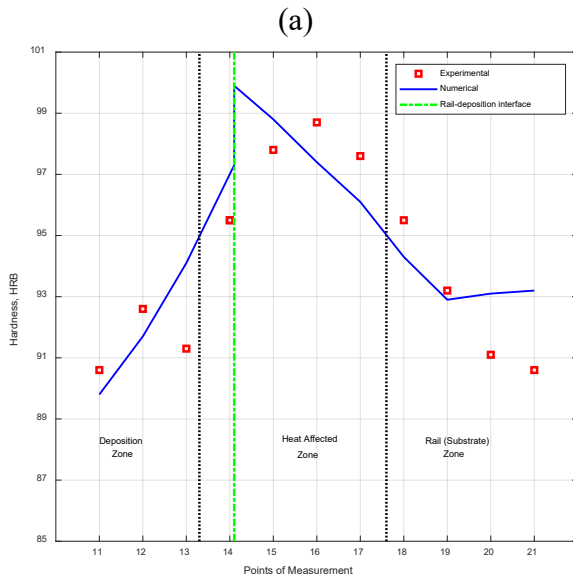
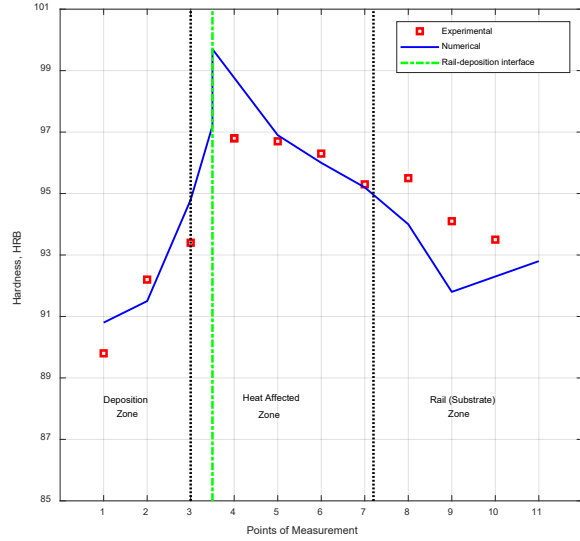
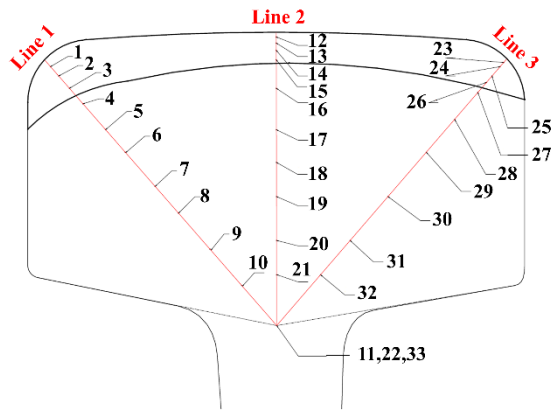
### 6.2.2. Hardness and microstructure distribution

Fig. 7 shows the measured hardness at different spots of the repaired rail. It is seen in the figure that the resulting hardness distribution offers that the repaired rail may be subdivided into three zones: (1) Deposition zone, where the upper layers are primarily consisted of untempered austenite and secondary  $\delta$ -ferrite and lower layers contain primary  $\delta$ -ferrite and tempered austenite due to the induced reheating cycles. (2) Heat-affected zone (HAZ) that encompasses the rail-deposition interface. Its deposition section contains austenite,  $\delta$ -ferrite, and Cr-depleted  $\delta$ -ferrite, and its rail section is majorly constructed of  $\alpha$ -ferrite and austenite. And (3) rail zone that is made of austenite and  $\alpha$ -ferrite.



**Fig. 6.6** Thermal contour distribution of the FE model versus the OM macrograph for dimensional comparison of dilution region between the numerical and experimental results at the (a) and (b) 5th, (c) and (d) 11th, and (e) and (f) 17th deposition row of the first and fifth deposition layers, respectively.





**Fig. 6.7** Experimental vs. numerical hardness results; (a) schematic map of the points and lines on which the hardness is measured; (b) hardness distribution along line 1, (c) line 2, and (d) line 3.

The numerically calculated hardness values are put together with the experimental hardness results in Fig. 7. A stepped increase in numerical hardness values is discernible at the rail-deposition interface, of which the reason is attributed to different hardness expressions in those two zones in the FE model. The involved errors in both hardness measurement and calculation may be ascribed by the implicated errors in hardness test such as repeatability, correlation, and accuracy and also by the included approximations in the FE model. Anyhow, with 2.5% of maximum deviation, there is a quite well agreement between the measured and predicted hardness results.

The distribution of austenite volume fraction,  $f_{\delta}$ , in the repaired rail is also calculated and put next to the predicted hardness distribution in Fig. 8. The presented results in this figure suggest an

inverse correlation between hardness and austenite volume fraction.

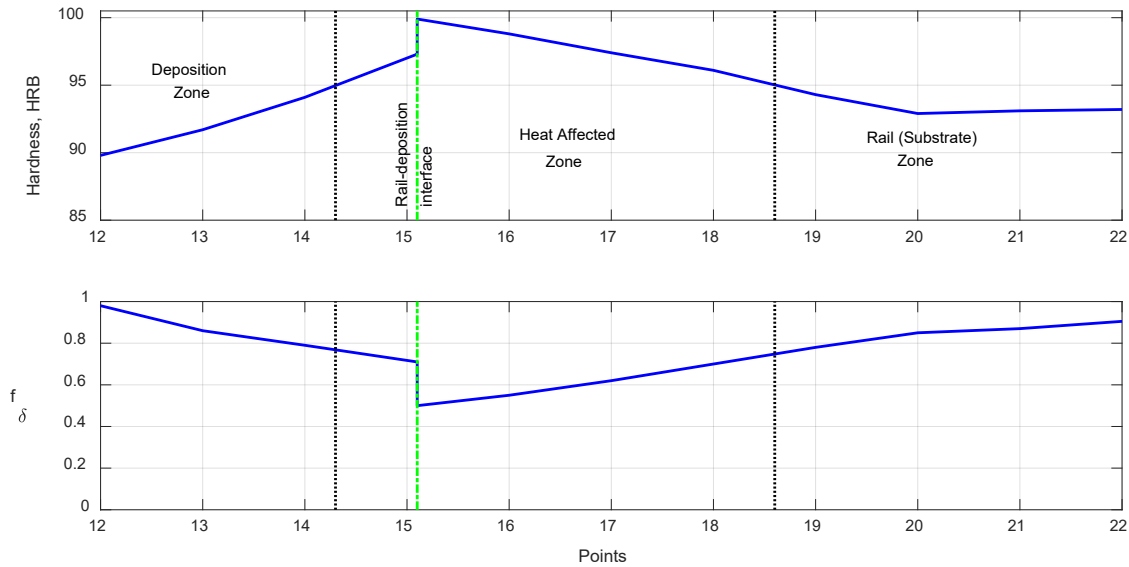


**Fig. 6.8** Distribution of hardness and austenite volume fraction,  $f_{\delta}$ , along line 2 (refer to Fig. 7a for configuration of line 2).

As it is evident in both Figs. 7 and 8, the hardest region locates inside the HAZ with an approximate value of 100 HRB near the rail-deposition interface. The top surface of the deposition zone, with the highest austenite concentration (Fig. 8b), has the lowest hardness (~90 HRB). The rail is not preheated in the current case study, and hence it acts as a huge heat extraction source during LPD. Therefore, fast cooling of the first deposition layer results in precipitation of  $\delta$ -ferrite, which subsequently leads to high hardness amount for the initial deposition layer that is adjacent to rail-deposition interface. The bed temperature for subsequent deposition layers will be higher than that for the first layer, which brings a lower rate of cooling. Smoother cooling rate results in higher austenite volume fraction that causes lower hardness in the middle layers compared to the first layer. However, when a deposition layer is reheated by the upper deposition layers,  $\delta$ -ferrite and Cr-depleted  $\delta$ -ferrite are precipitated in the microstructure and intensify the hardness. Since the top layer does not undergo a reheating cycle, it experiences a complete austenite transformation and thus has the lowest hardness among all the deposition layers (Fig. 8).

The upper zone of the rail that falls into the HAZ is exposed to the laser beam and heats up to elevated temperatures near 1500°C. This area is then gradually cooled down to room temperature and almost completely transfers back to  $\alpha$ -ferrite. Nevertheless, because the lower zone of the rail does not heat as high as the upper zone, a fraction of the microstructure remains austenite after complete cooling to 25°C. This fact describes the higher austenite and lower hardness in the lower zone of the rail rather than its upper region inside HAZ. Comparing this set of analysis on the microstructure distribution against those experimental findings presented in Sec. 3.1.2. shows a great agreement between the model predictions and real measurements.

### 6.2.3. Residual stress distribution

The longitudinal stress,  $\sigma_l$ , along  $x$  direction and transversal stress,  $\sigma_t$ , along  $z$  direction are the major driving forces to cause crack propagation along the corresponding directions (refer to Sec. 5.1.1, Fig. 1 for configuration of the reference coordination). Also, the normal stress,  $\sigma_n$ , along  $y$  direction is the leading motivation of delamination. Fig. 9 gives the derived numerical and experimental distribution of  $\sigma_l$ ,  $\sigma_t$ , and  $\sigma_n$  along  $x$ ,  $z$ , and  $y$  directions, respectively.

The experimental measurement of the residual stresses was presented in Sec. 5.1.1 and the resulting values were given in Sec. 5.1.1, Table 1. All of those measured values in Sec. 5.1.1, Table 1 are depicted as the red square-shaped dots in Fig. 9.

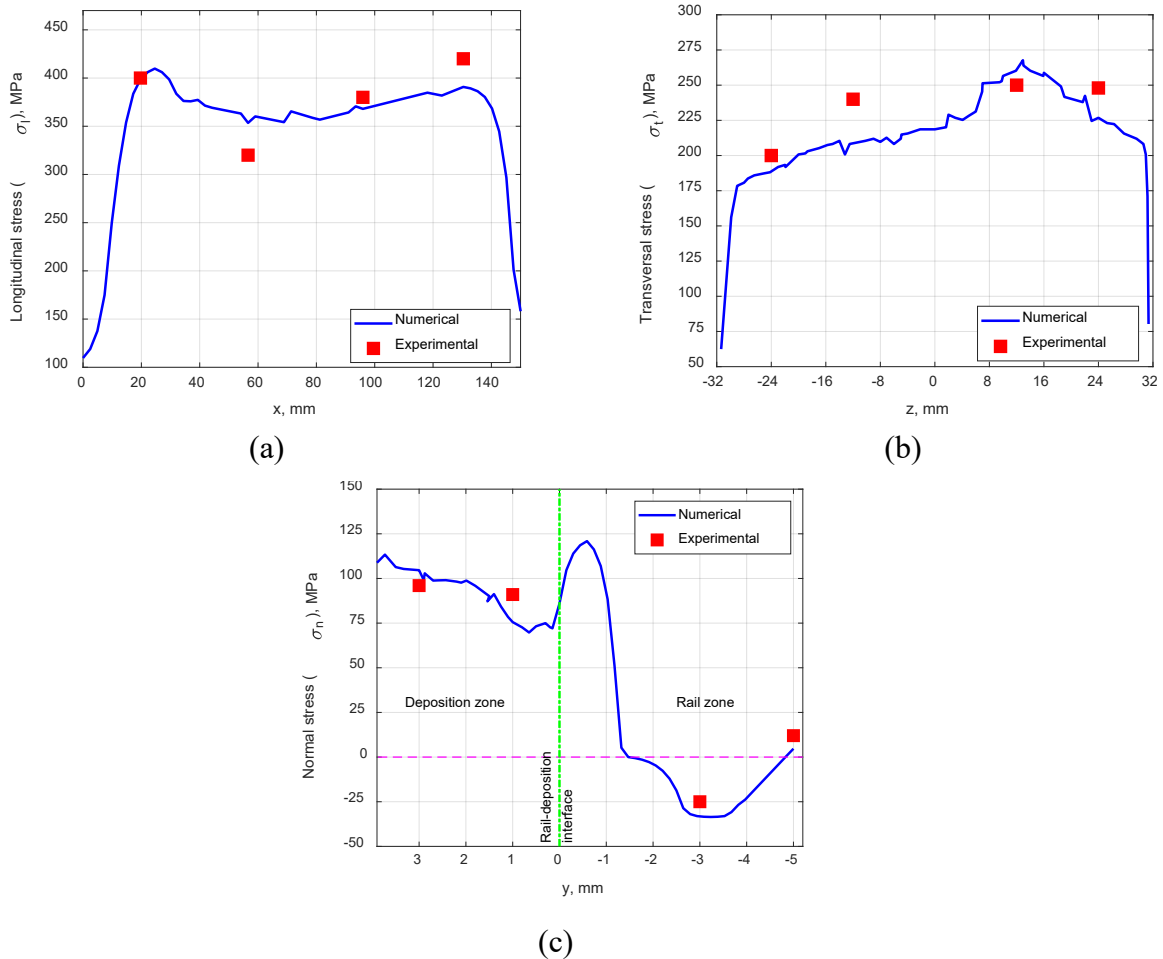


**Fig. 6.9** Experimental vs. numerical residual stress distribution; (a) longitudinal stress,  $\sigma_l$ , along  $x$  direction at  $(y, z) = (0, 0)$ , (b) transversal stress,  $\sigma_t$ , along  $z$  direction at rail-deposition interface for  $x = 0$ , and (c) normal stress,  $\sigma_n$ , along  $y$  direction at  $(x, z) = (0, 0)$ . Refer to Sec. 5.1.1, Fig. 1 for configuration of the reference coordination system.

Now, speaking of the numerical values, it is evident in Fig. 9a and b that  $\sigma_l$  and  $\sigma_t$  remain all tensile due to the applied tensile stress from rail to the deposition materials at the interface. Both of the  $\sigma_l$  and  $\sigma_t$  go through a sharp ascend/drop at the two ends of their calculation interval and achieve their

maximum value at the middle of the interval. The  $\sigma_l$  local peak values at  $x = 25$  and  $130$  mm are equal to  $410$  and  $390$  MPa, respectively, and the single peak value of  $\sigma_t$  at  $z = 13$  mm is  $270$  MPa. It is also observable that the numerical  $\sigma_l$  and  $\sigma_t$  graphs have an oscillating form rather than a smooth form. The reason of the presence of such oscillations is that the residual stress due to the deposition of every row is partially relieved once the adjacent row is deposited. According to Fig. 9a and b, there are more oscillations happening for  $\sigma_t$  rather than that for  $\sigma_l$ , of which the reason is that the deposition elements are not overlapped along the  $x$  direction, but there is a 50% overlap between the deposition rows along the  $z$  direction. More overlap leads to more stress relief and consequently more of those oscillations.

Regarding the numerically predicted distribution of  $\sigma_n$  in Fig. 9c, it remains tensile in the entire deposition zone ( $0 \leq y \leq 4$  mm). In the rail zone ( $-5 \text{ mm} \leq y \leq 0$ ), it achieves a maximum  $120$  MPa near rail-deposition zone at  $y = -0.5$  mm. It then sharply decays and alters to compressive and experiences a maximum compressive of  $33$  MPa at  $y = -3.2$  mm and finally becomes neutral at around  $y = -5$  mm. The reason that  $\sigma_n$  remains tensile to a specific depth of the rail zone is attributed to the dilution region that keeps the residual stress tensile down to the heat penetration depth of the substrate. The determinant factor that contributes to delamination is the gradient of  $\sigma_n$  at the rail-deposition interface. In the deposition zone,  $\sigma_n$  has an oscillating behavior which is due to the stress relief that happens during adding the upper layers upon the lower layers. As Fig. 9c depicts, the upper region of the deposition zone ( $2 \leq y \leq 4$  mm) has higher  $\sigma_n$  values than the lower region ( $0 \leq y < 2$  mm), because the upper layers are not reheated and consequently stress-relieved, as frequently as the lower layers do.

It can be deduced visually from Fig. 9 that the experimental results are comparable fairly well with the calculated data. The derived values show that the maximum difference between the measured and predicted stresses is as low as 10%. Both the experimental measurements and numerical calculations can be responsible for the errors. Increasing the number of counts in XRD analysis, eliminating the allocated approximations in choosing elastic constants, and refining the elements of the FE model can lead to a more accurate model and lower errors. The current FE model is viewed sufficient since the present errors are low enough to be neglected. Refining the FE model would considerably increase the calculation time. Hence, the present model for the ongoing aim is precise enough to provide reliable data for further parametric studies concerning the residual thermal stress during the LPD rail repair process.

In Chapter 7, the validated FE model is utilized to find the optimum LPD procedure in the matter of the deposition material and the preheating temperature to lead to the lowest residual stress in the LPD-repaired light rail.

## References for Chapter 6

- [1] G.E. Totten, M.A.H. Howes, T. Inoue, Handbook of residual stress and deformation of steel, ASM International (2002) ISBN: 978-0-87170-729-1.
- [2] I. Taberero, A. Lamikiz, S. Martínez, E. Ukar, L.N. López de Lacalle, Modelling of energy attenuation due to powder flow-laser beam interaction during laser cladding process, *J. Mater. Process. Technol.* 212(2) (2012) 516–522. <https://doi.org/10.1016/J.JMATPROTEC.2011.10.019>.
- [3] C. Liu, J. Lin, Thermal processes of a powder particle in coaxial laser cladding, *Opt. Laser Technol.* 35(2) (2003) 81–86. [https://doi.org/10.1016/S0030-3992\(02\)00145-7](https://doi.org/10.1016/S0030-3992(02)00145-7).
- [4] J. Lin, Concentration mode of the powder stream in coaxial laser cladding, *Opt. Laser Technol.* 31(3) (1999) 251–257. [https://doi.org/10.1016/S0030-3992\(99\)00049-3](https://doi.org/10.1016/S0030-3992(99)00049-3).
- [5] J.M. Jouvard, D.F. Grevey, F. Lemoine, A.B. Vannes, Continuous wave Nd:YAG laser cladding modeling: a physical study of track creation during low power processing, *J. Laser Appl.* 9(1) (1997) 43–50. <https://doi.org/10.2351/1.4745444>.
- [6] Y. Chew, J.H.L. Pang, G. Bi, B. Song, Thermo-mechanical model for simulating laser cladding induced residual stresses with single and multiple clad beads, *J. Mater. Process. Technol.* 224 (2015) 89–101. <https://doi.org/10.1016/J.JMATPROTEC.2015.04.031>.
- [7] A. Frenk, M. Vandyoussefi, J.D. Wagnière, W. Kurz, A. Zryd, Analysis of the laser-cladding process for stellite on steel, *Metall. Mater. Trans. B* 28(3) (1997) 501–508. <https://doi.org/10.1007/s11663-997-0117-0>.
- [8] Y. Zhu, Y. Yang, X. Mu, W.J. Wang, Z. Yao, H. Yang, Study on wear and ref performance of repaired damage railway wheels: assessing laser cladding to repair local defects on wheels, *Wear* 430–431 (2019) 126–136. <https://doi.org/10.1016/j.wear.2019.04.028>.
- [9] T. Roy, R. Abrahams, A. Paradowska, Q. Lai, P. Mutton, M. Soodi, P. Fasihi, W. Yan, Evaluation of the mechanical properties of laser clad hypereutectoid steel rails, *Wear* 432–433 (2019) 202930. <https://doi.org/10.1016/j.wear.2019.202930>.
- [10] Maintenance for railway engineering, American Railway Engineering and Maintenance-of-way Association (AREMA) Vol. 1: Track, Director of Administration (2014) ISSN: 1543-2254
- [11] K. Rajasekhar, C.S. Harendranath, R. Raman, S.D. Kulkarni, Microstructural evolution during solidification of austenitic stainless steel weld metals: a color metallographic and electron microprobe analysis study, *Mater. Charact.* 38(2) (1997) 53–65. [https://doi.org/10.1016/S1044-5803\(97\)80024-1](https://doi.org/10.1016/S1044-5803(97)80024-1).
- [12] ASTM A800/A800M-01, Standard practice for steel casting, austenitic alloy, estimating ferrite content thereof, ASTM International, West Conshohocken, Pennsylvania (2001). [https://doi.org/10.1520/A0800\\_A0800M-01](https://doi.org/10.1520/A0800_A0800M-01).
- [13] A. Deev, P. Kuznetsov, A. Zhukov, V. Bobyr, The structure and properties of the samples produced by selective laser melting of 410L steel-based metal powder, *Phys. Procedia* 89 (2017) 31-38. <https://doi.org/10.1016/j.phpro.2017.08.013>.
- [14] M.S.F. Lima, A.M.E. Santo, Phase transformations in an AISI 410S stainless steel observed in directional and laser-induced cooling regimes, *Mater. Res.* 15(1) (2012) 32-40. <https://doi.org/10.1590/S1516-14392012005000003>.
- [15] D.P. Koistinen, R.E. Marburger, A general equation prescribing the extent of the austenite-martensite transformation in pure iron-carbon alloys and plain carbon steels, *Acta Metall.* 7(1) (1959) 59-60. [https://doi.org/10.1016/0001-6160\(59\)90170-1](https://doi.org/10.1016/0001-6160(59)90170-1).
- [16] D. Yang, C. Hua, S. Qu, J. Xu, J. Chen, C. Yu, H. Lu, Isothermal transformation of  $\gamma$ -Co to

- $\epsilon$ -Co in Stellite 6 coatings, *Metall. Mater. Trans. A* 50 (2019) 1153–1161.  
<https://doi.org/10.1007/s11661-018-5057-6>.
- [17] R. Turrubiates-Estrada, A. Salinas-Rodriguez, H.F. Lopez, FCC to HCP transformation kinetics in a Co–27Cr–5Mo–0.23C alloy, *J. Mater. Sci.* 46 (2011) 254–262.  
<https://doi.org/10.1007/s10853-010-4969-3>.
- [18] K.P. Sołek, Ł. Rogal, P. Kapranos, Evolution of globular microstructure and rheological properties of Stellite™ 21 alloy after heating to semisolid state, *J. Mater. Eng. Perform.* 26 (2017) 115–123. <https://doi.org/10.1007/s11665-016-2421-9>.
- [19] C. Allibert, C. Bernard, N. Valignat, M. Dombre, Co-Cr binary system: experimental re-determination of the phase diagram and comparison with the diagram calculated from the thermodynamic data, *J. Less Common Met.* 59(2) (1978) 211–228.  
[https://doi.org/10.1016/0022-5088\(78\)90131-5](https://doi.org/10.1016/0022-5088(78)90131-5).
- [20] U.P. Singh, B. Roy, S. Jha, S.K. Bhattacharyya, Microstructure and mechanical properties of as rolled high strength bainitic rail steels, *Mater. Sci. Technol.* 17(1) (2001) 33–38.  
<https://doi.org/10.1179/026708301101509098>.
- [21] A.K. Gupta, H.N. Krishnamurthy, Y. Singh, K.M. Prasad, S.K. Singh, Development of constitutive models for dynamic strain aging regime in austenitic stainless steel 304. *Mater. Des.* 45 (2013) 616–627. <https://doi.org/10.1016/J.MATDES.2012.09.041>.
- [22] ASM Handbook, Properties and selection: irons, steels, and high-performance alloys, in: Elevated-temperature properties of stainless steels, ASM International 1 (1990) 930–949.  
<https://doi.org/10.31399/asm.hb.v01.a0001048>.
- [23] T. Han, C.H. Kuo, N. Sridharan, L.M. Headings, S.S. Babu, M.J. Dapino, Effect of preheat temperature and post-process treatment on the microstructure and mechanical properties of stainless steel 410 made via ultrasonic additive manufacturing, *Mater. Sci. Eng. A* 769 (2020) 138457. <https://doi.org/10.1016/j.msea.2019.138457>.
- [24] N. Hutasoit, W. Yan, R. Cottam, M. Brandt, A. Blicblau, Evaluation of microstructure and mechanical properties at the interface region of laser-clad Stellite 6 on steel using nanoindentation, *Metallogr. Microstruct. Anal.* 2 (2013) 328–336.  
<https://doi.org/10.1007/s13632-013-0093-5>.
- [25] F.J. Clauss, J.W. Weeton, Relation of microstructure to high-temperature properties of a wrought cobalt-base alloy Stellite 21, *AMS* (1953) 5385.  
<https://digital.library.unt.edu/ark:/67531/metadc56992/>.

## 7. Chapter 7 STUDY ON THE EFFECT OF PREHEATING AND DEPOSITION MATERIALS ON THE RESIDUAL STRESSES IN THE REPAIRED RAIL USING THE VERIFIED FE MODEL

### 7.1. Effect of preheating and deposition alloy

After the development and verification of the finite element (FE) model in Chapter 6 based on the no-preheating case and 304L stainless steel as the deposition material, further potential deposition alloys, i.e., 410L stainless steel, Stellite 6, and Stellite 21, are tried for LPD-repairing the light rail only through the numerical study. In this way, chemical compositions of other studied deposition alloys are also brought in Table 1. Model development and numerical study of further potential deposition materials for LPD-repairing of heavy rails is currently under investigation.

**Table 14** Chemical composition of the utilized LPD steel powders (wt.%).

Material	Co	Fe	C	Cr	Mn	Mo	Si	Ni	P	S	W
304L	-	Bal.	0.03	19.0	2.00	-	1.00	10.5	0.045	0.03	-
410L	-	Bal.	0.01	13.5	0.50	0.01	0.47	0.08	0.02	0.03	-
Stellite 6	Bal.	0.10	1.2	30.5	0.02	0.01	1.55	0.70	0.03	0.01	5.00
Stellite 21	Bal.	0.15	0.23	27.0	0.60	5.00	0.85	2.10	0.01	0.01	0.05

Based on the represented study plan in Table 2, the results are presented in four separate cases, i.e., Cases I, II, III, and IV, which explore 304L, 410L, Stellite 6, and Stellite 21 deposition tool steels, respectively. For each case, the residual stress distribution is given for five different rail-preheating cases, i.e.,  $T_i = 25^\circ\text{C}$ ,  $400^\circ\text{C}$ ,  $600^\circ\text{C}$ ,  $800^\circ\text{C}$ , and  $900^\circ\text{C}$ .

**Table 15** An overview of the employed study plan to investigate the residual stress out of the FE model results

Case no.	Deposition tool steel	Calculated residual stress*	Preheating Temperature, $T_i$ ( $^\circ\text{C}$ )				
<b>Case I</b>	304L stainless steel	$\sigma_1$ along x	25	400	600	800	900
		$\sigma_t$ along z	25	400	600	800	900
		$\sigma_n$ along y	25	400	600	800	900
<b>Case II</b>	410L stainless steel	$\sigma_1$ along x	25	400	600	800	900
		$\sigma_t$ along z	25	400	600	800	900
		$\sigma_n$ along y	25	400	600	800	900
<b>Case III</b>	Stellite 6	$\sigma_1$ along x	25	400	600	800	900
		$\sigma_t$ along z	25	400	600	800	900
		$\sigma_n$ along y	25	400	600	800	900
<b>Case IV</b>	Stellite 21	$\sigma_1$ along x	25	400	600	800	900
		$\sigma_t$ along z	25	400	600	800	900
		$\sigma_n$ along y	25	400	600	800	900



\* The parameters  $\sigma_l$ ,  $\sigma_t$ , and  $\sigma_n$  refer to the longitudinal, transversal, and normal stress, respectively. The coordination system along which the residual stresses are measured, are shown in Sec. 5.1.1, Fig. 1.

### 7.1.1. Case I

The residual stress distribution in the 304L repaired rail is given in Fig. 1. Because the 304L had higher value of thermal expansion coefficient than the rail (Sec. 6.1.3, Table 2), it tended to shrink faster than the rail. Consequently, the rail, as the stronger material, tries to harness the shrinkage of the deposition material by applying a tensile stress. Therefore, the  $\sigma_l$  and  $\sigma_t$  components remain tensile all over their measuring paths at the rail-deposition interface (Figs. 1a and b). For  $T_i = 25^\circ\text{C}$ , both  $\sigma_l$  and  $\sigma_t$  experience a sharp increase/decrease towards both ends of their paths.  $\sigma_l$  undergoes two local maximums of 410 and 390 MPa at  $x = 24.6$  and  $130.4$  mm, respectively, while  $\sigma_t$  encounters one peak of 268 MPa at  $z = 12.92$ mm. An inspection of the effect of preheating suggests that increasing the preheating temperature from  $25^\circ\text{C}$  to  $900^\circ\text{C}$  generally contributes to a changeover from the sharp stress distribution to a more uniform distribution. The deviation between the minimum and maximum values of  $\sigma_t$  (Fig. 1b) is decreased significantly by preheating, i.e., from 77% for  $T_i = 25^\circ\text{C}$  to 46% for  $T_i = 900^\circ\text{C}$ , which leads to a quite uniform stress distribution for the latter case. Regarding  $\sigma_l$  (Fig. 1a), by every increase in  $T_i$ , the two local maximum values shift towards the middle of the measuring path until they merge for  $T_i = 900^\circ\text{C}$  case, where only one blunt local maximum occurs at  $x = 83.64$  mm. On average, each step of increasing  $T_i$  results in about 25% reductions in both  $\sigma_l$  and  $\sigma_t$ . This notable reduction emerges from two objectivities, i.e., 1) the higher bed temperature leads to lower thermal gradients and 2) the temperature-dependent yield strength is decreased dramatically at high temperatures (Sec. 6.1.3, Table 2).

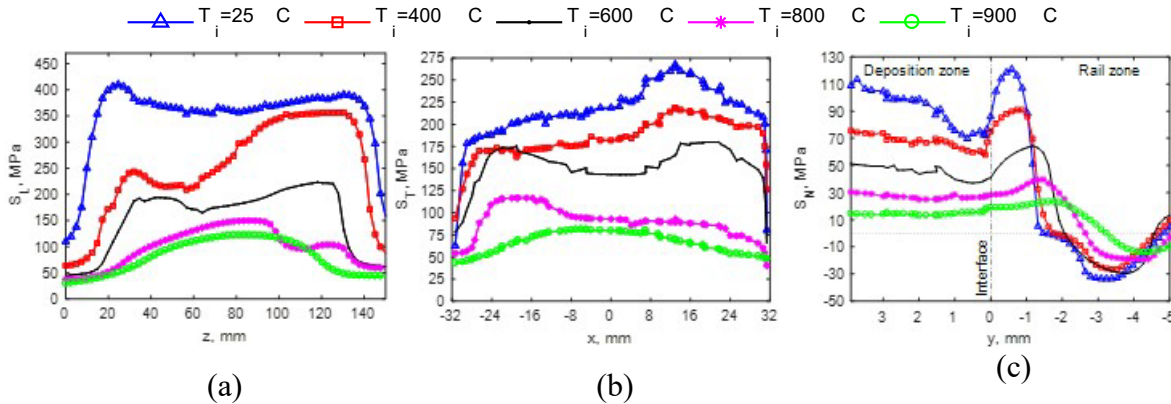


**Fig. 7.1** (a) Longitudinal, (b) transversal, and (c) normal residual stress distributions for 304L repaired rail (Case I) along paths along  $x$ ,  $z$ , and  $y$  directions, respectively. (Refer to Sec. 5.1.1, Fig. 1 for configuration of the coordinate system.)

Another important observation in the  $\sigma_l$  and  $\sigma_t$  distribution graphs is the presence of numerous local oscillations in every graph, especially for cases with lower values of  $T_i$ . These oscillations are ascribed to the fact that, due to the deposition of each clad, the induced residual stress is relieved partially when the adjacent clad is deposited. Considering the preheating trends in Figs. 1a and 1b, it is evident that the oscillations have eased off, and they gradually disappear as  $T_i$  is

increased. When the substrate is preheated and the first layer is deposited on a bed with higher temperature, there would be lower thermal gradients at the time of the deposition of a new high-temperature adjacent clad; therefore, no notable relief in the stress would be visible in the stress distribution graphs. Moreover, it is discernible that the  $\sigma_t$  distribution, shown in Fig. 1b, contains more of these local oscillations compared to those for the  $\sigma_l$  distribution in Fig. 1a for the same  $T_i$  value. This is because there is no overlap between two consecutive clads in the longitudinal direction, but there is a 50% of adjacent clad overlap in the transverse direction, which intensifies the stress-relief effect in the transverse direction, and, consequently, shows more severe stress oscillations.

The  $\sigma_n$  distribution in Fig. 1c remains tensile over all of the deposition zone until it reaches a maximum near, but slightly underneath, the rail-deposition interface. Then, it goes through a sharp decay and switches to compressive stress. The compressive stress area also experiences a maximum in the rail zone, and, ultimately, becomes neutral as it approaches about 5 mm beneath the rail-deposition interface. In the  $\sigma_n$  distribution along  $y$ , Fig. 1c, the region between the maximum-tensile and maximum-compressive points is defined as the heat affected zone (HAZ). The high gradient of  $\sigma_n$  at the rail-deposition interface is the predominant contributor to the separation of the deposition part from the rail. The other visible fact in Fig. 1c is that, for  $T_i = 25^\circ\text{C}$ ,  $\sigma_n$  increases gradually from the rail-deposition interface upwards to the free surface on the top, i.e., at  $y = 3.9$  mm. This behavior is attributed to two factors, i.e., 1) the upper deposition layers are subjected to faster cooling and shrinkage rates because they do not get reheated as frequently as the lower layers do and 2) the cooling-reheating cycles that the lower layers experience when the upper layers are being deposited, cause partial relief of the stress; this does not occur for the upper layers.

According to the graphs presented in Fig. 1c, the following major observations can be made concerning the effects of preheating: 1) increasing  $T_i$  shifts the tensile and compressive peaks deeper downwards to the rail zone, meaning that a higher preheating temperature deepens the HAZ; 2) the increment of preheating temperature squeezes the  $\sigma_n$  distribution curves to a smoother distribution, leading to a dramatic decrease in the HAZ stress gradient between maximum tensile and maximum compressive; 3) it mitigates the  $\sigma_n$  gradient at the rail-deposition interface, which will considerably decrease the chance of delamination; 4) the  $\sigma_n$  distribution in the deposition area ( $y > 0$ ) becomes more uniform as the  $T_i$  increases; the deviation between the maximum and minimum stress in the deposition zone tends toward zero, and the stress fluctuations between two consecutive layers gradually fade away. The amount of heat that can be extracted from the deposited layers through the bulk substrate decreases as the preheating temperature increases. Thus, for  $T_i = 25^\circ\text{C}$ , each deposited layer cools down enough to reside some reasonable stress, part of which will be released when the next layer is deposited. Increasing  $T_i$  helps to keep the bed temperature uniform and at a fairly high level throughout the entire deposition process. Subsequently, at the end of the deposition process, the deposition part is allowed to cool as a whole, integral component, concluding with a uniform stress distribution without any internal fluctuations between the layers.

### 7.1.2. Case II

Fig. 2 shows the residual stress distribution in the 410L repaired rail. For this case, for the same

reason described for Case I, both  $\sigma_l$  and  $\sigma_t$  remain tensile all over their measuring paths, respectively (Figs. 2a and b). The distribution pattern of  $\sigma_l$  and  $\sigma_t$  generally are similar to that for Case I. Even so, the overall values of  $\sigma_l$  and  $\sigma_t$  for the  $T_i = 25^\circ\text{C}$  condition for Case II (Figs. 2a and b) have been increased by about 45% and 40%, respectively, compared to the values for Case I (Figs. 1a and b); this is attributed to the higher average yield strength of 410L than that of 304L (Sec. 6.1.3, Table 2). Regarding the preheating cases, the  $\sigma_l$  values in Case II compared to Case I for  $T_i = 400^\circ\text{C}$ ,  $600^\circ\text{C}$ ,  $800^\circ\text{C}$ , and  $900^\circ\text{C}$  are higher by around 31%, 27%, 21%, and 14%, respectively. In addition, the  $\sigma_t$  values in Case II are higher by 39%, 24%, 22%, and 21% for  $T_i = 400^\circ\text{C}$ ,  $600^\circ\text{C}$ ,  $800^\circ\text{C}$ , and  $900^\circ\text{C}$ , respectively, than those in Case I. It is concluded that the overall difference of  $\sigma_l$  and  $\sigma_t$  between Cases I and II decreases as the  $T_i$  increases. This means that preheating at higher temperatures can, to some extent, diminish the dominance of the effects of the deposition material's properties on the resulting residual stresses. Also, it is perceptible in Sec. 6.1.3., Table 2 that the values of the thermal/mechanical properties of different materials become closer at elevated temperatures.

The normal stress distribution of 410L repaired rail along the y direction is illustrated in Fig. 2c. The general  $\sigma_n$  distribution follows the same motifs, similar to Case I, all along y direction, except for the deposition area. Moving from the rail-deposition interface ( $y = 0$ ) upwards to the surface of the repaired rail ( $y = 3.9$  mm),  $\sigma_n$  had an ascending trend for Case I (Fig. 1c), while it had a downward slope for Case II (Fig. 2c). According to Sec. 6.1.3., Table 2, the average values of specific heat,  $c_p$ , and thermal expansion coefficient,  $\alpha$ , for 410L deposition steel are 22% and 25% lower than for 304L, respectively. Thus, although the top layers are less exposed to reheating cycles than the lower layers, they do not cool down and shrink as fast as 304L, and hence, they reside less normal stress. Also, a lower  $\alpha$  coefficient causes lower thermal expansion and shrinkage, and, consequently, a lower deformation constraint exists along the depth direction, y, which ends up with a lower  $\sigma_n$  for the upper layers with the free surface on the top.

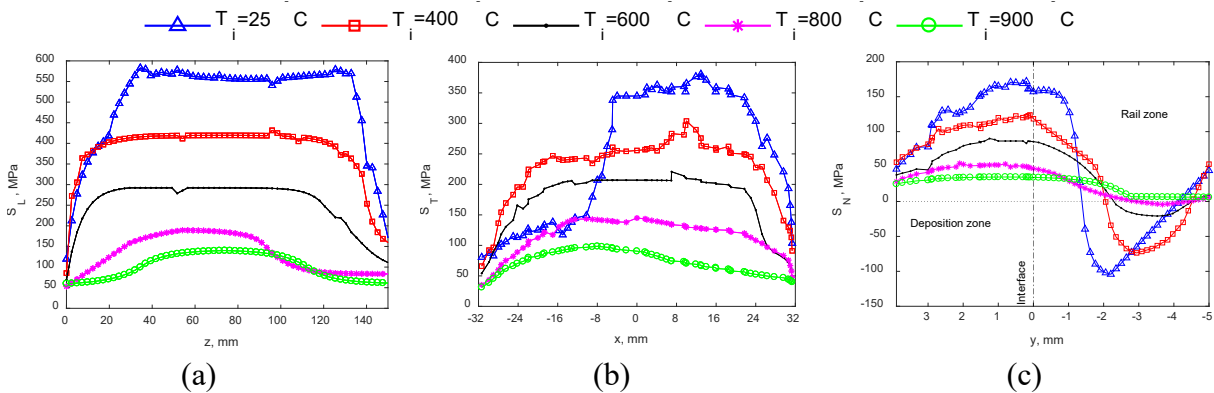


**Fig. 7.2** (a) Longitudinal, (b) transversal, and (c) normal residual stress distributions for 410L repaired rail (Case II) along x, z, and y directions, respectively. (Refer to Sec. 5.1.1, Fig. 1 for configuration of the coordinate system.)

Concerning the values, the overall  $\sigma_n$  values in Case II for  $T_i = 25^\circ\text{C}$ ,  $400^\circ\text{C}$ ,  $600^\circ\text{C}$ ,  $800^\circ\text{C}$ , and  $900^\circ\text{C}$  preheating conditions are increased by approximately 51%, 42%, 40%, 38%, and 36%, respectively, compared to the amounts for Case I (Figs. 1c and 2c). Again, this confirms the idea of the attenuation of material properties' effects on residual thermal stress at high temperatures.

### 7.1.3. Case III

The residual stress distribution in the Stellite 6 repaired rail is presented in Fig. 3. Based on the information in Sec. 6.1.3, Table 2, Stellite 6 has a higher strength, but a lower thermal expansion coefficient, than the rail, 304L, and 410L. Thus, during the cooling procedure, the rail starts to shrink faster than Stellite 6, and, therefore, Stellite 6, as the stronger material, would apply a tensile stress at the rail-deposition interface in order to seize against the rail's shrinkage. This fact supports the reason for the thoroughly tensile distribution of  $\sigma_l$  and  $\sigma_t$  all along their measuring paths in Figs. 3a and b, respectively. Referring to Fig. 3a,  $\sigma_l$  goes through sharp gradients at both ends and remains almost uniform in the middle for all of the preheating cases, except that the sharpness of those gradients at the two ends decreases as  $T_i$  increases; the same description can be given to the  $\sigma_t$  distribution in Fig. 3b. The average  $\sigma_l$  amounts for Case III are increased by 63%, 61%, 58%, 49%, and 45% for  $T_i = 25^\circ\text{C}$ ,  $400^\circ\text{C}$ ,  $600^\circ\text{C}$ ,  $800^\circ\text{C}$ , and  $900^\circ\text{C}$ , respectively, against those for Case II, and the  $\sigma_t$  values are increased by 58%, 51%, 51%, 48%, and 45%, respectively. Hence, the overall residual stresses increase more steeply from Case II to Case III, rather than those from Case I to Case II, of which the dominant reason is due to the deposition materials' deviation in strength for different cases; although 410L (Case II) is moderately stronger than 304L (Case I), Stellite 6 (Case III) is much stronger than 410L (Sec. 6.1.3, Table 2).

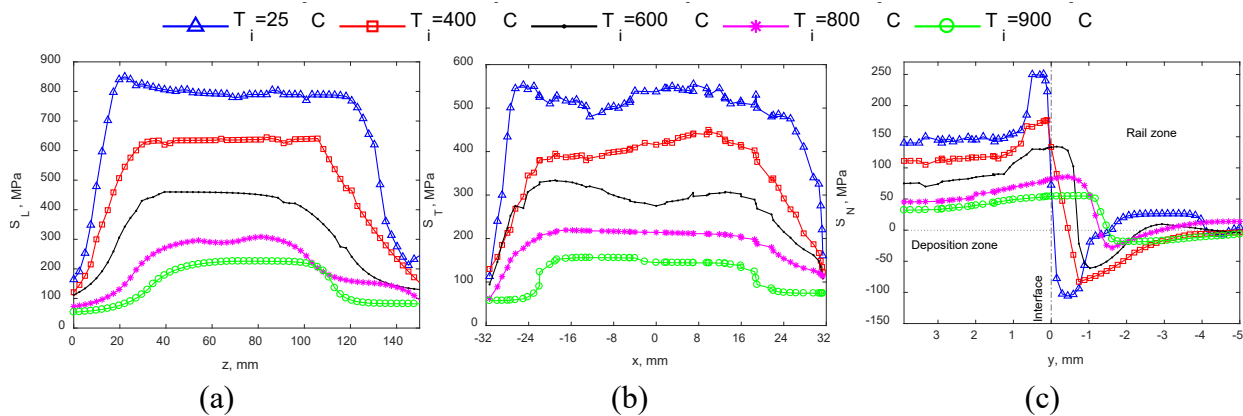


**Fig. 7.3** (a) Longitudinal, (b) transversal, and (c) normal stress distributions for Stellite 6 repaired rail (Case III) along  $x$ ,  $z$ , and  $y$  directions, respectively. (Refer to Sec. 5.1.1, Fig. 1 for configuration of the coordinate system.)

The  $\sigma_n$  diagram of the Stellite 6 repaired rail in Fig. 3c shows a quite uniform distribution in the deposition area for all  $T_i$  values. This consistency is due to the adequately low thermal expansion coefficient of Stellite 6, which minimizes thermal expansion and shrinkage during the deposition process, thereby minimizing the interlayer normal stresses. The lower specific heat is another effective parameter that causes all of the layers to cool down slowly enough not to cause any considerable increase in the stress on the upper layers. Sec. 6.1.3, Table 2 shows that the average thermal expansion coefficient of Stellite 6 is reduced by 12% and 33% compared to those for 410L and 304L, respectively, and the specific heat of Stellite 6 is, on average, lower than that for 410L and 304L by 13% and 29%, respectively. For  $T_i = 25^\circ\text{C}$ , despite the desirable  $\sigma_n$  distribution in the deposition area, an increase in  $\sigma_n$  occurs near the rail-deposition interface at  $y = 0.20$  mm, where the maximum tensile stress of 263 MPa is reached. Afterwards,  $\sigma_n$  experiences a sudden and significantly sharp diversion from tensile to compressive mode, until reaches the maximum

compressive stress of -143.7 MPa in the rail zone at  $y = -0.44$  mm. This extremely sharp  $\sigma_n$  gradient, which exists at the rail-deposition interface, would tremendously increase the risk of separating the deposition layer.

Based on the  $\sigma_n$  results in Fig. 3c, the advantageous effects of preheating are: 1) it essentially decreases the maximum tensile value, with a roughly 30% reduction by each increase in  $T_i$ ; 2) the location of the maximum tensile stress is shifted gradually downwards to the rail zone, until it reaches  $y = -0.74$  mm for  $T_i = 900^\circ\text{C}$ ; the HAZ also broadens along with this shifting, a phenomenon that eliminates any threat of failure in the deposition layers due to the high tensile amounts of  $\sigma_n$ ; 3) the  $\sigma_n$  gradient at the rail-deposition interface is decreased substantially by raising  $T_i$ , thereby effectively decreasing the risk of delamination.

#### 7.1.4. Case IV

The graphs in Fig. 4 illustrate the residual stress distribution in Stellite 21 repaired rail. A general comparison between the diagrams of Figs. 3 and 4 provides clear evidence that the distribution patterns of  $\sigma_l$ ,  $\sigma_t$ , and  $\sigma_n$  between Cases III and IV are fairly similar. Moreover, the average  $\sigma_l$ ,  $\sigma_t$ , and  $\sigma_n$  values of Case IV are 7%, 5%, and 4% higher than those for Case III. There are two justifications for such a close stress distribution: 1) it was described in Sec. 6.1.2 about how the microstructures of these two Co-based alloys are similar, which subsequently makes their defined kinetic models, and the corresponding developed equations, reasonably alike and 2) according to the data given in Sec. 6.1.3, Table 2, the predominant factors that affect the residual thermal stress, i.e., yield strength,  $Y_s$ , thermal expansion coefficient,  $\alpha$ , and specific heat,  $c_p$ , of Stellite 21 are, on average, 4% higher, 6% lower, and 4% lower than those for Stellite 6, respectively. However, even though the Stellite 21 material properties deviate insignificantly from those of Stellite 6, the higher value of  $Y_s$  and the lower values of  $\alpha$  and  $c_p$  still give the Stellite 21 repaired rail a higher, but smoother, stress distribution, although it does so to a limited extent.

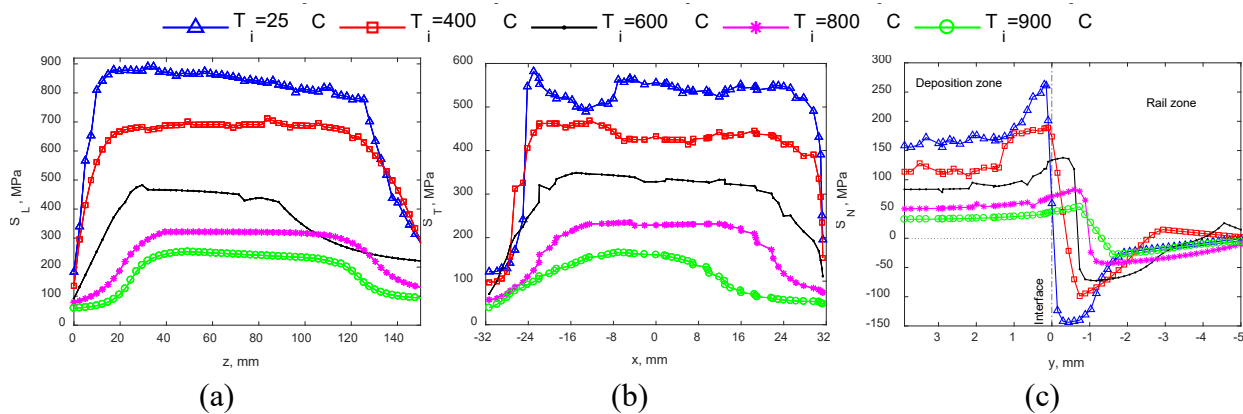


**Fig. 7.4** (a) Longitudinal, (b) transversal, and (c) normal stress distributions for Stellite 21 repaired rail (Case IV) along  $x$ ,  $z$ , and  $y$  directions, respectively. (Refer to Sec. 5.1.1, Fig. 1 for configuration of the coordinate system.)

## 7.2. Optimum preheating temperature and deposition alloy

All four studied cases in Sec. 7.1 for LPD-repair of light rail confirmed the positive effect of preheating on reducing and smoothing residual thermal stresses. Even so, on one hand, the experimental study of Fang et al. [1] showed that preheating to temperatures beyond 600°C would be either impractical or unjustifiably expensive, and on the other hand, Roy et al. [2] determined that preheating to temperatures below 400°C is insufficient to achieve the desired properties. Thus, preheating to 600°C would be the most optimum and realistic preheating approach. Therefore, hereafter, the residual stress results of the studied cases will be compared only based on the preheating condition of  $T_i = 600^\circ\text{C}$ .

Fig. 5 shows the residual stress distributions for different deposition materials at  $T_i = 600^\circ\text{C}$ . A close look at Sec. 6.1.3, Table 2 shows that the deposition materials in order of their yield strength, from the strongest to the weakest, are Stellite 21, Stellite 6, 410L, and 304L. As was discussed in Sec. 6.1.2, Stellite 6 and Stellite 21 have quite similar strengths. Therefore, Fig. 5 shows that Stellite alloys carry sensibly higher residual stresses than the stainless steels. Although Stellite 6 carries higher residual stresses at some local intervals of the measuring paths, the Stellite 21 generally contains the highest residual thermal stress in all three directions.

However, the magnitude of the residual stress is not the only decisive factor to determine the repaired rail's susceptibility to cracking and delaminating; the yield strength of the deposition alloy at room temperature is a second factor, and it is as critical as the first factor. Thus, to analyze the risk of the crack propagation and the layer separation for different cases with different deposition alloys, a new parameter, referred to as "normalized residual stress", is defined as the ratio of the residual stress to the room-temperature yield strength of the corresponding deposition material [3-5].

Fig. 6 gives the normalized residual stress distribution for different deposition alloys at  $T_i = 600^\circ\text{C}$ . Fig. 6a shows that Stellite 21 and 304L generally carry lower normalized  $\sigma_1$  than the other two alloys. Meticulously, although the overall normalized  $\sigma_1$  of both the 304L and Stellite 21 are almost equal ( $\sim 0.61$ ), Stellite 21 still gives a more uniform distribution. Hence, based only on normalized  $\sigma_1$  results, Stellite 21 would be picked as the final candidate material because it has the least and most uniform normalized longitudinal stress.

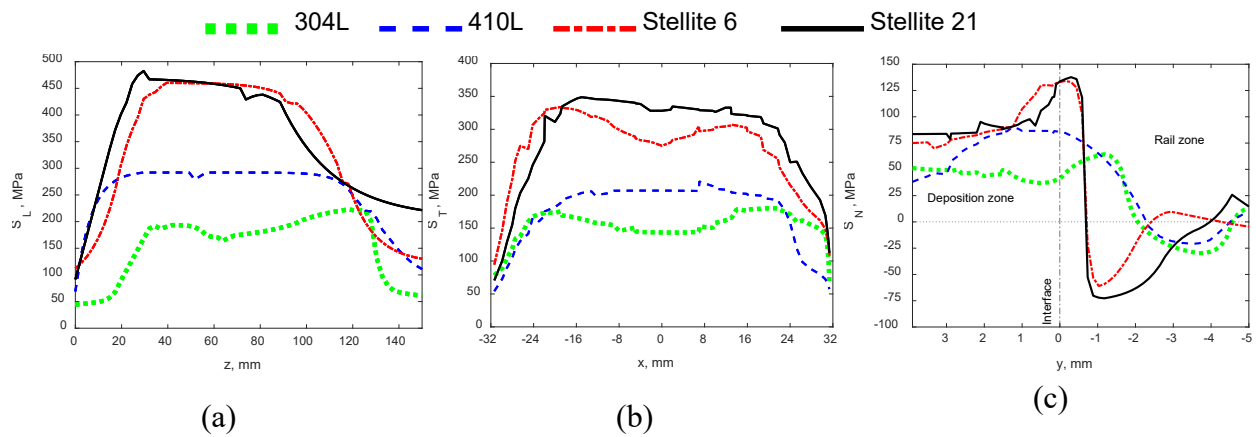




**Fig. 7.5** (a) Longitudinal, (b) transversal, and (c) normal stress distributions along x, z, and y directions, respectively, for the repaired rails with different deposition alloys at the preheating temperature of 600°C. (Refer to Sec. 5.1.1, Fig. 1 for configuration of the coordinate system.)

Regarding normalized  $\sigma_t$  (Fig. 6b), 410L and Stellite 21 contain the minimum average magnitudes of  $\sim 0.49$ . Even concerning uniformity, both 410L and Stellite 21 maintain the same normalized  $\sigma_t$  distribution pattern all along its measuring path. Therefore, if the final decision were made based only on the normalized  $\sigma_t$  results, one could say that 410L and Stellite 21 have the minimum normalized stress and, therefore, are the most compatible materials for repairing rails.

Normalization of  $\sigma_n$  is done by dividing the  $\sigma_n$  values in the deposition area and in the rail area by the average room-temperature yield strength of the deposition material and rail material, respectively. Therefore, Fig. 6c shows that there is a sudden increase towards the rail zone in the normalized  $\sigma_n$  graphs at the rail-deposition interface. The sharpness of this increased gradient and the risk of the deposition layer separation are directly correlated. Thus, in Fig. 6c, if one compares the increased gradient of different graphs at the rail-deposition interface, the likelihood of delamination, from the highest to the lowest, would be 410L, 304L, Stellite 21, and Stellite 6. Concerning the normalized  $\sigma_n$  values, Stellite 6 and Stellite 21 carry more tensile stress in the deposition zone than 304L and 410L. However, at the same time, Stellite alloys experience a higher maximum compressive stress in the rail zone than the stainless steel alloys. In addition, Stellite 21 remains compressive down to the depth of  $y = -3.8$  mm, whereas Stellite 6 switches to tensile sooner at  $y = -2.3$  mm. Hence, in a discussion solely depending on normalized  $\sigma_n$  diagrams, while Stellite 6 gives the lowest risk of delamination, Stellite 21 leads to the longest fatigue life due to the highest and broadest compressive stress distribution.

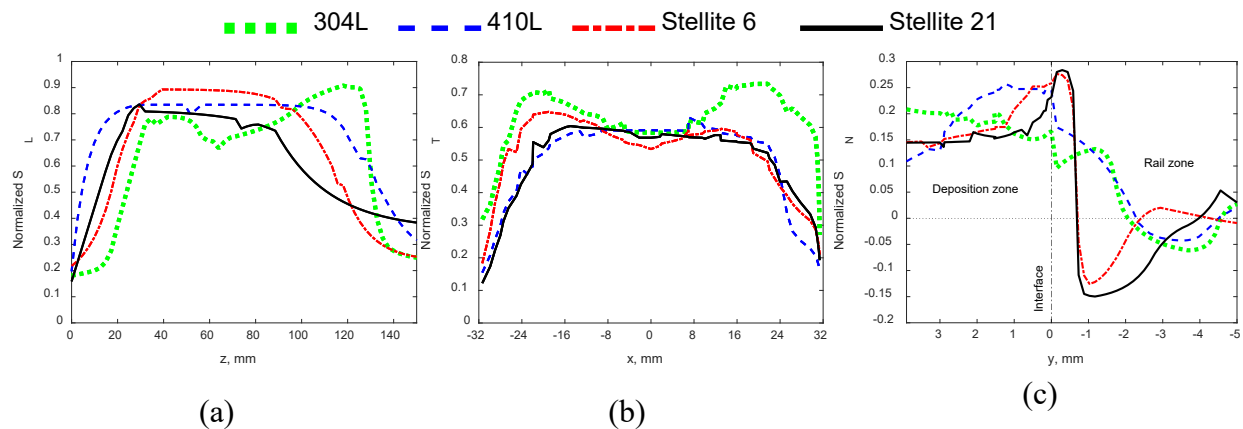


**Fig. 7.6** Normalized (a) longitudinal, (b) transversal, and (c) normal stress distributions along x, z, and y directions, respectively, for the repaired rails with different deposition alloys at the preheating temperature of 600°C. (Refer to Sec. 5.1.1, Fig. 1 for configuration of the coordinate system.)

Even though some deposition materials exhibited acceptable performance in a single normalized stress direction, the material that was recommended in all three stress analyses due to its favorable performance was Stellite 21. The lowest normalized  $\sigma_l$  and  $\sigma_t$  magnitudes in Stellite 21 promise the lowest chance of the crack propagation along the longitudinal and transversal directions at the



rail-deposition interface. Also, it was shown that Stellite 21 offers a reduced likelihood of delamination, as well as the longest fatigue life to the repaired rail. Thus, the calculations in the current study indicate that Stellite 21 is the most promising deposition material for repairing a 75-lb standard U.S. light rail with a preheating temperature of 600°C. A lab-scale experimental investigation on a Stellite 21 repaired rail also is recommended as the next phase of a feasibility study in order to examine the microstructure regarding the phase and micro-cracks distribution.

## References for Chapter 7

- [1] J.X. Fang, S.B. Li, S.Y. Dong, Y.J. Wang, H.S. Huang, Y.L. Jiang, B. Liu, Effects of phase transition temperature and preheating on residual stress in multi-pass & multi-layer laser metal deposition, *J. Alloys Compd.* 792 (2019) 928-937.  
<https://doi.org/10.1016/j.jallcom.2019.04.104>.
- [2] T. Roy, Q. Lai, R. Abrahams, P. Mutton, A. Paradowska, M. Soodi, W. Yan, Effect of deposition material and heat treatment on wear and rolling contact fatigue of laser clad rails, *Wear* 412–413 (2018) 69–81. <https://doi.org/10.1016/J.WEAR.2018.07.001>.
- [3] T. Mukherjee, W. Zhang, T. DebRoy, An improved prediction of residual stresses and distortion in additive manufacturing, *Comput. Mater. Sci.* 126 (2017) 360-372.  
<https://doi.org/10.1016/j.commatsci.2016.10.003>.
- [4] S.C. Cao, A.X.Y. Guo, A novel multiple impact model for predicting the residual stress state, *SSRN* (2022). <https://dx.doi.org/10.2139/ssrn.4102984>.
- [5] G. Peng, Z. Lu, Y. Ma, Y. Feng, Y. Huan, T. Zhang, Spherical indentation method for estimating equibiaxial residual stress and elastic–plastic properties of metals simultaneously, *J. Mater. Res.* 33(8) (2018) 884-897.  
<https://dx.doi.org/10.1557/jmr.2018.57>.

## 8. Chapter 8 FLEXURAL AND SHEAR STRENGTH EVALUATION

### 8.1. Flexural evaluation of the weld materials in SAW-repaired heavy rail

#### 8.1.1. Calculation of flexural and shear stress

Extraction of the bending specimen from the weld materials was described in detail in Sec. 2.3. Putting the sample under bending using the bending test machine, the force-displacement diagram is instantly extracted from the connected computer and shown in Fig. 1.

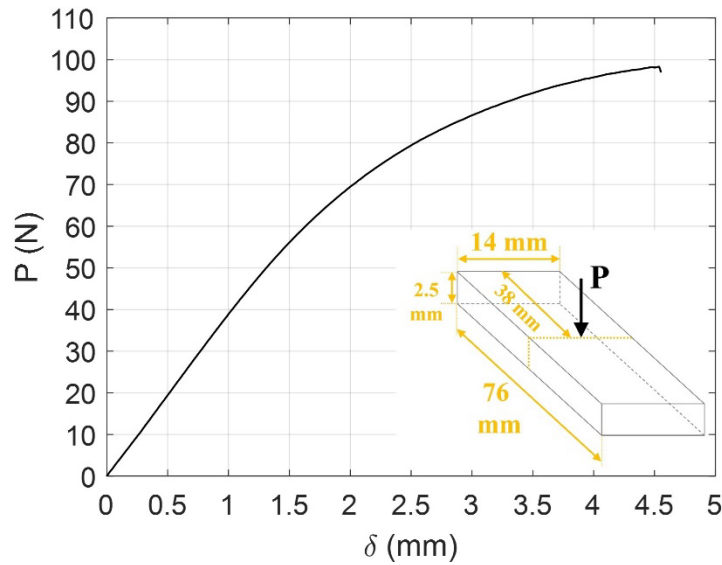


**Fig. 8.1** Force ( $P$ ) – displacement ( $\delta$ ) diagram extracted instantly from 3-point bending test of the thin specimen extracted from the weld materials of the SAW-repaired heavy rail.

To figure out the stress-strain diagram, the force and displacement data need to be transformed to the stress and strain data, respectively. The general scheme of the 3-point bending test setup is shown in Fig. 2. For the current case study of the thin sample,  $L = 76$  mm,  $b = 14$  mm, and  $h = 2.5$  mm (see Sec. 2.3, Fig. 6b for configuration of the dimensions).

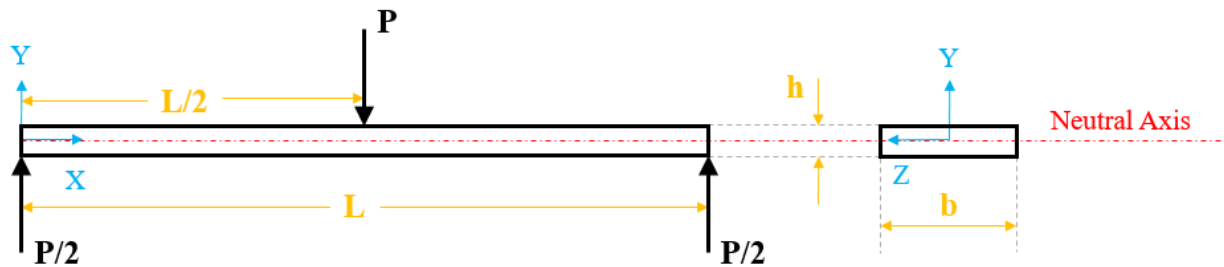


**Fig. 8.2** Schematic depiction of the 3-point bending test on the thin specimen extracted from weld materials.

When the P load is applied, the bending stress at the neutral axis is zero. It is seen in Fig. 2 that the neutral axis is located at the middle of the sample cross section, i.e., at a distance of  $h/2$  from the top surface and  $h/2$  from the bottom surface of the sample. Maximum compressive stress occurs at the top surface of the sample ( $y = h/2$  in Fig. 2) and maximum tensile takes place at the bottom surface ( $y = -h/2$  in Fig. 2). A stress distribution contour is shown in Fig. 3 for better clarification.

To calculate the applied maximum stress for any amount of the applied load, the moment and shear distribution in the specimen for any given load of P needs to be expressed. Based on the study by Sideridis and Papadopoulos [1], the maximum shear and bending in a 3-point bending test take place at the center, where the load is applied, with the following values:

$$V_{max} = \frac{P}{2} \quad (1)$$

$$M_{max} = \frac{PL}{4} \quad (2)$$

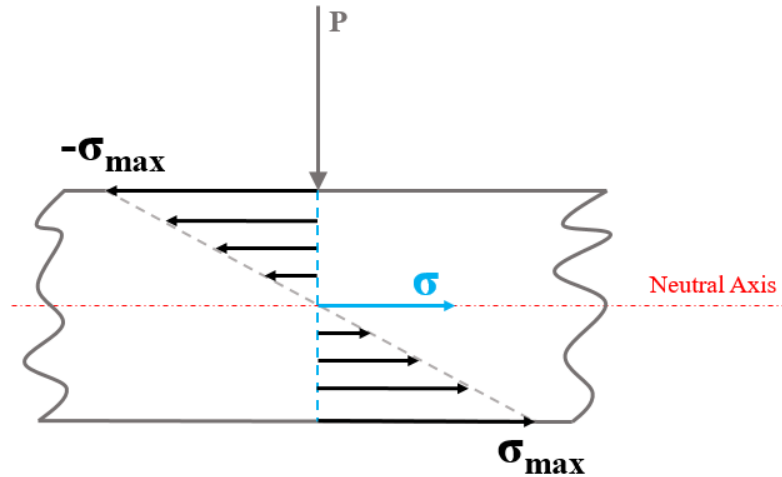


**Fig. 8.3** Bending stress distribution at the location of the applied 3-point bending test.

where  $V_{max}$  is the maximum shear force,  $M_{max}$  is the maximum moment, P is the applied force, and L is the distance between the two supports, which, here, is equal to 76 mm (refer to Sec. 2.3, Fig. 6b). Fig. 4 shows the shear and moment diagrams.

According to [1], the maximum bending stress,  $\sigma_{max}$ , is calculated using the following equation:

$$\sigma_{max} = \frac{M_{max}C}{I} \quad (3)$$

where  $M_{max}$  is expressed in Eq. 2, C is the distance from the neutral axis to the top/bottom surface, and I is the sample's moment of inertia. C and I are formulated as:

$$C = \frac{h}{2} \quad (4)$$

$$I = \frac{bh^3}{12} \quad (5)$$

Putting Eqs. 2, 4, and 5 into Eq. 3 results in:

$$\sigma_{max} = \frac{3PL}{2bh^2} \quad (6).$$

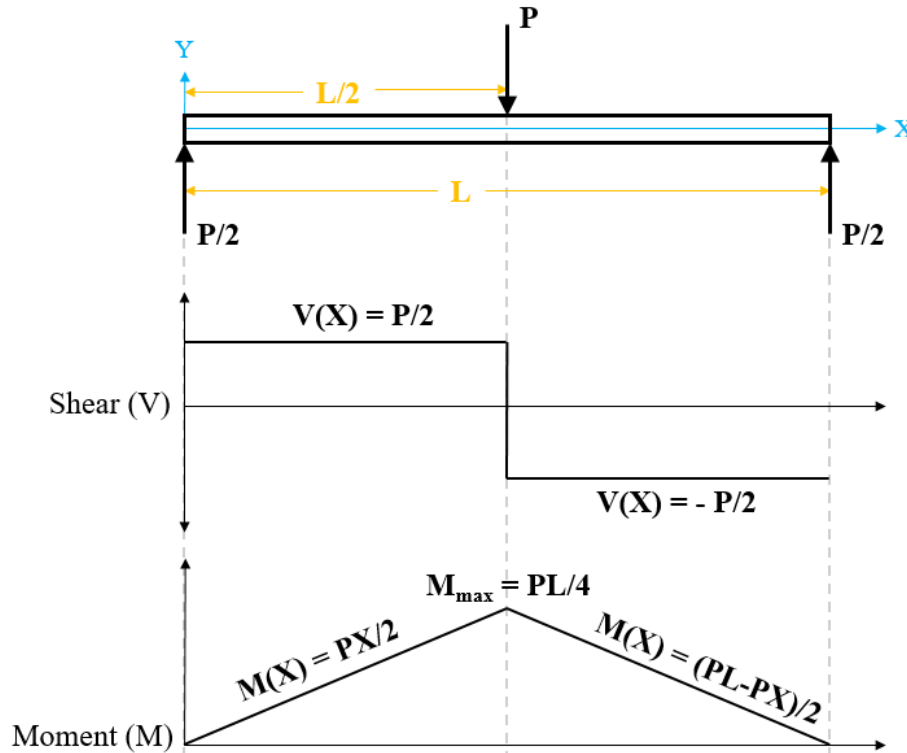


**Fig. 8.4** Shear and moment diagrams for the sample under bending load in 3-point bending test.

The shear force ( $V$ ), results in shear stress, i.e.,  $\tau_{xy}$ , which acts vertically, parallel to the cross section along the  $y$  direction. The average shear stress acting on the cross section could be calculated as the shear force ( $V$ ) divided by the cross-sectional area ( $A$ ). However, the shear stresses, as the shear flow pattern is shown in Fig. 5, are not distributed uniformly across the cross section of the specimen. As it can be seen in Fig. 5, the shear stress starts at zero at the free top/bottom surfaces, and reaches to its maximum value at the neutral axis. Therefore, as the average shear stress does not reflect the maximum or minimum shear stress, it is not very useful. Instead, the following equation can be used to calculate the shear stress at the cross section:

$$\tau_{xy} = \frac{VQ}{Ib} \quad (7)$$

where  $V$  is the applied shear force,  $Q$  is the first moment of area,  $I$  is the moment of inertia, and  $b$  is the width of the cross section. Derivation of this equation is given in [1] and will not be covered here. It should only be noted that it is based on considering equilibrium of stresses acting on small elements within the specimen. The Eq. 7 assumes that the shear stress is constant across the width, i.e.,  $b$ , of the cross section, and hence the shear stress is a function of the distance along the

specimen, i.e.,  $x$ , and the distance from the neutral axis, i.e.,  $y$  (refer to Fig. 2 for configuration of the coordinate system and the parameters).

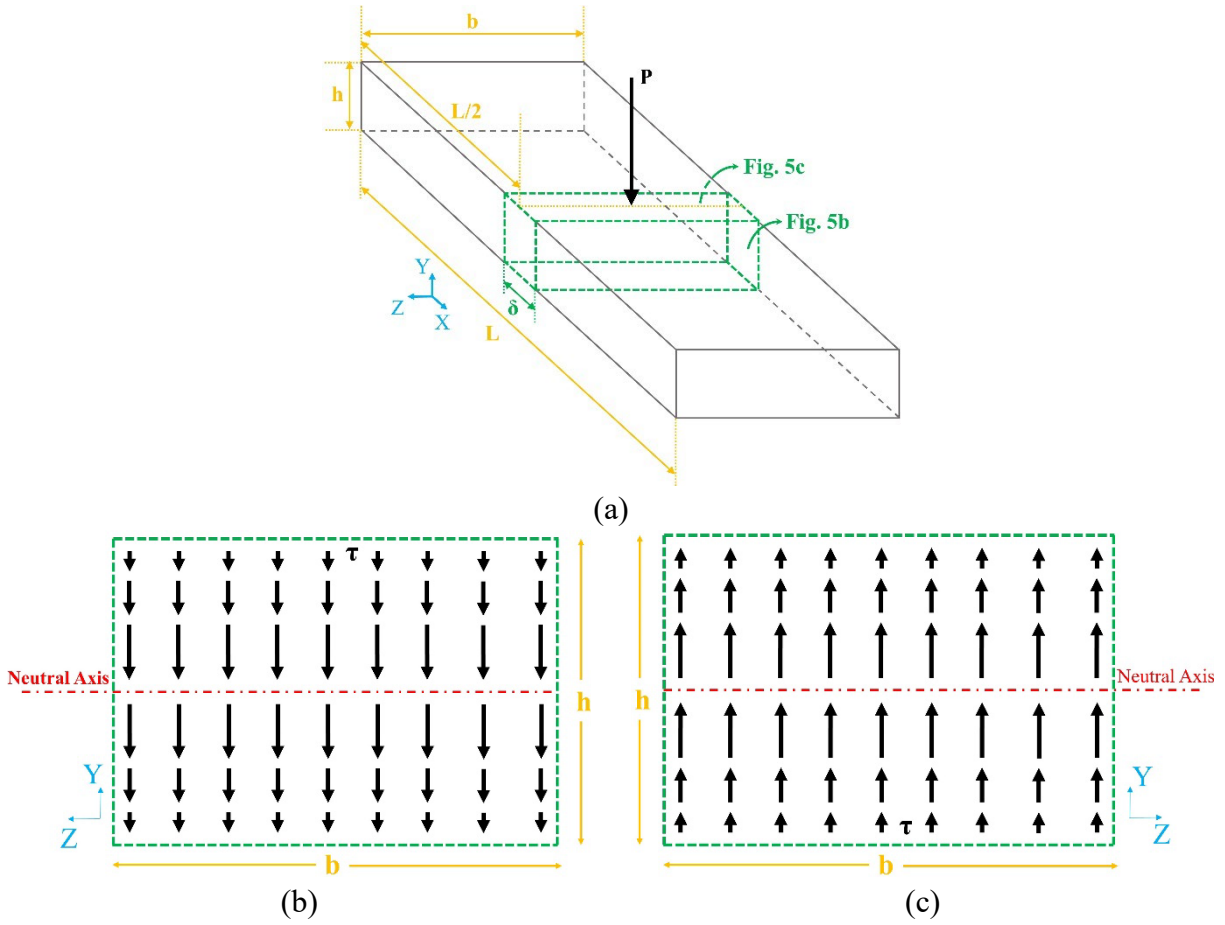


**Fig. 8.5** Shear flow diagram at the cross section of the thin bending specimen shown in Fig. 2.

The  $Q$  parameter in Eq. 7 is the first moment of area and is equal to:

$$Q = \frac{b}{2} \left( \frac{h^2}{4} - y^2 \right) \quad (8)$$

Therefore, at the neutral axis ( $y = 0$ ), where the maximum shear occurs, the  $Q$  is calculated as:

$$Q = \frac{bh^2}{8} \quad (9)$$

Putting Eqs. 1, 5, and 9 into Eq. 7, the maximum shear stress for any given load of  $P$  is:

$$\tau_{max} = \frac{3P}{4bh} \quad (10)$$

Further, calculation of strain based on the collected displacement data ( $\delta$ ) is carried out using the following equation:

$$\varepsilon = \frac{6\delta h}{L^2} \quad (11)$$

of which the derivation can be found in [1].

The extracted force-displacement data in Fig. 1 can now be transformed to stress-strain data. The force data ( $P$ ) are transformed to stress data ( $\sigma$ ) using Eq. 6 and considering that  $L = 76$  mm,  $b = 14$  mm, and  $h = 2.5$  mm (refer to Sec. 2.3, Fig. 6b for configuration of the dimensions). The displacement data ( $\delta$ ) are transformed to strain data ( $\varepsilon$ ) using Eq. 11 and considering that  $h = 2.5$  mm and  $L = 76$  mm. The stress-strain diagram is plotted in Fig. 6. It has to be noted that the acquired force-displacement data in Fig. 1 and the stress-strain data in Fig. 6 are taken from the bottom surface of the bending sample, i.e., the surface that is in tension during the 3-point bending test.

Referring to Fig. 6, the slope of the elastic region gives the Young's modulus of the weld material. Therefore, the modulus of elasticity of the weld materials is  $E = 196$  MPa. Using the 0.2%-offset method, where a line parallel with the elastic region is drawn starting from  $\varepsilon = 0.002$  mm/mm to intersect with the stress-strain diagram, the yield strength can be figured out. In this way, the stress-strain diagram in Fig. 6 gives the yield strength of the weld material as  $S_y = 53$  MPa. According to the developed standards by AREMA [2], a standard 136RE heavy rail should have a minimum yield strength of 300 MPa. Hence, for the SAW-repaired heavy rail, the yield strength ( $S_y$ ) is below the minimum requirement by AREMA, and it is concluded that the repaired rail will fail under the dynamic load of the train. The minimum yield strength of a light 75-lb/yd is 210 MPa [2], which is also above the material yield strength of the current weld tested.

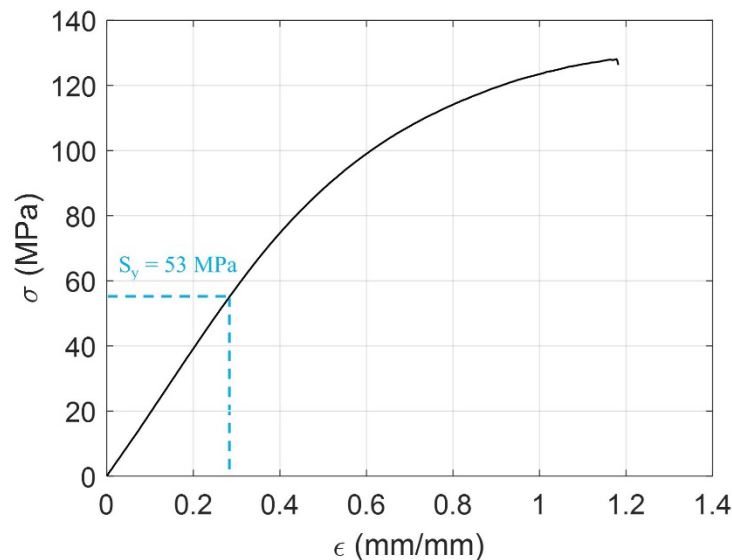




**Fig. 8.6** The resultant stress-strain diagram from the 3-point bending test of the thin specimen extracted from the weld materials of the SAW-repaired heavy rail. The related force-displacement diagram is given in Fig. 1.

This kind of interpretation of the results is only valid if the sample is failed only due to bending and not shear. Calculating the shear stress at the breakage point using Eq. 10 gives  $\tau_f = 2$  MPa which is very low value compared to the flexural failure stress, i.e., 126 MPa. However, it does not guarantee that the sample did not undergo any shear failure. To carry out the better analysis the broken cross sections of the bending sample are examined using SEM.

Another important factor that is to be analyzed, is the maximum elongation percentage of the specimen at the time of failure. During the 3-point bending test, the bending sample is deflected by an amount of  $\delta$ , as shown in Fig. 7. The initial length of the sample is  $L$ , where the distance between one of the supports to the point of load is  $L/2$ , as seen in Fig. 7. Therefore, the final length of the deflected sample,  $L_2$ , can be estimated following the Pythagorean theorem:

$$L_2/2 = \sqrt{(L/2)^2 + \delta^2} \quad (12)$$

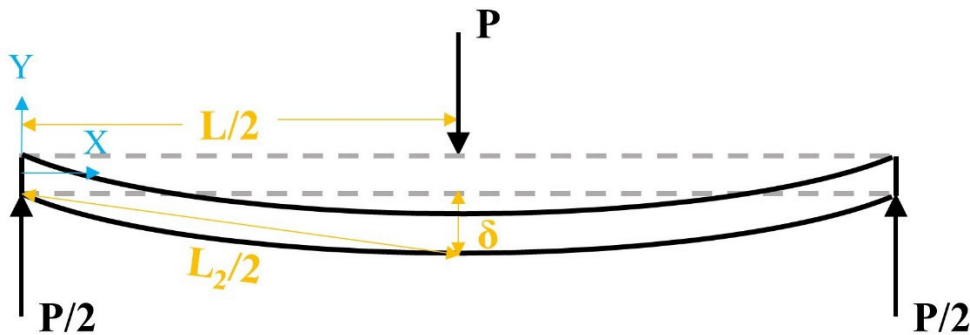


**Fig. 8.7** A schematic view of the deflected thin bending specimen.

Therefore, the percentage of the sample elongation can be calculated as follows:

$$Elongation \% = \frac{L_2/2 - L/2}{L/2} \times 100 = \frac{L_2 - L}{L} \times 100 \quad (13)$$

Therefore, for the bending sample with the initial length of  $L = 76$  mm and maximum deflection of  $\delta = 4.55$  mm, the specimen is elongated 0.71% with the final length of  $L_2 = 76.54$  mm at the time of failure. The elongation is much lower than 5%, which means that the specimen has gone through a brittle failure and the cracks started to propagated at the early stages of deflection.

### 8.1.2. Failure mode analysis

The fracture surface of the bending specimen is examined by SEM to help clarify and discuss the possible failure mode occurred during the 3-point bending test. Fig. 8 illustrates a clear observation

of the fracture surface.

In Fig. 8a, the fracture surface can generally be divided into two regions; the lower region that was under tensile during the 3-point bending test, and the upper region that was under compression during bending. A closer look at the fracture surface in Fig. 8b shows that the light vertical cleavage signs initiate from the lower region, continue to somehow upper than the middle, but do not reach all way to the top. As observable in Fig. 8b, the upper region lacks those cleavage signs; this is probably due to the fact that no fracture has been initiated from the upper region. Besides, looking at the border around the fracture surface in Fig. 8a, the lower horizontal borderline along with the lower section of the right vertical borderline are appeared lighter than the other sections of the borderlines. This, again, confirms the idea of initiation of failure from the lower region, i.e., tensile region. As the compression region mostly lacks any sign of cleavage, there is a rare chance that shear had any part in the fracture of the specimen during 3-point bending test.

It can also be inferred from Fig. 8 that the neutral axis has not been perfectly located in the middle; it has shifted a little bit towards the top surface. This interpretation is because the cleavages are started from the bottom surface and extended to upper than the middle of the fracture surface.

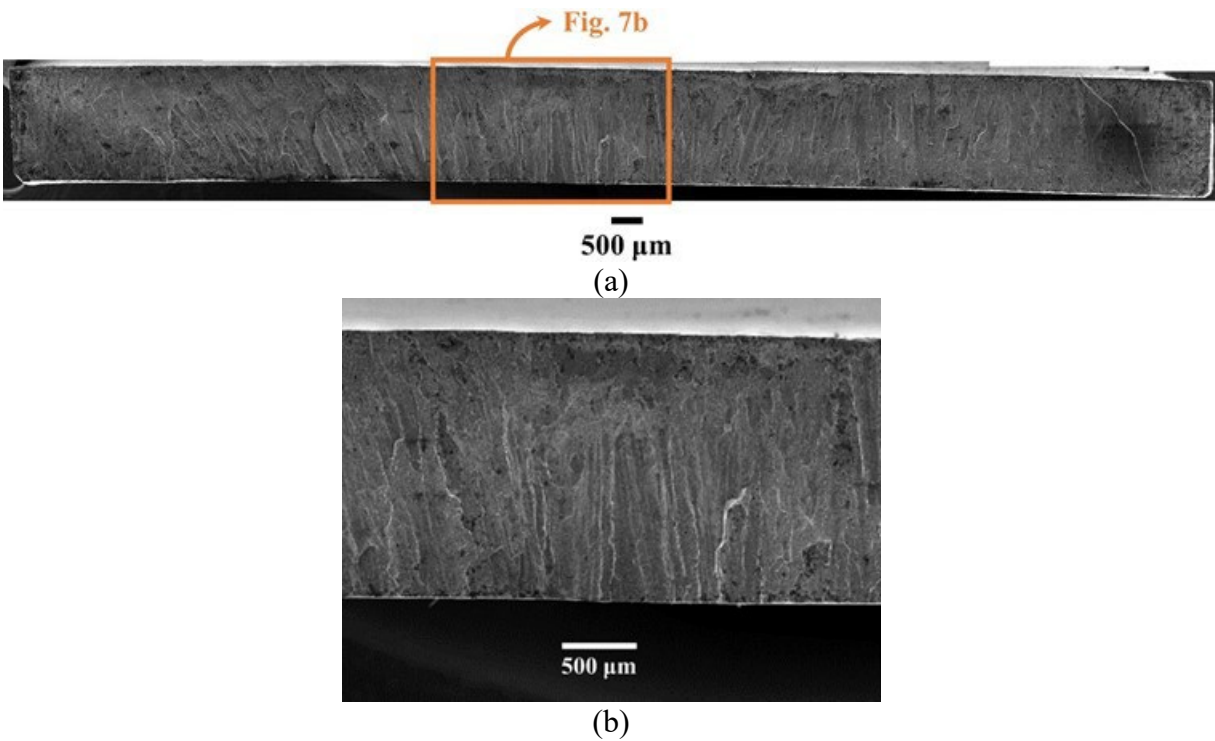


**Fig. 8.8** SEM macrograph from the fracture surface of the 3-point bending specimen; (a) an overall view from the whole fracture surface and (b) a closer view to the surface.

Another visible phenomenon in the fracture surface shown in Fig. 8 are the numerous small and large black-colored sites that might be micro-pores as a result of defective welding, dimples as a result of flexural failure in 3-point bending test, or carbon-concentrated lands due to the inconsistent chemical distribution. To discuss this issue, some of those black islands are scanned using EDS. These typical captured sites along with their corresponding chemical composition are

presented in Fig. 9.

The scanned region in Fig. 9e is a typical region with no special signs of black spots or cleavage. This region represents a regular region that most probably presents the regular chemical composition of the weld materials.

On one hand, comparing Figs. 9c and 9g to Fig. 9e shows a quite close chemical composition; although carbon content in Fig. 9g is slightly higher than that for Fig. 9e, they still fairly fall in identical category of carbon content interval. This means that those black islands shown in Figs. 9c and 9g do not represent any carbon-intruded area, and they may represent a dimple or a pore as microstructural deficiency in the weld. Comparing the oxygen content of Fig. 9e against Figs. 9c and 9g, it is seen that the scanned areas of Figs. 9c and 9g contain considerably higher fraction of oxygen than the regular, i.e., than that of Fig. 9e. This strengthens the idea that the black lands in Figs. 9c and 9g are actually representing a pore with some amount of entrapped air.

On the other hand, it is evident that those studied black islands in Figs. 9b, 9d, and 9f have a quite higher carbon concentration than the regular expectation, i.e., the 5.3 wt.% in Fig. 9e. Besides, their oxygen content is fairly close to the regular fraction, i.e., the 2.6 wt.% in Fig. 9e, which almost rejects the hypothesis that these spots might be an air-entrapped pore. Hence, it is inferred that the visible black spots in Figs. 9b, 9d, and 9f show a carbon-concentrated area, and there is a rare chance that they are the signs of some kind of dimple or pore.

All such discovered inconsistencies, i.e., the inconsistent chemical distribution and the micro-pore in the microstructure of the sample, can contribute in shifting the neutral axis from the middle axis towards the top or bottom surface; the fact that was described earlier and is visible in Fig. 8b. Also, the such a low measured yield strength (53 MPa) of the sample as an output of the 3-point bending test is most probably due to all those deficiencies, i.e., the chemical inconsistency and the pores. These deficiencies could lead to the premature failure of the bending specimen. It was found in Sec. 4.2.1 that the weld materials of the SAW-repaired heavy rail have a high hardness in the range of 50 to 60 HRC. Based on the developed relationships by Juvinall and Marshek [6] for estimating the strength properties of a steel from its hardness, the yield strength of a steel can be estimated through the measured hardness using the following equation:

$$S_y = 3.62H_B - 206.84 \text{ MPa} \quad (14)$$

where  $S_y$  is the yield strength and  $H_B$  is the Brinell hardness number. Using the measured hardness data in Se. 4.2.1 and estimating the yield strength using Eq. 14, Table 1 is developed.

**Table 16** Estimation of the yield strength of the weld materials of the SAW-repaired rail based on the measured hardness data using the developed relationship by Juvinall and Marshek [6], i.e., Eq. 14.

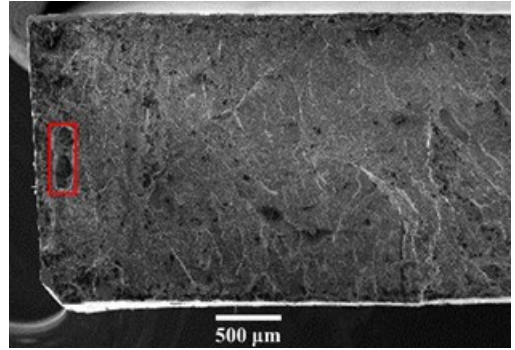
Brinell hardness number ( $H_B$ )	Yield strength, $S_y$ (MPa)
187	469

175	427
198	511
205	535
218	582
223	602
218	582
223	602
211	558
218	582
218	582
223	602
218	582
223	602

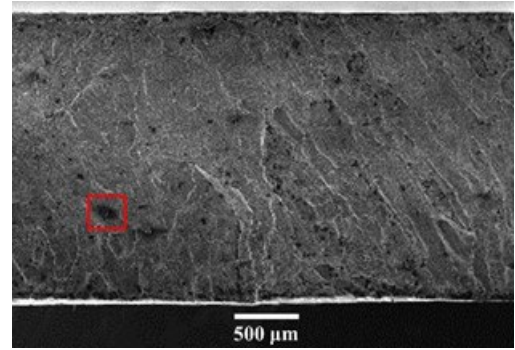
Based on the acquired data in Table 1, it is seen that such a hard weld material should have a yield strength in the order to 500-600 MPa. Therefore, such a low yield strength of the bending specimen (53 MPa) is definitely due to the existing deficiencies in the weld.



500 μm  
(a)



(b)



(c)

Fe	C	Cr	Mn	Si	O	Fe	C	Cr	Mn	Si	O
Bal.	27.4	2.0	1.6	1.4	1.2	Bal.	6.4	2.3	2.1	4.61	14.3

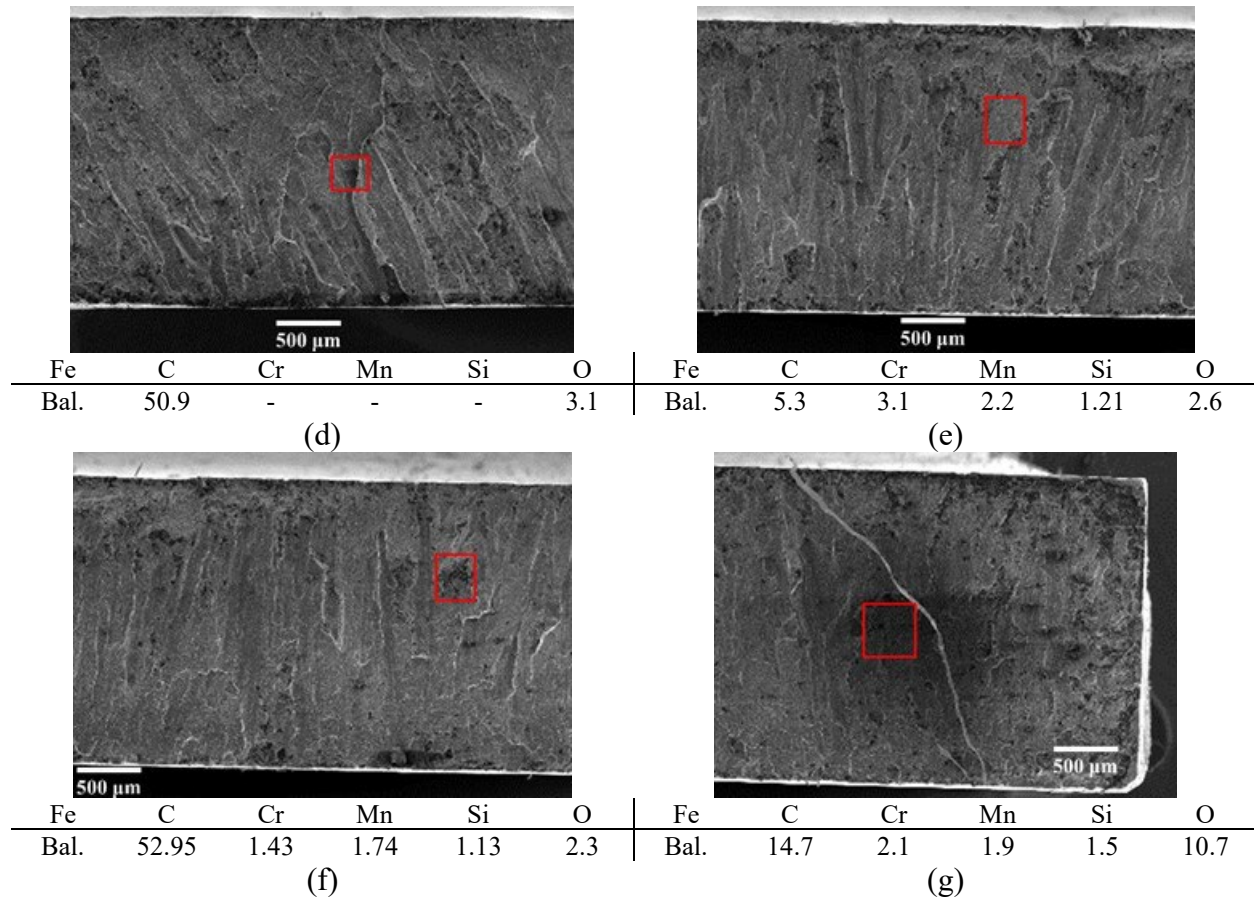


**Fig. 8.9** EDS scan analysis of different locations of the fracture surface of the bending specimen to figure out the nature of the observable black islands based on their chemical composition (each chemical element is represented by its wt.%).

## 8.2. Flexural evaluation at the rail-weld interface in SAW-repaired heavy rail

### 8.2.1. Calculation of flexural and shear stress

Extraction of the bending specimen from the rail-weld interface was described in detail in Sec. 2.3. The sample is put under bending using the bending test machine in a way that the bending load is applied to the rail side, i.e., the rail side is at the top and mostly under compression, and the weld side is at the bottom and under tensile. The force-displacement diagram is instantly extracted from the connected computer and shown in Fig. 10.

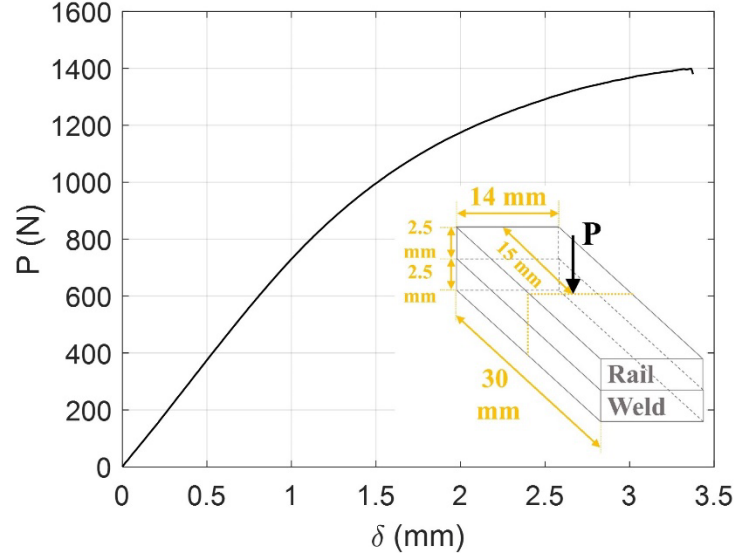


**Fig. 8.10** Force (P) – displacement ( $\delta$ ) diagram extracted instantly from 3-point bending test of the thick specimen extracted from the rail-weld interface of the SAW-repaired heavy rail.

The general load setup is like the previous case discussed in Sec. 8.1.1 for the weld sample and shown in Fig. 2, except that the current case is a composite sample, containing rail and weld materials, and hence it should not be assumed in the calculation that the neutral axis will be located exactly at the middle of the cross section. Therefore, Eq. 6, that was presented for a bending specimen with homogeneous material, will not work for the current case. In the rail-weld-interface sample, the mechanical properties between the rail and the weld materials differ, which means that Eq. 6 should be modified.

According to the study by Deng et al. [3], to take into account the plastic deformation in a 3-point bending strength, the typical Eq. 6 needs to be multiplied by a modification factor. According to Deng's recommendation in [3], the following modification factor is good to be considered for the hardfacing steels:

$$\sigma_f = 0.8 \times \left(1 - \frac{4h}{3\pi L}\right) \times \left(\frac{3PL}{2bh^2}\right) \quad (15).$$

For the current specimen that is made of two materials, the tensile/compressive stress determination method needs modification [4]. The offset of the neutral axis from the middle plane, i.e., from the rail-weld interface, needs to be determined. This shifting of the neutral axis ( $d_{NA}$ ) is illustrated graphically in Fig. 11 for a better clarification.

At the cross section of the specimen during bending, the resultant force should be zero. This fact can be expressed as:

$$\int \sigma_t ds = \int \sigma_c ds \quad (16)$$



where  $\sigma_t$  is the tensile normal stress, and  $\sigma_c$  is the compressive normal stress. The normal stress is generally defined as follows:

$$\sigma = \frac{Ey}{r} \quad (17)$$

with  $E$  as the modulus of elasticity,  $y$  the distance from the neutral axis, and  $r$  the neutral axis curvature. Combining Eqs. 16 and 17 results in:

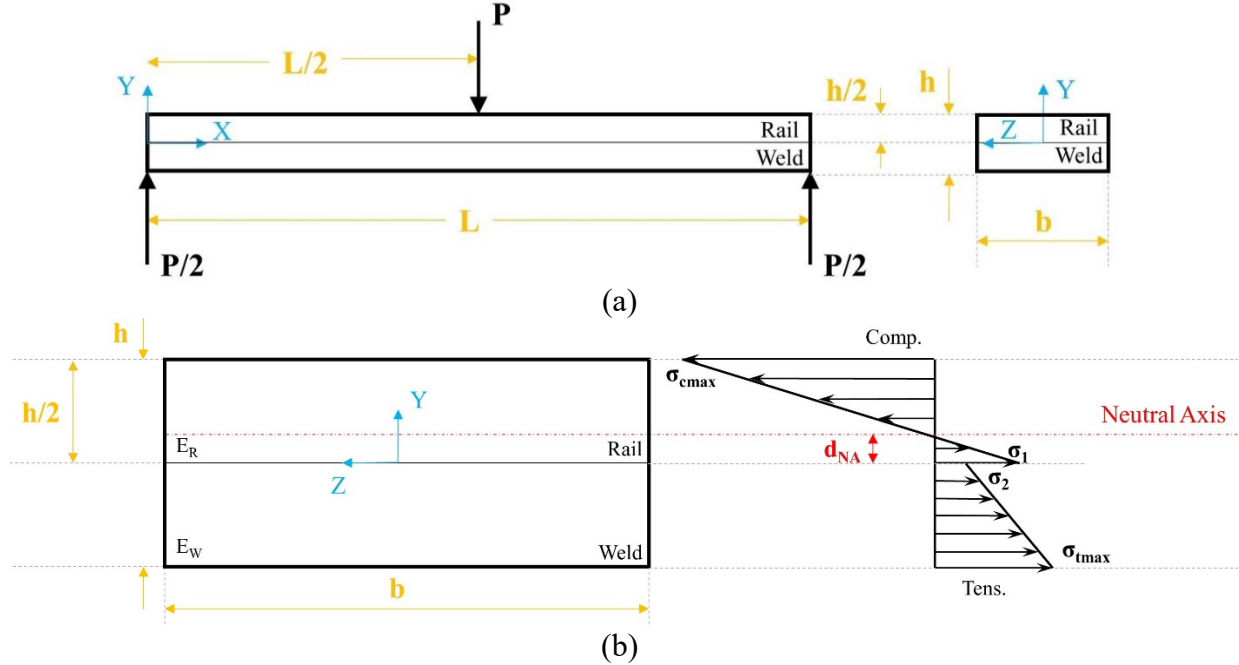


**Fig. 8.11** (a) Schematic depiction of the 3-point bending test on the thick specimen extracted from rail-weld interface, and (b) a closer look at the cross section of the specimen in Y-Z plane.

$$\frac{E_R}{2r} \times \left(\frac{h}{2} - d_{NA}\right)^2 = \frac{E_R \times d_{NA}^2}{2r} + \frac{h}{4} \times \left(\frac{E_W \times d_{NA}}{r} + \frac{E_W \times (d_{NA} + h/2)}{r}\right) \quad (18)$$

where  $E_R$  and  $E_W$  represent the modulus of elasticity of the rail and the wheel, respectively,  $h$  is the thickness of the thick bending specimen, and  $d_{NA}$  is the distance of the shifted neutral axis from the middle plane (see Fig. 11 for a graphical sense of the parameters). The neutral axis offset ( $d_{NA}$ ) can be derived from Eq. 18 as follows:

$$d_{NA} = \frac{h(E_R - E_W)}{4(E_R + E_W)} \quad (19).$$

For a unit magnitude of the bending force, i.e.,  $P = 1$ , the applied stress at the rail-weld interface in the rail area can be expressed as (see Fig. 11):



$$\sigma_1 = \frac{d_{NA}}{h/2 - d_{NA}} \quad (20)$$

the applied stress at the rail-weld interface in the weld area is (see Fig. 11):

$$\sigma_2 = \frac{E_W d_{NA}}{E_R (h/2 - d_{NA})} \quad (21)$$

and the maximum flexural tensile stress at the bottom surface of the weld is (see Fig. 11):

$$\sigma_{tmax} = \frac{E_W (h/2 + d_{NA})}{E_R (h/2 - d_{NA})} \quad (22).$$

Hence, the resulting moment at the cross-sectional plane of the bending specimen can be formulated as follows (see Fig. 11):

$$\begin{aligned} M_0 &= \int_{d_{NA}}^{h/2} \frac{y}{(h/2 - d_{NA})} b y dy + \int_{-h/2}^{d_{NA}} \frac{E_W}{E_R} \frac{y}{(h/2 - d_{NA})} b y dy \\ &= \frac{b}{3(h/2 - d_{NA})} \left( (h^3/8 - d_{NA}^3) + E_W/E_R (h^3/8 + d_{NA}^3) \right) \end{aligned} \quad (23).$$

Based on what was discussed in Sec. 8.1.1 and shown in Fig. 4, the maximum applied bending in a 3-point bending test is  $PL/4$ . Therefore, the failure flexural tensile stress ( $\sigma_f$ ) is:

$$\sigma_f = \sigma_{tmax} \times \frac{PL/4}{M_0} = \frac{PL}{4} \times \frac{1}{M_0} \times \frac{E_W (h/2 + d_{NA})}{E_R (h/2 - d_{NA})} \quad (24).$$

Combining the modification factor for plastic deformation, that was presented in Eq. 15, with Eq. 24, the failure bending strength is:

$$\sigma = 0.8 \times \left( 1 - \frac{4h}{3\pi L} \right) \times \frac{PL}{4} \times \frac{1}{M_0} \times \frac{E_W (h/2 + d_{NA})}{E_R (h/2 - d_{NA})} \quad (25).$$

As it was shown in Secs. 6.1.3 and 8.1.2, the elastic moduli of the weld and rail materials are  $E_W = 196$  MPa and  $E_R = 210$  MPa, respectively. To provide a strict reference, the elastic moduli of the heavy and light rails, deposited weld materials on the current bending specimen, and the Lincore-40S weld wire are listed in Table 2. As it was described in Sec. 2.3, the thick bending sample extracted from the rail-weld interface has a thickness of  $h = 5$  mm. Putting these parameters into Eq. 19 gives the neutral axis offset equal to  $d_{NA} = 0.04$  mm. Considering that the thick bending specimen has a width of  $b = 14$  mm, from Eq. 23 it can be calculated that  $M_0 = 57.31$  mm<sup>3</sup>. It was illustrated in Sec. 2.3, Fig. 6d that a span length of  $L = 30$  mm is put between the supports. Having all these parameters along with the recorded failure load of  $P = 1398.91$  N in the 3-point bending test of the thick specimen (Fig. 10), the failure bending stress can be calculated using Eq. 25, which is equal to:

$$\sigma_f = 131 \text{ MPa} \quad (26).$$

Now, using Eq. 25, the extracted force-displacement data in Fig. 10 can be transformed to stress-strain data. The displacement data ( $\delta$ ) are transformed to strain data ( $\epsilon$ ) using Eq. 11 and considering that  $h = 2.5 \text{ mm}$  and  $L = 30 \text{ mm}$ . The stress-strain diagram is plotted in Fig. 12. It has to be noted that the acquired force-displacement data in Fig. 10 and the stress-strain data in Fig. 12 are taken from the bottom surface of the bending sample, i.e., the weld surface that is in tension during the 3-point bending test.

Referring to Fig. 12, the slope of the elastic region gives the Young's modulus of the weld material. Therefore, the modulus of elasticity of the weld materials is  $E = 182 \text{ MPa}$ , which is fairly close to the gained Young's modulus from the thin specimen. Using the 0.2%-offset method, where a line parallel with the elastic region is drawn starting from  $\epsilon = 0.002 \text{ mm/mm}$  to intersect with the stress-strain diagram, the yield strength can be figured out. In this way, the stress-strain diagram in Fig. 12 gives the yield strength of the weld material as  $S_y = 57 \text{ MPa}$ , which is almost a perfect match to the measured yield strength from the thin specimen. According to the developed standards by AREMA [2], a standard 136RE heavy rail should have a minimum yield strength of 300 MPa. Hence, for the SAW-repaired heavy rail, the yield strength ( $S_y$ ) is below the minimum requirement by AREMA, and, again, it is concluded that the repaired rail will fail under the dynamic load of the train.

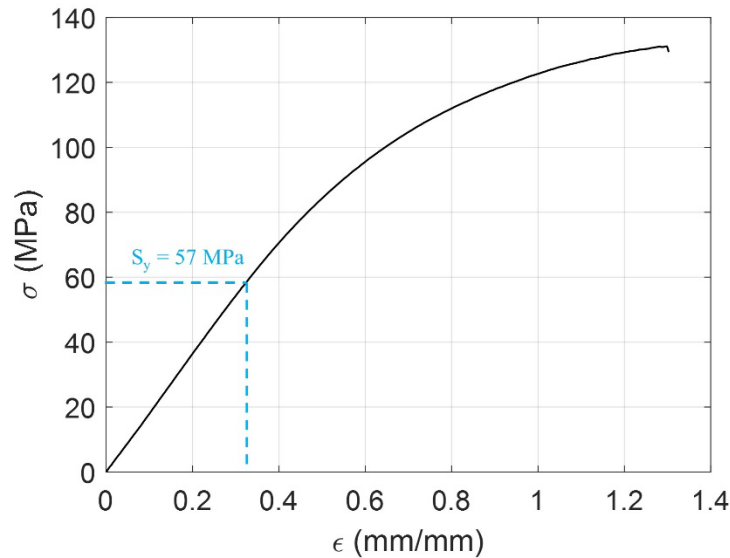


**Fig. 8.12** The resultant stress-strain diagram from the 3-point bending test of the thick specimen extracted from the rail-weld interface of the SAW-repaired heavy rail. The related force-displacement diagram is given in Fig. 10.

Regarding the shear stress, as was given in Eq. 7, it is calculated as  $\tau = VQ/Ib$ . It was presented in Fig. 4 that the maximum shear force during a 3-point bending test is:

$$V = \frac{P}{2} \quad (27).$$

**Table 17** Young's modulus of the rail and weld materials.

Material	Heavy rail	Light rail	Deposited weld	Lincore 40-S weld wire
Yield strength (MPa)	210	203	196	185

By dividing the cross section of the thick bending sample shown in Fig. 11b into 3 areas, an area division can be provided as illustrated in Fig. 13, which is ideal for calculating the first moment of area (Q). Referring to Fig. 13, the first moment of area of the thick bending specimen can be calculated as [4]:

$$\begin{aligned}
 Q &= A_1y_1 + A_2y_2 + A_3y_3 \\
 &= \left( b \left( \frac{h}{2} - d_{NA} \right) \right) \left( \frac{1}{2} \left( \frac{h}{2} - d_{NA} \right) \right) + (bd_{NA}) \left( \frac{d_{NA}}{2} \right) \\
 &+ \left( \left( b \frac{E_R}{E_W} \right) \left( \frac{h}{2} \right) \right) \left( \frac{1}{2} \left( \frac{h}{2} + d_{NA} \right) \right) \\
 &= \frac{b}{2} \left( 2d_{NA}^2 + \frac{h^2}{4} \left( \frac{E_R}{E_W} + 1 \right) + hd_{NA} \left( \frac{E_R}{2E_W} - 1 \right) \right)
 \end{aligned} \quad (28).$$

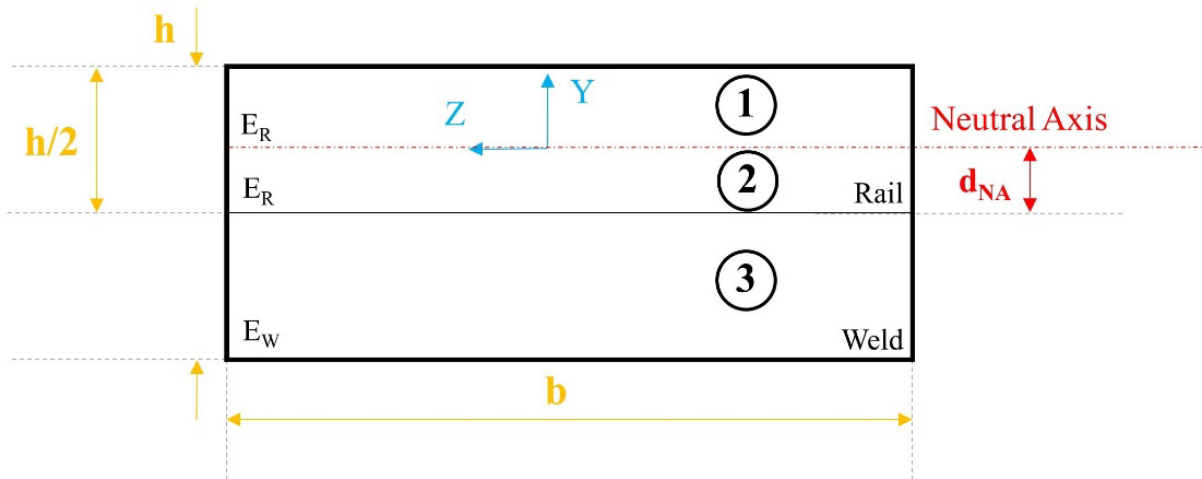


**Fig. 8.13** Cross section of the bending specimen divided into 3 zones as a reference for calculation of the first moment of area and moment of inertia.

Referring to Fig. 13, the equivalent moment of inertia (I) for the composite thick bending specimen can be calculated as follows [4]:

$$\begin{aligned}
I &= (I_1 + A_1 d_1^2) + (I_2 + A_2 d_2^2) + (I_3 + A_3 d_3^2) \\
&= \left[ \frac{b \left(\frac{h}{2} - d_{NA}\right)^3}{12} + \left( b \left(\frac{h}{2} - d_{NA}\right) \right) \left( \frac{1}{2} \left(\frac{h}{2} - d_{NA}\right) \right)^2 \right] \\
&\quad + \left[ \frac{b d_{NA}^3}{12} + (b d_{NA}) \left( \frac{d_{NA}}{2} \right)^2 \right] \\
&\quad + \left[ \frac{\left( b \frac{E_R}{E_W} \right) \left(\frac{h}{2}\right)^3}{12} + \left( b \frac{E_R}{E_W} \left(\frac{h}{2}\right) \right) \left( \frac{1}{2} \left(\frac{h}{2} + d_{NA}\right) \right)^2 \right]
\end{aligned} \tag{29}.$$

Putting Eqs. 27, 28, and 29 into Eq. 7, and replacing all the parameters with their corresponding values defined for the thick bending specimen extracted from the rail-weld interface, the failure shear stress can be calculated as:

$$\tau_f = 84 \text{ MPa} \tag{30}.$$

For the thick sample with a length of  $L = 30$  mm and maximum deflection of  $\delta = 3.37$  mm, using Eqs. 12 and 13 it is calculated that the sample is elongated 2.5% with the final length of  $L_2 = 30.75$  mm at the time of failure. Although the elongation percentage is much higher for this sample compared to the thin sample, it is still less than 5% and therefore gives the fact that the sample has most probably experienced a brittle failure.

### 8.2.2. Failure mode analysis

It was found in the last section that at the failure point of the thick bending specimen, a 131 MPa of flexural tensile stress (Eq. 26) and an 84 MPa of shear stress (Eq. 30) are applied simultaneously. What is to be discussed here is about the percentage of contribution of each type of stress in the resulting fracture, i.e., to find out if the thick specimen is ultimately failed as a result of pure bending, as a result of pure shear, or as a combined result of both of them.

Generally, the shear strength of a high-carbon hard steel alloy is about 0.7 of its tensile strength [5]. For the current under-investigation thick specimen, it is found that it has a 131 MPa of flexural tensile stress. Therefore, following Lomax's findings [5], it should have a shear strength around  $0.7 \times 131 = 92$  MPa. The 3-point bending test showed that the specimen was carrying a shear stress of 84 MPa at the moment of failure, which gives a great chance of shear stress contribution in its ultimate failure/fracture. Figuring out the principal stresses, as shown in Fig. 14, it is seen that the maximum shear stress is 106.5 MPa, which goes beyond the expected shear strength of 92 MPa. This supports the idea of shear involvement in the fracture of the thick bending specimen.

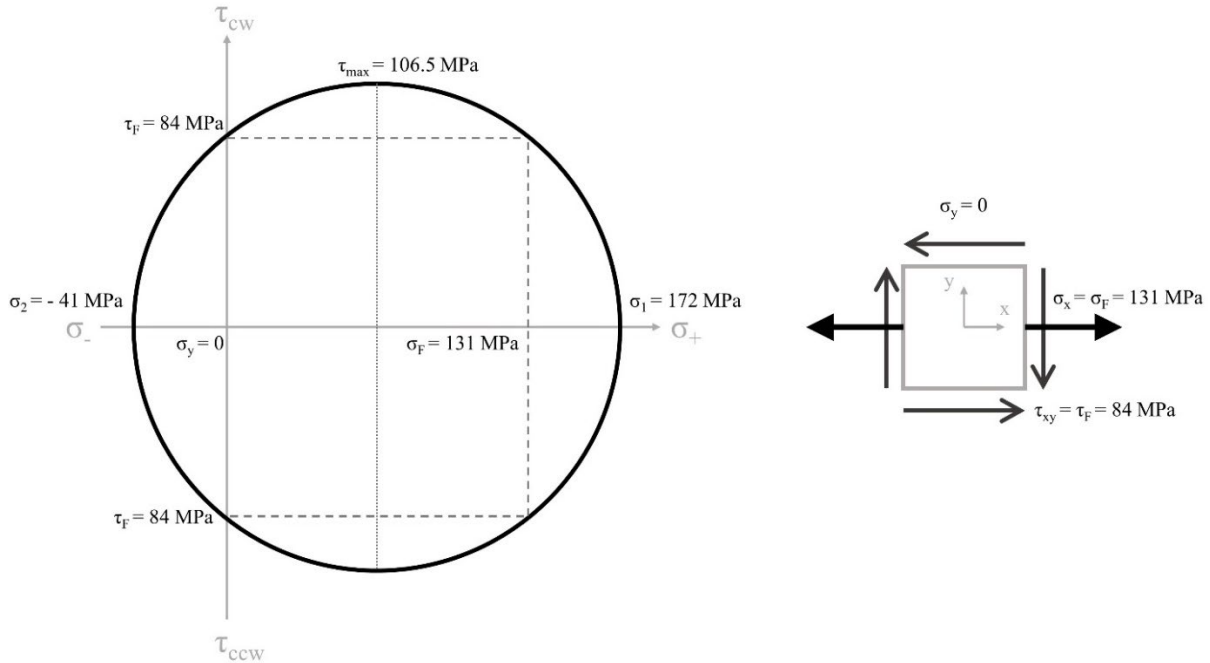


**Fig. 8.14** Mohr's circle drawn based on the applied plane and shear failure stresses to the thick bending specimen extracted from the rail-weld interface.

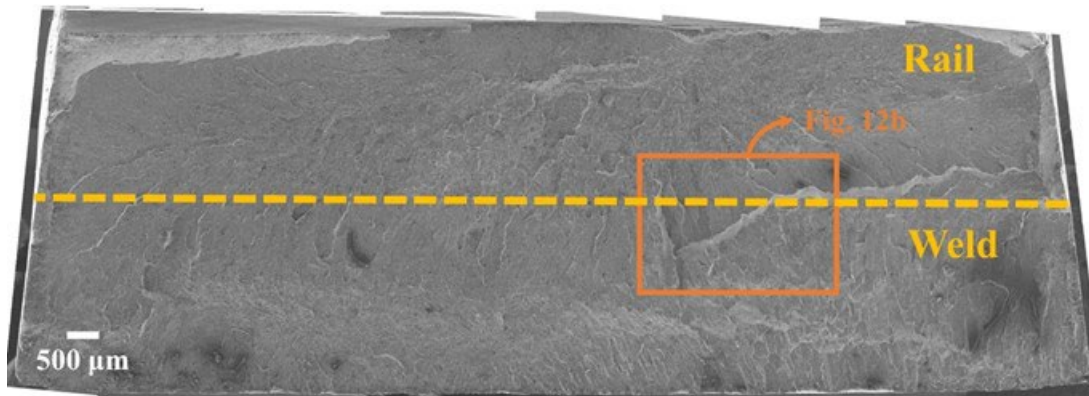
The fracture surface of the thick bending specimen extracted from rail-weld interface is captured using SEM and shown in Fig. 15. It is observable in Fig. 15a that the lower half of the fracture surface, i.e., the weld side, is populated by massive amount of cleavage signs with light appearance. These mostly vertical light-colored lines of cleavage have a very sparse distribution in the upper half, i.e., the rail side, compared to the lower weld side. These cleavage signs show that the normal flexural tensile stress in the weld region was a pivotal contributor of the specimen failure during the 3-point bending.

The other visible fact in Fig. 15a is an elongated sign of combined cleavage and crack at the right side of the fracture surface that is developed in the middle plane of the sample, i.e., at the rail-weld interface. A closer look into it in Fig. 15b shows minor signs of cracks around the elongated cleavage line. These symptoms give a strong evidence that shear stress was also partially involved in the fracture of the specimen at the failure point.

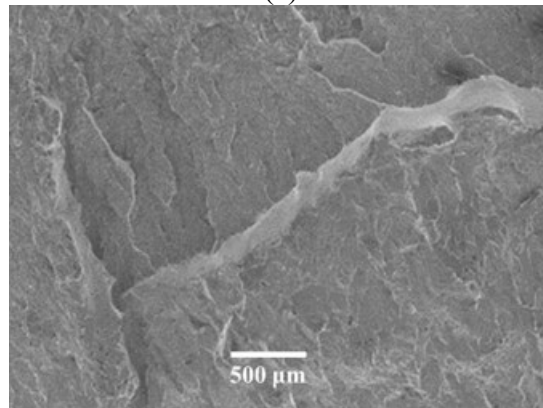
It is concluded that the repaired rail can tolerate shear stresses up to 84 MPa at the rail-weld interface before facing any failure, and the weld material on the top have a tensile bending strength of 131 MPa, which is below the minimum 450 MPa ultimate tensile strength required for the heavy 136RE rails [2].

In Fig. 9, the chemical distribution at different points of the weld materials were scanned to show if the existing black spots are representing a pore, air trap, or a carbon intruded site. It was found that these pores and air bubbles are the main reasons of such a low yield strength and the premature failure of the bending sample. To make sure that this is a valid conclusion, the rail section is also chemically scanned using EDS to check the chemical consistency through the rail material. Fig.

16 shows a random EDS scan of the thick bending specimen at different points of the rail side, i.e., the compression side. It is observable that the despite a slight deviation of the weight percentage of each element between different sites (less than 5%), there is a consistent chemical distribution throughout the entire rail section. This confirms the fact that the weld material suffers from an inconsistent structure which was the reason of neutral axis shifting in the thin bending specimen, and premature failure of both the thin and the thick bending specimens.

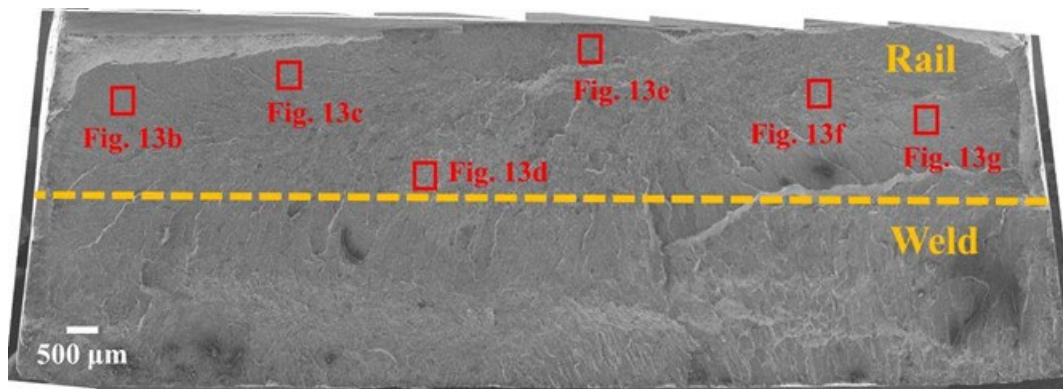


(a)

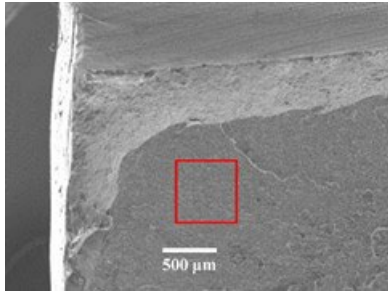


(b)

**Fig. 8.15** SEM macrograph from the fracture surface of the thick 3-point bending specimen extracted from the rail-weld interface; (a) an overall view from the whole fracture surface and (b) a closer view to the surface.

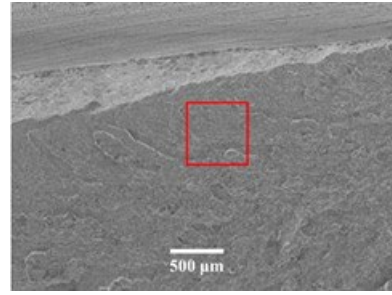


(a)



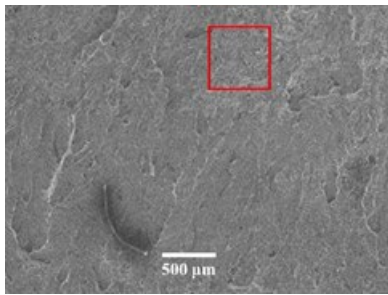
Fe	C	Cr	Mn	Si	O
Bal.	13.7	2.0	3.8	1.0	2.0

(b)



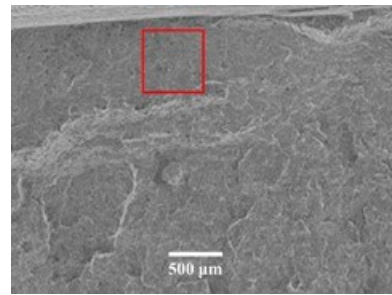
Fe	C	Cr	Mn	Si	O
Bal.	1.8	2.3	2.5	0.5	2.6

(c)



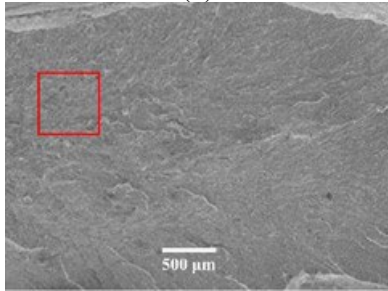
Fe	C	Cr	Mn	Si	O
Bal.	8.97	2.5	3.3	0.8	1.4

(d)



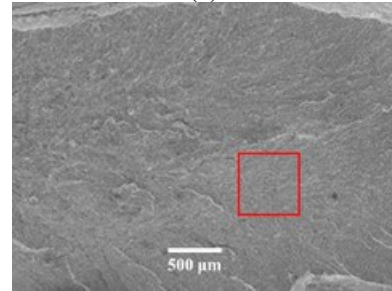
Fe	C	Cr	Mn	Si	O
Bal.	13.42	0.8	3.1	0.5	4.4

(e)



Fe	C	Cr	Mn	Si	O
Bal.	12.9	2.0	3.4	0.3	2.4

(f)



Fe	C	Cr	Mn	Si	O
Bal.	9.62	1.7	2.9	0.4	1.8

(g)

**Fig. 8.16** EDS scan analysis of random locations of the upper side of the fracture surface of the thick bending specimen to figure out the chemical consistency of the rail material compared to that of the weld material shown in Fig. 9 (each chemical element is represented by its wt.%).

To get a clearer visualization regarding the chemical consistency throughout the rail and weld areas, the given data in Figs. 9 and 16 are re-presented in the form of graphs in Fig. 17. Each chemical element is presented in a separate graph. The y-axis of each graph shows the weight percentage of the chemical element, and the x-axis shows the location of measuring the weight percentage of the chemical element in Figs. 9 and 16; for example, the measurement location b for C graph in Fig. 17 means the weight percentage of C that was measured for weld in Fig. 9b and for rail in Fig. 16b. An overall look at Fig. 17 shows how sensibly the weight percentage of each individual chemical element goes through sharp fluctuations for the weld material, while the rail



material experiences a smooth distribution for every individual element at different locations of measurement; this fact is especially more observant for carbon, silicon and oxygen elements in Fig. 17. The presented graphs in Fig. 17 are put together in a single graph in Fig. 18 for a clearer demonstration regarding the elements with the most fluctuations. One can conclude from Fig. 18 that the carbon and oxygen are those elements that their weight percentage fluctuates greater than the other elements. The reason for oxygen oscillations can be attributed to the presence of air bubbles and air-entrapped holes in the deficient weld structure. The significant oscillation of carbon may be due to the high carbon content of the weld wire, flux particles, and the rail. When these three high-carbon components fuse together during submerged arc welding, then the carbon content near the rail area might be higher as a result of rail's carbon diffusion into the weld microstructure. This again confirms the chemical inconsistency in the weld material, while the rail has a plain chemical distribution. This metallurgical inconsistency in the weld zone could be the major contributor of the premature failure during the 3-point bending test.

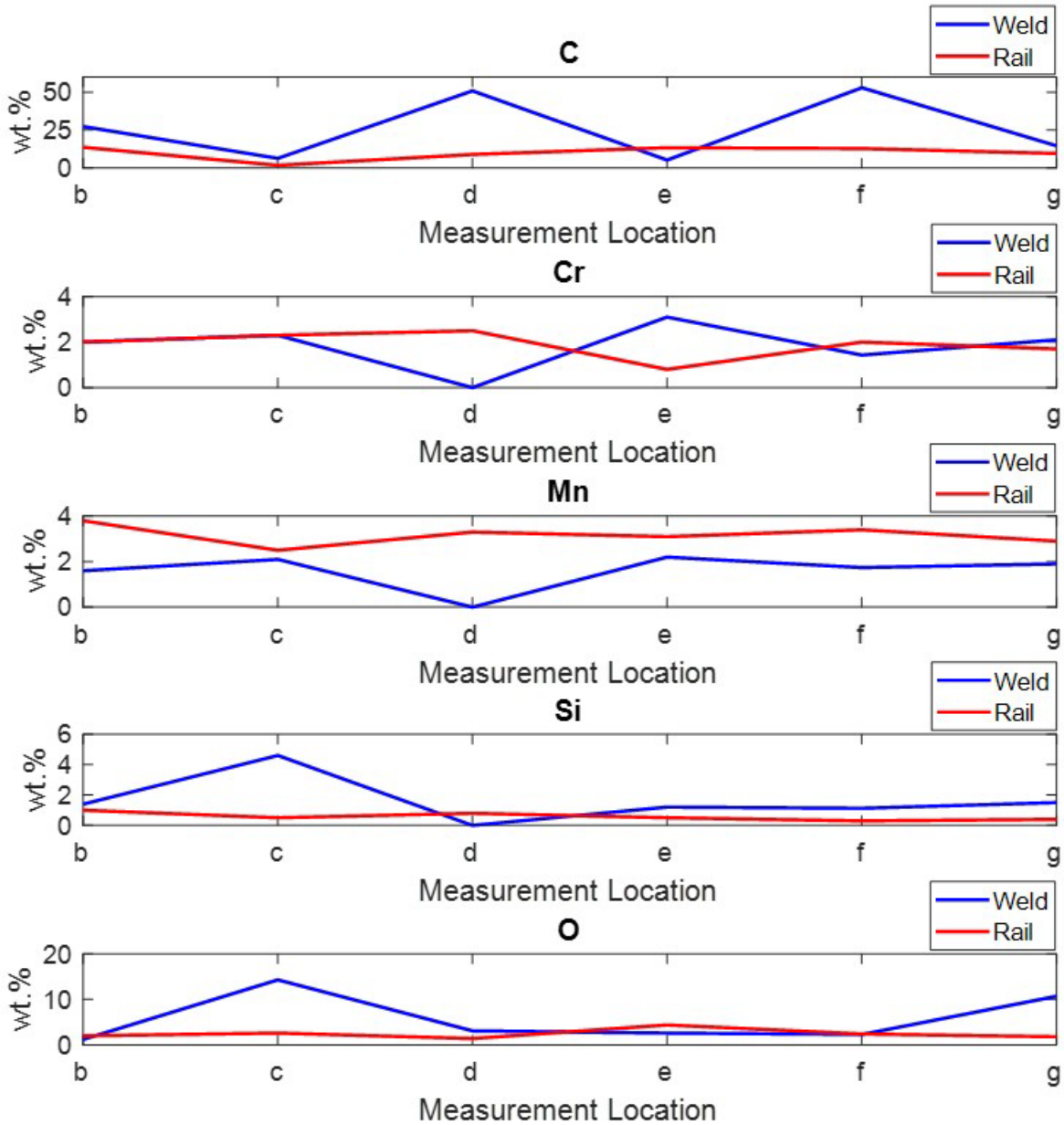


**Fig. 8.17** Distribution of the weight percentage of different chemical elements in separate graphs throughout the weld and rail areas. The b-g measurement locations on the x-axis correspond to the locations where EDS chemical measurement is conducted, as shown in Figs. 9b-g and Figs. 16b-g for the weld and rail materials, respectively.

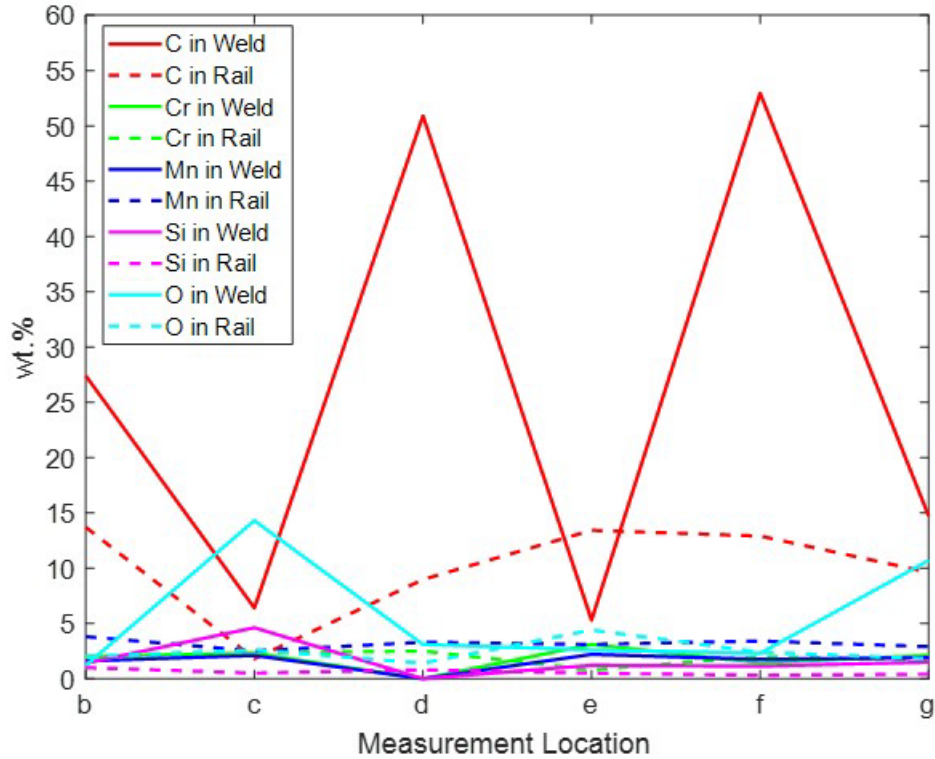


**Fig. 8.18** Distribution of the weight percentage of different chemical elements in a single graph throughout the weld and rail areas. The b-g measurement locations on the x-axis correspond to the locations where EDS chemical measurement is conducted, as shown in Figs. 9b-g and Figs. 16b-g for the weld and rail materials, respectively.

The presented experiments in Chapter 8 could give valuable results and could act as a great bedrock to find the best next step for modifying and improving the rail properties. However, all the results and discussions in Secs. 8.1 and 8.2 are only based on a single thin bending specimen and a single thick bending specimen, respectively. This makes the results unreliable. In order to validate the results, all the testing procedures need to be repeated for at least another 2 times, for each of the thin and thick specimens separately. In this way, after comparing the results and making sure of the test repeatability, the validated outcomes can be utilized for the next step of the experiments.

## References for Chapter 8

- [1] E. Sideridis, G.A. Papadopoulos, Short-Beam and Three-Point-Bending Tests for the Study of Shear and Flexural Properties in Unidirectional-Fiber-Reinforced Epoxy Composites, Wiley InterScience (2003). <https://doi.org/10.1002/app.20382>
- [2] AREMA Manual for Railway Engineering, Chapter 4: Rail, American Railway Engineering and Maintenance-of-way Association (2020)
- [3] H. Deng, H. Shi, S. Tsuruoka, Influence of coating thickness and temperature on mechanical properties of steel deposited with Co-based alloy hardfacing coating, Surf. Coat. Technol. 204(23) (2010) 3927-3934. <https://doi.org/10.1016/j.surfcoat.2010.05.013>
- [4] F.P. Beer, J.E. Russel Johnson, Mechanics of materials, McGraw-Hill (2014) 7th edition.
- [5] М.Г. Ломак, Strength and fatigue life of hard alloys, Metallurgical Industry Press (1990) 1th edition.
- [6] R.C. Juvinall, K.M. Marshek, Fundamentals of machine component design, John Wiley & Sons (2012) 5th edition.

## **9. Chapter 9 MODIFIED FINITE ELEMENT MODELING AND VALIDATION OF SUBMERGED ARC WELDING FOR REPAIRING 136RE HEAVY RAILS**

The constant wear and tear experienced by rail surfaces due to continuous loading necessitates repairs for maintaining optimal performance within railway networks. Traditional repair methods are not only time-consuming but also costly, motivating the exploration of innovative alternatives. This study focuses on the development of a finite element (FE) model to simulate the submerged arc welding (SAW) process, which serves as an additive manufacturing technique for restoring 136-lb/yd (136RE) rails, commonly utilized in heavy freight and passenger rail systems across the United States.

To validate the developed FE model, a series of experimental laboratory investigations were conducted. A worn section of the 136RE rail was carefully chosen for this study. After the rail's surface underwent milling and flattening, the submerged arc welding process was employed to rebuild the rail, utilizing a 1/8-inch Lincore 40-S depositing wire. The reconstructed rail sample was then subjected to experimental tests, including tensile testing, which provided the essential mechanical properties required to validate the simulation process.

The FE model encompasses all conceivable interactions, including thermal, mechanical, and phase transformations. This simulation employs an element-birth-and-kill method, examining the thermal distribution within the sample across different sections. By considering the thermal history and phase change relations, the model predicts the mechanical properties of the repaired rail. The validated model showcases substantial potential in exploring and predicting mechanical properties and thermal distribution during the SAW process for heavy rail repair.

### **Introduction**

Rail tracks' durability is influenced by wear and rolling contact fatigue [1]. Various types of damages commonly arise on railway tracks, predominantly attributable to side wear, fatigue cracks, head checks, and spalling [2]. Switches, crossings, and curves are particularly prone to side wear, making their maintenance expenses significantly higher compared to straight sections of rail tracks. The primary cause of defects in rail tracks, mainly side wear, is the combination of normal and tangential stresses. Consequently, numerous studies have been undertaken to analyze and model the forces, moments, and contact area at the wheel/rail interface [3]–[7]. Rail defects have the potential to initiate and propagate cracks, ultimately causing spalling and, in severe cases, complete rail fracture. Consequently, another line of research has embraced rail grinding as a method to eliminate surface defects and prevent the progression of such cracks [8]–[10]. The grinding process can adversely affect rail longevity and increase operational costs [11], [12].

In response to the limitations of cost and weight in manufacturing rail profiles with high resistance to wear and rolling contact fatigue, the utilization of surface coatings as a form of surface treatment has gained prominence. Various surface coating technologies, such as shielded metal arc welding (SMAW), have been developed as alternative approaches based on specific applications and coating types. For instance, Saiful Akmal and Wahab researched the application of SMAW for repairing damaged surfaces of UIC-54 rails in the Malaysian railway network [13]. De Becker et

al. [14] are also developing a mobile system for automated on-site repair of the railway network in the United Kingdom. Kabo et al. [15] developed a numerical model to examine the rolling contact fatigue performance and material defects in weld-repaired rails in Sweden. Furthermore, Xin et al. [16] conducted a valuable numerical study in the Netherlands, investigating repair welding and grinding of standard European rails using finite element modeling.

Regarding studying standard rails utilized in the United States railway system, the current research group is the sole entity concentrating on repairing them through overlay weld techniques. Previous investigations in the United States have explored laser cladding to repair damaged surfaces in both light transit rails [17], [18] and heavy freight/passenger rails [19]. Another research endeavor examined submerged arc welding (SAW) applications for repairing light rails [20]. This present study represents the first examination of the mechanical and metallurgical properties of a standard U.S. heavy rail undergoing SAW repair.

Repairing a damaged railhead surface offers significant advantages over conventional replacement methods, primarily due to its ease of implementation and avoiding extensive manipulation and reconstruction of the rail infrastructure. Although some minor surface grinding and cutting are necessary for overlay welding on the railhead, this approach ensures that the original strength of the rail base is maintained. However, previous studies [21]–[25], including the author's research [17]–[20] have demonstrated that a surface-welded rail is more susceptible to cracking and premature failure than an integral parent rail. Consequently, conducting a comprehensive investigation into the strength properties, hardness, residual stress, and distribution of inclusions, pores, and cracks in a weld-repaired rail becomes essential. Notably, no study has been published that investigates explicitly the repair of heavy-duty rails used in the standard railway network of the United States using the submerged arc welding (SAW) method as mentioned in previous research [20], various arc-based methods, such as shielded metal arc welding (SMAW), gas tungsten arc welding (GTAW), submerged arc welding (SAW), and plasma arc welding (PAW), can be employed for surface welding. Among these methods, SAW is considered the most suitable for multi-layer, high-thickness welding due to its superior quality and productivity[26], [27].

In this research, a three-dimensional coupled temperature-displacement numerical model is developed using the commercial ANSYS software. This model aims to analyze the thermo-mechanical behavior of residual thermal stresses generated during the manufacturing of the worn part of the rail using the submerged arc welding (SAW) process. This specific configuration is referred to as Case I in the study. To examine the impact of preheating on thermal stresses, two additional cases involving different preheating methods and subsequent cooling rates are investigated to determine the optimal preheating approach. In Case II, preheating is applied by placing hot plates beneath the railhead during the cooling process of the additive part to reduce residual thermal stress. In Case III, hot plates are positioned at the railhead's bottom and sides. The results obtained from all three cases are compared to evaluate the state of thermal stress at the weld/rail interface. The safety margin of thermal stresses is determined by comparing the results to the yield strength of the material.

## METHODOLOGY

The rail to be repaired in this study is a worn 136RE rail commonly employed in freight and passenger railway networks across the United States. The specimen analyzed in this research was a 30-cm section of the worn rail, as depicted in Figure 1. The chemical composition of the high-carbon steel utilized in manufacturing the 136RE rail is provided in Table 1.

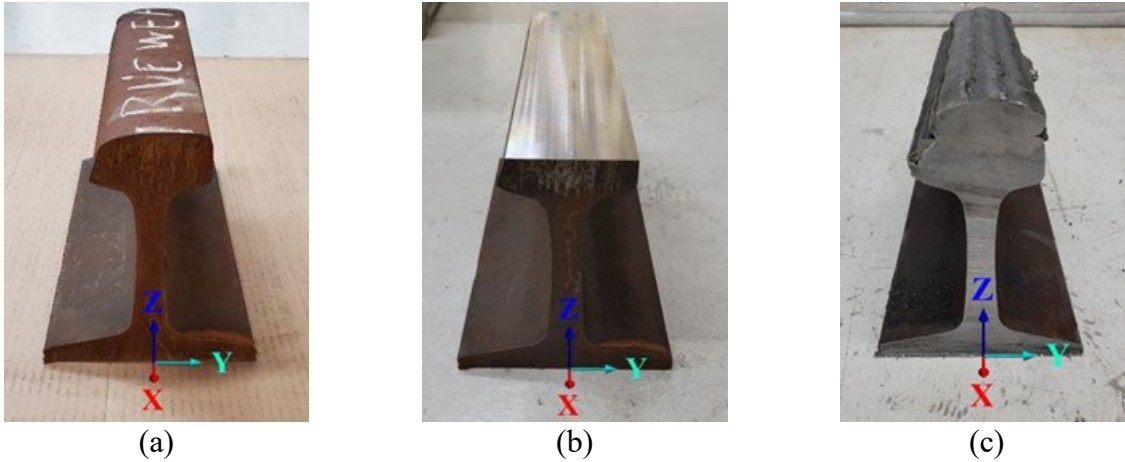


Figure 9.1 (a) The to-be-repaired 136RE worn rail; (b) milled rail; (c) repaired rail

Table 1 Chemical composition of the rail and the SAW wire (wt. %)

Material	Fe	C	Cr	Mn	Mo	Si	Ni	P	S
Rail	Bal.	0.80	0.03	0.23	-	0.04	0.14	0.01	0.01
		± 0.06	± 0.01	± 0.03		± 0.01	± 0.04	± 0.005	± 0.005
Wire	Bal.	0.12	0.50	2.75	0.85	3.30	-	-	-
		± 0.05	± 0.03	± 0.30	± 0.05	± 0.20			

Table 2 Chemical composition of the neutral Lincolnweld 801 submerged arc flux (wt. %)

SiO <sub>2</sub>	CO <sub>2</sub>	CrO	MoO <sub>3</sub>	MnO	Fe <sub>2</sub> O <sub>3</sub>
10.0	21.2	8.9	18.4	14.2	22.7
± 0.9	± 0.8	± 0.2	± 0.9	± 0.8	± 1.0

For the SAW process, the selected depositing wire was the 1/8-inch Lincore 40-S hard-facing submerged arc wire. This specific wire was chosen due to its excellent characteristics in terms of rolling and sliding wear properties. Moreover, it is compatible with carbon steel and suitable for depositing up to 5 layers. The chemical composition of the SAW wire used is provided in Table 1. To complement the process, the neutral Lincolnweld 801 submerged arc flux was employed as the recommended and compatible flux, and its chemical composition is detailed in Table 2.

To facilitate the SAW process on a flat substrate, the surface of the worn railhead undergoes milling and flattening. Before commencing the SAW process, the milled surface is further prepared



by grinding, polishing, and cleaning with acetone to eliminate loose mill scales, rust, and micro contaminants. The milled rail can be observed in Figure 1b, while Figure 1c depicts the rail after the SAW process, referred to as the surfaced rail. This emerged rail serves as the final product on which all mechanical and metallurgical assessments will be carried out.

The key distinction between conventional arc welding and SAW lies in covering flux. In SAW, the wire and the arc are effectively shielded beneath a layer of flux grains, protecting against oxidation. Another advantage of submerging the welding area within the flux stream is that it remains insulated from excessive radiation heat loss, resulting in a cleaner weld. By preventing potential heat loss mechanisms like radiation, convection, or energy scattering from wire to rail, the energy efficiency can be increased by 90% or even more. This heightened efficiency yields significant benefits, including enhanced weld reliability and a high deposition rate.

The SAW process involves the development of an arc between the filler wire and the railhead, which serves as the substrate. Simultaneously, flux grains are dispensed onto and around the arc area through a hopper. This forms a covering envelope at the arc zone, solidifying the melt pool on the railhead's surface where the arc is burned. The flux grains close to the envelope melt and solidify, forming a thin layer known as slag, which will be removed once the SAW process is completed. The current SAW process for overlay repairing the damaged railhead surface utilizes an open-circuit voltage ranging from approximately 25 to 36 V, a weld current of 150 A, a travel speed of 23 mm/s, and a wire feed rate of 21 mm/s.

### Process Physical description

In the following, Nomenclature and related Subscripts describe the process given. Also, the governing equations for this process are defined as follows:

- $T$  temperature ( $K$ )
- $x, y, z$  coordinate
- $\vec{V}$  velocity vector ( $m/s$ )
- $u, v, w$  velocity component ( $m/s$ )
- $\vec{g}$  gravity vector ( $m^2/s$ )
- $p$  pressure ( $Pa$ )
- $\nu$  kinematic viscosity ( $m^2/s$ )
- $\beta$  thermal expansion coefficient ( $K^{-1}$ )
- $\alpha_f$  thermal diffusivity of air ( $m^2/s$ )
- $\alpha_s$  thermal diffusivity of solid body ( $m^2/s$ )
- $q_{in}$  incident radiative heat flux ( $W/m^2$ )
- $q_{out}$  net radiative heat flux from the surface ( $W/m^2$ )
- $\Omega$  hemispherical solid angle ( $sr$ )
- $I_{in}$  intensity of the incoming ray ( $W/sr$ )
- $\vec{s}$  ray direction vector
- $\vec{n}$  normal vector pointing out of the domain
- $\varepsilon$  emissivity
- $\epsilon$  strain

- $\sigma$  stress ( $Pa$ )
- $C$  fourth-order material stiffness tensor ( $N/m$ )
- $H'$  strain-hardening rate ( $Pa$ )
- $\vartheta$  Poisson's ratio
- $E$  elastic modulus ( $Pa$ )
- $e$  deviatoric strain
- $\gamma$  engineering strain
- $t$  time ( $s$ )

### Subscripts

- $h$  hot body
- $c$  cold body
- $w$  wall
- $e$  elastic
- $p$  plastic
- $T$  thermal
- $eq$  equivalent (von-Mises)
- $zz$  longitudinal direction of principal stress
- $xx$  transversal direction of principal stress
- $yy$  normal direction of principal stress

Continuity equation:

$$\vec{\nabla} \cdot \vec{V} = 0 \quad (1)$$

Momentum equation:

$$\frac{D\vec{V}}{Dt} = -\frac{1}{\rho} \vec{\nabla} p + \nu \vec{\nabla}^2 \vec{V} + \vec{g} \beta (T - T_c) \quad (2)$$

Energy equation for fluid medium:

$$\frac{DT}{Dt} = \alpha_f (\vec{\nabla}^2 \cdot T) \quad (3)$$

Energy equation for a still solid region without internal heat generation is:

$$\frac{\partial T}{\partial t} = \alpha_s (\vec{\nabla}^2 \cdot T) \quad (4)$$

The radiation intensity approaching a point on a wall surface can be integrated to yield the incident radiative heat flux:

$$q_{in} = \int_{\vec{s} \cdot \vec{n} > 0} q_{in} \vec{s} \cdot \vec{n} d\Omega \quad (5)$$

The net radiative heat flux from the surface is then computed as:

$$q_{out} = (1 - \varepsilon_w)q_{in} + \varepsilon_w\sigma T_w^4 \quad (6)$$

### Numerical Modeling

To simulate the effects of thermal stresses, a three-dimensional model of the worn rail and weld layers is created using SolidWorks 2022. The new rail profile adheres precisely to the AREMA standard profiles (136 lb/yd [136RE]), while the worn profile is obtained from the provided rail specimen. The combined new and worn rail profiles are depicted in Figure 2.

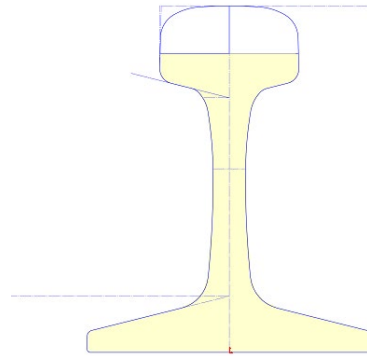


Figure 9.2 Original and worn rail profiles

A grid independence test is performed during the thermal study (finite volume) step to reduce computational time and ensure confidence in the results. As a result, a grid system consisting of 90,792 elements is employed for calculations. Among these elements, 9,792 belong to the rail part, and 81,000 are associated with the weld part. Different mesh zones generated in the solid bodies are illustrated in Figure 3.

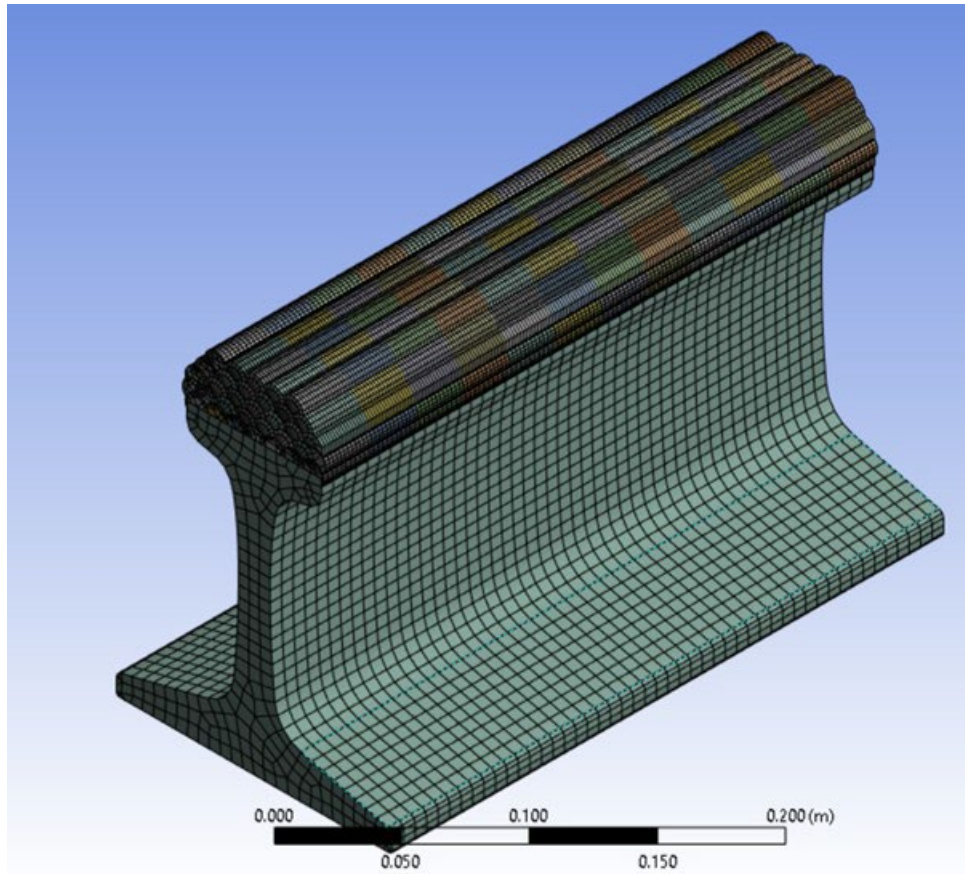


Figure 9.3 mesh zones generated in the solid bodies

The model is divided into two sections: simulation of the process in a welding pass and simulation of the process in the entire cross-section area. This division is due to the nature of the welding process. After a complete row of welding, it can be assumed the entire row has the same temperature, and it should save a huge amount of calculation without losing much accuracy, considering that the first line of welding will also be simulated. Assuming that the additive layer in the 3D printing process reaches the temperature of  $1700^{\circ}\text{C}$  and the ambient temperature (typical for SAW temperature) is  $22^{\circ}\text{C}$ . The model is divided into two sets of elements with different material properties: the rail material and the weld material. The material properties are imported based on the data provided in Table 2.

The element birth-and-kill technique is incorporated to build up the worn part of the railhead in the FE. Each element was considered with a length of 25mm, so there are 12 elements in each pass. According to welding speed, the time steps of this method are applied to the model. Considering this method, the welding process can be simulated as an internal heat generation with  $3.8\text{e}009\text{ W/m}^3$ . The generated heat can be extracted from the current and voltage of the process by an adjustment to ensure that the melting pool's temperature will be provided ( $T=1700^{\circ}\text{C}$ ). The shape of the elements was estimated according to the actual weld profile in the real sample.

The thermal history field and subsequent residual stresses are analyzed through sequential thermo-mechanical analyses utilizing the commercial finite element code ANSYS 2023 R1. The thermal heat transfer analysis replicates the cooling process using the transient thermal method, and the results of this analysis are used as initial conditions for the subsequent finite element analysis.

### Model Results

Using numerical modeling, comprehensive information can be obtained regarding temperature distribution. As before mentioned, to reduce the computational calculation this model is divided into two main sections. In the first section, the model properties are validated by examining one welding row. In this regard, the result is shown in the figure 5. Figure 4 also shows the procedure modeling. This model is a result of finite element try and error to find the optimum element size and heat generation properties as the controllable inputs.

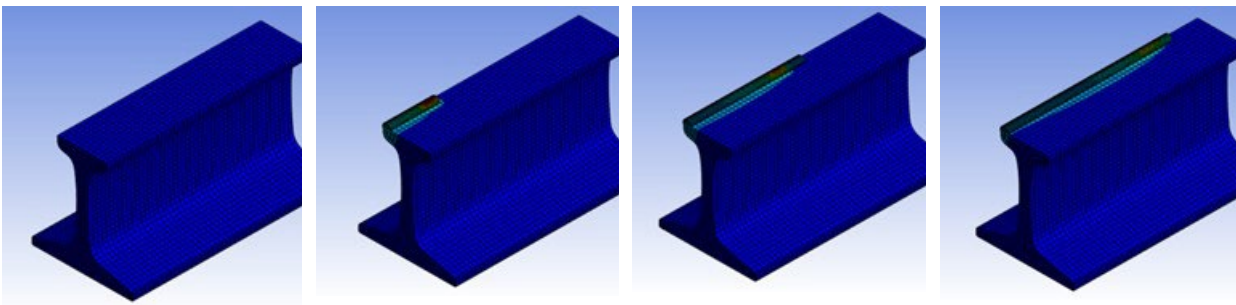


Figure 9.4 Graphical show of the model's procedure (step1)

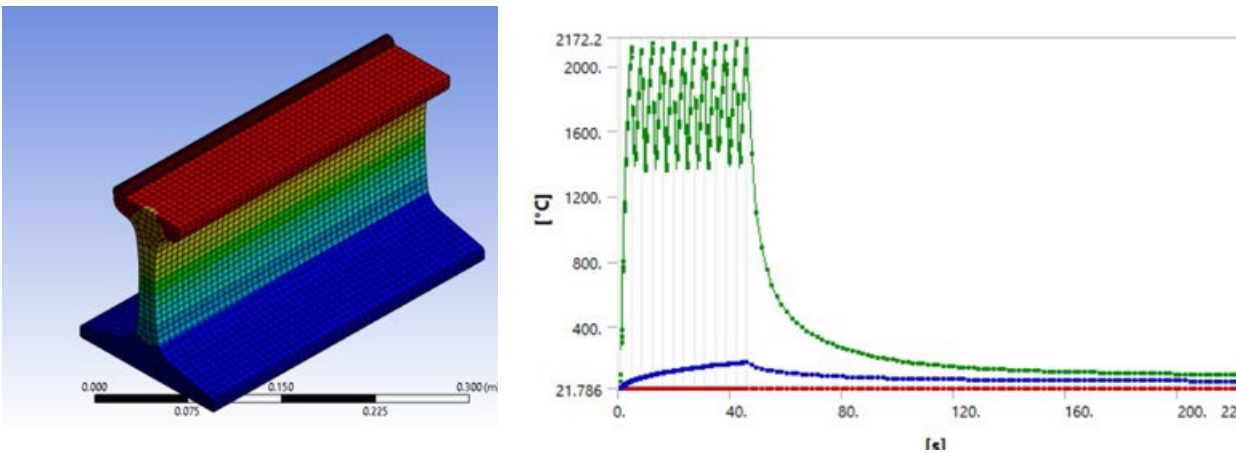


Figure 9.5 Graphical and numerical temperature distribution resulted from the model

The welding process is modeled on a 2D scale in the second step. In this section, only the first element got involved in the model. The first step's result shows that this assumption does not affect the entire process. Figure 5 illustrates the profile temperature result and historical temperature

profile in the sample. This thermal history shows that in the Fe-Cr phase (Figure 6) what is the mechanical properties of the simulated maple. The dotted line in this diagram according to the table 3.

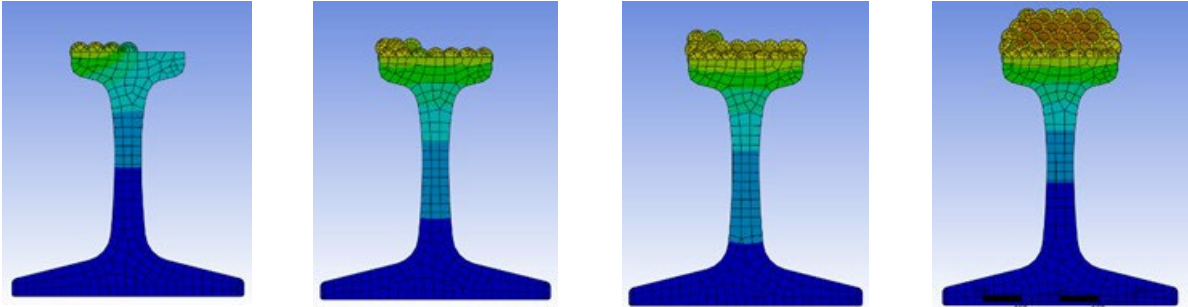


Figure 9.6 Graphical show of the model’s procedure (step 2)

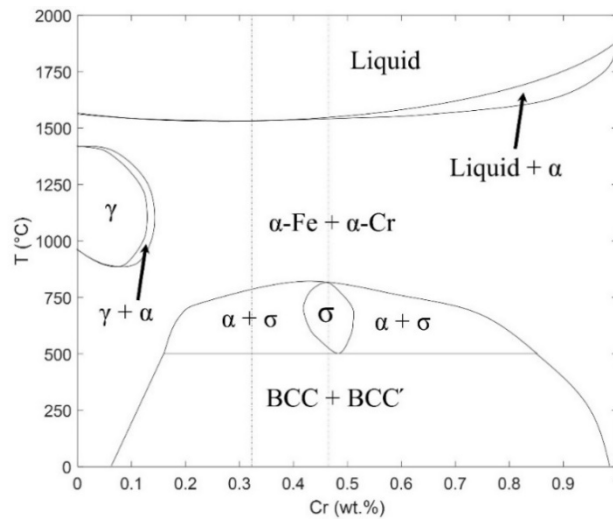


Figure 9.7 Fe-Cr phase diagram for the Lincore 40-S hard-facing wire used in the SAW process

Table 3 Chemical composition (wt. %) of different areas of the repaired rail (Areas are addressed graphically in Fig. 4.)

Area	Fe	C	Cr	Mn	Mo	Si
Layer 4	Bal.	0.067 ± 0.007	0.32 ± 0.05	1.25 ± 0.20	0.82 ± 0.03	3.42 ± 0.40
Layer 3	Bal.	0.028 ± 0.007	0.39 ± 0.05	1.93 ± 0.20	0.80 ± 0.03	3.26 ± 0.40
Layer 2	Bal.	0.016 ± 0.007	0.41 ± 0.05	2.55 ± 0.20	0.73 ± 0.03	3.12 ± 0.40

Layer 1	Bal.	0.017 ± 0.007	0.47 ± 0.05	2.19 ± 0.20	0.73 ± 0.03	2.94 ± 0.40
HAZ	Bal.	0.23 ± 0.06	0.12 ± 0.01	1.01 ± 0.20	0.03 ± 0.01	0.53 ± 0.40
Rail	Bal.	0.80 ± 0.06	0.03 ± 0.01	0.23 ± 0.03	-	0.04 ± 0.01

The Fe-Cr phase diagram shows that the Lincore 40-S weld wire, containing approximately 0.5 wt.% chromium (as stated in Table 1), consists of a mixture of BCC phases with Fe-rich (BCC) and Cr-rich (BCC') alloy compounds at room temperature.. At  $0 \leq \text{Cr-wt.\%} < 0.12$ , the austenite with the lightest appearance in HCl-etched carbon steel nucleates. Then, at  $\text{Cr-wt.\%} \geq 0.12$ , a combined  $\alpha\text{-Fe} + \alpha\text{-Cr}$  phase forms, which starts with the dominance of the light-etched  $\alpha\text{-Fe}$  at  $\text{Cr-wt.\%} = 12$  and smoothly transforms to a dark-etched,  $\alpha\text{-Cr}$ -dominant compound as the  $\text{Cr-wt.\%}$  leans towards 1.

Table 2 shows a declined flow of Cr-wt.% from Layer 1 to Layer 4. The liquidus weld drops at 1600 – 1700 °C, and the preheated railhead surface has a temperature of 200 – 300 °C, so the weld materials start to experience an initially fast cooling procedure down to 500 – 700 °C during the first layer. At the beginning of the second layer, Layer 1 is reheated and has a long exposure at a higher temperature range, 700 – 1000 °C. Layer 2, with a higher initial substrate temperature (500 – 700 °C), remains at elevated temperatures around 700-1000 °C until the third layer starts. This trend proves that the top layers are exposed to higher temperature ranges, i.e., higher than 500 – 800 °C. Prolonged exposures to temperatures in the range of 500 – 800 °C give enough time for the  $\alpha \rightarrow \sigma$  transition—besides, a higher wt.% of Cr results in higher precipitated  $\sigma$  but lower Cr-wt.% gives a lower fraction of the brittle  $\sigma$  phase in the final microstructure. This explains why the semi-dark  $\sigma$  fraction decreases from Layer 1 to 4. By moving to the upper layers, the number of reheating opportunities (and the length of the 500 – 800 °C exposure time) decreases, hence the chance of  $\alpha \rightarrow \sigma$  decreases. Another observable fact is that, as the Cr-wt.% decreases from Layer 1 to Layer 4 (Table 2), the volume fraction of the Cr-rich  $\alpha$ , i.e.,  $\alpha\text{-Cr}$ , falls, and that of the Fe-rich  $\alpha$ , i.e.,  $\alpha\text{-Fe}$ , increases. Therefore, layer 1 contains the highest, and layer 4 (Fig. 5c) has the lowest amount of this dark  $\alpha\text{-Cr}$  volume fraction among layers. In addition, the wt.% of the ferrite stabilizers (Mo and Si) has an increasing trend from Layer 1 to Layer 4 (Table 2), leading to the increment of the ferrite phase and increasing the light-etched  $\alpha\text{-Fe}$  area in the upper layers.

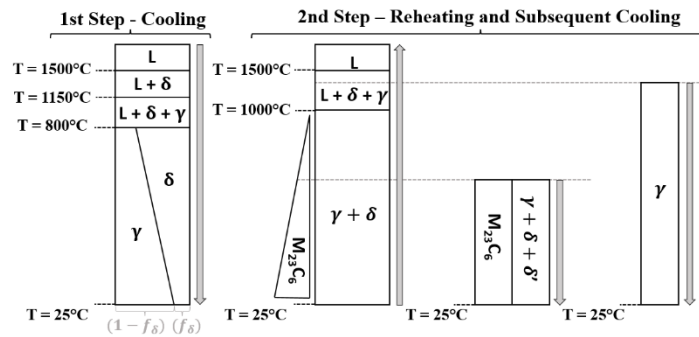
This diagram is modeled in the computational model based on the following diagrams. These diagrams are the linear forms of the phase diagram.

Table 4 Temperature- and Microstructure-Dependent Material Properties of Substrate (Rail) and Deposition Materials; Used in Fe Modeling of Additive Manufacturing (Lpd) Process

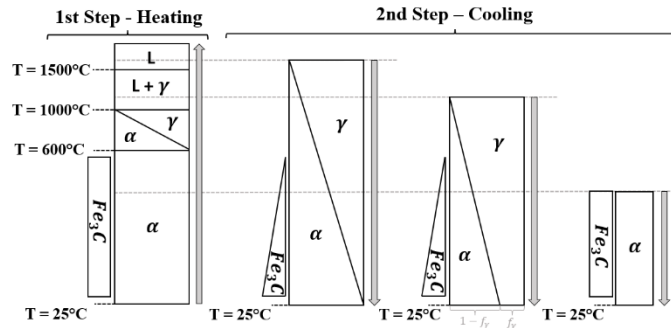
Material		T (°C)	E (GPa)	$\nu$	$\alpha$ (10-5/°C)	c (J/kg°C)	K (W/m°C)
304L Stainless Steel (Deposition Material)	$\delta$	25	-	-	-	-	-
		600	134	0.34	1.73	745	18.9
		1000	19	0.41	1.82	984	15.5
		1500	19	0.41	1.82	971	13.2



	$\gamma$	25	200	0.29	1.73	510	15.5
		600	141	0.37	1.87	687	22.4
		1000	19	0.45	1.97	953	28.7
		1500	-	-	-	-	-
C-Mn (880 grade) steel (Substrate Material)	$\alpha + Fe_3C$	25	203	0.26	1.2	434	60.5
		600	110	0.33	1.4	638	41.6
		1000	-	-	-	-	-
		1500	-	-	-	-	-
	$\gamma$	25	-	-	-	-	-
		600	-	-	-	-	-
		1000	19	0.4	1.47	886	12.6
		1500	19	0.4	1.47	886	12.6



(a)



(b)

Figure 9.8 A Schematic Diagram of the Microstructure Evolution Pattern Defined in Fe Modeling During the Additive Manufacturing (Lpd) Process, and its Cyclic Heating and Cooling for (A) Deposition Materials (304l Stainless Steel), and (B) Substrate (Rail).  $\Delta$ :  $\Delta$  Ferrite; A: A Ferrite; and  $\Gamma$ : Austenite

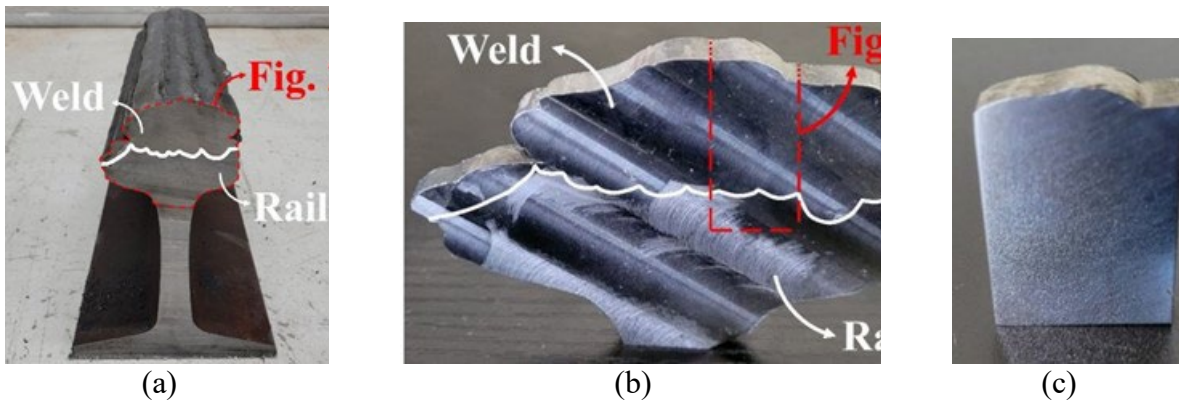
## Experimental validificatiuon

### Hardness test

The Rockwell C hardness test is the best scale for high/mild carbon steels, conforming to ASTM E18 [28]. The Rockwell C scale's applied major and minor loads are 150 kgf and 10 kgf, respectively. A LECO hardness tester is used for this purpose. Fig. 2e shows the assigned test plan on the transverse section, using the slices cut from the repaired rail shown in Fig. 2b based on the test protocol provided by the American Railway Engineering and Maintenance-of-way Association (AREMA) [29].

### Tensile test

The prepared tensile samples are illustrated in Fig. 2f and Fig. 2g. Four specimens are extracted from different regions of the base railhead and weld. The test method follows ASTM E8M[30], and the load requirement is assigned as per AREMA [29]. The test specimens are machined and dimensioned based on ASTM E8M. The standard test jig, recommended by ASTM E8M, is bundled with a hydraulic compression system as the major component of the test setup. A constant crosshead velocity of 2.5 mm/min is used for the tensile test.



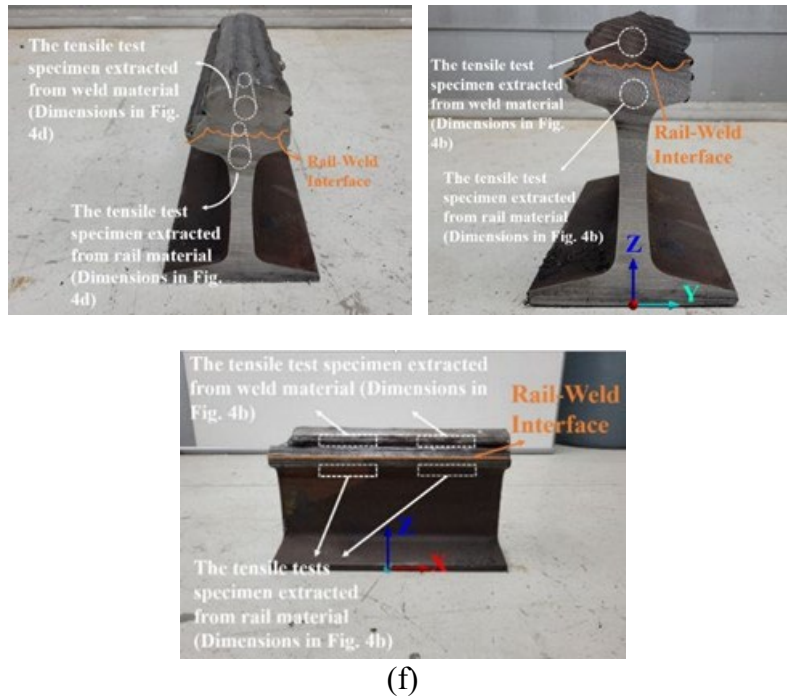
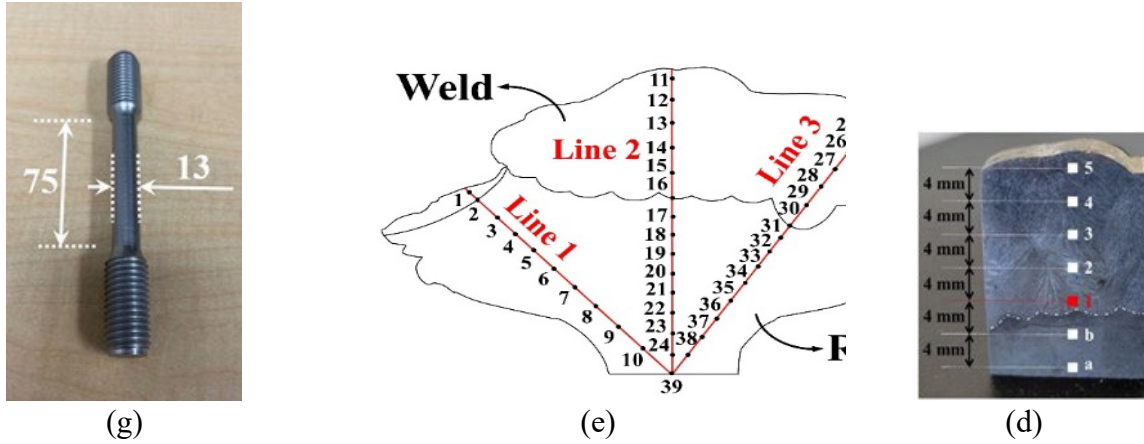


Figure 8 (a) the Repaired Rail; (b) the extracted slice from the repaired rail; (c) the extracted, polished XRD specimen from the slice; (d) the etched XRD specimen; (e) the hardness test plan; (f) Locations where the tensile specimens are extracted from the weld and the rail materials; (b) dimensions of a typical tensile test specimen (all dimensions are in millimeters)

### Conclusion

In this chapter, a 3D model was modified and a coupled finite volume-finite element method was utilized to investigate the thermo-mechanical effects of high-temperature additive materials on the rail during the SAW process for repair purposes on worn rails. Three cases were examined to analyze the impact of preheating on the residual thermal stress induced at the rail/additive interface. The key findings can be summarized as follows:

- 1- In phase one, the stress distribution revealed that in each pass of welding, the temperature result leans to a temperature, which in the second phase is used in the rest of the conclusion.
- 2- To mitigate the rapid cooling rate, Case II was introduced, where two hot plates were placed at the bottom of the railhead to maintain elevated temperatures at the rail and rail/additive interface for a longer duration. This approach led to a reduction of approximately 40% in the final induced thermal stress. However, both Case I and Case II exhibited a sudden increase in stress at the edges of the transversal line of the rail/weld interface. This phenomenon occurred because the edge points experienced the fastest cooling rate due to direct exposure to airflow and the ambient wall. Consequently, these points rapidly lost heat through various heat transfer mechanisms, including conduction, convection, and radiation.
- 3- To address this issue, Case III was introduced, where two additional hot plates were positioned at the sides of the railhead. By doing so, these hot plates shielded the edges of the interface from direct exposure to the ambient environment. It was observed that this approach effectively mitigated the residual stresses at the edges, eliminating the sudden stress increases observed in the previous cases.

Overall, the study demonstrated the influence of numerical methods in simulation of welding process on the distribution of residual thermal stress at the rail/weld interface. The findings highlighted the importance of controlling the cooling rate and providing thermal insulation to minimize thermal stresses and ensure the integrity of the printed components.

## References for chapter 10

- [1] S. R. Lewis, R. Lewis, and D. I. Fletcher, "Assessment of laser cladding as an option for repairing/enhancing rails," *Wear*, vol. 330–331, pp. 581–591, May 2015, doi: 10.1016/j.wear.2015.02.027.
- [2] W. J. Wang, J. Hu, J. Guo, Q. Y. Liu, and M. H. Zhu, "Effect of laser cladding on wear and damage behaviors of heavy-haul wheel/rail materials," *Wear*, vol. 311, no. 1–2, pp. 130–136, Mar. 2014, doi: 10.1016/j.wear.2014.01.011.
- [3] B. Paul, "A Review of Rail-Wheel Contact Stress Problems."
- [4] P. A. Montenegro and R. Calçada, "Wheel–rail contact model for railway vehicle–structure interaction applications: development and validation," *Railway Engineering Science*, 2023, doi: 10.1007/s40534-023-00306-4.
- [5] B. Liu and S. Bruni, "Analysis of Wheel-Roller Contact and Comparison with the Wheel-Rail Case," *Urban Rail Transit*, vol. 1, no. 4, pp. 215–226, Dec. 2015, doi: 10.1007/s40864-015-0028-3.
- [6] T. Telliskivi and U. Olofsson, "Contact mechanics analysis of measured wheel-rail profiles using the finite element method," in *Proceedings of the Institution of Mechanical Engineers, Part F: Journal of Rail and Rapid Transit*, 2001, pp. 65–72. doi: 10.1243/0954409011531404.
- [7] W. Yan and F. D. Fischer, "Applicability of the Hertz contact theory to rail-wheel contact problems."
- [8] W. Zhai, J. Gao, P. Liu, and K. Wang, "Reducing rail side wear on heavy-haul railway curves based on wheel-rail dynamic interaction," in *Vehicle System Dynamics*, Taylor and Francis

Ltd., May 2014, pp. 440–454. doi: 10.1080/00423114.2014.906633.

[9] “The\_Art\_and\_Science\_of\_Rail\_Grinding”.

[10] A. Kapoor, J. H. Beynon, D. I. Fletcher, and M. Loo-Morrey, “Computer simulation of strain accumulation and hardening for pearlitic rail steel undergoing repeated contact,” in *Journal of Strain Analysis for Engineering Design*, Jul. 2004, pp. 383–396. doi: 10.1243/0309324041223935.

[11] “d940f7aa37ad31fbbe878e79fd401199”.

[12] A. Mazzù, C. Petrogalli, and M. Faccoli, “An integrated model for competitive damage mechanisms assessment in railway wheel steels,” *Wear*, vol. 322–323, pp. 181–191, Jan. 2015, doi: 10.1016/j.wear.2014.11.013.

[13] M. N. SaifulAkmal and M. N. Wahab, “Characterization of UIC-54 Rail Head Surface Welded by Hardfacing Using Flux-Cored Steel Wire,” in *Lecture Notes in Mechanical Engineering*, Springer Science and Business Media Deutschland GmbH, 2021, pp. 763–775. doi: 10.1007/978-981-15-9505-9\_68.

[14] D. De Becker, J. Dobrzanski, M. Goh, and L. Justham, “Towards the development of a deposition technology for an automated rail repair system,” May 2020, pp. 100–102. doi: 10.31256/Vz2Jt4I.

[15] E. Kabo, A. Ekberg, and M. Maglio, “Rolling contact fatigue assessment of repair rail welds,” *Wear*, vol. 436–437, Oct. 2019, doi: 10.1016/j.wear.2019.203030.

[16] L. Xin, V. Markine, and I. Shevtsov, “Analysis of the effect of repair welding/grinding on the performance of railway crossings using field measurements and finite element modeling,” *Proc Inst Mech Eng F J Rail Rapid Transit*, vol. 232, no. 3, pp. 798–815, Mar. 2018, doi: 10.1177/0954409717693960.

[17] E. Mortazavian, Z. Wang, and H. Teng, “Effect of heat treatment on microstructure and hardness of a worn rail repaired using laser powder deposition,” *International Journal of Transportation Science and Technology*, vol. 11, no. 2, pp. 406–422, Jun. 2022, doi: 10.1016/j.ijst.2021.05.004.

[18] E. Mortazavian, Z. Wang, and H. Teng, “Finite Element Investigation of Thermal-kinetic-mechanical Evolutions during Laser Powder Deposition as an Innovative Technique for Rail Repair,” *International Journal of Advanced Manufacturing Technology*, vol. 118, no. 1–2, pp. 319–342, Jan. 2022, doi: 10.1007/s00170-021-07873-y.

[19] E. Mortazavian, Z. Wang, and H. Teng, “Measurement of Residual Stresses in Laser 3d Printed Train Rail Using X-Ray Diffraction Technique,” 2021.

[20] E. Mortazavian, Z. Wang, and H. Teng, “Repair of light rail track through restoration of the worn part of the railhead using submerged arc welding process,” *International Journal of Advanced Manufacturing Technology*, vol. 107, no. 7–8, pp. 3315–3332, Apr. 2020, doi: 10.1007/s00170-020-05208-x.

[21] B. L. Josefson and J. W. Ringsberg, “Assessment of uncertainties in life prediction of fatigue crack initiation and propagation in welded rails,” *Int J Fatigue*, vol. 31, no. 8–9, pp. 1413–1421, Aug. 2009, doi: 10.1016/j.ijfatigue.2009.03.024.

[22] A. Masoudi, M. Davarpanah Jazi, M. Mohrekesh, and R. Masoudi Nejad, “An investigation of rail failure due to wear using statistical pattern recognition techniques,” *Eng Fail Anal*, vol. 134, Apr. 2022, doi: 10.1016/j.engfailanal.2022.106084.

[23] H. Desimone and S. Beretta, “Mechanisms of mixed mode fatigue crack propagation at rail butt-welds,” *Int J Fatigue*, vol. 28, no. 5–6, pp. 635–642, May 2006, doi: 10.1016/j.ijfatigue.2005.07.044.

- [24] A. Skyttebol, B. L. Josefson, and J. W. Ringsberg, "Fatigue crack growth in a welded rail under the influence of residual stresses," *Eng Fract Mech*, vol. 72, no. 2, pp. 271–285, Jan. 2005, doi: 10.1016/j.engfracmech.2004.04.009.
- [25] R. Masoudi Nejad, Z. Liu, W. Ma, and F. Berto, "Fatigue reliability assessment of a pearlitic Grade 900A rail steel subjected to multiple cracks," *Eng Fail Anal*, vol. 128, Oct. 2021, doi: 10.1016/j.engfailanal.2021.105625.
- [26] "Submerged\_Arc\_Welding".
- [27] S. Bharathi, A. Arul, M. Moshi, S. R. Sundara Bharathi, R. Rajeshkumar, and R. Kumar, "Factors Influencing Submerged Arc Welding On Stainless Steel-A Review," vol. 11, no. 2, 2016, [Online]. Available: [www.arpnjournals.com](http://www.arpnjournals.com)

## **10. Chapter 10 ADDITIONAL MECHANICAL AND METALLURGICAL ASSESSMENT OF SUBMERGED ARC SURFACED RAIL**

The railhead surface is constantly subject to several destructive interactions, such as wheel-rail rolling contact fatigue [1], frictional burns due to wheel slippage [2], and ballast flying damage [3]. Therefore, a practical repair method may be applied to restore the damaged surface of the railhead to ensure the comfort and security of riding the trains. Minor surface damages on a railhead can be rehabilitated using surface grinding, an easy railway maintenance technique appropriate for immediate and extensive application [4]. Although this method can effectively eliminate the point defects, the grinding length should be long enough to compensate for the vertical winding impact. Hence, grinding is not a sensible repair in case of moderate railhead surface damage. Instead, removing the damaged area and rebuilding the lost material using an additive manufacturing technique is practical. This overlay rail repair idea originated from a patent by Kral et al. in 2004 [5]; ever since, several have been devoted to investigating various build-up methods for repairing conventional rails in different countries.

Overlay arc welding of UIC60 rails is assessed by a couple of research groups in Korea [6-8]. Feng et al. [9] analyzed the pros and cons of online welding and post-heat treatment of standard rails in China. Another research study in China focused on surface repairing U75V rails using laser-directed energy deposition [10]. In Thailand, Suwanpinij et al. [11] demonstrated improved surface properties of surface-welded R260 and R350HT rails compared to the base rail material. Srikarun [12] also investigated the abrasive wear performance of R260 rails that are repaired by shield metal arc welding (SMAW). Repairing of damaged surface of UIC-54 rails used in the Malaysia railway network using SMAW is investigated by Saiful Akmal and Wahab [13]. A research group thoroughly explores laser cladding of hypereutectoid Australian rails and its upgrading and downgrading effects at Monash University [14]. De Becker et al. [15] are developing a mobile system for automated on-site repair of the damaged railway network in the United Kingdom. A numerical model investigating the rolling contact fatigue performance and material defects of a weld-repaired rail is developed by Kabo et al. [16] in Sweden. Another valuable numerical study was conducted by Xin et al. [17] in the Netherlands, in which repair welding and grinding of standard European rails are surveyed using finite element modeling.

Regarding the investigation of the standard rails used in the United States railway system, the current team is the only research group thus far that has focused on repairing them using overlay weld techniques. One line of investigation was solely devoted to laser cladding of damaged rail surfaces, both the light transit rails [18,19] and heavy freight/passenger rails [20] in the United States. A separate line of research assessed the submerged arc welding (SAW) technique for repairing light rails [21]. The current paper is the first study focused on evaluating the mechanical and metallurgical properties of a standard U.S. heavy rail repaired using SAW.

Each type of rail repair method, i.e., a laser-based method like laser cladding or an arc-based method like SAW, has its benefits and drawbacks. Therefore, without in-depth investigation, a specific method cannot be immediately determined as the best option in all mechanical and metallurgical aspects. Instead, the most proper technique should be determined based on factors such as rail type, repair quality, cost, and railway network occupation time.

Surface repairing a damaged railhead has significant advantages over the conventional



replacement approach, especially since it is much easier to implement and does not require manipulating and rebuilding the rail infrastructure. Although some minor surface grinding and cutting are required for overlay welding on the railhead surface, it allows the rail base to maintain its original strength. Nevertheless, it is shown in quite a lot of former studies [22-26], including authors' studies [18-21], that a surface welded rail is much more vulnerable to cracking and premature failure than an integral parent rail. Therefore, it is necessary to thoroughly investigate the strength properties, Hardness, residual stress, and distribution of inclusions, pores, and cracks in a weld-repaired rail. However, no study has been published investigating the SAW-repairing of heavy-duty rails used in the standard railway network of the U.S. As was mentioned in the former research as well [21], there are several potential arc-based methods for surface welding, such as SMAW, gas tungsten arc welding (GTAW), submerged arc welding (SAW), and plasma arc welding (PAW). However, SAW is the most proper method for multi-layer, high-thickness welding while delivering the highest quality and productivity [27,28].

Through some experiments, this study investigates the mechanical and metallurgical properties of a SAW-repaired standard U.S. heavy rail. These tests include micro-hardness Measurement, X-ray diffraction (XRD) for residual stress measurement, microstructural evaluation using an optical microscope (O.M.) and scanning electron microscope (SEM), and tensile test. First, the material properties of the rail base, weld wire, and flux particles are presented. Second, a summarized description of the SAW process and incorporated processing parameters are given. Sample preparation strategies for each experiment are then thoroughly described. Finally, the results are presented and discussed, and some solutions to modify the existing properties and mitigate the residual stresses are suggested for future studies.

## **2. Experimental**

### **2.1. Materials**

The to-be-repaired rail is a worn 136RE rail utilized in most freight/passenger railway networks across the United States. The studied specimen is a 30-cm cut of the worn rail, as shown in Fig. 1a. Chemical composition of the high-carbon 136RE rail steel is listed in Table 1.

The depositing wire for the SAW process is chosen to be a 1/8-in Lincore 40-S hard-facing submerged arc wire because of its distinguished rolling and sliding wear properties. In addition, this wire is specifically compatible with carbon steel and appropriate for depositing up to 5 layers. Table 1 gives the chemical composition of the utilized SAW wire. The neutral Lincolnweld 801 submerged arc flux is used as the recommended and compatible flux, of which the chemical composition is demonstrated in Table 2.

The surface of the worn railhead is milled and flattened for a better SAW process on a flat substrate. The milled surface is also ground, polished, and cleaned with acetone to remove all loose mill scales, rust, and micro contaminants before starting the SAW process. The milled rail is shown in Fig. 1b. The SAW-surfaced rail, i.e., surfaced rail, is shown in Fig. 1c. This is the final product on which all the mechanical and metallurgical assessments will be conducted.

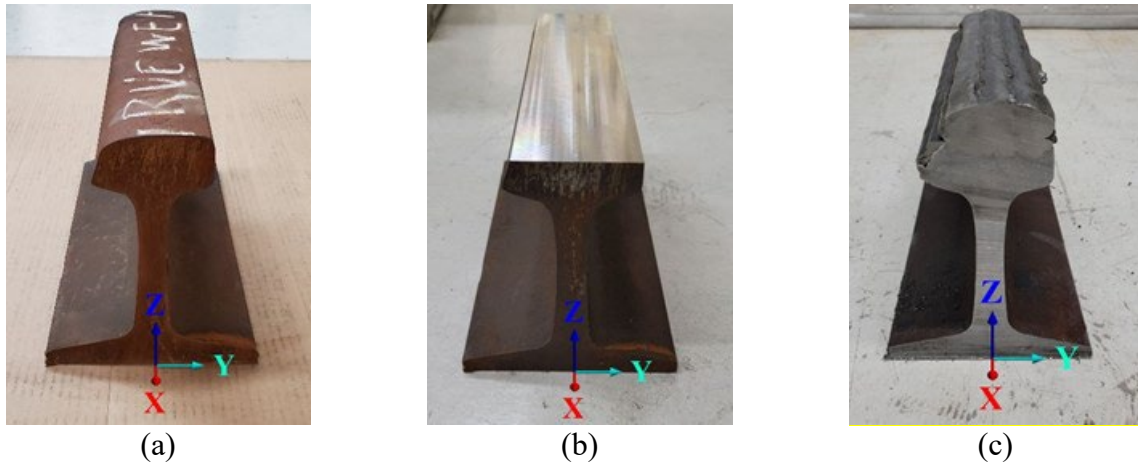


Figure 10.1 (a) The to-be-repaired 136RE worn rail, (b) milled rail, and (c) repaired rail

**Table 1** Chemical composition of the rail and the SAW wire (wt.%)

Material	Fe	C	Cr	Mn	Mo	Si	Ni	P	S
Rail	Bal.	0.80	0.03	0.23	-	0.04	0.14	0.01	0.01
		± 0.06	± 0.01	± 0.03	-	± 0.01	± 0.04	± 0.005	± 0.005
Wire	Bal.	0.12	0.50	2.75	0.85	3.30	-	-	-
		± 0.05	± 0.03	± 0.30	± 0.05	± 0.20	-	-	-

**Table 2** Chemical composition of the neutral Lincolnweld 801 submerged arc flux (wt.%)

SiO <sub>2</sub>	CO <sub>2</sub>	CrO	MoO <sub>3</sub>	MnO	Fe <sub>2</sub> O <sub>3</sub>
10.0	21.2	8.9	18.4	14.2	22.7
± 0.9	± 0.8	± 0.2	± 0.9	± 0.8	± 1.0

## 2.2. Submerged Arc Welding (SAW)

The featured difference between regular arc welding and SAW is the covering flux. The wire and the arc are technically buried under flux grains to stay immune from oxidation. Another advantage of submerging the welding spot into the flux stream is that it stays free of any extreme radiation heat loss, which keeps it a very clean weld. Blocking potential heat loss mechanisms, such as radiation, convection, or scattering the transferring energy from wire to the rail, helps increase energy efficiency by close to 90% or even higher. The valuable outcomes of such a high efficiency are great weld reliability and a high deposition rate.

An arc is developed between the wire as the filler material in the SAW process. This arc applies from the wire to the railhead as the substrate. At the same time, flux grains are flown on and around the arc area through a hopper. Therefore, a covering envelope is developed at the arc zone to solidify the melt pool where the arc is burnt on the railhead surface. The flux grains near the envelope melt, firm, and establish a thin coat on the weld, which is called slag and will be removed

after finishing the SAW process. An open-circuit voltage of 25~36 V, 150 A of weld current, 23 mm/s of travel speed, and 21 mm/s of wire feed rate are utilized for the current SAW process, i.e., overlay repairing of damaged railhead surface. Further details and explanations about the SAW process in tandem with a schematic figure can be found in the former study [21].

## 2.3. Sample preparation and test method

### 2.3.1. XRD residual stress measurement

The experiments' first step starts with preparing samples for XRD stress measurement, the stress distribution all over the weld material, and part of the rail material. Slices used to extract samples are cut, as shown in Fig. 2b. A rectangular specimen is extracted from the piece to contain all the weld layers, the rail-weld interface, and the rail. Fig. 2c shows the extracted XRD specimen.

The XRD stress measurement on the specimen surface is performed using a Bruker D8 Discovery X-ray diffractometer that contains a  $\text{CuK}\alpha$  radiation source and a constant 1.5406 Å wavelength. The voltage and current of the X-ray tube are 40 kV and 40 mA, respectively. The measurement area is controlled through a 1-mm pinhole collimator. Based on the study by Ghasri-Khouzani et al. [31], an X-ray beam originated from a  $\text{CuK}\alpha$  source and aimed at a non-austenitic steel surface has an average penetration depth of 5 µm. Accordingly, to mitigate the surface roughness and to ensure that there are no surface spikes taller than 5 µm to interrupt the X-ray beams, pasted diamond suspensions on SiC papers are used to polish the specimen down to 1 µm. The extracted, polished specimen is visible in Fig. 2c. A thickness of 750 µm is removed from the sample surface due to polishing.

The sample is etched to remove the relaxed residual stresses on the polished sample surface due to cutting and polishing. The incorporated etchant is an HCL-based solution made from HCL (30 ml),  $\text{H}_2\text{O}_2$  (1.5 ml), and  $\text{H}_2\text{O}$  (10 ml). The etched sample is presented in Fig. 2d. Each course of 30-second etching removes around 50 µm of the sample thickness. Then, the etching course is repeated until the XRD-measured stress on the surface is stabilized and externally-induced residual stresses are entirely removed. The related graphs of this step of testing validation will be presented and discussed in the Results section. The locations where residual stress is measured using XRD are shown in Fig. 2d as numbered white spots on the etched sample, except for spot 1, shown in red. The stress at spot 1 is frequently measured at each sample preparation step, i.e., before and after polishing and after each etching course. This Measurement ensures that the existing error factors are eliminated, i.e., surface roughness and externally-induced residual stresses. Once the sample is etched enough that the measured stress at spot 1 is stabilized, stress at the other spots is measured.

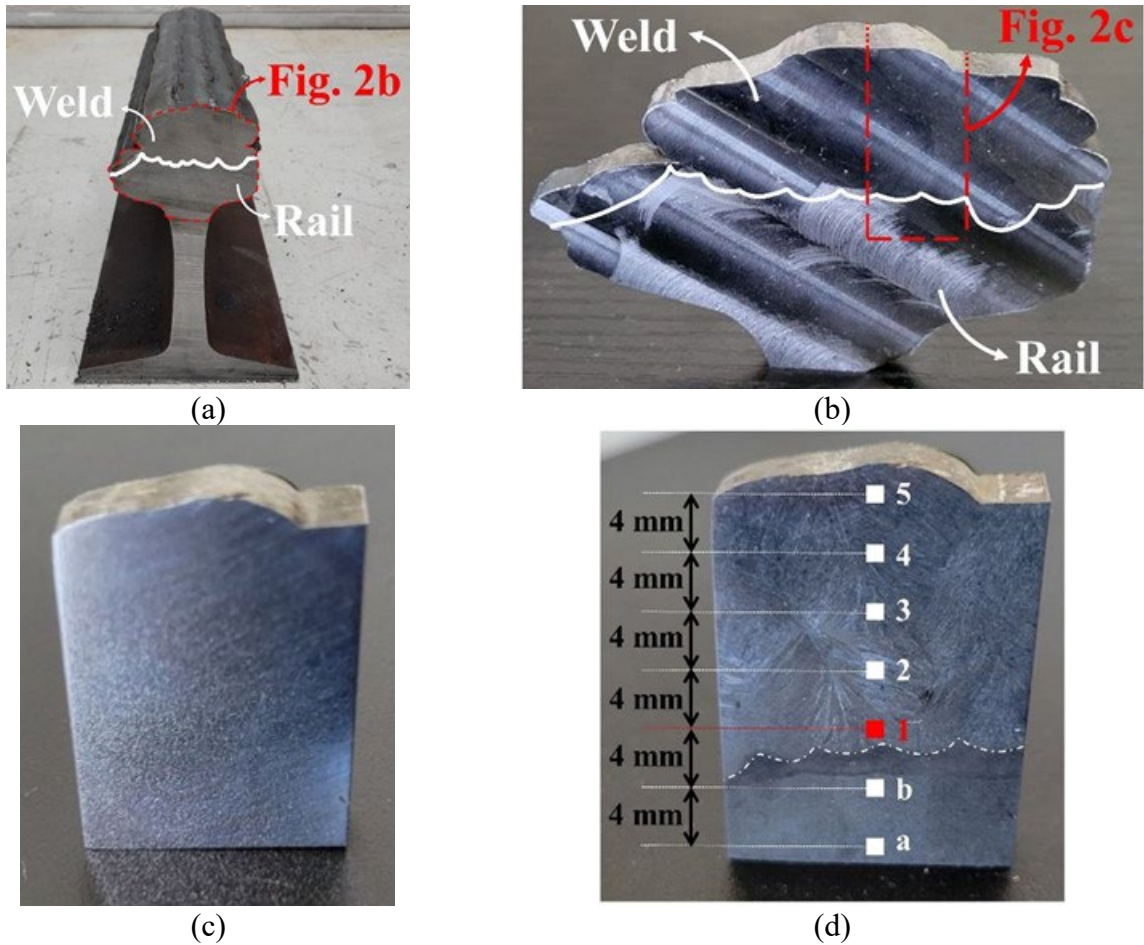


Figure 10.2(a) Repaired Rail, (b) The extracted slice from the repaired rail, (c) the extracted, polished XRD specimen from the slice, and (d) the etched XRD specimen

As another contribution to validating the XRD test results, surface roughness is measured at each step of sample preparation to ensure that it does not exceed  $1\ \mu\text{m}$  after polishing and etching. A Dektak 6M stylus profiler is used to do so. The profiler has a diamond-tip stylus with a diameter of  $25\ \mu\text{m}$ . At each run, the stylus applies a 10 mg contact load on the surface and scans a 2-mm length for 13 seconds, which gives 3,900 data points. The roughness of the gained profile data has a horizontal resolution of  $1 \times 10^{-5}\ \mu\text{m}$  and a vertical resolution of  $1 \times 10^{-5}\ \mu\text{m}$ . The existing noises are removed from the raw data using a cubic spline filter to reach the roughness profile accuracy. The study in [32] gives more details about this noise-removal method.

### 2.3.2. SEM/OM analysis

The etched sample shown in Fig. 2d and the destructed samples under tensile tests, which will be described in later sections, are used for O.M. and SEM metallographic examination.

O.M. morphology is carried out using a Leica DM750M optical microscope, and SEM

investigation is performed through a JEOL JSM-5610 scanning electron microscope. Chemical composition variations between different weld layers, rail, and heat-affected zone (HAZ) are tracked with an Oxford ISIS electron-dispersive X-ray spectroscopy (EDS) detector coupled with the SEM device.

### 2.3.3. Hardness test

The third step is to measure the Hardness all over the repaired railhead, including weld material and base material, using the slices cut from the repaired rail shown in Fig. 2b and Fig. 3a.

Rockwell C hardness test is the best scale for high/mild carbon steels, conforming to ASTM E18 [29]. The applied major and minor loads for the Rockwell C scale are 150 kgf and 10 kgf, respectively. A LECO hardness tester is used for this purpose in this regard. Fig. 3b shows the assigned test plan on the transverse section of the slice. The numbered black spots show the measurement locations. The red lines and black measuring spots in Fig. 3b follow the standard test protocol provided by American Railway Engineering and Maintenance-of-way Association (AREMA) [30].

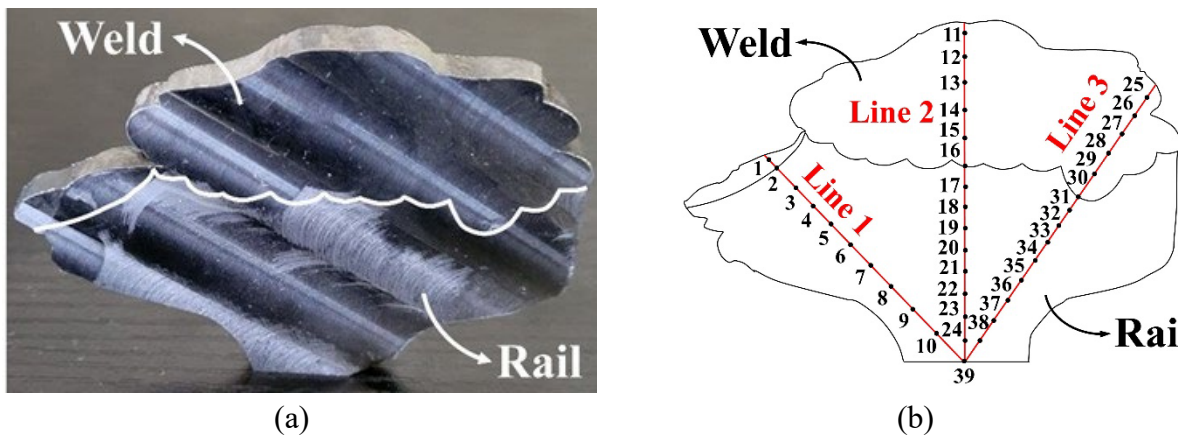


Figure 10.3 (a) Extracted slice as the hardness test specimen and (b) the hardness test plan

### 2.3.4. Tensile test

The prepared tensile samples are illustrated in Fig. 4. Four specimens are extracted from different regions of the base railhead and weld. The test method follows ASTM E8M [33], though the load requirement is assigned as per AREMA [30]. The test specimens are machined and dimensioned based on ASTM E8M. The standard test jig recommended by ASTM E190 [34] and bundled with a hydraulic compression system as the major components of the test setup. In addition, 2.5 mm/min of constant crosshead velocity is used for the tensile test.



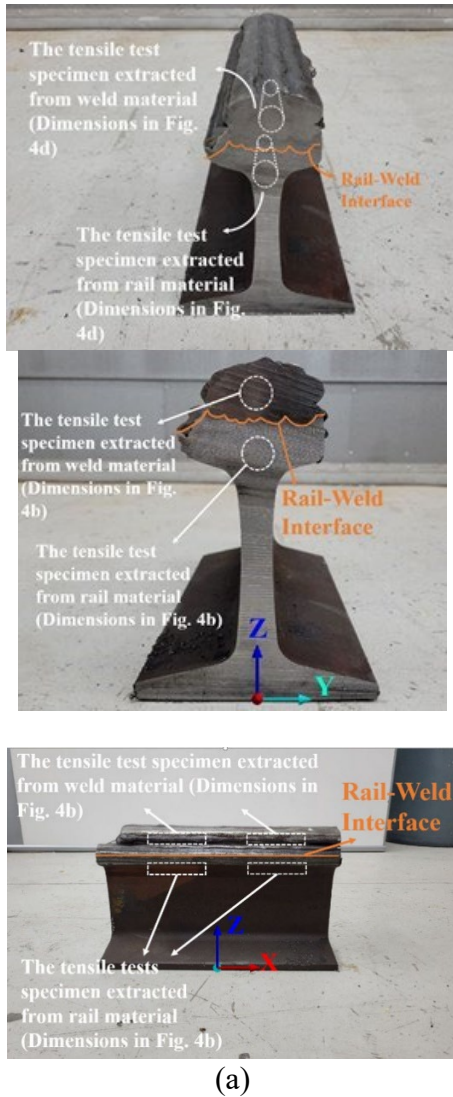


Figure 10.4(a) Locations of extracting the tensile specimens from weld and rail materials, (b) typical tensile test specimen dimensions (all dimensions are in millimeters), (c) the tensile test specimen fixed in the machine test jigs.

### 3. Results and Discussion

#### 3.1. XRD residual stress measurement

##### 3.1.1. Surface Roughness

A stylus profiler measures the XRD specimen's surface roughness before polishing in the as-built condition, after polishing, and after the first step of etching to ensure that the height of the surface spikes does not exceed  $5 \mu\text{m}$  (see sec. 2.3.1).

The measured surface profiles are given in Fig. 5. A horizontal dashed line represents the graphs' median plane at the zero- $\mu\text{m}$  level. A considerable roughness in the order of  $25\text{-}50 \mu\text{m}$  is seen for

the As-built specimen in Fig. 5. Spikes are located where a positive roughness (higher than the median plane) is captured, and pits exist where there is a negative roughness (lower than the median plane). This order of  $\pm 50 \mu\text{m}$  suggests that the X-ray beams with only a  $5 \mu\text{m}$  penetration depth will be interrupted by the surface spikes and pits, so any stress measurement will not be reliable.

The surface roughness of the Polished specimen in Fig. 5 shows a  $0.4\text{-}0.8 \mu\text{m}$  order of roughness, which is significantly lower than the  $5\text{-}\mu\text{m}$  penetration depth of the X-ray beam. The Etched specimen also offers the same  $0.4\text{-}0.8 \mu\text{m}$  order of roughness and proves that etching will not affect the surface finish quality that much to be a concern for the XRD test. This matter promises that the surface roughness will not affect the X-ray stress measurement accuracy on the etched specimen.

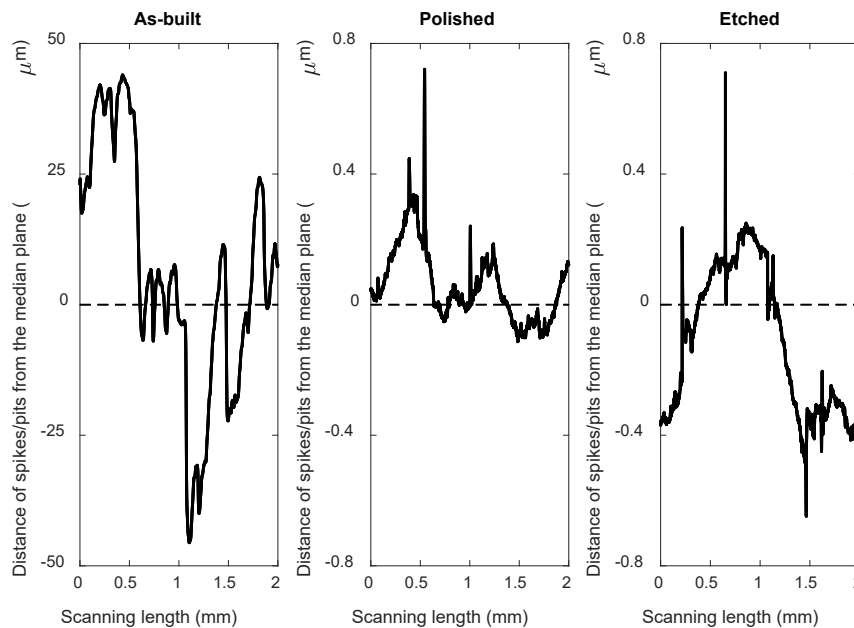


Figure 10.5 Surface roughness measurement of the XRD specimen at different conditions; before polishing (i.e., As-built), after polishing (i.e., Polished), and after etching (i.e., Etched)

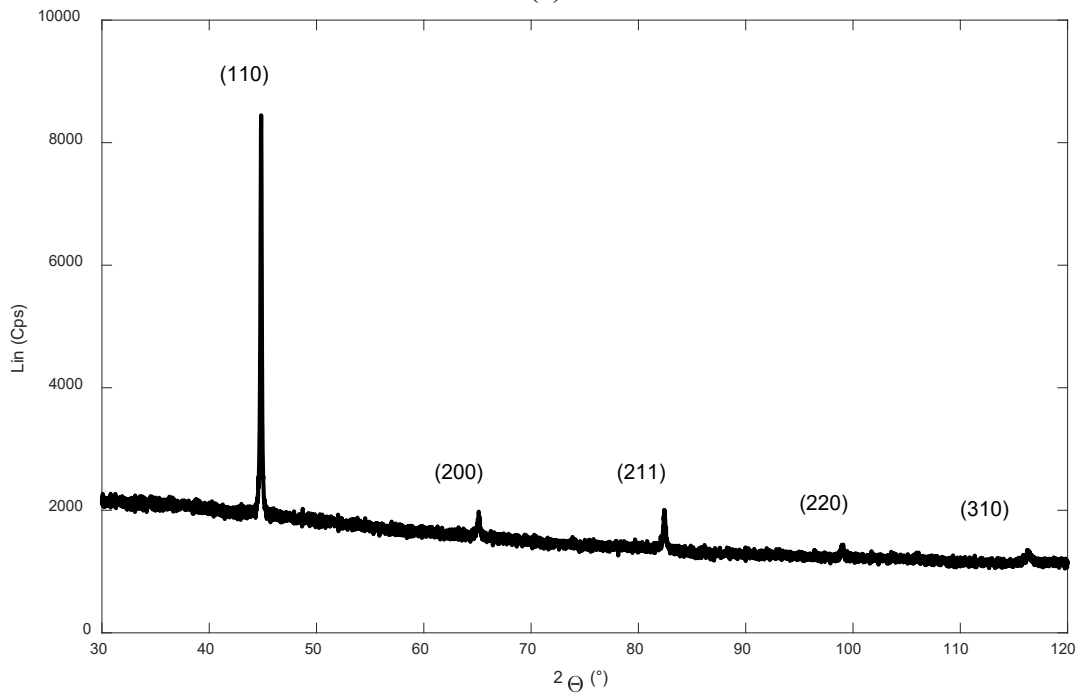
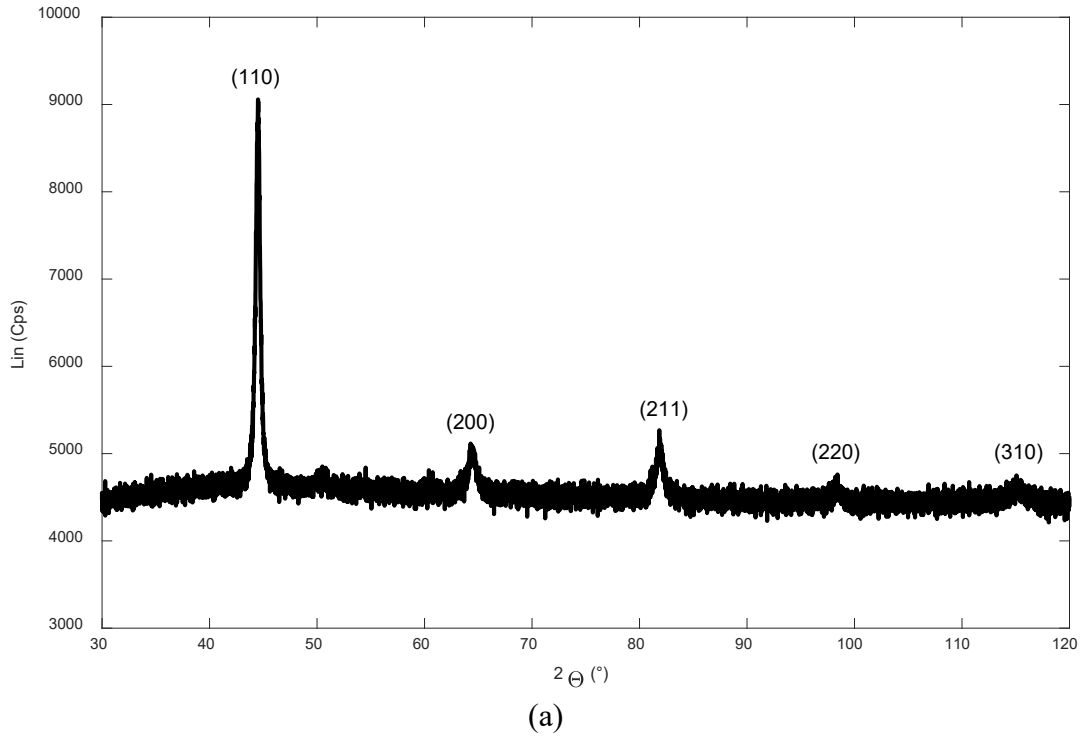
### 3.1.2. Stress measurement strategy

A typical XRD phase scan analysis from the weld and rail materials is given in Figs. 6a and 6b, respectively. As it is intended to obtain a precise measurement of strain owing to lattice spacing variations, the residual stresses are recommended to be measured at the highest possible diffraction angles as long as it does not considerably affect the measurement accuracy [35].

According to Fig. 6a, the stress in the weld section (points 1 to 5 in Fig. 2d) is measured at the BCC(310) diffraction peak (diffraction angle ( $2\theta$ ) of  $115.1^\circ$ ). Furthermore, residual stress measurement in the rail section (points *a* and *b* in Fig. 2d) is conducted at the diffraction peak of BCC(310), which is located at the diffraction angle of  $116.2^\circ$  (Fig. 6b).



The  $\sin^2\psi$  method is utilized for stress calculation. Starting from  $\psi=0^\circ$  and stepwise adding five equal offsets up to  $\psi=45^\circ$ , a total of six  $\psi$  points are taken into account. The assigned range of diffraction angle for the XRD measurements is  $114^\circ \leq 2\theta \leq 118^\circ$  with a stepwise increment of 0.02, where 0.8 seconds per step of counting accumulation is employed. Sliding gravity is used for the peak evaluation, and data correction for Lorentz-polarization background and absorption is undertaken.



(b)

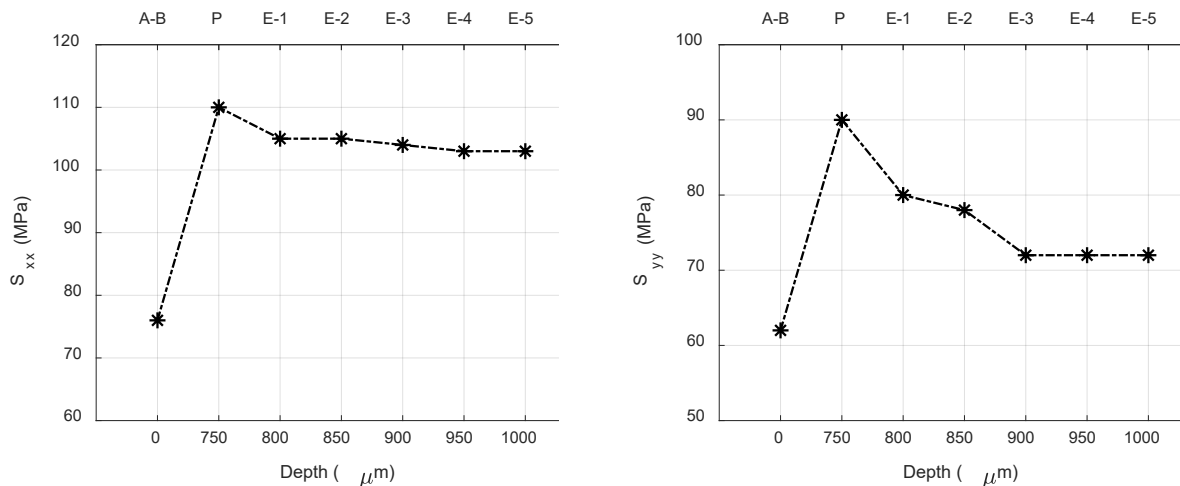
Figure 10.6 XRD phase scan analysis at the (a) weld section and (b) rail section of the repaired rail

### 3.1.3. Measurement Verification

The Polished sample (shown in Fig. 2c) is etched in several steps until the measured stress is stabilized. This stabilization happens when further layer removal would not result in sensible changes in the measured stresses. This action is to validate residual stresses measurement using XRD and ensure no additional residual stresses affect the results,

Per Fig. 2d, spot 1 (shown in red) is picked as the base point at which stress measurement is performed at different stages of the specimen. These stages include the As-built stage (A-B in Fig. 7), Polished (P in Fig. 7), and Etched (E1-E5 in Fig. 7, the sample is etched five times after polishing, indicated as E-1 after the first time of etching, E-2 after the second time of etching, and so on. The Depth parameter in Fig. 7 represents the distance of the existing surface of the specimen from the base surface in the As-built condition. For example, polishing removed 750  $\mu\text{m}$  from the As-built surface, and each step of etching removes another 50- $\mu\text{m}$  layer from the specimen surface. The measured in-plane longitudinal and transversal stresses, i.e.,  $S_{xx}$  and  $S_{yy}$  (refer to Fig. 1 to configure the  $x$  and  $y$  coordination), are shown in Figs. 7a and 7b, respectively. Polishing could cause a shifting of around 45-50% in the measured stress value. The first reason for such an intensive increase in measured stress can be to remove the interrupting surface spikes, let the X-ray beams penetrate enough to the surface, and measure the existing residual stresses instead of scattering them around. The second reason can be inducing the surface's extra residual stresses during polishing. In addition, the sample is also etched to remove that extra portion of the residual stresses, i.e., the one applied through polishing.

Fig. 7 shows that five etching steps could decrease the measured  $S_{xx}$  and  $S_{yy}$  by 7% and 20%, respectively. A difference between the values of P and E-5 can be seen in this diagram. This difference is technically due to the removing residual stresses caused by polishing. It can be interpreted that Figs. 7a and 7b show no difference between the measured stress in the E-4 and E-5 stages for both the  $S_{xx}$  and  $S_{yy}$ . Hence, the E-5 specimen is used hereafter for measuring stress at the rest of the spots shown in Fig. 2d.



(a)

(b)

Figure 10.7 Measured residual stresses using the XRD method at spot 1 (shown in red in Fig. 2d) along the (a) longitudinal and (b) transversal directions at different stages of the specimen; As-built (A-B), Polished (P) and first to fifth time of etching (E-1 to E-5)

### 3.1.4. Measured stress distribution

Longitudinal and transversal residual stresses, i.e.,  $S_{xx}$  and  $S_{yy}$ , are measured on the E-5 specimen at all the spots shown in Fig. 2d, and Fig. 8 shows their results. The lower  $x$ -axis shows the distance of each spot from spot 5 (based on Fig. 2d), and the upper  $x$ -axis marks the corresponding spot number. It should be noted that spots 1 to 5 are located in the weld zone, spot 5 is the farthest, spot 1 is the closest spot to the rail-weld interface, and spots  $a$  and  $b$  are in the rail zone, where spot  $b$  is closer to the rail-weld interface. From the graphs shown in Fig. 8, the rail-weld interface falls somewhere between 16 to 20 mm from spot 5, i.e., between spots 1 and  $b$ .

According to Fig. 8a, the weld zone carries only tensile  $S_{xx}$  with the maximum values of 91 and 103 MPa located at spots 5 and 1, respectively, representing the top surface of the weld and the area near the rail-weld interface, respectively. The minimum tensile  $S_{xx}$  of 55 MPa in the weld area is found in the middle section at spot 3. A tensile-to-compressive stress transition happens at the rail-weld interface, i.e., from spot 1 to  $b$ , where the maximum tensile  $S_{xx}$  of 103 MPa in the weld section transforms to the maximum compressive  $S_{xx}$  of 10 MPa in the rail section. It is seen that  $S_{xx}$  in the lower areas of the rail (i.e., point  $a$ ) switches back to tensile but stays at low and relatively negligible values.

Regarding the transversal stress ( $S_{yy}$ ) in Fig. 8b, almost the same pattern can be figured out. The maximum tensile  $S_{yy}$  values of 78 and 75 MPa in the weld materials are found at spots 5 and 1, respectively. A compressive stress of 2 MPa is located at spot  $b$ , in the rail area close to the rail-weld interface. A near-zero  $S_{yy}$  happens in lower areas of the rail at spot  $a$ .

At the time of starting the SAW process, a sudden temperature rise happens, which leads to a rapid expansion of the rail surface. However, the deposited weld layer tends to shrink due to fast cooling through convection with the air and conduction with the bulk rail substrate. The collision of the two phenomena causes applied stresses due to expansion-shrinkage interactions. These stresses are tensile from rail to weld and compressive from weld to rail (spots 1 and  $b$  in Fig. 8, respectively). After depositing the first weld layer, the substrate is already at a high temperature, so depositing other layers will not experience high tensile stress similar to the first layer. This matter explains the lower tensile stresses in the middle layers (spots 2 to 4 in Fig. 8). However, the last weld layer, i.e., the top layer, cools down faster than the lower layers due to direct exposure to the air. Besides, unlike the lower weld layers, the top layer cannot relieve a portion of its residual stress by getting reheated owing to depositing a new layer on the top. That is why the tensile stress grows again in the upper areas of the weld (spot 5 in Fig. 8).

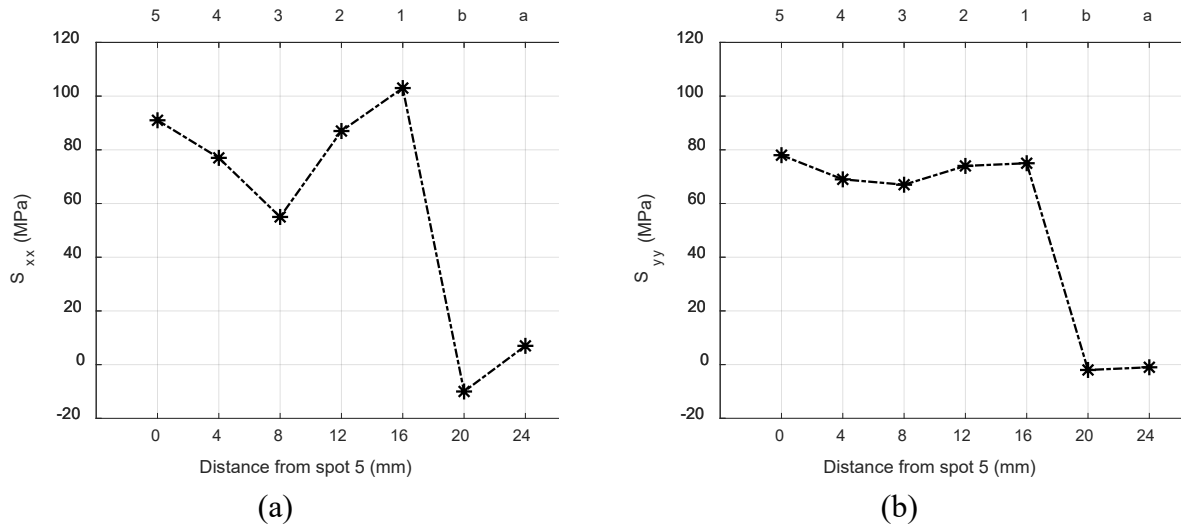


Figure 10.8 Measured (a) longitudinal and (b) transversal residual stresses using XRD on the E-5 specimen at all the spots shown in Fig. 2d; the upper  $x$ -axis shows the spot numbers, and the lower  $x$ -axis shows their distance from spot 5

### 3.2. Microstructural Analysis

Optical Microscope (O.M.) captures from the etched specimen, which is extracted from the repaired rail, are shown in Fig. 9. In Fig. 9a, the etched specimen is divided into three areas of weld, heat-affected zone (HAZ), and rail. It is seen in Fig. 9b that the weld area contains four layers with different compositions/orientations in the microstructure. A closer look into the microstructure of the fourth, third, second, and first weld layers is shown in Figs. 9c, 9d, 9e, and 9f, respectively. Close-up O.M. captures from the HAZ, and rail can be found in Figs. 9h and 9j, respectively. The interfaces between weld and HAZ and between HAZ and rail are in Figs. 9g and 9i, respectively. The distribution of the chemical elements throughout the examined areas in Fig. 9 is given in Table 3.

Fig. 9j shows that a dendritic thin lamellar pearlite microstructure is detectable for the rail. It is obviously seen that the rail microstructure contains coarse, light islands of pro-eutectoid ferrite and dark-etched, dendritic pearlite lamellae that are randomly oriented. Sporadic signs of dissipated carbides are also traceable over the pearlitic-ferritic matrix.

Per the  $Fe-Cr$  phase diagram shown in Fig. 10, the utilized Lincore 40-S weld wire with around 0.5 weight percentage ( $wt.\%$ ) of chromium (referring to Table 1) has a mixture of BCC phases containing  $Fe$ -rich (BCC) and  $Cr$ -rich (BCC') alloy compounds at room temperature. The XRD analysis showed the weld material's general BCC phase (Sec. 3.1.2). A linked investigation and four weld layers' chemical distribution resulted in no chance of austenite ( $\gamma$ ) formation. The link investigation can be found as a dotted line in Fig. 10. Table 3 also shows weld layers' chemical distributions with a  $Cr$ - $wt.\%$  interval of 0.32 to 0.47. The  $\gamma$  loop falls between 0 to 0.12  $wt.\%$  of  $Cr$  content, which is not contained in the current case study. Hence, it is guaranteed that none of the distinguished phases in the O.M. morphology represent any austenite. A close inspection of the weld layers in Figs. 9c to 9f suggest three discernible regions, primarily categorized based on their brightness appearances. The light region represents the Alpha-ferrite ( $\alpha$ - $Fe$ ) phase, the dark

network stands for the acicular Alpha-chromium ( $\alpha$ -Cr) phase, and the brittle sigma ( $\sigma$ ) phase appears as a semi-dark zone. A general rule of thumb attributed to the *Fe-Cr* phase diagram is that as the *Cr-wt.%* increases from 0 to 1, a light-etched to dark-etched transition occurs; the austenite with the lightest appearance in an HCL-etched carbon steel nucleates at  $0 \leq Cr-wt.\% < 0.12$ , then, at  $Cr-wt.\% \geq 0.12$ , a combined  $\alpha$ -Fe +  $\alpha$ -Cr phase forms, which starts with the dominance of the light-etched  $\alpha$ -Fe at  $Cr-wt.\%=12$  and smoothly transforms to a dark-etched,  $\alpha$ -Cr-dominant compound as the *Cr-wt.%* leans towards 1. Table 3 shows a declined flow of *Cr-wt.%* from Layer 1 to 4. The liquidus weld drops at 1600-1700°C, and the preheated railhead surface has a temperature of 200-300°C, so the weld materials start to experience an initially fast cooling procedure down to 500-700°C during the first layer of welding on the railhead surface. The temperature range with a closer tendency to the railhead temperature because of the large amount of bulk material. It then remains at that temperature interval for a while. Anyway, once the second layer is started to weld on top of the first layer, Layer 1 is reheated and has a chance for long exposure at a higher temperature range, i.e., 700-1000°C. In the meantime, Layer 2, with a higher initial substrate temperature (i.e., 500-700°C), remains at elevated temperatures around 700-1000°C until the third layer starts to get welded on top of it. This trend proves that the top layers are exposed to higher ranges of temperature, i.e., higher than 500-800°C. Based on Fig. 10, for the utilized *Fe-Cr* weld alloy where *Cr-wt.%* is measured to be in the 0.32-0.47 range, long exposures to 500-800°C give enough time for  $\alpha \rightarrow \sigma$  transition. The longer the exposure time, the higher the fraction of  $\alpha$  would have the opportunity to transform to the brittle  $\sigma$ . Besides, higher *wt.%* of Cr, i.e., closer to 0.47, leads to a higher chance of complete  $\alpha \rightarrow \sigma$  transition at 500-800°C, while lower *Cr-wt.%*, i.e., closer to 0.32, yields to partial  $\alpha \rightarrow \sigma$  transformation. In other words, higher *wt.%* of Cr results in higher precipitated  $\sigma$  but lower *Cr-wt.%* gives a lower fraction of the brittle  $\sigma$  phase in the final microstructure. This fact clearly explains why the fraction of the semi-dark  $\sigma$  area decreases from Layer 1 (Fig. 9f) to Layer 2 (Fig. 9e), to Layer 3 (Fig. 9d), to Layer 4 (Fig. 9c). Layer 1 with higher reheating opportunities had longer available time to stay at 500-800°C and undertake the  $\alpha \rightarrow \sigma$  transformation process. By moving to the upper layers, the number of reheating opportunities decreases, and the length of the 500-800°C exposure time decreases, hence the chance of  $\alpha \rightarrow \sigma$  decreases. Therefore, lower fraction of brittle  $\sigma$  remains in the final microstructure at room temperature. Another observable fact is that as the *Cr-wt.%* decreases from Layer 1 to Layer 4 (see Table 3), the volume fraction of the Cr-rich  $\alpha$ , i.e.,  $\alpha$ -Cr, decreases, and that of the Fe-rich  $\alpha$ , i.e.,  $\alpha$ -Fe, increases. Therefore, layer 1 (Fig. 9f), with the highest amount of lowest *Cr-wt.%*, contains the highest dark  $\alpha$ -Cr volume fraction among the four weld layers. While layer 4 has (Fig. 9c) the lowest amount of this fraction. Another contributor to the increment of the ferrite phase in the upper layers is that the *wt.%* of the ferrite stabilizers (*Mo* and *Si*) has an increasing trend from Layer 1 to Layer 4 (Table 3). So this matter describes the increasing of the light-etched  $\alpha$ -Fe area from the first layer (Fig. 9f) to the fourth (Fig. 9c).

When layers of materials are welded on the top of a substrate, the sandwiched HAZ, based on the findings of Shen et al. [36], contains a combined mixture of the weld and the substrate materials. On the one hand, based on Fig. 9g, as we go down from weld to the HAZ, the concentration of  $\alpha$ -Cr increases, and  $\alpha$ -Fe is dissipated throughout the dark  $\alpha$ -Cr matrix. Table 3 shows that the ferritizers (i.e., *Mo* and *Si*) experience a significant descent from Layer 1 downwards to the HAZ. Therefore, in their absence,  $\alpha$ -Fe does not have enough stability and easily dissipates in favor of  $\alpha$ -Cr. On the other hand, referring to Fig. 9i, moving upward from rail to the HAZ, the dark pearlite has been segregated and moved on to the HAZ, but a minor fraction of the pro-eutectoid ferrite

could successfully migrate through to the HAZ. Hence, the core of the HAZ, as observable in Fig. 9h, mainly consists of pearlite and  $\alpha$ -Cr, with dark appearances, and contains a minor fraction of ferrite with light appearance.

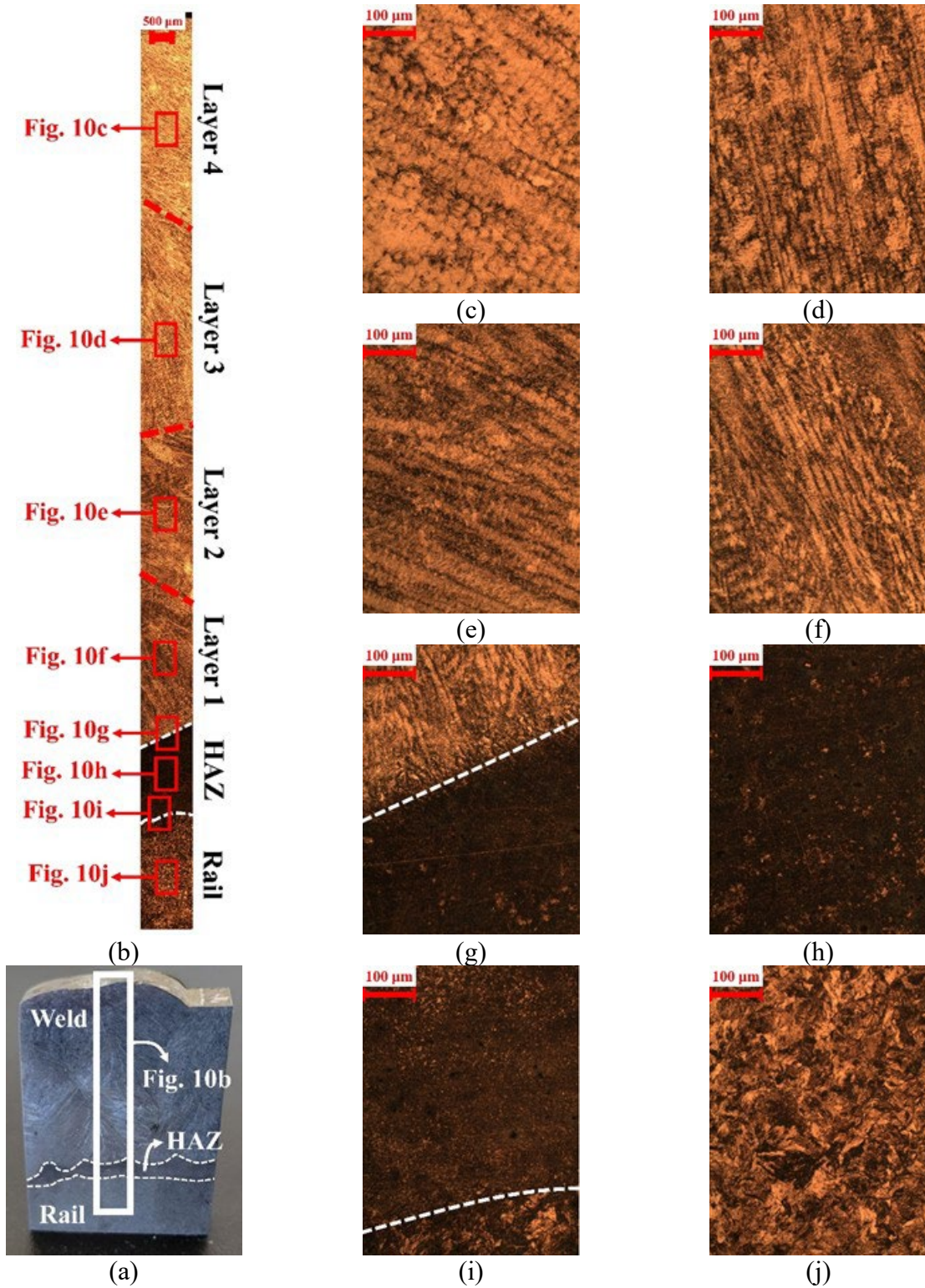


Figure 10.9(a) An etched specimen extracted from the head of the repaired rail, (b) A thorough O.M. capture from the entire weld zone with the four layers deposited, the heat-affected zone (HAZ), and the rail; closer O.M. shots are taken from (c) fourth, (d) third, (e) second, and (f) first weld layers, (g) weld-HAZ interface, (h) HAZ, (i) HAZ-rail interface, and (j) rail

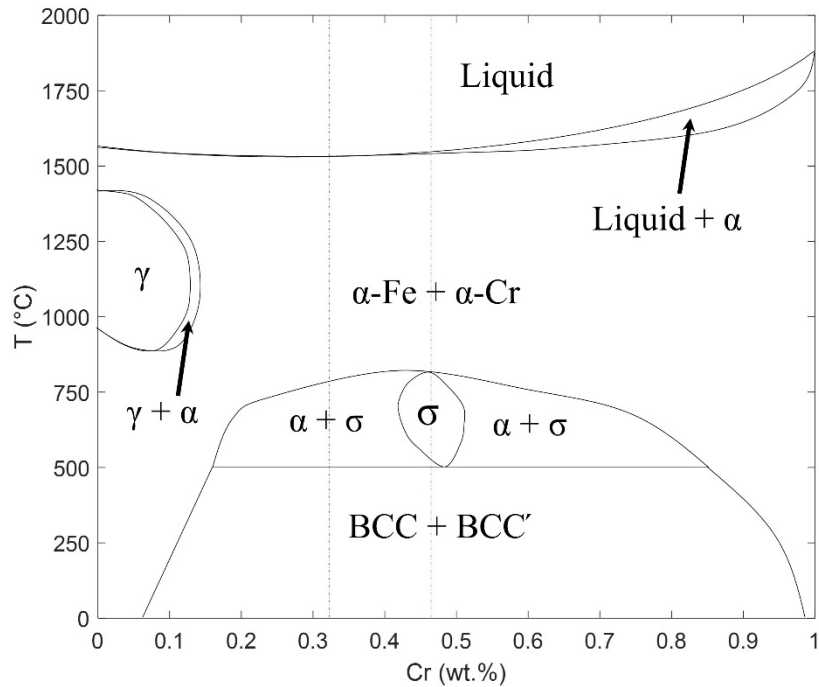


Figure 10.10 Fe-Cr phase diagram for the Lincore 40-S hard-facing wire used in the SAW process

**Table 3** Chemical composition (wt.%) of different areas of the repaired rail (Areas are graphically addressed in Fig. 10)

Area	Fe	C	Cr	Mn	Mo	Si
Layer 4	Bal.	0.067 ± 0.007	0.32 ± 0.05	1.25 ± 0.20	0.82 ± 0.03	3.42 ± 0.40
Layer 3	Bal.	0.028 ± 0.007	0.39 ± 0.05	1.93 ± 0.20	0.80 ± 0.03	3.26 ± 0.40
Layer 2	Bal.	0.016 ± 0.007	0.41 ± 0.05	2.55 ± 0.20	0.73 ± 0.03	3.12 ± 0.40
Layer 1	Bal.	0.017 ± 0.007	0.47 ± 0.05	2.19 ± 0.20	0.73 ± 0.03	2.94 ± 0.40
HAZ	Bal.	0.23 ± 0.06	0.12 ± 0.01	1.01 ± 0.20	0.03 ± 0.01	0.53 ± 0.40
Rail	Bal.	0.80 ± 0.06	0.03 ± 0.01	0.23 ± 0.03	-	0.04 ± 0.01

### 3.3. Hardness Test

Per AREMA regulations [30], the distribution of Hardness along the three lines, shown in Fig. 11a, should be maximum at the surface of the railhead, i.e., points 1, 11, and 25 in Fig. 11a, and then undergo a smooth declination towards the minimum Hardness at the root of the railhead, i.e., point 39 in Fig. 11a.



Fig. 11 gives the hardness distribution along the repaired railhead's left, middle, and right gauges (i.e., Lines 1, 2, and 3, respectively, in Figs. 11b, 11c, and 11d, respectively). The minimum required Hardness assigned by AREMA [30] for heavy 136RE rails, equal to 32 HRC, is shown as a horizontal dash-dot line in all the graphs. The vertical dashed line in each graph locates the rail-weld interface. Therefore, the areas on the left side of the vertical dashed lines in Figs. 11b, 11c, and 11d represent the weld area, and the areas on the right side of them stand for the rail area. It is evident in Figs. 11b-d that the average measured Hardness at the weld zone along Lines 1, 2, and 3 are 54, 59.5, and 60 HRC, respectively. The mean Hardness measured in the rail section along Lines 1, 2, and 3 is 37, 35, and 36 HRC, respectively. Therefore, the overall Hardness in the weld and rail areas is estimated as 58 HRC and 36 HRC, respectively. The results imply that the hardness results meet the standard AREMA requirement: the maximum occurs at the head, and the minimum occurs at the root of the repaired railhead. The Hardness of the repaired rail in almost all the regions is higher than the minimum required 32 HRC. Still, it fails to meet the AREMA standards regarding a smooth declination, from the maximum at the head to the minimum at the root. Graphs in Figs. 11b-d shows a sharp, step decrease of Hardness at the rail-weld interface, moving from the weld area to the rail zone.

The most challenging phase present in the weld material is the brittle  $\sigma$  phase. The sigma phase can significantly increase the Hardness. Unlike martensite, the sigma phase in the railhead microstructure is not against AREMA regulations. However, it substantially affects the material ductility by increasing the brittleness, which raises the chance of premature cracking and failure of the rail under dynamic wheel-rail load. Therefore, while the weld's higher (about 80% higher than the minimum required) seems satisfying, it might make the deposited weld too brittle and hence need some post-heat-treatment (e.g., tempering) to alleviate the Hardness down to some values closer to the minimum 32 HRC. So, not only can the Hardness meet the minimum standards, but also the material becomes more ductile to decrease the chance of early cracking and premature failure. Another contributor phase to getting a high hardness in the weld zone is the  $\alpha$ -Fe phase. The volume fractions of  $\sigma$  and  $\alpha$ -Fe respectively decrease and increase in weld layers from the base rail to the top surface (Sec. 3.2). Hence although one of the hardness-increment-contributors (i.e., the volume fraction of  $\sigma$ ) decreases, the other contributor (i.e., the volume fraction of  $\alpha$ -Fe) increases in the upper layers. So this matter explains the almost constant, high Hardness in the weld area (Fig. 11). The Hardness of the weld zone remains between 55 to 60 HRC, and no considerable fluctuation occurs.

As the hard  $\alpha$ -Fe and the brittle  $\sigma$  phases disappear in the HAZ while the mild-hardness  $\alpha$ -Cr increases, the Hardness suddenly descends from 55-60 HRC to around 40 HRC. After that, in the rail area with the standard pearlitic-ferritic phase, the hardness values match the standard expected values between 32 to 42 HRC, converging to 32 HRC at the root of the repaired rail (Fig. 11). Thus, a proper choice of heat treatment, such as tempering, can dissolve the brittle  $\sigma$  phase and help to augment the ferrite phase in the weld zone. This microstructural transformation could make a consistent hardness distribution all over the repaired railhead and aid the weld material's Hardness to reduce to the standard 32-40 HRC interval.

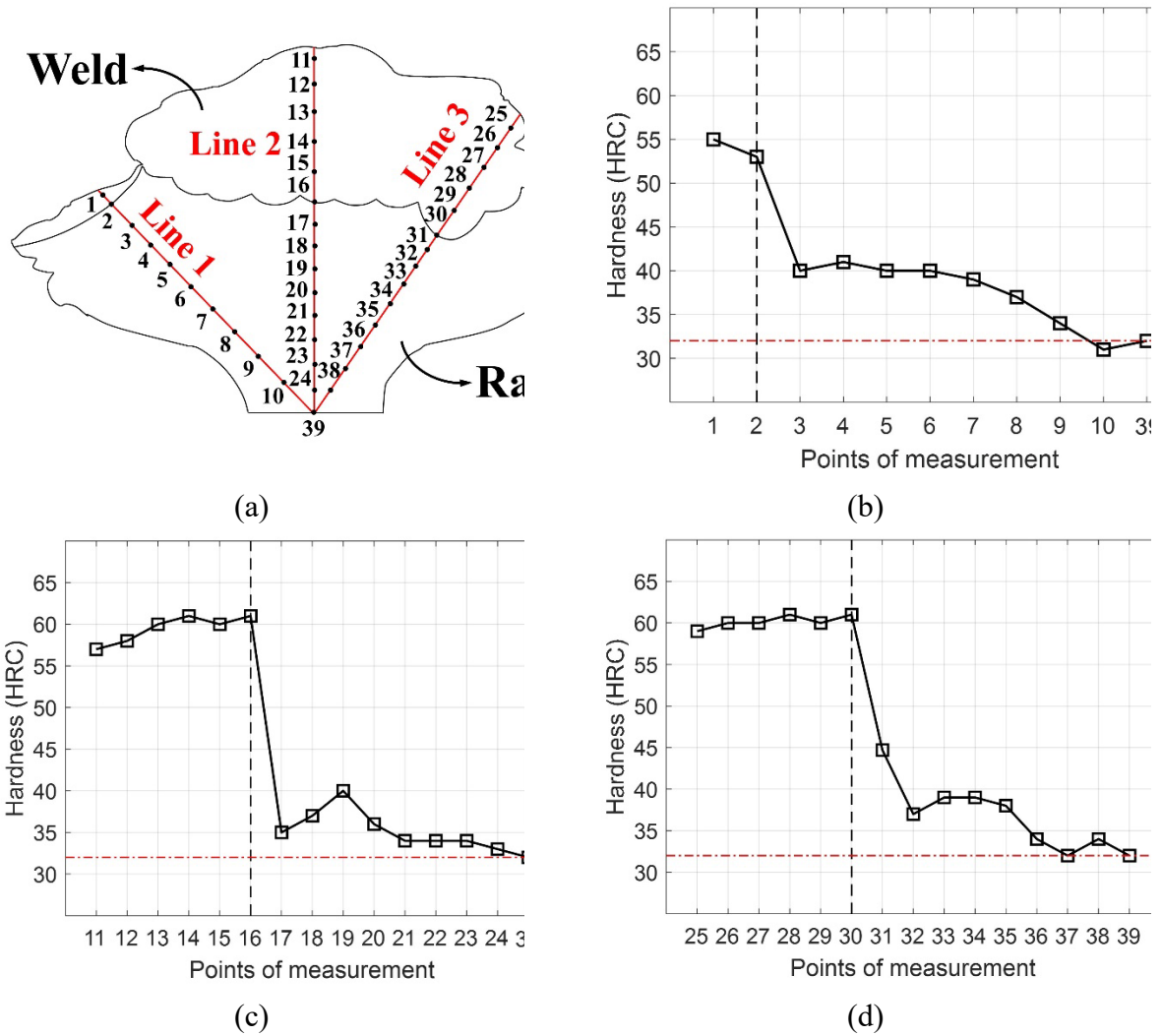


Figure 10.11 Hardness distribution on the head of the repaired rail showing the (a) hardness test plan and hardness distribution along (b) Line 1, (c) Line 2, and (d) Line 3; the vertical dashed line in all of the graphs located the rail-weld interface and the horizontal red dash-dot line shows the minimum acceptable Hardness based on AREMA standards [30]

### 3.4. Tensile Test

Four specimens were prepared based on the explanation in Sec 2.3.4. Two of them were extracted from the weld area, and the other two from the base area of the rail. The two base samples were used to check the results from the weld samples. The results also assessed to meet the AREMA regulations [30]. Fig. 12 shows the stress-strain diagrams resulting from the samples. The average data used for every two specimens from the weld or base area. Extracted data from the tensile test and, after averaging and removing noises, formed the diagrams shown in Fig. 12.

Failure shape is one of the essential characteristics of each tensile sample. In this regard, fig 13 shows two samples from the weld area broke with a cross-section perpendicular to the tensile axis. This matter is due to the brittle weld metal structure mentioned in Sec. 3.3. In contrast, base area

samples showed a ductile form. Fig 12.b. indicates that the base area samples passed the elastic region and went to the plastic part. Although the base samples did not break according to the maximum load tensile machine limitation, these results are still proper to compare with the weld area samples. This matter also approved the previous statement regarding ductility in the base area and being brittle in the weld area (Sec. 3.3.). As was mentioned in Sec. 3.3., a heat treatment process, such as tempering, should be considered in the weld area.

From the diagram of Fig. 12.a., the Ultimate Tensile Strength (UTS) be calculated as 550 MPa. This value can still meet the AREMA regulations [30]. However, as mentioned before, the brittle structure can cause a considerable flaw in the rail surface. The difference between the weld area's behavior and the base area indicates that the weld area can tolerate static loads. However, fatigue and dynamic loads can cause a significant problem. It could be mentioned that Yield Strength ( $S_y$ ) is 700 MPa by consideration of the 0.2% offset method (shown in Fig. 12.b.).

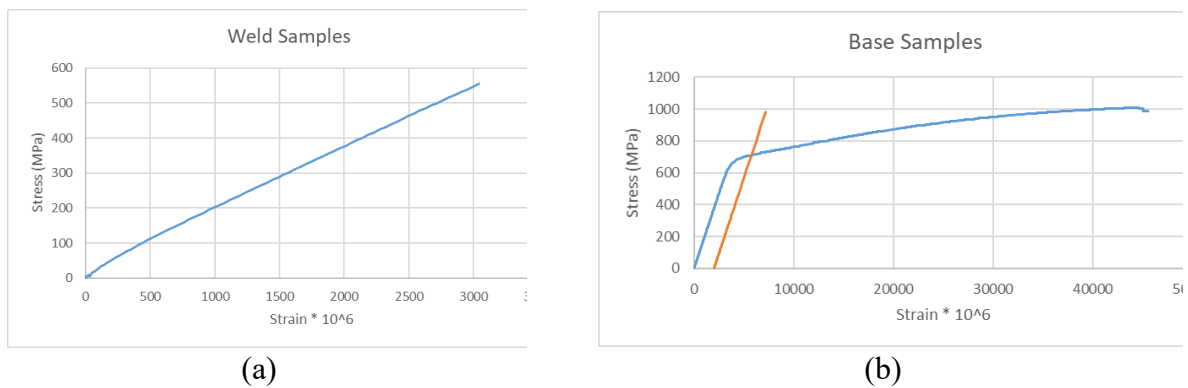


Figure 10.12 Stress-Strain diagram resulting from tensile tests on samples of (a) weld area and (b) base area



Figure 10.13 Failure shapes of the weld area samples

## Conclusion and Future Work

The current study has assessed the mechanical and metallurgical properties of a standard U.S. heavy rail repaired using SAW (Submerged Arc Surfaced), focusing on the weld area. Some different experiments have been designed and implemented to investigate the goal of this research, including XRD residual stress measurement, SEM/OM analysis, hardness test, and tensile test.

Through these tests, a comprehensive interpretation has resulted regarding the method of heavy rail repair by SAW welding.

The experiments show that the repaired weld area of the rail can give proper mechanical strength. However, the quality of the repaired area cannot reach the original rail's steel according to the brittle structure of this area. Therefore, the focus needs to be on the improvement of this structure. Progress in this area can help us achieve a reliable method of rail repair and could be beneficial in other heavy steel weld repair applications, such as structures. Some preheating ways, like tempering, seem suitable in this regard, but they still need more study, which can be material for future research.

## References

- [1] R. Masoudi Nejad, F. Berto, 2022. Fatigue crack growth of a railway wheel steel and fatigue life prediction under spectrum loading conditions, *Int. J. Fatigue*, 157, 106722. <https://doi.org/10.1016/j.ijfatigue.2022.106722>
- [2] S. Zhang, M. Spiryagin, Q. Lin, H. Ding, Q. Wu, J. Guo, Q. Liu, W. Wang, 2022. Study on wear and rolling contact fatigue behaviours of defective rail under different slip ratio and contact stress conditions, *Tribol. Int.*, 169, 107491. <https://doi.org/10.1016/j.triboint.2022.107491>
- [3] G. Epasto, F. Distefano, L. Gu, H. Mozafari, E. Linul, 2020. Design and optimization of Metallic Foam Shell protective device against flying ballast impact damage in railway axles, *Mater. Des.*, 196, 109120. <https://doi.org/10.1016/j.matdes.2020.109120>
- [4] K. Zhou, H. Ding, W. Wang, J. Guo, Q. Liu, 2022. Surface integrity during rail grinding under wet conditions: Full-scale experiment and multi-grain grinding simulation, *Tribol. Int.*, 165, 107327. <https://doi.org/10.1016/j.triboint.2021.107327>
- [5] R.F. Kral, S.A. Mayhill, M.Q. Johnson, M.E. Rovnyak, D.J. Coomer, 2004. Method of repairing a rail, U.S. Patent, US7520415B2 2004
- [6] J.W. Seo, J. Kim, S.J. Kwon, H.K. Jun, 2019, Effects of laser cladding for repairing and improving wear of rails, *Int. J. Precis. Eng. Manuf.*, 20, 1207–1217. <https://doi.org/10.1007/s12541-019-00115-y>
- [7] S.H. Lee, S.H. Kim, Y.S. Chang, H.K. Jun, 2014. Fatigue life assessment of railway rail subjected to welding residual and contact stresses, *J. Mech. Sci. Technol.*, 28, 4483–4491. <https://doi.org/10.1007/s12206-014-1016-3>
- [8] H.K. Jun, J.W. Seo, I.S. Jeon, S.H. Lee, Y.S. Chang, 2016. Fracture and fatigue crack growth analyses on a weld-repaired railway rail, *Eng. Fail. Anal.*, 59, 478–492. <https://doi.org/10.1016/j.engfailanal.2015.11.014>
- [9] Q. Feng, H. Song, 2022. Analysis on the operation methods of rail welding and postweld heat treatment in the track change overhaul of existing railway lines, *J. Phys.: Conf. Ser.*, 2152, 012018. <https://doi.org/10.1088/1742-6596/2152/1/012018>
- [10] P. Chen, L. Chen, J. Xu, S. Huang, Z. Xia, 2021. Formation mechanism of pearlite during thermal cycling in U75V steel rail repaired by laser directed energy deposition, *J. Laser Appl.*, 33, 032017. <https://doi.org/10.2351/7.0000446>
- [11] P. Suwanpinij, T. Thonondaeng, P. Kumma, B. Suksawat, G. Lothongkum, 2022. Control of the bainitic structure for a wear-resisting hard-faced rail track, *Mater. Test.*, 64 (1), 1-10. <https://doi.org/10.1515/mt-2021-2076>

- [12] B. Srikarun, S. Petchsang, P. Muangjunburee, 2021. Study of abrasive wear of railway welding steel repair, grade R260, Princess of Naradhiwas University Journal, 13 (1) , 209–255. <https://li01.tci-thaijo.org/index.php/pnujr/article/view/241123>
- [13] M.N. SaifulAkmal, M.N. Wahab, 2021, Characterization of UIC-54 rail head surface welded by hardfacing using flux-cored steel wire, In: M.N. Osman Zahid et al. (eds), Recent trends in manufacturing and materials towards industry 4.0. Lecture notes in mechanical engineering. [https://doi.org/10.1007/978-981-15-9505-9\\_68](https://doi.org/10.1007/978-981-15-9505-9_68)
- [14] T. Roy, A. Paradowska, R. Abrahams, M. Law, P. Mutton, M. Soodi, W. Yan, 2020. Residual stress in laser clad heavy-haul rails investigated by neutron diffraction, J. Mater. Process. Technol., 278, 116511. <https://doi.org/10.1016/j.jmatprotec.2019.116511>
- [15] D. De Becker, J. Dobrzanski, Y.M. Goh, L. Justham, 2020. Towards the development of a deposition technology for an automated rail repair system, UKRAS20 Conference: Robots into the Real World Proceedings, 100-102. <https://doi.org/10.31256/Vz2Jt4I>
- [16] E. Kabo, A. Ekberg, M. Maglio, 2019. Rolling contact fatigue assessment of repair rail welds, wear, 436–437, 203030. <https://doi.org/10.1016/j.wear.2019.203030>
- [17] L. Xin, V. Markine, I. Shevtsov, 2018, Analysis of the Effect of repair welding/grinding on the performance of railway crossings using field measurements and finite element modeling. Proc. Inst. Mech. Eng. F: J. Rail Rapid Transit, 232 (3), 798-815. <https://doi.org/10.1177/0954409717693960>
- [18] E. Mortazavian, Z. Wang, H. Teng, 2022, Finite element investigation of thermal-kinetic-mechanical evolutions during laser powder deposition as an innovative technique for rail repair, Int. J. Adv. Manuf. Technol., 118, 319–342. <https://doi.org/10.1007/s00170-021-07873-y>
- [19] E. Mortazavian, Z. Wang, H. Teng, 2021, Effect of heat treatment on microstructure and Hardness of a worn rail repaired using laser powder deposition, Int. J. Transp. Sci. Technol. <https://doi.org/10.1016/j.ijst.2021.05.004>
- [20] E. Mortazavian, Z. Wang, H. Teng, 2021. Measurement of residual stresses in laser 3D printed train rail using X-ray diffraction technique, Proceedings of the ASME 2021 IMECE, V02AT02A005. <https://doi.org/10.1115/IMECE2021-69822>
- [21] E. Mortazavian, Z. Wang, H. Teng, 2020. Repair of light rail track through restoration of the worn part of the railhead using submerged arc welding process, Int. J. Adv. Manuf. Technol., 107, 3315–3332. <https://doi.org/10.1007/s00170-020-05208-x>
- [22] B.L. Josefson, J.W. Ringsberg, 2009. Assessment of uncertainties in life prediction of fatigue crack initiation and propagation in welded rails, Int. J. Fatigue, 31 (8–9), 1413-1421. <https://doi.org/10.1016/j.ijfatigue.2009.03.024>
- [23] A. Masoudi, M. Davarpanah Jazi, M. Mohrekesh, R. Masoudi Nejad, 2022. An investigation of rail failure due to wear using statistical pattern recognition techniques, Eng. Fail. Anal., 134, 106084. <https://doi.org/10.1016/j.engfailanal.2022.106084>
- [24] H. Desimone, S. Beretta, 2006. Mechanisms of mixed mode fatigue crack propagation at rail butt-welds, Int. J. Fatigue, 28 (5–6), 635-642. <https://doi.org/10.1016/j.ijfatigue.2005.07.044>
- [25] A. Skyttebol, B.L. Josefson, J.W. Ringsberg, 2005. Fatigue crack growth in a welded rail under the influence of residual stresses, Eng. Fract. Mech., 72 (2), 271-285. <https://doi.org/10.1016/j.engfracmech.2004.04.009>
- [26] R. Masoudi Nejad, Z. Liu, W. Ma, F. Berto, 2021. Fatigue reliability assessment of a pearlitic Grade 900A rail steel subjected to multiple cracks, Eng. Fail. Anal., 128, 105625. <https://doi.org/10.1016/j.engfailanal.2021.105625>

- [27] S. Bharathi, A. Arul, M. Moshi, S.R. Sundara Bharathi, R. Rajeshkumar, R. Kumar, 2016. Factors influencing submerged arc welding on stainless steel—a review. *APRN J. Eng. Appl. Sci.*, 11 (2). ISSN: 1819-6608
- [28] P.T. Houldcroft, 1989. *Submerged-arc welding*. Abington Publishing, U.K. ISBN: 1855730022
- [29] ASTM International, Designation: E18 – 20, 2020. Standard test methods for Rockwell hardness of metallic materials. <https://doi.org/10.1520/E0018-20>
- [30] AREMA Manual for Railway Engineering, 2020. Chapter 4: Rail. American Railway Engineering and Maintenance-of-way Association.
- [31] M. Ghasri-Khouzani, H. Peng, R. Rogge, R. Attardo, P. Ostiguy, J. Neidig, R. Billo, D. Hoelzle, M.R. Shankar, 2017. Experimental Measurement of residual stress and distortion in additively manufactured stainless steel components with various dimensions, *Mater. Sci. Eng. A*, 707, 689-700. <https://doi.org/10.1016/j.msea.2017.09.108>
- [32] C.Y. Poon, B. Bhushan, 1995. Comparison of surface roughness measurements by stylus profiler, AFM and noncontact optical profiler, *wear*, 190(1), 76-88. [https://doi.org/10.1016/0043-1648\(95\)06697-7](https://doi.org/10.1016/0043-1648(95)06697-7)
- [33] ASTM International, Designation: E8/E8M – 21, 2021. Standard test methods for tension testing of metallic materials. [https://dx.doi.org/10.1520/E0008\\_E0008M-21](https://dx.doi.org/10.1520/E0008_E0008M-21)
- [34] ASTM International, Designation: E190 – 21, 2021. Standard test method for guided bend test for ductility of welds. <https://doi.org/10.1520/E0190-21>
- [35] [M.E. Fitzpatrick, A.T. Fry, P. Holdway, F.A. Kandil, J. Shackleton, L. Suominen, 2002. Determination of residual stresses by X-ray diffraction. National Physical Laboratory, Measurement Good Practice Guide No. 52.](#)
- [36] L. Shen, J. Zhou, X. Ma, X.Z. Lu, J.W. Tu, X. Shang, F. Gao, J.S. Zhang, 2017. Microstructure and mechanical properties of hot forging die manufactured by bimetal-layer surfacing technology, *J. Mater. Process. Technol.*, 239, 147–159. <https://doi.org/10.1016/J.JMATPROTEC.2016.08.020>



## 11. Chapter 11 LAB TESTS ON RAILS WITH ESAB SAW EQUIPMENT

### Purpose of the tests

After explorative tests using SAW equipment from Miller and ESAB companies in 2022 and 2023, both demonstrated to be superior than LPD technologies in terms of productivity and cost, while maintaining potentially great printing quality, even though LPD could deliver good rail strength, but the printing speed and volume are too slow for industrial application.

Among the two industry-caliber SAW printers, Miller is less reliable in motion control during 3D printing train rail. In addition, Miller machine is equipped with one printing head only, which ESAB can operate with dual head, that potentially could double the 3D printing productivity. We are also impressed with the ESAB lab capabilities and team, which are not seen from other places.

The focus of this research is now on using ESAB SAW printer to explore parameters such as wire, travel speed, flux, voltage, ampere, pre-heat, and inter-pass, to meet the AREMA requirements for train rail [1], which include yield strength, tensile strength, elongation rate, and hardness. Surely there are other requirements [2,3], but those four are critical and could be lab verified in a few weeks each time.

### Test scenarios

The ESAB SAW equipment below (figure1) is used as the 3D printer during test. The machine has a control console on top (figure 2), which can be programmed to print train rail with different parameters layer by layer. Wires are packed in two rolls and mounted on the back of the machine, which automatically feed into the equipment to the printing zone.





Figure 11.1 ESAB SAW equipment



Figure 11.2: Control console

Parameters used in test of heavy rails and light rails, such as wire material, wire diameter, flux, layer, pass, travel speed, voltage, ampere, pre-heat, and inter-pass, etc., are given in Table 1 and Table 4, respectively.

Table 1: Test parameter for heavy rail

	1	2	3	4	5	6
Wire	Thermaclad 446	Thermaclad 446	Thermaclad 446	Thermaclad 438	Thermaclad 446	Thermaclad 446G
Wire Diameter	5/32"	5/32"	5/32"	1/8"	5/32"	2024/1/16
Flux	R20	R20	R20	R20	R20	R20
Layer #	I-5	I-8	I-2	63-8	1-8	1-9
Pass #	I-24	I-39	1-11	11-42	1-40	1-19
Polarity	DC+	DC+	DC+	DC+	DC+	DC+
ESO	1.25	1.25	1.25	1	1.25	2024/5/8
Amperage	650	650	650	550	650	
Voltage	32	32	32	30	32	27
Travel Speed	24 ipm	24	24	23	24	
Pre-Heat	650°F	none	300		650	
Inter-pass	750°F	800	800		800	

Date	5/10/2024	6/20/2024	6/27/2024	6/27/2024	7/18/2024	7/18/2024
Cooling	Air + ceramic insulation	Air only	Air + ceramic insulation	Air + ceramic insulation	Oven 650F 2hr	Oven 650F 2hr

Table 2: Test parameter for light rails

	1	2a	2b	3	3	4	4	85	66	8
Wire	Thermaclad 446	Thermaclad 446	Thermaclad 446	Thermaclad 446	Thermaclad 438	Thermaclad 446	Thermaclad 438	Thermaclad 446	Thermaclad 446G	Thermaclad 446
Wire Diameter	5/32"	5/32	5/32	5/32	1/8"	5/32	1/8	5/32	1/6	5/32
Flux	R20	R20	R20	R20	R20	R20	R20	R20		R20
Layer #	1-8	1-2	3-7	1-3	4-8	1-3	4-7	1-6	1	1-6
Pass #	1-36	1-10	11-32	1-12	13-33	1-13	14-28	1-30	1	1-30
Polarity	DC-	AC	AC	DC+	DC+	DC+	DC+	DC+	DC+	DC+
ESO	1.25	1.25	1	1.25	1	1.25	1	1.25	5/8/24	1.25
Amperage	650	AC	AC	650	550	650	550	650		650
Voltage	34	35	35	32	30	32	30	32	27	32
Travel Speed	24	24	24	24	23	24	23	24		24
Pre-Heat	650°F	650	650	650	650	600	600	650	600	650
Inter-pass	750°F	800	800	800	800	800	800	800	800	800
Date	5/23/2024	5/30/2024	5/30/2024	6/6/2024	6/6/2024	6/13/2024	6/13/2024	7/24/2024	7/29/2024	9/11/2024
Cooling	Air + ceramic insulation	Air + ceramic insulation	Air + ceramic insulation	Air + ceramic insulation	Air + ceramic insulation	Air + ceramic insulation	Air + ceramic insulation	Oven 650F 2hr	Oven 650F 2hr	Oven 650F 4hr

Six sets of 3D printing configurations for heavy rails (136-lb/yd) and eight sets for light rails (75-lb/yd), as shown in Table 1 and Table 2, are printed on top of the existing rail surface layer by layer. Results are discussed in the next section. Lab test data are given in the Appendix I.

Table 3 summarizes the requirements for heavy and light rails in terms of yield strength, tensile strength, and elongation rate [1,2], therefore, is used in selecting printing wires. There are only two qualified: Thermaclad 438 and Thermaclad 446, which are capable of delivering tensile strength and yield strength for heavy and light rails. ESAB has two wire diameter options: 1/8" and 5/32", which are all being tested at different voltage and amperage during operation.

## The results

Results of six different printing configurations for heavy rails is summarized in Table 3, among them, one set of the 3D printing configuration (data 1) shows it exceeds the AREMA standards for

rail yield strength, the tensile strength of the rail is in the range but slightly below the AREMA standards. The rail micro-hardness is much higher (data given in the Appendix I) and rail elongation rate is lower than the standards. More studies are needed on the results.

Results of eight different printing configurations for light rails is summarized in Table 4. Among all sets of test data, three sets of 3D printing configurations are promising, with both rail yield strength and tensile strength exceeding the AREMA standards. However, similar to heavy rails, the rail micro-hardness is higher than standards and the rail elongation rate is low. More analyses are needed on the results as some data were finished in September 2024.

Table 3: Required mechanical properties of rails [1,2]

Mechanical property	(Unit)	Light Rail	Heavy Rail
Yield strength	(MPa)	460	830
Tensile strength	(MPa)	511	980
Elongation	(%)	10	10

Table 4: Summarize test data in for light rails

	Test Data (PSI)			AREMA Standard (PSI)			Note
	Tensile Strength	Yield Strength	Elongation Rate	Tensile Strength	Yield Strength	Elongation Rate	
Heavy rail 1	137,000	122,000	2.6%	142,100	120,350	10%	5/29/2024
Heavy rail 2	77,000	63,100	3.15%	142,100	120,350	10%	7/5/2024
Heavy rail 3	100,000	n/a	0.946%	142,100	120,350	10%	7/19/2024
Heavy rail 4	78,400	59,000	2.79%	142,100	120,350	10%	7/19/2024
Heavy rail 5	99,200	64,300	7.59%	142,100	120,350	10%	7/30/2024
Heavy rail 6	86,400	64,500	3.42%	142,100	120,350	10%	7/30/2024

Note: 1) data in blue exceeds AREMA required standards;

2) data in green is slightly below the AREMA standards.

Table 5: Summarize test data in for heavy rails

	Test Data			AREMA Standard			Note
	Tensile Strength	Yield Strength	Elongation Rate	Tensile Strength	Yield Strength	Elongation Rate	
Light rail 1	426.2 mPa	358.6 mPa	2%	511 mPa (74,100 psi)	460 mPa (66,700 psi)	10%	5/8/2024
Light rail 2	x-ray only	n/a	n/a	74,100 psi	66,700 psi	10%	6/4/2024
Light rail 3	134,000 psi	95,400 psi	2.5%	74,100 psi	66,700 psi	10%	6/28/2024
Light rail 4	110,000	n/a	0.95%	74,100 psi	66,700 psi	10%	6/28/2024
Light rail 5	84,500	n/a	9.75%	74,100 psi	66,700 psi	10%	8/16/2024
Light rail 6	136,000	114,000	1.5%	74,100 psi	66,700 psi	10%	8/16/2024
Light rail 7	86,200	11,500	0.293 %	74,100 psi	66,700 psi	10%	9/11/2024
Light rail 8	157,000	113,000	1.55%	74,100 psi	66,700 psi	10%	9/26/2024

Note: 1) data in green exceeds AREMA required standards;

2) Hardness are tested separately and data are reported in the next section.

Lab test results indicate that 3D printing train rails is capable of achieving both yield strength and tensile strength to the AREMA requirements for light rails. But only the yield strength exceeds the requirement for heavy rails. The tensile strength is slightly below the requirements. However, rail hardness in both cases for heavy and light rails is above the AREMA standards, and the elongation rate is below requirements. To solve the hardness and elongation problems, we applied heat treatment to some of the printed rails, improvements are observed, but the satisfactory procedure and parameters are yet to be developed before the project comes to an end.

## **Conclusions and recommendation**

3D printing technologies has been revolutionizing many industries in the last few decades, however, application in heavy and dynamic loading situation, such as train rail is yet to be developed [4]. Some 3D printing technique offers excellent mechanical properties, such as mechanical strength, but due to its rapid cooling nature, materials after 3D printing exhibits low elongation rate and high hardness.

In our lab tests, parameters in data 1 is capable of printing heavy rail with satisfactory yield strength, but more adjustment in wire is needed to improve tensile strength.

With light rails, multiple successes were achieved in 3D printing with yield strength and tensile strength due to light rail requirements are lower than heavy rail.

In all cases, heat treatment procedure needs to be further investigated. Researchers from South Korea [5] 3D printed train wheel using a well-established tempering process and achieved good results. We are fully aware of that train wheel is different from rail in material composition and property. Therefore, post heat treatment techniques are different accordingly.

SAW technique, by nature, it melts pre-formulated wire with electric arc, and using flux to shield oxygen, nitrogen, and other gases from forming air bubbles in the molten metals as they solidify on top of a worn rail. Therefore, excellent mechanical property is achievable in the printing layers with this technology. However, the molten zone is relatively small in volume and freezing process is rapid, which leads to high hardness, low elongation, and stress formation [6-9]. To overcome these issues, heat treatment needs to be paired with SAW process.

The recommendation for future work is as followings:

- 1) Heat treatment (tempering) is not often given top priority in 3D printing train rails among many researchers, however, our lab test results prove that it is equally important as 3D printing technology development.
- 2) 3D printing light train rail is viable in our lab test. Future researchers may focus on light rail first before heavy rail.
- 3) 3D printing heavy rail is more challenging and therefore, better wires need to be explored to further enhance the mechanical property of the printed rail.
- 4) Other tests, such as fatigue, are needed once the heat treatment technology is successfully developed.

Overall speaking, 3D printing technology could revolutionize the way how industry fix wear and damage on train rail. This research proves that mechanical strength (tensile and yield) is achievable through 3D printing for train rail, especially for light rail. More work needs to be done for tempering rail after 3D printing and also more research is needed on testing other mechanical properties before it could be commercialized.

### Reference for Chapter 11

- [1] AREMA Manual for Railway Engineering, Chapter 4: Rail, American Railway Engineering and Maintenance-of-way Association (2020).
- [2] M.P. Hughes-Cromwick, M. Dickens, Public Transportation Fact Book. 71st edition, American Public Transportation Association, Washington, DC (2020). <https://www.apta.com/wp-content/uploads/APTA-2020-Fact-Book.pdf>.
- [3] ASTM E18-15, Standard test methods for Rockwell hardness of metallic materials, ASTM international (2015). <https://doi.org/10.1520/E0018-15>.
- [4] E. Mortazavian, Z. Wang, H. Teng, Thermal-mechanical study of 3D printing technology for rail repair, IMECE2018-86315 (2019) V002T02A052. <https://doi.org/10.1115/IMECE2018-86315>.
- [5] Byeong-Choo Coo, and Young-Jin Lee, Railway Vehicle Wheel Restoration by Submerged Arc Welding and Its Characterization, 14 May 2020 (doi: 10.3390/sci2020033)
- [6] S. Bharathi, A. Arul, M. Moshi, S. R. Sundara Bharathi, R. Rajeshkumar, and R. Kumar, “Factors Influencing Submerged Arc Welding On Stainless Steel-A Review,” vol. 11, no. 2, 2016, [Online]. Available: [www.arpnjournals.com](http://www.arpnjournals.com)
- [7] P.T. Houldcroft, Submerged-arc welding, Abington Publishing (1989) UK. ISBN: 1855730022.
- [8] M. Ghasri-Khouzani, H. Peng, R. Rogge, R. Attardo, P. Ostiguy, J. Neidig, R. Billo, D. Hoelzle, M.R. Shankar, Experimental measurement of residual stress and distortion in additively manufactured stainless steel components with various dimensions, Mater. Sci. Eng. A 707 (2017) 689-700. <https://doi.org/10.1016/j.msea.2017.09.108>
- [9] H. Essoussi, S. Elmouhri, S. Ettaqi, E. Essadiqi, Heat treatment effect on mechanical properties of AISI 304 austenitic stainless steel, Proc. Manuf. 32 (2019) 883–888. <https://doi.org/10.1016/j.promfg.2019.02.298>.

## Chapter 12 CONCLUSIONS AND RECOMMENDATIONS

In this study, two different AM repair mechanisms, i.e., SAW and LPD, are investigated for repairing two types of worn rails that are most prevalently used in the U.S. transportation system, i.e., 75-lb/yd light rail and 136-lb/yd heavy rail. To achieve this goal, modification and evaluation of the AM-repair procedures are conducted through both experimental lab measurements and numerical analyses, simultaneously. The goal is to obtain optimum AM-repair process parameters in which the repaired rail gets the highest failure strength, the lowest cracks and pores, and the lowest residual stress.

To summarize, the method for finding the optimum AM-repair process parameters for a specific type of rail and a specific AM technique is as follows:

1. Microstructure morphology, chemical distribution, hardness, and residual stresses in the repaired rail sample are investigated using OM, SEM, EDS, hardness tester, and XRD tools. In this way, the existing drawbacks in the repaired rail (e.g. martensite occupation in the railhead or high residual stresses at the rail-deposition interface) are determined.
2. The under-study AM rail repair process (SAW or LPD) is simulated and modeled using FE analysis. The model predictions in the matter of the distribution of microstructure, hardness, and residual stress are compared against the experimental outcomes in order to verify the FE model.
3. Based on the specified defects of the repaired rail in the experimental evaluation, modification approaches such as preheating, altering the deposition/weld materials, post-heat treatment, and altering the AM-repair process parameters are considered to enhance the repaired rail's properties with ultimate aim of enhancing its fatigue performance.
4. The proposed modification approaches are tried through the validated FE model to find the best combination of parameters, materials, and pre- and post-processes that lead to the strongest repaired rail.
5. The confirmed optimum combination of parameters is tried experimentally to ensure that the satisfactory outcomes are gained in reality as well. Through many hundreds of lab tests, one set of 3D printing configuration with wire composition produced yield strength exceeding the AREMA standards for heavy rail, tensile strength slight below the standard. Three sets of 3D printing configurations with wire composition produced both yield strength and tensile strength exceeding the AREMA standards for light rails. However, 3D printed rail hardness exceeds the AREMA requirement and rail elongation are low. Indicating post heat treatment is equally important in design and development the 3D printing techniques for rail repair. All lab data for heavy and light rails are given in the Appendix I.

This research presents multiple options including the powder/wire material for the SAW/LPD process, the SAW/LPD process parameters, and the pre- and post-process treatments for a typical AM-repairing of a light/heavy rail in a way to gain the highest fatigue strength for the repaired rail. The other valuable outcome of this research is a reliable FE model to allow parametric studies on a rail-repair procedure without the need to further costs for the experimental tests. Microstructural and mechanical characteristics of the modified and un-modified repaired rails are


provided and discussed in detail. The utilized equations in developing the FE model along with the validation procedure are presented in details.

This study provides a novel and efficient way of restoring worn rails on site without the need of removing them from the tracks. This approach would save a considerable amount of time and cost for the U.S. railroad industry, specifically in the railway maintenance section.



# Appendix I

## ESAB Test Data on Submerged Arc Surfaced Rail



**WTTI** WELDER TRAINING AND TESTING INSTITUTE  
 WWW.WTTI.COM 1144 N. GRAHAM ST. • ALLENTOWN, PA 18109 • TEL 610-820-9551 • FAX 610-820-0271

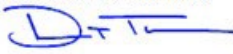
**LABORATORY TEST REPORT**

LABORATORY TEST NUMBER: 24050697  
 COMPANY NAME: ESAB Welding & Cutting Products  
 IDENTIFICATION ON SAMPLE: Delivered Coupon Identified as HR-1  
 MATERIAL SPECIFICATION: Delivered Material Identified as Unspecified Weld Metal on Unspecified Rail  
 DIMENSIONS: Approx. 0.625" Overlay  
 TYPE OF TEST: Test for Information Only

**TENSILE TEST RESULTS** TEST DATE: 5/29/2024  
 LAW TT-1, Current Revision  
 MINIMUM TENSILE REQUIRED: Not Specified

SPECIMEN ID	OD (in)	THICKNESS (in)	AREA (sq in)	TENSILE	TENSILE	YIELD	YIELD	ELONGATION (%)	LOCATION & TYPE OF FAILURE
				LOAD (lbs)	STRENGTH (psi)	LOAD (lbs)	STRENGTH (psi)		
1	0.2530	0.1265	0.0503	6,900	137,000	6,130	122,000	2.6	BM-Ductile

NOTES: Reduction of Area: 0.3%  
 FINAL RESULTS: INFO ONLY  
 TEST(S) CONDUCTED IN ACCORDANCE WITH: ASTM E8  
 TEST(S) CONDUCTED BY: KRG  
 REPORT DATE: 5/31/2024  
 APPROVED BY: Dennis T. Tobash CWI / WTTI WTTI Job #: JOB34550

SIGNATURE: 

**QUALITY POLICY STATEMENT**

The services reported in this document were performed in accordance with Welder Training and Testing Institute's Quality System, governed by Quality Manual, Rev. 10, 1/4/23 and AFS Accredited Test Facility (Cert. #000201). WTTI is accredited by A2LA to ISO 17025 for the test methods listed on Testing Cert. 3430.01 and 3430.02. The Scope of Accreditation is available at www.wti.com. This document shall not be modified or reproduced except in full, without written approval of the laboratory.

These recorded results represent only the specimen(s) tested and are in compliance with applicable code(s), standard(s), and/or contract requirement(s). At no point during testing or inspection at WTTI's facility has this item come into direct contact with mercury, mercury compounds, or devices containing single boundary containment of such. The sample tested meets the requirements of the specification listed however measurement uncertainty has not been analyzed to make a statement of conformance for destructive testing.

Page 1 of 1

Figure A1. Lab Report 1: Heavy Rail #1 - 24050697

**LABORATORY TEST REPORT**

**LABORATORY TEST NUMBER:** 24050850  
**COMPANY NAME:** ESAB Welding & Cutting Products  
**IDENTIFICATION ON SAMPLE:** Delivered Coupon Identified as ID: LR1  
**MATERIAL SPECIFICATION:** Delivered Material Identified as Unspecified Carbon Steel  
**THICKNESS:** 1.050" Overlay  
**TYPE OF TEST:** Test for Information Only  
**OTHER:** Unspecified Filler Metal

**TENSILE TEST RESULTS**

TEST DATE: 6/4/2024

LAW TT-1, Current Revision

MINIMUM TENSILE REQUIRED: Not Specified

SPECIMEN ID	OD (in)	THICKNESS (in)	AREA (sq in)	TENSILE	TENSILE	YIELD	YIELD	ELONGATION (%)	LOCATION & TYPE OF FAILURE
				LOAD (lbs)	STRENGTH (psi)	LOAD (lbs)	STRENGTH (psi)		
1	0.5030	n/a	0.1990	12,286	61,800	10,300	52,000	2	BM-Ductile

NOTES: Reduction of Area: 1.5%

FINAL RESULTS: INFO ONLY

TEST(S) CONDUCTED IN ACCORDANCE WITH: ASTM E8

TEST(S) CONDUCTED BY: KRG

REPORT DATE: 6/4/2024

APPROVED BY: Dennis T. Tobash CWI / WTTI

WTTI Job #: JOB34627

SIGNATURE: 

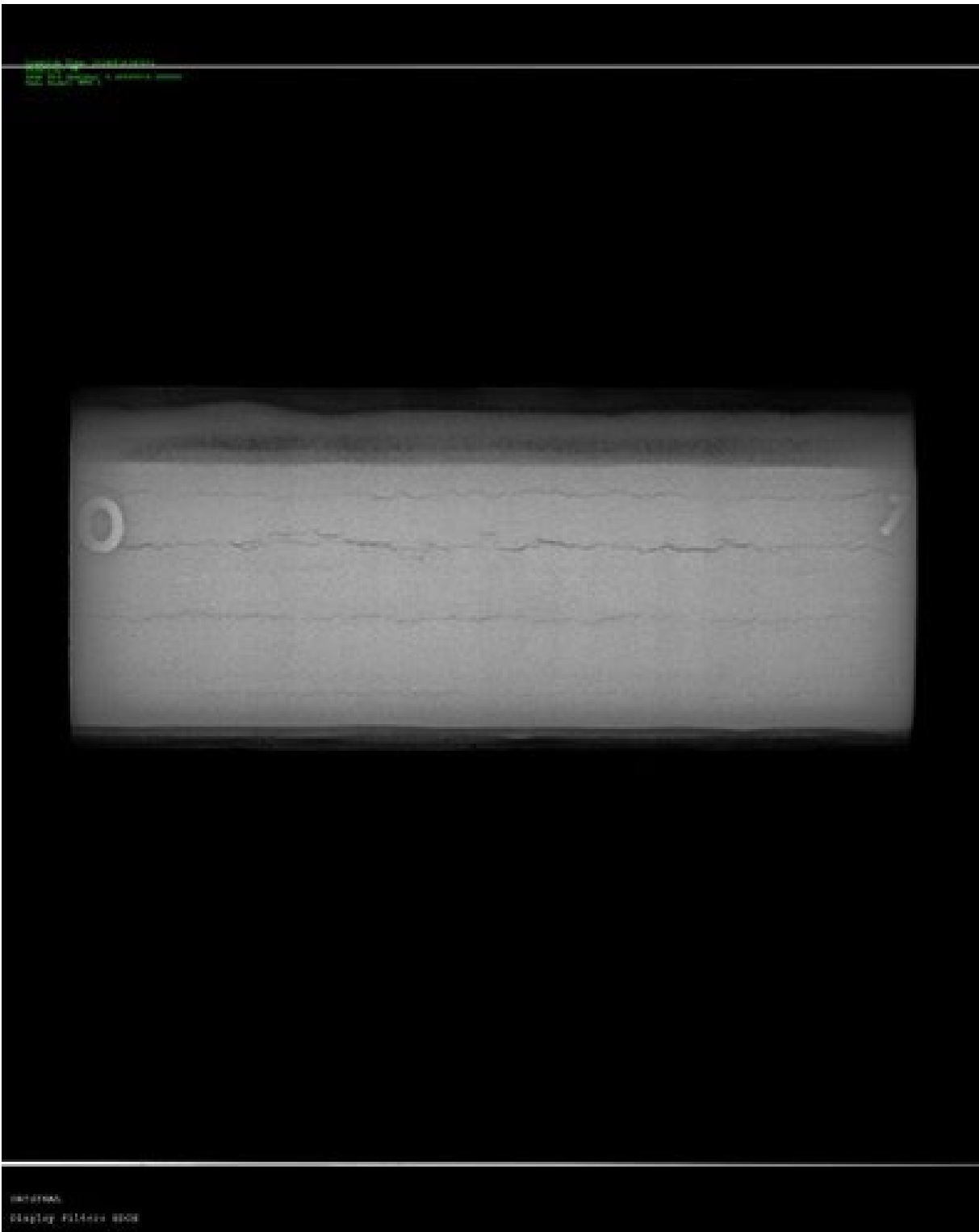
**QUALITY POLICY STATEMENT**



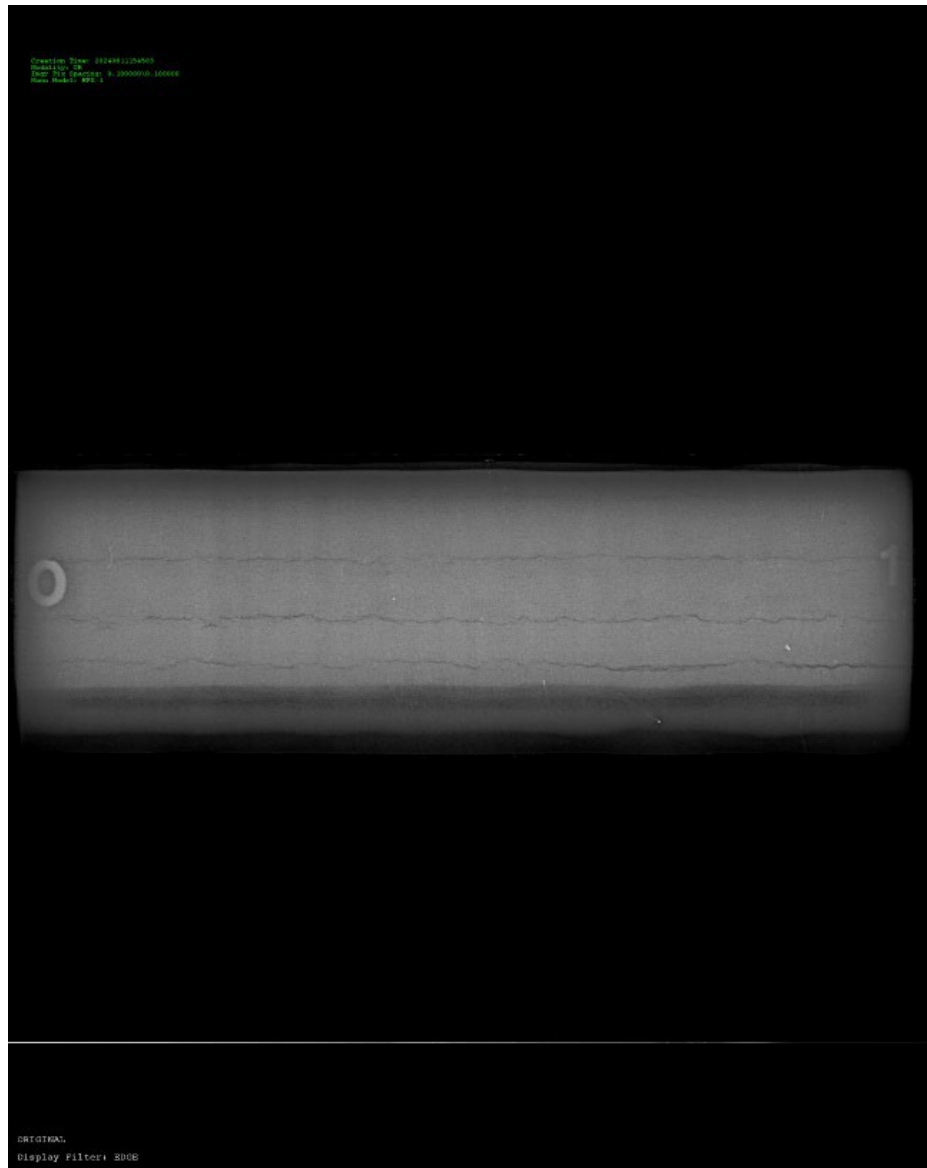
The services reported in this document were performed in accordance with Welder Training and Testing Institute's Quality System, governed by Quality Manual, Rev. 19, 1/4/23 and AWS Accredited Test Facility (Cert. #900201). WTTI is accredited by A2LA to ISO 17025 for the test methods listed on Testing Cert. 3430.01 and 3430.02. The Scope of Accreditation is available at www.wti.com. This document shall not be modified or reproduced except in full, without written approval of the laboratory.

These recorded results represent only the specimen(s) tested and are in compliance with applicable code(s), standard(s), and/or contract requirement(s). At no point during testing or inspection at WTTI's facility has this item come into direct contact with mercury, mercury compounds, or devices containing single boundary containment of such. The sample tested meets the requirements of the specification listed however measurement uncertainty has not been analyzed to make a statement of conformance for destructive testing.

Figure A2. Lab Report 2: Light Rail #1 – 24050850



(a)



(b)

Figure A3. Lab Report 3: Light Rail #2. No tensile, sample cracked. Here is an X-Ray of the buildup

**LABORATORY TEST REPORT**

**LABORATORY TEST NUMBER:** 24060265  
**COMPANY NAME:** ESAB Welding & Cutting Products  
**IDENTIFICATION ON SAMPLE:** Delivered Coupon Identified as ID: LR3  
**MATERIAL SPECIFICATION:** Delivered Material Identified as Unspecified Carbon Steel  
**THICKNESS:** 0.875" Overlay  
**TYPE OF TEST:** Test for Information Only  
**OTHER:** Unspecified Filler Metal

**TENSILE TEST RESULTS**

TEST DATE: 6/28/2024

LAW TT-1, Current Revision

MINIMUM TENSILE REQUIRED: Not Specified

SPECIMEN ID	OD (in)	THICKNESS (in)	AREA (sq in)	TENSILE	TENSILE	YIELD	YIELD	ELONGATION (%)	LOCATION & TYPE OF FAILURE
				LOAD (lbs)	STRENGTH (psi)	LOAD (lbs)	STRENGTH (psi)		
1	0.5050	0.2525	0.2000	26,778	134,000	19,100	95,400	2.5	BM-Ductile

NOTES: Reduction of Area: 2.3%

FINAL RESULTS: INFO ONLY

TEST(S) CONDUCTED IN ACCORDANCE WITH: ASTM E8

TEST(S) CONDUCTED BY: KRG

REPORT DATE: 6/28/2024

APPROVED BY: Dennis T. Tobash CWI / WTTI

WTTI Job #: JOB34807

SIGNATURE: 

**QUALITY POLICY STATEMENT**



The services reported in this document were performed in accordance with Welder Training and Testing Institute's Quality System, governed by Quality Manual, Rev. 19, 1/4/23 and AWS Accredited Test Facility (Cert. #900201). WTTI is accredited by A2LA to ISO 17025 for the test methods listed on Testing Cert. 3430.01 and 3430.02. The Scope of Accreditation is available at www.wtt.com. This document shall not be modified or reproduced except in full, without written approval of the laboratory.  
 These recorded results represent only the specimen(s) tested and are in compliance with applicable code(s), standard(s), and/or contract requirement(s). At no point during testing or inspection at WTTI's facility has this item come into direct contact with mercury, mercury compounds, or devices containing single boundary containment of such. The sample tested meets the requirements of the specification listed however measurement uncertainty has not been analyzed to make a statement of conformance for destructive testing.

Figure A4 Lab Report 4: Light Rail #3 - 24060265

**LABORATORY TEST REPORT**

**LABORATORY TEST NUMBER:** 24060321  
**COMPANY NAME:** ESAB Welding & Cutting Products  
**IDENTIFICATION ON SAMPLE:** Delivered Coupon Identified as ID: LR4  
**MATERIAL SPECIFICATION:** Delivered Material Identified as Unspecified Carbon Steel with Unspecified Weld Metal Overlay  
**THICKNESS:** 0.875" Overlay  
**TYPE OF TEST:** Test for Information Only  
**OTHER:** Unspecified Filler Metal

**TENSILE TEST RESULTS**

TEST DATE: 6/28/2024

LAW TT-1, Current Revision

MINIMUM TENSILE REQUIRED: Not Specified

SPECIMEN ID	OD (in)	THICKNESS (in)	AREA (sq in)	TENSILE LOAD (lbs)	TENSILE STRENGTH (psi)	YIELD LOAD (lbs)	YIELD STRENGTH (psi)	ELONGATION (%)	LOCATION & TYPE OF FAILURE
1	0.5080	0.2540	0.2030	22,371	110,000	n/a	n/a	0.95	BM-Ductile

**NOTES:** Yield Strength would not obtain during testing.  
 Reduction of Area: 0.0%

**FINAL RESULTS:** INFO ONLY

**TEST(S) CONDUCTED IN ACCORDANCE WITH:** ASTM A 370

**TEST(S) CONDUCTED BY:** KRG

**REPORT DATE:** 6/28/2024

**APPROVED BY:** Dennis T. Tobash CWI / WTTI

WTTI Job #: JOB34851

**SIGNATURE:** 

**QUALITY POLICY STATEMENT**



The services reported in this document were performed in accordance with Welder Training and Testing Institute's Quality System, governed by Quality Manual, Rev. 19. 1/4/23 and AWS Accredited Test Facility (Cert. #900201). WTTI is accredited by A2LA to ISO 17025 for the test methods listed on Testing Cert. 3430.01 and 3430.02. The Scope of Accreditation is available at www.wti.com. This document shall not be modified or reproduced except in full, without written approval of the laboratory.

These recorded results represent only the specimen(s) tested and are in compliance with applicable code(s), standard(s), and/or contract requirement(s). At no point during testing or inspection at WTTI's facility has this item come into direct contact with mercury, mercury compounds, or devices containing single boundary containment of such. The sample tested meets the requirements of the specification listed however measurement uncertainty has not been analyzed to make a statement of conformance for destructive testing.

Figure A5 Lab Report 5: Light Rail #4 - 24060321



**LABORATORY TEST REPORT**

**LABORATORY TEST NUMBER:** 24060473  
**COMPANY NAME:** ESAB Welding & Cutting Products  
**IDENTIFICATION ON SAMPLE:** Delivered Coupon Identified as ID: HR2  
**MATERIAL SPECIFICATION:** Delivered Material Identified as Unspecified Carbon Steel with Unspecified Overlay  
**THICKNESS:** 0.750" Overlay  
**TYPE OF TEST:** Test for Information Only

**TENSILE TEST RESULTS**

TEST DATE: 7/5/2024

*LAW TT-1, Current Revision*

MINIMUM TENSILE REQUIRED: Not Specified

SPECIMEN ID	OD (in)	THICKNESS (in)	AREA (sq in)	TENSILE LOAD (lbs)	TENSILE STRENGTH (psi)	YIELD LOAD (lbs)	YIELD STRENGTH (psi)	ELONGATION (%)	LOCATION & TYPE OF FAILURE
1	0.5040	0.2520	0.1990	15,337	77,000	12,600	63,100	3.15	WM-Ductile

NOTES: Reduction of Area: 1.5%

FINAL RESULTS: INFO ONLY

TEST(S) CONDUCTED IN ACCORDANCE WITH: ASTM E8

TEST(S) CONDUCTED BY: TRR

REPORT DATE: 7/5/2024

APPROVED BY: Dennis T. Tobash CWI / WTTI

WTTI Job #: JOB35014

SIGNATURE: 

**QUALITY POLICY STATEMENT**



The services reported in this document were performed in accordance with Welder Training and Testing Institute's Quality System, governed by Quality Manual, Rev. 19, 1/4/23 and AWS Accredited Test Facility (Cert. 0900201). WTTI is accredited by A2LA to ISO 17025 for the test methods listed on Testing Cert. 3430.01 and 3430.02. The Scope of Accreditation is available at [www.wtti.com](http://www.wtti.com). This document shall not be modified or reproduced except in full, without written approval of the laboratory.

These recorded results represent only the specimen(s) tested and are in compliance with applicable code(s), standard(s), and/or contract requirement(s). At no point during testing or inspection at WTTI's facility has this item come into direct contact with mercury, mercury compounds, or devices containing single boundary containment of such. The sample tested meets the requirements of the specification listed however measurement uncertainty has not been analyzed to make a statement of conformance for destructive testing.

Figure A6 Lab Report 6: Heavy Rail #2 – 24060473



**LABORATORY TEST REPORT**

**LABORATORY TEST NUMBER:** 24070039  
**COMPANY NAME:** ESAB Welding & Cutting Products  
**IDENTIFICATION ON SAMPLE:** Delivered Coupon Identified as ID: HR3  
**MATERIAL SPECIFICATION:** Delivered Material Identified as Unspecified Carbon Steel with Unspecified Weld Metal Overlay  
**THICKNESS:** 1.125" Weld Overlay  
**TYPE OF TEST:** Test for Information Only

**TENSILE TEST RESULTS**

**TEST DATE:** 7/19/2024

*LAW TT-1, Current Revision*

**MINIMUM TENSILE REQUIRED:** Not Specified

SPECIMEN ID	OD (in)	THICKNESS (in)	AREA (sq in)	TENSILE LOAD (lbs)	TENSILE STRENGTH (psi)	YIELD LOAD (lbs)	YIELD STRENGTH (psi)	ELONGATION (%)	LOCATION & TYPE OF FAILURE
1	0.5030	0.2515	0.1990	19,910	100,000	n/a	n/a	0.946	BM-Brittle

**NOTES:** Reduction of Area: 0.6%  
 Specimen did not display a discernable yield point during testing.

**FINAL RESULTS:** INFO ONLY

**TEST(S) CONDUCTED IN ACCORDANCE WITH:** ASTM E8

**TEST(S) CONDUCTED BY:** KRG

**REPORT DATE:** 7/19/2024

**APPROVED BY:** Dennis T. Tobash CWI / WTTI

**WTTI Job #:** JOB35061

**SIGNATURE:** 

**QUALITY POLICY STATEMENT**



The services reported in this document were performed in accordance with Welder Training and Testing Institute's Quality System, governed by Quality Manual, Rev. 19, 1/4/23 and AWS Accredited Test Facility (Cert. 8900201). WTTI is accredited by A2LA to ISO 17025 for the test methods listed on Testing Cert. 3430.01 and 3430.02. The Scope of Accreditation is available at www.wtti.com. This document shall not be modified or reproduced except in full, without written approval of the laboratory.

These recorded results represent only the specimen(s) tested and are in compliance with applicable code(s), standard(s), and/or contract requirement(s). At no point during testing or inspection at WTTI's facility has this item come into direct contact with mercury, mercury compounds, or devices containing single boundary containment of such. The sample tested meets the requirements of the specification listed however measurement uncertainty has not been analyzed to make a statement of conformance for destructive testing.

Figure A7 Lab Report 7: Heavy Rail #3 - 24070039

**LABORATORY TEST REPORT**

**LABORATORY TEST NUMBER:** 24070097  
**COMPANY NAME:** ESAB Welding & Cutting Products  
**IDENTIFICATION ON SAMPLE:** Delivered Coupon Identified as ID: HR4  
**MATERIAL SPECIFICATION:** Delivered Material Identified as Unspecified Carbon Steel with Unspecified Weld Metal Overlay  
**THICKNESS:** 1.00" Weld Overlay  
**TYPE OF TEST:** Test for Information Only

**TENSILE TEST RESULTS**

**TEST DATE:** 7/19/2024

*LAW TT-1, Current Revision*

**MINIMUM TENSILE REQUIRED:** Not Specified

SPECIMEN ID	OD (in)	THICKNESS (in)	AREA (sq in)	TENSILE LOAD (lbs)	TENSILE STRENGTH (psi)	YIELD LOAD (lbs)	YIELD STRENGTH (psi)	ELONGATION (%)	LOCATION & TYPE OF FAILURE
1	0.5030	0.2515	0.1990	15,581	78,400	11,700	59,000	2.79	BM-Ductile

**NOTES:** Reduction of Area: 2.5%

**FINAL RESULTS:** INFO ONLY

**TEST(S) CONDUCTED IN ACCORDANCE WITH:** ASTM E8

**TEST(S) CONDUCTED BY:** KRG

**REPORT DATE:** 7/19/2024

**APPROVED BY:** Dennis T. Tobash CWI / WTTI

**WTTI Job #:** JOB35126

**SIGNATURE:** 

**QUALITY POLICY STATEMENT**



The services reported in this document were performed in accordance with Welder Training and Testing Institute's Quality System, governed by Quality Manual, Rev. 19, 1/4/23 and AWS Accredited Test Facility (Cert. 0900201). WTTI is accredited by A2LA to ISO 17025 for the test methods listed on Testing Cert. 3430.01 and 3430.02. The Scope of Accreditation is available at www.wtti.com. This document shall not be modified or reproduced except in full, without written approval of the laboratory.

These recorded results represent only the specimen(s) tested and are in compliance with applicable code(s), standard(s), and/or contract requirement(s). At no point during testing or inspection at WTTI's facility has this item come into direct contact with mercury, mercury compounds, or devices containing single boundary containment of such. The sample tested meets the requirements of the specification listed however measurement uncertainty has not been analyzed to make a statement of conformance for destructive testing.

Figure A8 Lab Report 8: Heavy Rail #4 – 24070097

**LABORATORY TEST REPORT**

**LABORATORY TEST NUMBER:** 24070238  
**COMPANY NAME:** ESAB Welding & Cutting Products  
**IDENTIFICATION ON SAMPLE:** Delivered Coupon Identified as ID: HR5  
**MATERIAL SPECIFICATION:** Delivered Material Identified as Unspecified Carbon Steel with Unspecified Weld Metal Overlay  
**THICKNESS:** 1.00" Weld Overlay  
**TYPE OF TEST:** Test for Information Only

**TENSILE TEST RESULTS**

**TEST DATE:** 7/30/2024

*LAW TT-1, Current Revision*

**MINIMUM TENSILE REQUIRED:** Not Specified

SPECIMEN ID	OD (in)	THICKNESS (in)	AREA (sq in)	TENSILE	TENSILE	YIELD	YIELD	ELONGATION (%)	LOCATION & TYPE OF FAILURE
				LOAD (lbs)	STRENGTH (psi)	LOAD (lbs)	STRENGTH (psi)		
1	0.5010	n/a	0.1970	19,547	99,200	12,700	64,300	7.59	BM-Ductile

**NOTES:** Reduction of Area: 9.5%

**FINAL RESULTS:** INFO ONLY

**TEST(S) CONDUCTED IN ACCORDANCE WITH:** ASTM E8

**TEST(S) CONDUCTED BY:** KRG

**REPORT DATE:** 7/31/2024

**APPROVED BY:** Dennis T. Tobash CWI / WTTI

**WTTI Job #:** JOB35241

**SIGNATURE:** 

**QUALITY POLICY STATEMENT**



The services reported in this document were performed in accordance with Welder Training and Testing Institute's Quality System, governed by Quality Manual, Rev. 19, 1/4/23 and AWS Accredited Test Facility (Cert. #900201). WTTI is accredited by A2LA to ISO 17025 for the test methods listed on Testing Cert. 3430.01 and 3430.02. The Scope of Accreditation is available at www.wtti.com. This document shall not be modified or reproduced except in full, without written approval of the laboratory.

These recorded results represent only the specimen(s) tested and are in compliance with applicable code(s), standard(s), and/or contract requirement(s). At no point during testing or inspection at WTTI's facility has this item come into direct contact with mercury, mercury compounds, or devices containing single boundary containment of such. The sample tested meets the requirements of the specification listed however measurement uncertainty has not been analyzed to make a statement of conformance for destructive testing.

Figure A9 Lab Report 9: Heavy Rail #5 - 24070238

**LABORATORY TEST REPORT**

**LABORATORY TEST NUMBER:** 24070239  
**COMPANY NAME:** ESAB Welding & Cutting Products  
**IDENTIFICATION ON SAMPLE:** Delivered Coupon Identified as ID: HR6  
**MATERIAL SPECIFICATION:** Delivered Material Identified as Unspecified Carbon Steel with Unspecified Weld Metal Overlay  
**THICKNESS:** 1.00" Weld Overlay  
**TYPE OF TEST:** Test for Information Only

**TENSILE TEST RESULTS**

**TEST DATE:** 7/30/2024

*LAW TT-1, Current Revision*

**MINIMUM TENSILE REQUIRED:** Not Specified

SPECIMEN ID	OD (in)	THICKNESS (in)	AREA (sq in)	TENSILE LOAD (lbs)	TENSILE STRENGTH (psi)	YIELD LOAD (lbs)	YIELD STRENGTH (psi)	ELONGATION (%)	LOCATION & TYPE OF FAILURE
1	0.5010	n/a	0.1970	17,041	86,400	12,700	64,500	3.42	BM-Ductile

**NOTES:** Reduction of Area: 2.9%

**FINAL RESULTS:** INFO ONLY

**TEST(S) CONDUCTED IN ACCORDANCE WITH:** ASTM E8

**TEST(S) CONDUCTED BY:** KRG

**REPORT DATE:** 7/31/2024

**APPROVED BY:** Dennis T. Tobash CWI / WTTI

**WTTI Job #:** JOB35241

**SIGNATURE:** 

**QUALITY POLICY STATEMENT**



The services reported in this document were performed in accordance with Welder Training and Testing Institute's Quality System, governed by Quality Manual, Rev. 19, 1/4/23 and AWS Accredited Test Facility (Cert. #900201). WTTI is accredited by A2LA to ISO 17025 for the test methods listed on Testing Cert. 3430.01 and 3430.02. The Scope of Accreditation is available at www.wtti.com. This document shall not be modified or reproduced except in full, without written approval of the laboratory.

These recorded results represent only the specimen(s) tested and are in compliance with applicable code(s), standard(s), and/or contract requirement(s). At no point during testing or inspection at WTTI's facility has this item come into direct contact with mercury, mercury compounds, or devices containing single boundary containment of such. The sample tested meets the requirements of the specification listed however measurement uncertainty has not been analyzed to make a statement of conformance for destructive testing.

Figure A10 Lab Report 10: Heavy Rail #6 - 24070239



**LABORATORY TEST REPORT**

**LABORATORY TEST NUMBER:** 24080089  
**COMPANY NAME:** ESAB Welding & Cutting Products  
**IDENTIFICATION ON SAMPLE:** Delivered Coupon Identified as LR5  
**MATERIAL SPECIFICATION:** Delivered Material Identified as Unspecified Carbon Steel with Unspecified Overlay  
**DIMENSIONS:** 0.650"  
**TYPE OF TEST:** Test for Information Only

**TENSILE TEST RESULTS**

**TEST DATE:** 8/16/2024

*LAW TT-1, Current Revision*

**MINIMUM TENSILE REQUIRED:** Not Specified

SPECIMEN ID	WIDTH (in)	THICKNESS (in)	AREA (sq in)	TENSILE LOAD (lbs)	TENSILE STRENGTH (psi)	YIELD LOAD (lbs)	YIELD STRENGTH (psi)	ELONGATION (%)	LOCATION & TYPE OF FAILURE
1	0.5030	0.2515	0.1990	16,788	84,500	n/a	n/a	9.75	WM-Ductile

**NOTES:** Reduction of Area: 9.7%

**FINAL RESULTS:** INFO ONLY

**TEST(S) CONDUCTED IN ACCORDANCE WITH:** ASTM E8

**TEST(S) CONDUCTED BY:** KRG

**REPORT DATE:** 8/28/2024

**APPROVED BY:** Dennis T. Tobash CWI / WTTI

**WTTI Job #:** JOB35439

**SIGNATURE:** 

**QUALITY POLICY STATEMENT**



*The services reported in this document were performed in accordance with Welder Training and Testing Institute's Quality System, governed by Quality Manual, Rev. 19, 1/4/23 and AWS Accredited Test Facility (Cert. 9900201). WTTI is accredited by A2LA to ISO 17025 for the test methods listed on Testing Cert. 3430.01 and 3430.02. The Scope of Accreditation is available at www.wtti.com. This document shall not be modified or reproduced except in full, without written approval of the laboratory.*

*These recorded results represent only the specimen(s) tested and are in compliance with applicable code(s), standard(s), and/or contract requirement(s). At no point during testing or inspection at WTTI's facility has this item come into direct contact with mercury, mercury compounds, or devices containing single boundary containment of such. The sample tested meets the requirements of the specification listed however measurement uncertainty has not been analyzed to make a statement of conformance for destructive testing.*

Figure A11 Lab Report 11: Light Rail #5 - 24080089

**LABORATORY TEST REPORT**

**LABORATORY TEST NUMBER:** 24080090  
**COMPANY NAME:** ESAB Welding & Cutting Products  
**IDENTIFICATION ON SAMPLE:** Delivered Coupon Identified as LR6  
**MATERIAL SPECIFICATION:** Delivered Material Identified as Unspecified Carbon Steel with Unspecified Overlay  
**DIMENSIONS:** 0.700"  
**TYPE OF TEST:** Test for Information Only

**TENSILE TEST RESULTS**

**TEST DATE:** 8/16/2024

*LAW TT-1, Current Revision*

**MINIMUM TENSILE REQUIRED:** Not Specified

SPECIMEN ID	WIDTH (in)	THICKNESS (in)	AREA (sq in)	TENSILE	TENSILE	YIELD	YIELD	ELONGATION (%)	LOCATION & TYPE OF FAILURE
				LOAD (lbs)	STRENGTH (psi)	LOAD (lbs)	STRENGTH (psi)		
1	0.5020	0.2510	0.1980	26,862	136,000	22,600	114,000	1.5	WM-Ductile

**NOTES:** Reduction of Area: 2.2%

**FINAL RESULTS:** INFO ONLY

**TEST(S) CONDUCTED IN ACCORDANCE WITH:** ASTM E8

**TEST(S) CONDUCTED BY:** KRG

**REPORT DATE:** 8/28/2024

**APPROVED BY:** Dennis T. Tobash CWI / WTTI

**WTTI Job #:** JOB35439

**SIGNATURE:** 

**QUALITY POLICY STATEMENT**



The services reported in this document were performed in accordance with Welder Training and Testing Institute's Quality System, governed by Quality Manual, Rev. 19, 1/4/23 and AWS Accredited Test Facility (Cert. #900201). WTTI is accredited by A2LA to ISO 17025 for the test methods listed on Testing Cert. 3430.01 and 3430.02. The Scope of Accreditation is available at [www.wtti.com](http://www.wtti.com). This document shall not be modified or reproduced except in full, without written approval of the laboratory.

These recorded results represent only the specimen(s) tested and are in compliance with applicable code(s), standard(s), and/or contract requirement(s). At no point during testing or inspection at WTTI's facility has this item come into direct contact with mercury, mercury compounds, or devices containing single boundary containment of such. The sample tested meets the requirements of the specification listed however measurement uncertainty has not been analyzed to make a statement of conformance for destructive testing.

Figure A12 Lab Report 12: Light Rail #6 - 24080090

**LABORATORY TEST REPORT**

**LABORATORY TEST NUMBER:** 24080456  
**COMPANY NAME:** ESAB Welding & Cutting Products  
**IDENTIFICATION ON SAMPLE:** Delivered Coupon Identified as LR7  
**MATERIAL SPECIFICATION:** Delivered Material Identified as Unspecified Carbon Steel with Unspecified Overlay  
**DIMENSIONS:** 0.750"  
**TYPE OF TEST:** Test for Information Only

**TENSILE TEST RESULTS**

**TEST DATE:** 9/11/2024

*IAW TT-1, Current Revision*

*MINIMUM TENSILE REQUIRED: Not Specified*

SPECIMEN ID	OD (in)	THICKNESS (in)	AREA (sq in)	TENSILE LOAD (lbs)	TENSILE STRENGTH (psi)	YIELD LOAD (lbs)	YIELD STRENGTH (psi)	ELONGATION (%)	LOCATION & TYPE OF FAILURE
1	0.3530	0.1765	0.0979	8,433	86,200	1,120	11,500	0.293	BM-Ductile

**NOTES:** Reduction of Area: 0.5%

**FINAL RESULTS:** INFO ONLY

**TEST(S) CONDUCTED IN ACCORDANCE WITH:** ASTM E8

**TEST(S) CONDUCTED BY:** KRG

**REPORT DATE:** 9/11/2024

**APPROVED BY:** Dennis T. Tobash CWI / WTTI

**WTTI Job #:** JOB35674

**SIGNATURE:** 

**QUALITY POLICY STATEMENT**



The services reported in this document were performed in accordance with Welder Training and Testing Institute's Quality System, governed by Quality Manual, Rev. 19, 1/4/23 and AWS Accredited Test Facility (Cert. #900201). WTTI is accredited by A2LA to ISO 17025 for the test methods listed on Testing Cert. 3430.01 and 3430.02. The Scope of Accreditation is available at www.wtti.com. This document shall not be modified or reproduced except in full, without written approval of the laboratory.

These recorded results represent only the specimen(s) tested and are in compliance with applicable code(s), standard(s), and/or contract requirement(s). At no point during testing or inspection at WTTI's facility has this item come into direct contact with mercury, mercury compounds, or devices containing single boundary containment of such. The sample tested meets the requirements of the specification listed however measurement uncertainty has not been analyzed to make a statement of conformance for destructive testing.

Figure A13 Lab Report 13: Light Rail #8



**ESAB**  
MicroMacro-Hardness Test Report

Date: 26-06-2024  
Tester: Francis LeClaire  
Program: UNLV Light Rail 4  
Job: Test job # 1



Job data

Mean	Minimum	Maximum	Range	Std. deviation
415.2	275.0	485.3	210.3	70.8

Hardness Trace

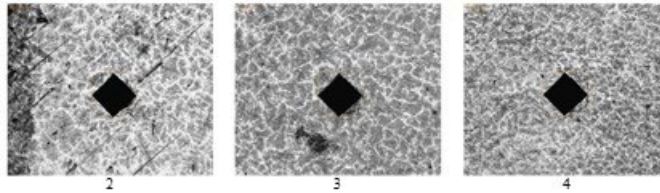
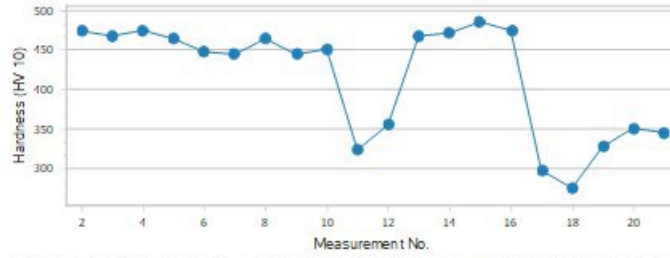


Figure A14 Lab Report 14: Hardness Test

UNLV Rail Project

ThermaClad 446 Wire

5/29/2024

	Heavy Rail-SubArc DCEP	Converted	Specification
<b>Ultimate Tensile Strength (psi)</b>	137,000	944.6 N/mm <sup>2</sup>	980 N/mm <sup>2</sup> Minimum (980MPa)
<b>Yield Strength (psi)</b>	122,000	841.2 N/mm <sup>2</sup>	511 N/mm <sup>2</sup> Minimum (830MPa)
<b>% Elongation</b>	2.60	2.6	10% minimum
<b>% Reduction of Area</b>	0.395	0.395	None
		<b>Converted Avg.</b>	
<b>Microhardness HV10-Layer 5</b>	389.4, 402.8	378	310 HB min (318Hv)
<b>Microhardness HV10-Layer 4</b>	394.7, 389.4	375	310 HB min
<b>Microhardness HV10-Layer 3</b>	422.9, 417.0	399	310 HB min
<b>Microhardness HV10-Layer 2</b>	461.2, 465.3	435	310 HB min
<b>Microhardness HV10-Layer 1</b>	584.7, 552.3	514	310 HB min

Figure A15 Lab Report 15: Heavy Rail strength and hardness



Figure 16 Lab Report 16: Printing zone 1

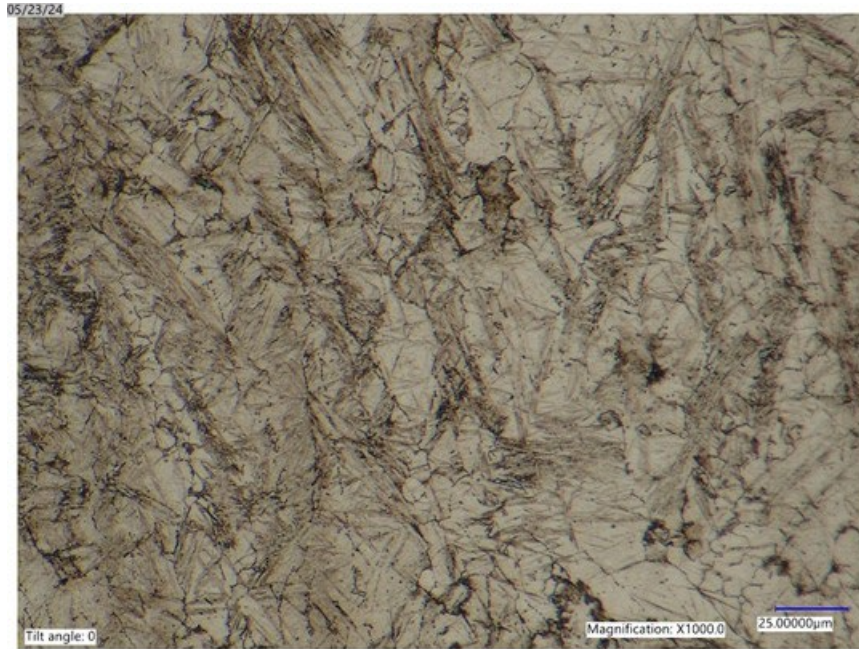


Figure A17 Lab Report 17: Printing zone 2



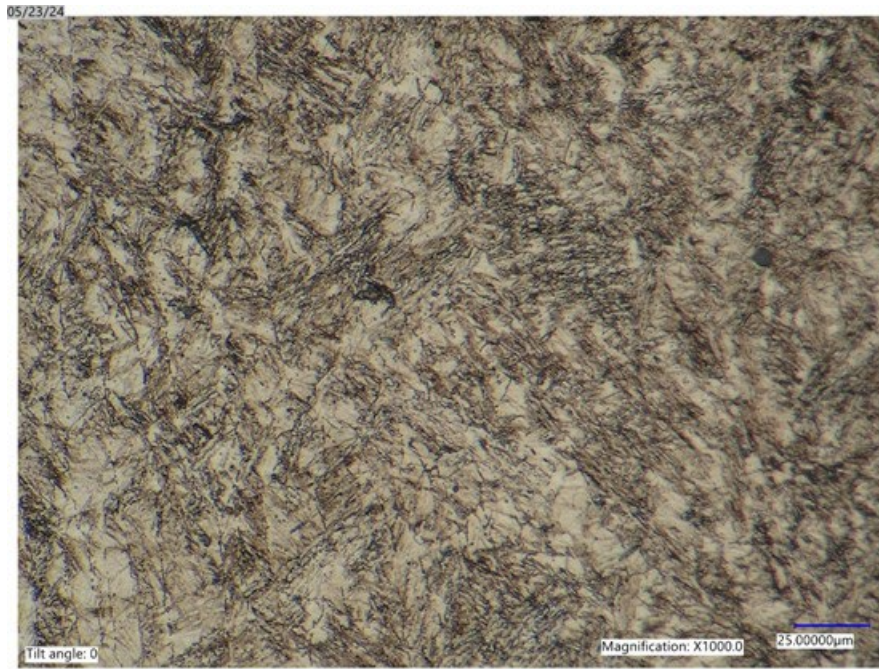


Figure A18 Lab Report 18: Printing zone 3

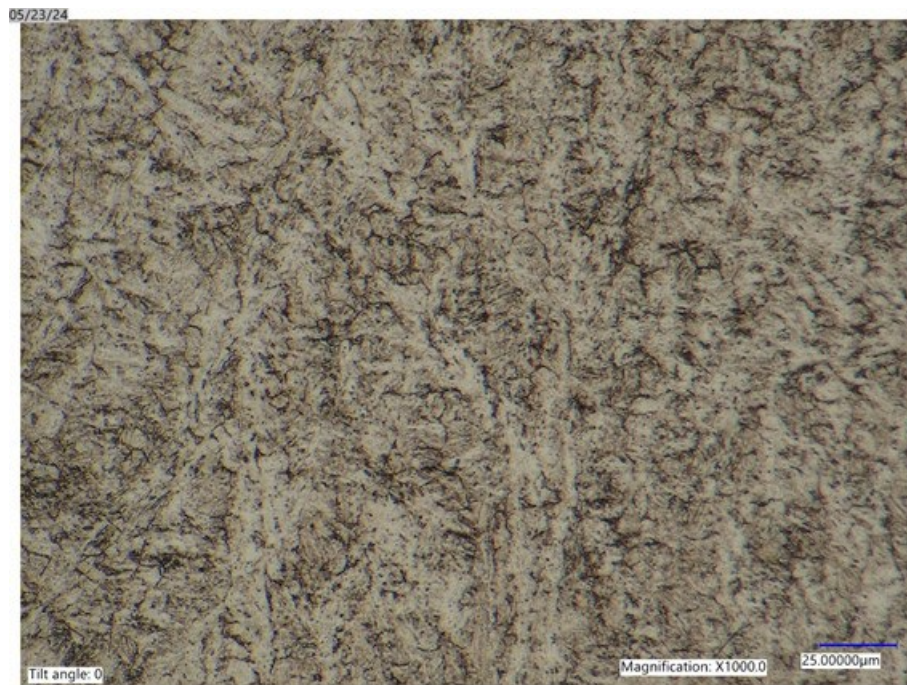


Figure 19 Lab Report 19: Printing zone 4



Figure 20 Lab Report 20: Printing zone 5

## **ACKNOWLEDGEMENTS**

This study was conducted with the support from the USDOT Tier 1 University Transportation Center on Railroad Sustainability and Durability.



## ABOUT THE AUTHOR

**Mr. Ershad Mortazavian** was a graduate student when he worked on this project. He has his master's and bachelor's degrees in mechanical engineering from the University of Kashan and University of Kashan, respectively.

**Mr. Arman Ali Mohammadi** was a graduate student when he worked on this project. He obtained his master's and bachelor's degrees in mechanical engineering from the University of Tehran and Isfahan University of Technology, respectively.

**Dr. Zhiyong Wang** is an associate professor in the Department of Mechanical Engineering at the University of Nevada, Las Vegas. His research interests include 3D printing heavy metals and bio materials, advanced material manufacturing, and CVD process for mono crystal materials. He has a Ph.D. in mechanical engineering from the Harbin Institute of Technology.

**Dr. Hualiang (Harry) Teng** is a professor in the Department of Civil and Environmental Engineering and construction. His expertise includes railroad engineering and management, intelligent transportation systems, highway safety, and air quality analysis. He was the director of the Railroad University Transportation University at UNLV.